

Optical Diagnostics for Structural Health Monitoring of Inaccessible Systems

Tamer Yilmaz Cosgun

Submitted for the degree of Doctor of Philosophy

School of Engineering and Physical Sciences

Heriot-Watt University

November 2022

The copyright in this thesis is owned by the author. Any quotation from the thesis or use of any of the information contained in it must acknowledge this thesis as the source of the quotation or information.

Abstract

The work in this thesis is concerned with the development of optical sensors for the structural health monitoring of systems with inaccessible components in the presence of ionising radiation. Two primary approaches to determine structural health are investigated, these being the implementation of distance measurement sensors (to assess, for example, the occurrence of creep/cracking) and gas sensors (to assess the occurrence of outgassing which can be indicative of chemical ageing).

Distance measurement sensors are developed using fibre optic Fabry-Pérot interferometry (FPI) measured in reflection. A fast-Fourier transform (FFT) of the reflected interference spectrum is incorporated to demodulate the signal and extract cavity length information. To mitigate noise and enhance measurement accuracy and sensitivity, spectrum reconstruction in the form of a function-fitting algorithm (FFA) is developed, the input of which is fed by the FFT output. The FFA demonstrates measurement improvements of approximately one-and-a-half orders of magnitude.

To situate the fibre FPI sensors within spatially confined, closely positioned components, turning mirrors are fabricated on two cores of multi-core fibre (MCF) which redirect the fibre-guided light perpendicular to the fibre axis in opposite directions. This allows for the absolute distance between component parts to be determined as Fabry-Pérot cavities are formed on both sides of the MCF. Three different turning-mirror fabrication processes are developed, the results from each are compared and discussed.

The distance measurement capabilities are expanded to that of a two-point measurement system to allow for tilt measurement competencies. This facilitates further comprehensiveness with regards to structural health monitoring. Further, two optical gas sensors are investigated, both based on the principle of absorption spectroscopy. One consists of evanescent wave generation in a tapered fibre and the other of incoherent broadband cavity-enhancement. Modelled and experimental results are presented and limitations are discussed.

To my mum, baba, sister, and the love of my life.

Acknowledgements

I would first and foremost like to thank my academic supervisor, Bill MacPherson – his seemingly unending knowledge on fibre sensors and his problem solving ability has helped me more times than I can count. This appreciation is also extended to the other members of the Applied Optics and Photonics research group at Heriot-Watt University, namely Adrian Dzipalski, who I could rely on undoubtedly for assistance and expert insight, as well as Wojciech Gora, Paulina Morawska, Ben Michie, Loki Muniraj, Mark McDonald, Stephen Dondieu, and Donald Risbridger, with whom it was a pleasure to share the laboratory space with.

Secondly, I would like to thank Simon Brooks, my initial industrial supervisor at AWE, and also Matthew Kingston, who later took over this role. Both provided excellent feedback and, at times, much needed encouragement. I would also like to thank those who have contributed towards maintaining the ongoing collaboration between Heriot-Watt University and AWE, primarily Richard Carter, Robert Maier, and Scott McCulloch, who have all provided valuable comments and insight towards this work.

There are portions of work covered in this thesis which would have simply not been possible if not for the collaborative effort of certain colleagues. I would like to give special thanks to Calum Ross and Mark Leonard, both who played critical roles in the fabrication of the Fabry-Pérot fibre sensors studied in this thesis.

Finally, I would like to thank those dearest to me. My mother, Havva, my father, Yilmaz, my sister, Tanay, and my other half, Beatrice. These wonderful people have helped me in more ways than I could simply list with words – It is immeasurable.

Research Thesis Submission

Please note this form should be bound into the submitted thesis.

| | | | |
|---|---------------------|----------------|-----|
| Name: | Tamer Yilmaz Cosgun | | |
| School: | EPS | | |
| Version: <small>(i.e. First, Resubmission, Final)</small> | Final | Degree Sought: | PhD |

Declaration

In accordance with the appropriate regulations I hereby submit my thesis and I declare that:

1. The thesis embodies the results of my own work and has been composed by myself
2. Where appropriate, I have made acknowledgement of the work of others
3. The thesis is the correct version for submission and is the same version as any electronic versions submitted*.
4. My thesis for the award referred to, deposited in the Heriot-Watt University Library, should be made available for loan or photocopying and be available via the Institutional Repository, subject to such conditions as the Librarian may require
5. I understand that as a student of the University I am required to abide by the Regulations of the University and to conform to its discipline.
6. I confirm that the thesis has been verified against plagiarism via an approved plagiarism detection application e.g. Turnitin.

ONLY for submissions including published works


Please note you are only required to complete the Inclusion of Published Works Form (page 2) if your thesis contains published works)

7. Where the thesis contains published outputs under Regulation 6 (9.1.2) or Regulation 43 (9) these are accompanied by a critical review which accurately describes my contribution to the research and, for multi-author outputs, a signed declaration indicating the contribution of each author (complete)
8. Inclusion of published outputs under Regulation 6 (9.1.2) or Regulation 43 (9) shall not constitute plagiarism.

* Please note that it is the responsibility of the candidate to ensure that the correct version of the thesis is submitted.

| | | | |
|-------------------------|---|-------|------------|
| Signature of Candidate: |  | Date: | 03/11/2022 |
|-------------------------|---|-------|------------|

Submission

| | |
|--|---|
| Submitted By <small>(name in capitals)</small> : | TAMER YILMAZ COSGUN |
| Signature of Individual Submitting: |  |
| Date Submitted: | 03/11/2022 |

For Completion in the Student Service Centre (SSC)

| | | | | | | |
|--|-----------|-----|----|----------|-----|----|
| Limited Access | Requested | Yes | No | Approved | Yes | No |
| E-thesis Submitted (mandatory for final theses) | | | | | | |
| Received in the SSC by <small>(name in capitals)</small> : | | | | Date: | | |

Table of Contents

List of Abbreviations

Nomenclature

| | |
|--|-----------|
| Chapter 1. Introduction | 1 |
| 1.1 Interferometry | 1 |
| 1.2 Spectroscopy..... | 3 |
| 1.3 Fibre optic technology | 5 |
| 1.4 Scope and motivation | 6 |
| 1.5 Thesis layout..... | 7 |
| Chapter 2. Literature review | 9 |
| 2.1 Introduction | 9 |
| 2.2 Distance measurements | 10 |
| 2.2.1 Mechanical devices..... | 11 |
| 2.2.2 Optical devices..... | 12 |
| 2.2.3 Other devices | 19 |
| 2.2.4 Conclusions | 20 |
| 2.3 Gas sensing | 21 |
| 2.3.1 Electrochemical gas sensors | 22 |
| 2.3.2 Mass-sensitive gas sensors | 23 |
| 2.3.3 Magnetic gas sensors | 25 |
| 2.3.4 Thermometric gas sensors | 27 |
| 2.3.5 Optical gas sensors | 29 |
| 2.3.6 Conclusions | 32 |
| Chapter 3. Fabry-Pérot interferometry and cavity demodulation | 34 |
| 3.1 Introduction | 34 |
| 3.2 Principles of Fabry-Pérot interferometry..... | 34 |
| 3.2.1 Mathematical model | 34 |
| 3.2.2 Fabry-Pérot interferometry using optical fibres | 37 |

| | |
|---|-----------|
| 3.3 Demodulation methods..... | 41 |
| 3.3.1 Fast-Fourier transform | 43 |
| 3.3.2 Function-fitting algorithm | 44 |
| 3.4 Evaluation of demodulation methods using LabVIEW virtual instruments (VI).. | 47 |
| 3.5 Experimental evaluation of demodulation methods | 50 |
| 3.5.1 Experimental configuration | 51 |
| 3.5.2 Normal cleaved fibre | 52 |
| 3.5.3 45° angle cleaved fibre | 54 |
| 3.6 Conclusions | 57 |
| Chapter 4. Fibre optic probes for distance measurements | 59 |
| 4.1 Introduction | 59 |
| 4.2 Fibre characteristics and limitations | 60 |
| 4.2.1 Single-core fibre | 60 |
| 4.2.2 Multi-core fibre..... | 61 |
| 4.2.3 Fan-out system and insertion loss..... | 66 |
| 4.3 Focused-ion beam milling | 69 |
| 4.4 Femtosecond laser inscription and selective chemical etching | 72 |
| 4.4.1 Subtractive modification..... | 72 |
| 4.4.2 Fabrication of fused-silica component..... | 75 |
| 4.5 Sensor performance analysis | 79 |
| 4.6 Conclusions | 87 |
| Chapter 5. Fibre optic probes for tilt measurements | 89 |
| 5.1 Introduction | 89 |
| 5.2 Differential Fabry-Pérot interferometry | 90 |
| 5.3 Sensor design and considerations | 92 |
| 5.3.1 Component fabrication | 92 |
| 5.3.2 Total internal reflection considerations | 93 |
| 5.3.3 Parasitic optical cavities | 97 |

| | |
|--|------------|
| 5.3.4 Tilt effects on return signal..... | 100 |
| 5.4 Sensor performance analysis | 104 |
| 5.4.1 Experimental configuration | 104 |
| 5.4.2 Results | 105 |
| 5.5 Conclusion..... | 107 |
| Chapter 6. Gas speciation measurements | 109 |
| 6.1 Introduction | 109 |
| 6.2 Principles of absorption spectroscopy | 109 |
| 6.3 Evanescent wave fibre optic sensor..... | 111 |
| 6.3.1 Fibre tapering..... | 112 |
| 6.3.2 Evanescent wave simulation..... | 115 |
| 6.3.3 Discussion of limitations | 117 |
| 6.4 Incoherent broadband cavity-enhanced absorption spectroscopy | 119 |
| 6.4.1 Mathematical model | 119 |
| 6.4.2 Modelled absorption of NO ₂ | 122 |
| 6.4.3 Cavity design considerations | 126 |
| 6.4.4 Experimental configuration | 129 |
| 6.4.5 Experimental investigation and problem identification..... | 131 |
| 6.5 Conclusions | 137 |
| Chapter 7. Discussion and conclusions | 139 |
| 7.1 Overview and discussion..... | 139 |
| 7.2 Future work | 142 |
| 7.2.1 Lens fabrication on fused-silica component..... | 142 |
| 7.2.2 Flame polishing | 143 |
| 7.2.3 Zeolites | 145 |
| 7.3 Concluding remarks..... | 147 |
| References | 149 |

List of Abbreviations

| | |
|---------|--|
| AWE | Atomic Weapons Establishment |
| CCD | Charged-coupled device |
| CEAS | Cavity-enhance absorption spectroscopy |
| CRDS | Cavity ringdown spectroscopy |
| DFT | Discrete Fourier transform |
| EFPI | Extrinsic Fabry-Pérot interferometer/interferometry |
| EM | Electromagnetic |
| EW | Evanescent wave |
| EWFS | Evanescent wave fibre optic sensor/sensing |
| FFA | Function-fitting algorithm |
| FFT | Fast-Fourier transform |
| FIB | Focused-ion beam |
| FLISE | Femtosecond laser induced selective etching |
| FPI | Fabry-Pérot interferometer/interferometry |
| FSR | Free spectral range |
| FWHM | Full width at half maximum |
| IBBCEAS | Incoherent broadband cavity-enhanced absorption spectroscopy |
| IDT | Interdigital transducer |
| IFPI | Intrinsic Fabry-Pérot interferometer/interferometry |
| ISE | Ion selective electrode |
| LDLS | Laser driven light source |
| MCF | Multi-core fibre |
| MFD | Mode field diameter |
| NA | Numerical aperture |
| OPD | Optical path difference |
| PMT | Photomultiplier tube |
| ppb | Parts per billion |
| ppm | Parts per million |
| QCM | Quartz crystal microbalance |
| RNG | Random number generator |
| ROC | Radius of curvature |

| | |
|------|-----------------------------------|
| SAW | Surface acoustic wave |
| SCF | Single-core fibre |
| SEM | Scanning electron microscope |
| SERS | Surface-enhanced Raman scattering |
| SHM | Structural health monitoring |
| SLE | Selective laser-induced etching |
| SNR | Signal-to-noise ratio |
| SSE | Sum of squares error |
| TEM | Transverse electromagnetic mode |
| TIR | Total internal reflection |
| TOF | Time of flight |
| ULAE | Ultra-fast laser assisted etching |
| ULI | Ultrafast laser inscription |
| UV | Ultraviolet |
| VOC | Volatile organic compound |
| WLI | White light interferometry |

Nomenclature

| | |
|---------------|----------------------------------|
| D | Distance |
| λ_m | Modulation wavelength |
| E | Electrical potential |
| \mathcal{R} | Universal gas constant |
| \mathcal{T} | Temperature |
| η | Number of moles |
| F | Faraday constant |
| A | Absorbance |
| χ_m | Molar magnetic susceptibility |
| ε | Molar extinction coefficient |
| c | Concentration |
| l | Length |
| I | Light intensity |
| δ | Phase difference |
| n | Refractive index |
| d | Cavity length |
| λ | Wavelength |
| R | Reflectivity |
| $L(dB)$ | Signal loss measured in decibels |
| c | Speed of light in free space |
| ν | Optical frequency |
| f | Frequency |
| θ | Angle |
| σ | Absorption cross-section |
| α | Absorption coefficient |
| L | Optical signal loss |
| N_A | Avogadro's constant |
| P | Pressure |
| V | Volume |

Chapter 1

Introduction

A sea of photons that cumulatively display the quantifiable emergent properties of energy and frequency: Light. Over centuries, methods to generate, contain, and control light to exploit its interaction with matter have been developed, whether to illuminate a dark room, or to transmit information across the World seemingly instantaneously. As the understanding deepened, the applications expanded.

The experiments of Bouguer in the early 18th century [1], later cited by Lambert [2], and further built upon by Beer [3] in the mid-19th century, pathed the way for using light as a measurement tool. In this case, measuring the chemical and optical properties of substances as a result of its absorbing interaction with light. By the late 19th century, the experiments of Michelson and Morley [4] established a new way in which light can be used as a measurement tool: The measurement of distances became possible, in a way analogous to a ruler, but with much greater precision and accuracy, based upon the sub-micron scale of the wavelength of light.

Over one hundred years of technological developments have allowed these concepts to flourish. The advent of the laser in the 1960s catapulted the field of photonics into new territories. What was once spearheaded by Bouguer-Lambert-Beer and Michelson-Morley is to this day being further explored and advanced. These being the techniques of spectroscopy and interferometry.

1.1 Interferometry

In terms of optical metrology, which is the use of light to define measurements, the manipulation of light is only as useful as its detectability. The electromagnetic (EM) spectrum is broad, spanning from gamma and x-rays ($\sim 10^{19} - 10^{17}$ Hz) through ultraviolet (UV), visible, and (near-)infrared ($\sim 10^{15} - 10^{13}$ Hz) to microwaves and

radio waves ($\sim 10^9 - 10^3$ Hz). The UV – near-infrared region may be considered the more useful band of the EM spectrum for optical metrology, yet these frequencies are simply too high to directly measure their oscillations. Therefore, methods which exploit their wave-like properties are employed which manifest detectable effects, one of the most rudimentary of which is to combine waves of differing frequencies. When two waves with frequencies f_1 and f_2 are combined, they will interfere with one another in a way that results in a beat frequency, f_b , where $f_b = |f_1 - f_2|$, as illustrated in Figure 1.1.

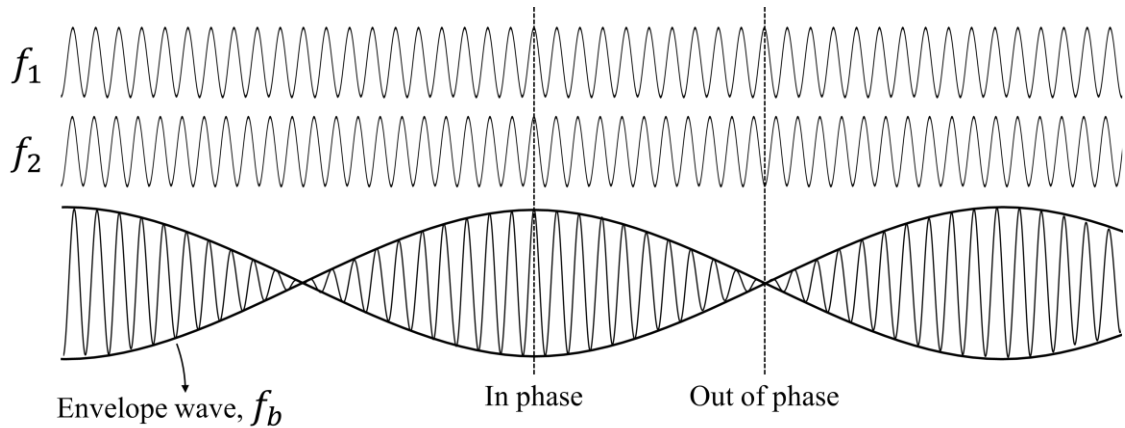


Figure 1.1: Illustration of two waves with different frequencies interfering with one another to form an envelope wave with a characterised beat frequency.

The constituent frequencies that form the envelope wave can be finely tuned or selected to produce a beat frequency in the kHz regime, thereby creating a wave detectable through standard techniques (e.g., by using the appropriate photodiode connected to an oscilloscope). A single frequency could also be used, where a second frequency is induced by some external effect, such as a temperature variation – measurement of the corresponding beat frequency, through careful calibration, can therefore behave as a sensor for said temperature variation.

If both frequencies are identical, then there is no beat frequency upon the combination of both constituent frequencies, but they instead interfere constructively or destructively (or anything in between) depending on the relative phase difference. As illustrated in Figure 1.2, where there is no relative phase difference, the waves constructively interfere and their amplitudes are combined additively (Figure 1.2 (a)), and where a relative phase difference of π radians is introduced, the waves destructively interfere and their amplitudes are combined in a manner where the outcome is subtractive (Figure 1.2 (b)).

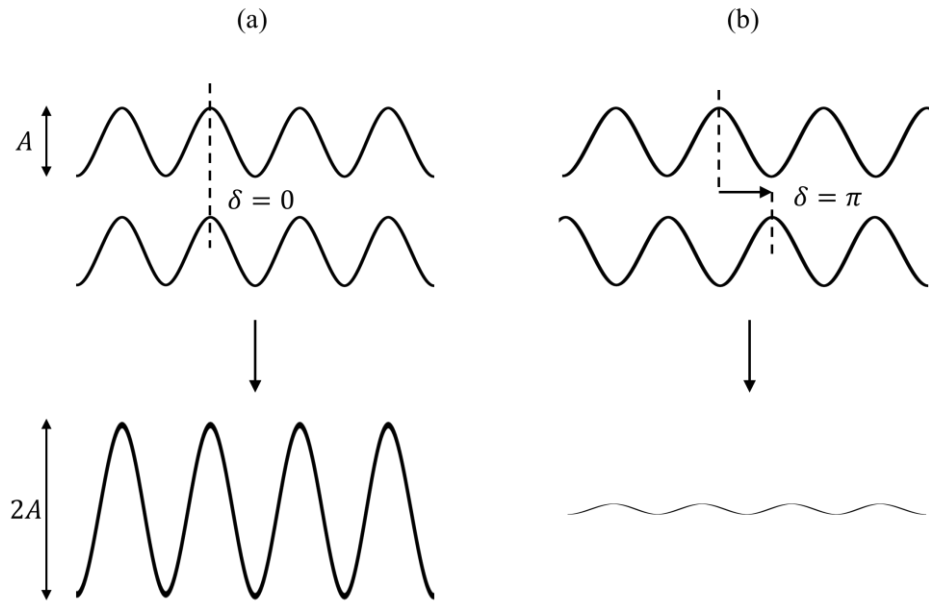


Figure 1.2: Illustration of the combination of two waves with the same frequency that result in (a) constructive interference and (b) destructive interference.

Bright (constructive) and dark (destructive) fringes are continually generated for each 2π relative phase shift. Where the wavelength of the light used is known, this transition from bright to dark to bright, and so on, can be correlated to a physical distance. Interferometry in this manner has become a pillar in optical distance measurements. Theoretically, using a shorter wavelength (i.e., higher frequency) should elicit a higher resolution distance measurement, but operating outside the UV – near-infrared band can introduce complications with the require equipment such as light sources and detectors. While interferometry can enable distance-based measurements, detecting light in other ways yields the possibility of different measurands. One such technique is spectroscopy.

1.2 Spectroscopy

Spectroscopy is the study of light not at a single wavelength nor the EM spectrum as a collective, but as a series of individual wavelengths that comprise it. When light is incident upon a material or substance, generally speaking, there are three types of interaction which may occur: the light may reflect, transmit through (refract), and/or be absorbed. Each of these interactions, when studied closely enough, are non-trivial. In fact, the particular way in which any of these interactions take place at specific wavelengths can provide important information about the substance in question. For example, Raman spectroscopy offers a technique to identify substances by the way specific incident wavelengths of light are scattered. Further, absorption spectroscopy, as the name suggests, utilises the absorption that occurs at specific wavelengths to identify substances. A comprehensive discussion regarding these techniques and more can be found in § 2.3.5.

Similarly, as with interferometric techniques, the usefulness of spectroscopy is only revealed when the detection of light is possible. In this case, the detection of light at each individual wavelength across the input spectrum. For this to be achieved, there must first be a mechanism to “split” light into its constituent wavelengths. In the mid-17th century, Newton discovered that the white light of sunlight, when passed through a small hole and then through a prism, dispersed itself into the colours of the rainbow, which when recombined formed white light once again [5]. The experimental advances of Fraunhofer in the early 19th century enabled spectroscopy to become what it is today [6]. By modern standards, a typical spectrometer will disperse broadband light by a diffraction grating and collected by a detector as illustrated in Figure 1.3, either all at once by means of a charged-coupled device (CCD) (Figure 1.3(a)), or point-by-point with a photodetector and a rotating diffraction grating (Figure 1.3(b)).

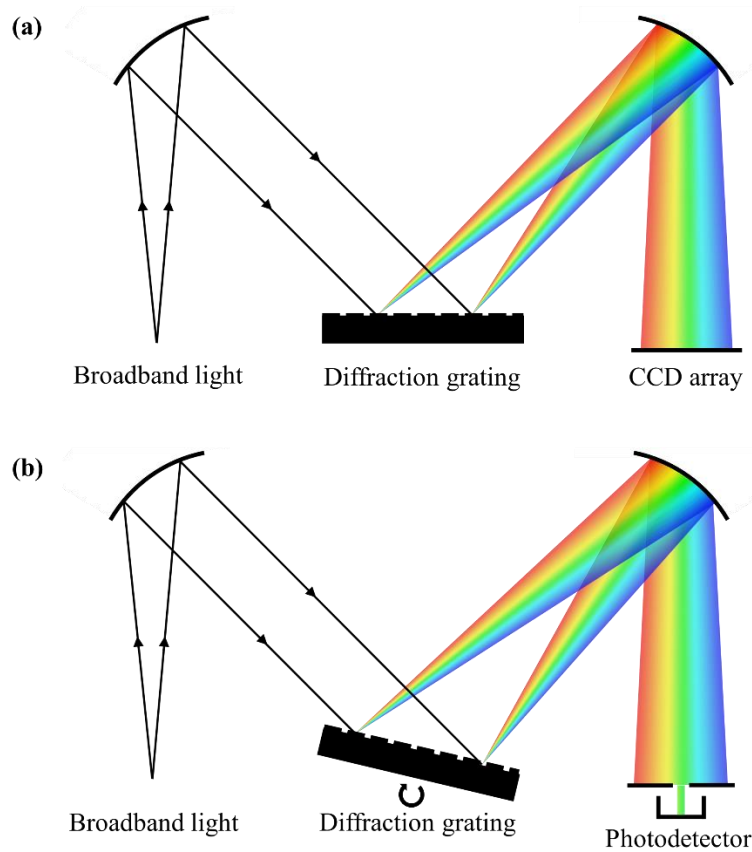


Figure 1.3: Illustration of modern spectroscopic techniques used to disperse broadband light into its constituent wavelengths where (a) a CCD array is used to capture all the dispersed light simultaneously and (b) a photodetector is used in conjunction with a rotating diffraction grating to measure each wavelength individually.

Although interferometric and spectroscopic techniques have contributed vastly to the field of photonics and have established measurement acquisition with high accuracy and resolution, the development of optical fibres have allowed these technologies to expand beyond the bounds of laboratories in a significant scale.

1.3 Fibre optic technology

The concept of guiding light by total internal reflection had first been described by Daniel Colladon in 1842 [7], where a “light fountain” was demonstrated by the reflections of light rays within a stream of water. Nowadays, a typical optical fibre takes the form of a glass rod, although by modern standards many different fibre types exist, such as hollow core and plastic optical fibres.

Significant developments have elevated fibre optic technology to the standards recognised today. Throughout its conception in the mid-20th century, limitations in draw capabilities and imperfections in the glass resulted in comparatively high attenuation loss fibres. The recognition that the attenuation was largely due to impurities that could be removed, along with improved fibre drawing processes, subsequently lead to worldwide deployment, particularly in telecommunications. The purity of the glass used in modern fibre cables results in far less attenuation than in electrical copper cables.

Beyond telecommunications, optical fibres also readily lend themselves to sensing and imaging applications with capabilities in remote sensing, as they can be deployed over long distances, and multiplexing of sensing elements. Due to their dielectric nature, they are immune to electromagnetic interference and so are viable in areas where this would otherwise be of concern. The fragility of fibres, however, may limit their deployment in engineering structures, but with appropriate protective layers this issue can be mitigated. Fibre sensitivity to temperature, stress, and strain can be observed but these effects are usually small and require more elaborate configurations to detect. Optical fibres can therefore be considered a robust means by which bulk optics within a sensing system can be replaced or by which light can be delivered to a sensing area in a hostile environment.

1.4 Scope and motivation

The Atomic Weapons Establishment, AWE, are responsible for the manufacture, maintenance, and development of the United Kingdom's nuclear deterrent [8]. Part of AWE's objectives is to implement optical sensors which complement their existing sensing capabilities. The work in this thesis addresses this objective.

Among AWE's activities is ensuring the safety and structural condition (i.e., structural health) of the nuclear deterrent is maintained. This is achieved by in-situ monitoring of the materials and aging effects occurring within the structure. Due to the inherent safety of optical sensor technologies compared to conventional electronic sensors (or sensors which may generate or require heat/combustion), and inert nature of its core components, it is desired to implement optical methods for in-situ monitoring applications. This also alleviates the concern regarding the presence of ionising radiation where electronic devices are not viable due to lifetime constraints. Minimal interaction with the structure is desired for in-situ monitoring in this context, and as such long-term stability of the sensing technology is required that extends to multiple years.

The health of a structure can deteriorate in a number of ways, where some relevant examples are: creep, which can result in the slow displacement of component parts; cracking, which can lead to a sudden change in component separation; and outgassing, which is the release of gas within a system which can be indicative of chemical aging. These effects are not mutually exclusive, where outgassing, for example, may very well lead to the occurrence of creep as a result of compounded residual stress/strain. As such, a comprehensive investigation is desired where gas sensing and distance measurements by optical means are explored.

The integrity of these systems, which are hermetically sealed, must be retained. Therefore, measurement acquisition is required to be conducted without effecting or altering the chemical equilibria of the system (i.e., non-extractive and non-consuming). Regarding gas speciation measurements, gases of particular interest include CO_x , NO_x , H_2O , and O_2 , where a sensor capable of detection limits in the parts per million (ppm) regime is required. As for distance measurements, accuracy and resolution in the nm regime are required, where the sensor is to be deployable in confined spaces (as small as a mm) and capable of sub-mm to mm range measurements. Both gas and distance measurement sensors must be compatible with the sensing environment, insofar that the sensing technology is inert and has no interaction with the sensing environment beyond its primary function.

1.5 Thesis layout

The following chapter explores the various sensing technologies for distance measurement and gas detection that could be implemented in structural health monitoring applications. The most suitable to address the problem at hand are then identified.

Based on these conclusions, the remaining chapters investigate, develop, and optimise the sensing techniques and devices. Chapter 3 is devoted to the principles of Fabry-Pérot interferometry and the development of cavity demodulation methods to accurately extract cavity length information. A function-fitting algorithm is designed to operate in conjunction with a fast-Fourier transform of the measurement signal, the performance of which is evaluated computationally and experimentally using singlemode, single-core fibre. A fibre cleaved at 45° is also used, as redirecting the light perpendicular to the fibre axis is of primary interest, based on conclusions drawn thus far.

In Chapter 4, expansion from single-core to multi-core fibre is investigated, alongside fabrication processes that are applied to the fibre end to allow for the appropriate

redirection of light. The fabrication processes investigated include focused-ion beam milling and laser assisted etching. Optimised results of each fabrication process are outlined and the performance of each sensor is assessed.

Chapter 5 explores the development of a fibre tilt sensor. This is built upon a particular sensor developed in the previous chapter, where a single-point measurement device is expanded to a two-point measurement device. The sensor operating principle, design, and signal effects are discussed and the performance is evaluated.

Chapter 6 is concerned with gas detection and gas speciation measurements using optical techniques based on absorption spectroscopy. The principles of absorption spectroscopy are detailed and its integration with fibre tapering and cavity enhancement techniques are explored. Firstly, fibre tapering is investigated where the practical tapering capabilities are demonstrated which define certain parameters used in computational simulations. Secondly, incoherent broadband cavity enhanced absorption spectroscopy is investigated where modelled results and design considerations are discussed. Relevant limitations and challenges are identified and conclusions are drawn.

Finally, in Chapter 7, a discussion is conducted regarding the thesis work as a collective, potential future work is considered, and concluding remarks are made.

Chapter 2

Literature review

2.1 Introduction

The work in this thesis is concerned with the measurement of distance and gas detection, and as such this chapter reviews the various methods by which this can be achieved. To summarise in brief, the measurement problem requires optical structural health monitoring within a hermetically sealed and hazardous system. Although optical means are desired due to compatibility with the specific sensor application requirements outlined in § 1.4, other sensing technologies are also reviewed to allow for contextualisation among the many sensor designs within their respective fields. The review of sensor technologies beyond that of optical devices also establishes a more thorough understanding of the potential compatibility issues with the measurement problem.

Due to the vastness of information regarding the concepts covered in this chapter (where each could likely fill a book), a range of fundamental aspects are outlined which are deemed to be of sufficient relevance to the work presented here. Where each succeeding chapter is prefaced with an introduction and elaborates on the science and technology relevant to that chapter, the following review provides a short overview of each concept with sufficient depth for drawing conclusions. It is worth noting that although an attempt at comprehensiveness is made, where deemed appropriate, later sections are referred to which present further detail and on occasion, new concepts.

2.2 Distance measurements

At its origin, many systems for length measurements were based on the human body. The inch, for example, was defined as the breadth of a man's thumb [9], and the foot, as the name suggests, was defined by the length of a human foot [10]. Thankfully, these systems have since been replaced with definitions that are more robust and consistent, but many iterations were developed from body-based standards to modern-day definitions. The metre, once defined as one ten-millionth of the distance from the equator to the North Pole through Paris, was redefined as the length of a prototype metre bar. Physical associations were then abandoned in favour of a more universal approach, where the metre is now defined as the distance by which light in a vacuum travels in $1/299\,792\,458$ seconds [11].

The importance of accurate and precise distance measurement acquisition cannot be overstated, whether for construction, tool alignment, or systems monitoring. Many of the techniques and technologies developed to achieve this are discussed in the following subsections. Although the measurement problem outlined in § 1.4 lends itself to optical device integration, other methods beyond those of optical means are discussed also. This is primarily to provide a comprehensive review of the many distance measurement devices that exist, in turn allowing a broader framework for comparison, highlighting the advantages and disadvantages of each within a wider context.

As with many sensing and measurement devices, the metrics of performance are not always easily comparable – what may be deemed important to one application may be insignificant to another. For example, where the measurement sensitivity (which is the smallest detectable change in the measurand) is relevant for one particular device, this may be less-so for another, where instead the repeatability (which is the consistency between repeated independent measurements) is quantified. Where the measurement acquisition is continuous, both the sensitivity and the repeatability may be correlated to, and limited by, the noise level, introducing another layer of ambiguity – if a continuous measurement device specifies its sensitivity, this may carry implications regarding its repeatability and noise level. There is also often an implied relation between a device's sensitivity and its resolution, where the resolution is, simply put, the smallest value the output reading provides. It is not uncommon for the resolution to be defined instead as the *meaningful* smallest value the output reading provides, which in effect is synonymous with sensitivity. In other words, the resolution and sensitivity are equivalent only if they

are both defined in terms of the measurand. As such, where the source work has specified resolution or sensitivity, this will be quoted verbatim in the following review.

2.2.1 Mechanical devices

Although mechanical distance measurement devices may sound rudimentary (as it possibly provokes recollection to that of a metre stick or ruler), there are in fact sophisticated and precision engineered tools which are capable of highly accurate measurement acquisition.

Simplistic in their operation, callipers function by having a fixed and a sliding jaw which make contact with an object to define the length to be measured (see Figure 2.1(a)). This measurement can be performed in a number of ways. The Vernier scale utilises mechanical interpolation between graduation markings on a linear scale to assist with reducing measurement uncertainty. Commercial Vernier scale callipers are capable of measurement resolution and accuracy of $\pm 20 \mu\text{m}$ and $\pm 80 \mu\text{m}$ respectively [12]. Additionally, digital callipers function by measuring the change in capacitance that occurs as a result of the capacitive array present within the sliding jaw moving with respect to the beam. Commercial digital callipers are capable of measurement resolution and accuracy of $\pm 10 \mu\text{m}$ and $\pm 20 \mu\text{m}$ respectively [13]. Depending on the model, callipers can typically measure up to 10's of centimetres.

Similar in their operation, micrometers are another form of mechanical linear measuring tool. The micrometer is comprised of a rotating ratchet which induces a linear actuation of the spindle upon the anvil (i.e., the two parts by which the measurement length is defined, see Figure 2.1(b)). This differs from the calliper's clamping motion, as a result offering an improved resolution and accuracy of $\pm 0.1 \mu\text{m}$ and $\pm 0.5 \mu\text{m}$ respectively [14]. Typically, micrometers are capable of measuring lengths in the 10's of millimetres.

Referring to the specification criteria outlined in § 1.4, although certain mechanical devices are indeed capable of providing measurement accuracy and resolution appropriate for the measurement problem, the most significant limiting factor is that of their physical size, thereby rendering them unsuitable for further consideration.

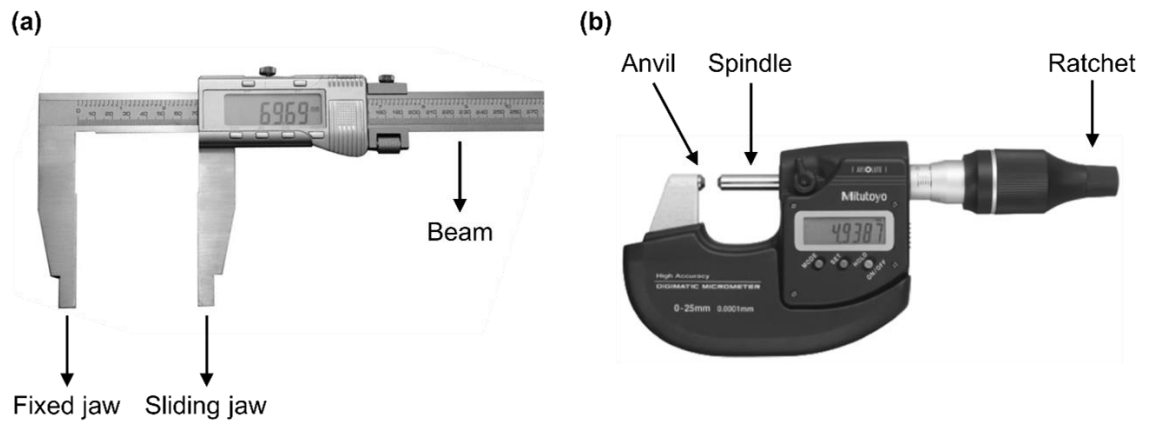


Figure 2.1: (a) Image of digital callipers, adapted from [13]. (b) Image of digital micrometer, adapted from [14].

2.2.2 Optical devices

There is an expansive list of optical techniques that can be employed for distance measurements. In this review, these have been categorised as *Geometrical techniques*, *Time of flight techniques*, and *Interferometric techniques*. Where particular techniques or details have been omitted for concision, references are provided for further reading.

Geometrical techniques

One such geometrical technique is that of triangulation, which itself can be described separately as passive triangulation and active triangulation.

Passive triangulation is illustrated in Figure 2.2. The same point on the target is imaged by two cameras with a known separation, X , each tilted to known angles α and β . The two cameras and the baseline separation form a triangle, which can be solved to determine the unknown distance, D , by equation (2.1) [15]:

$$D = \frac{X}{\frac{1}{\tan \alpha} + \frac{1}{\tan \beta}} \quad (2.1)$$

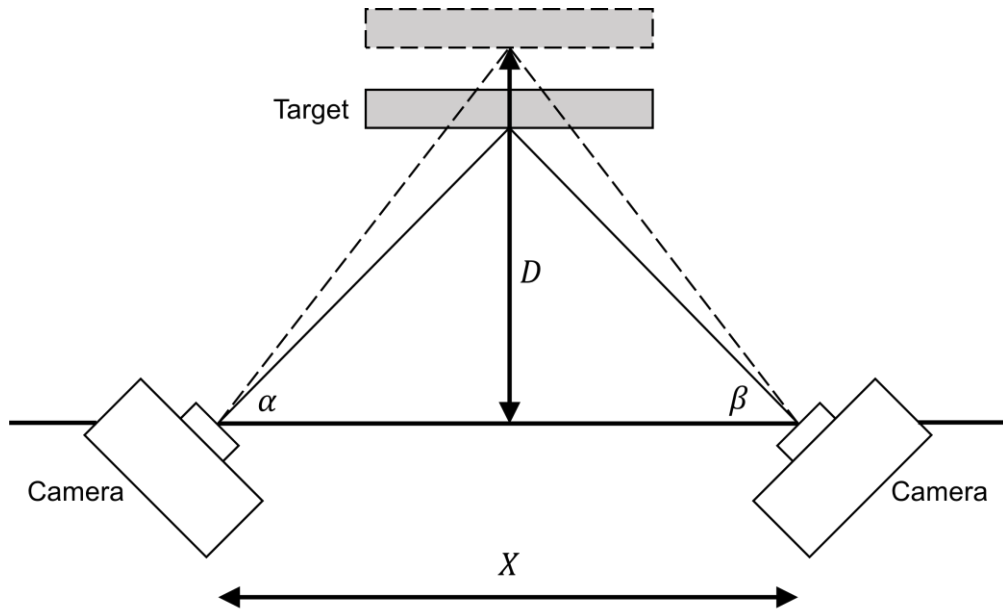


Figure 2.2: Illustration of passive triangulation where two cameras with a known separation and tilt angles image the target to determine its distance from the baseline.

Similar to this is active triangulation, which is illustrated in Figure 2.3. A laser source can be used to illuminate the target surface, after which laterally displaced camera lens optics image the laser spot on the target onto a detector. With known distances E and F , and measuring the value of G , the unknown distance D can be determined by the formation of similar triangles using equation (2.2) [16]. Similarly, by introducing a structured pattern, shape measurement can also be achieved.

$$\frac{D}{E} = \frac{F}{G} \quad (2.2)$$

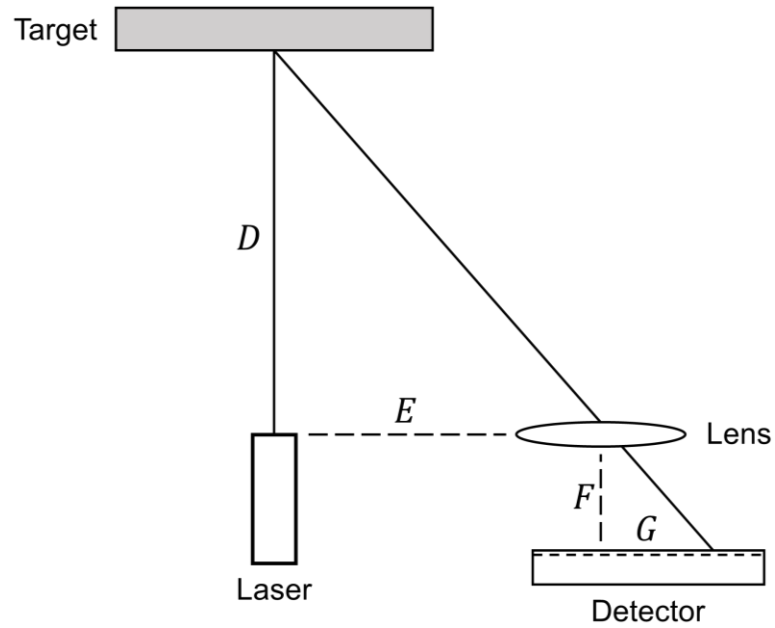


Figure 2.3: Illustration of active triangulation where a laser spot on the target is imaged on a laterally displaced detector. The target distance, D , is determined by the formation of similar triangles.

By introducing a structured pattern, a shape measurement can also be achieved. The resolution of active triangulation-based distance measurement devices predominantly depends on the size of the laser spot size and the detector pixel size [17], where the resolution will vary within the designed working range, i.e., the resolution is highest when the target is closest and vice versa. Commercial optical triangulation devices demonstrate an accuracy of $\pm 0.6 \mu\text{m}$ and a resolution of $\pm 0.038 \mu\text{m}$ at a measurement range of 2mm and $\pm 3.815 \mu\text{m}$ at a measurement range of 200 mm [18].

Beyond that of triangulation, other geometrical techniques such as confocal sensors may also provide a means for distance measurement. The confocal principle, also well-known in confocal microscopes, is the use of optics purposed for both tightly focusing light onto a target emitted from an aperture, as well as focusing the light scattered from the target back into the aperture. As such, optical fibres are typically well-suited for confocal sensor applications. Figure 2.4 illustrates the operating principle of a confocal sensor.

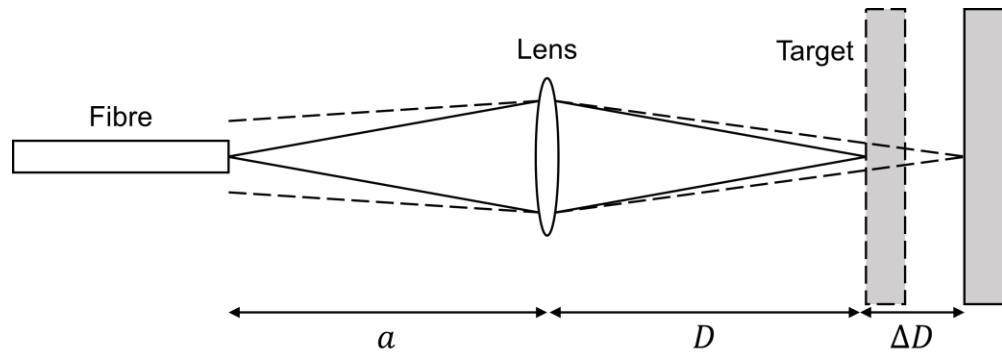


Figure 2.4: Illustration of confocal sensor where the change in the target distance can be determined by adjusting either the lens or fibre position to maximise the return signal.

The maximum return signal is found when the target is positioned at the image plane defined by the optics. When the target surface is longitudinally displaced, either the lens or the fibre position is adjusted to retain the return signal strength, which can then be correlated to the change in target distance in the case for monochromatic light [19]. Where polychromatic light is used, the corresponding wavelength with the strongest return signal can be used to infer the target distance [20]. Commercial confocal sensor devices are capable of measurement resolutions better than $0.1 \mu\text{m}$ across a range of a few millimetres, where longer ranges in the 10's of millimetres are possible but with diminished resolution [21].

Both triangulation and confocal techniques offer accuracy and resolution capabilities which satisfy the specification criteria outlined in § 1.4. However, the requirement for bulk optics inhibits applicability to confined spaces, preventing these techniques from further consideration with regards to the present measurement problem.

Time of flight techniques

Another optical approach for measuring distance is that of time of flight (TOF) techniques, which can be separated into direct TOF and indirect TOF. Direct TOF, simplistically described, determines distance by measuring the time it takes for light to travel from the sensor to the target surface and back [22]. These typically operate using a laser in the visible or near-IR spectrum with nanosecond pulse duration [16]. Regarding targets that are at a distance greater than $\sim 50 \text{ m}$, which corresponds to a far greater round trip transit time compared to the pulse width, distance measurement can be acquired without additional complex temporal considerations other than the TOF [16]. Where

shorter distances are concerned, the temporal pulse shape needs to be accounted for to retain accurate measurement of the time delay between pulse peaks. Further detail regarding such considerations for short range measurements can be found in [23] and [24].

Regarding indirect TOF, the target distance is measured using the phase shift that occurs between the intensity-modulated transmitted and reflected signals. Figure 2.5 illustrates this concept.

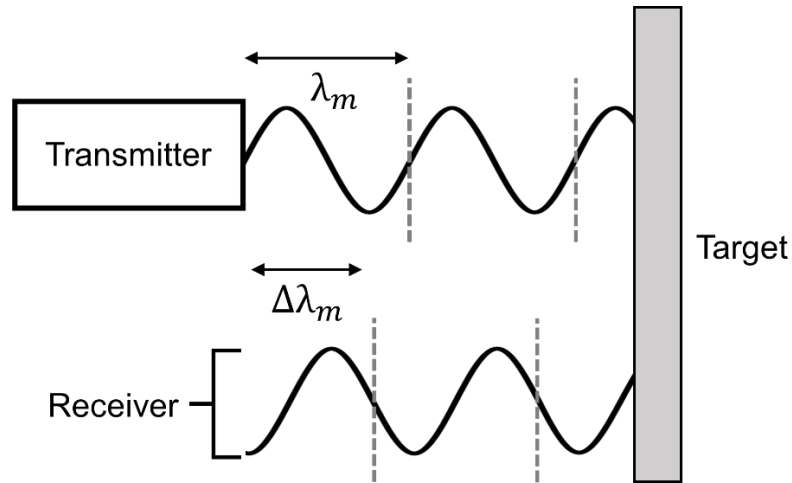


Figure 2.5: Illustration of indirect time-of-flight where the distance measurement is achieved by the phase-shift that occurs between the transmitted and reflected light which is intensity modulated, where each complete modulation cycle is indicated. Transmitted and reflected signals are vertically offset for clarity.

If the transmitted signal is sinusoidally modulated with a modulation wavelength of λ_m , then the target distance, D , can be determined from equation (2.3):

$$D = \frac{1}{2}(M\lambda_m + \Delta\lambda_m), \quad (2.3)$$

where M is an integer equal to the number of modulation wavelengths. If M is known, then an outcome similar to that of Figure 2.5 can be achieved where the target distance can be measured unambiguously as the phase is unwrapped. If M is unknown, then the distance measurement is ambiguous. The modulation wavelength can be extended such that unambiguous distance measurement can be achieved for $M = 0$, however the further λ_m is extended, the more the measurement uncertainty increases [16].

TOF sensors are capable of measurement ranges in the 10's of kilometres with accuracies of ± 1 m [25], down to ranges in the vicinity of metres with accuracies of ± 4 mm [26].

It is clear that TOF sensors excel in long range applications. However, where the specification criteria outlined in § 1.4 are concerned, TOF sensors fall short. Although they are inherently compatible with the sensing environment (in that they pose no concern regarding the hazardous environment in which they would be deployed) as they utilise optical means of distance measurement acquisition, they are incompatible with the other criteria – sub- μm accuracy and resolution within a confined space.

Interferometric techniques

When measurements acquired using interferometric techniques are considered, strictly speaking, some of these in fact determine displacement, such as the Michelson interferometer (see Figure 2.6).

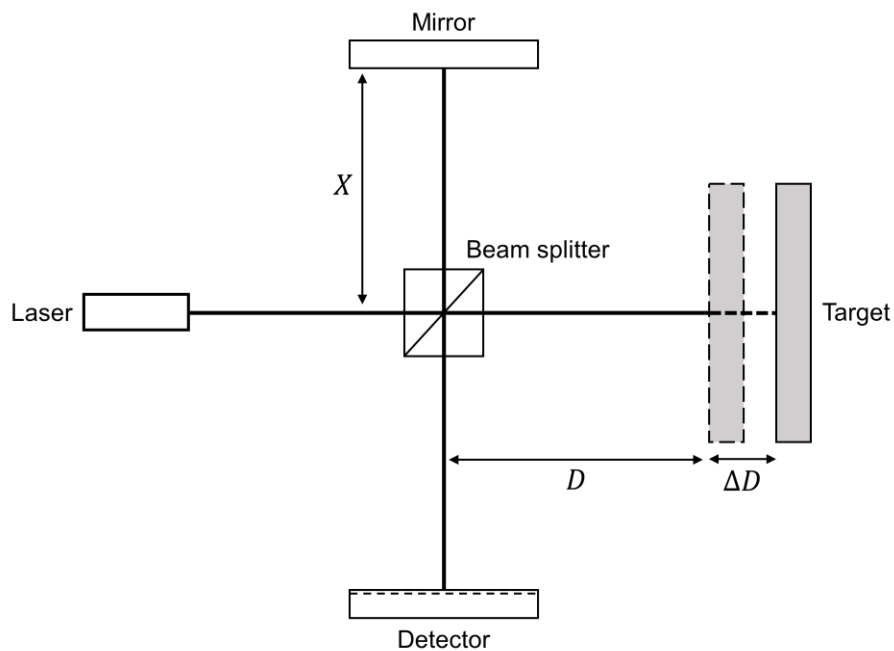


Figure 2.6: Illustration of a simple Michelson interferometer configuration.

The Michelson interferometer may be considered one of the simplest forms of interferometric configurations, yet certainly not insignificant. A beam splitter divides the incoming coherent light, directing one portion to a fixed mirror and the remaining portion to the target. Linearly polarised light is typically used in this configuration, but as will be reviewed later, other interferometric techniques which do not use linearly polarised

light are also possible. Upon reflection at each interface the beams combine once again, the resulting interference of which is monitored by measuring the interference intensity. The interference condition is then altered by the displacement of the target, and so said displacement can be determined by measuring the interference. Interference in this manner is briefly summarised in § 1.1 and further detailed in § 3.2.1. The measurement of sub-wavelength displacements is often achieved [16].

Absolute distance can also be obtained by interferometric techniques utilising multiwavelength or scanning interferometry. Such methods include Fabry-Pérot interferometry (FPI) [27] and white light interferometry (WLI) [28] [29].

Detailed discussion on the operating principles of FPI can be found in § 3.2, but to summarise: When light is incident upon a target consisting of multiple interfaces in the direction of propagation, a portion of light will reflect at each interface (where the amount of reflection is dependent on the material properties). The reflected beams will then interfere constructively or destructively (or anything in between) depending on; (i) the distance between interfaces, (ii) the wavelength of light, and (iii) the refractive index of the medium. Assuming the refractive index is constant, if the wavelength of light is scanned across a range of wavelengths, the interference that occurs as the beams recombine will transition between constructive and destructive interference. As the distance between interfaces then changes, the rate at which this transition occurs also changes – a greater distance between interfaces corresponds to a more rapid transition in constructive-to-destructive interference, and the opposite is also true. Information regarding the distance between interfaces can therefore be extracted by the optical spacing of interference fringes. In other words, the interference spectrum can be demodulated to yield distance information (see § 3.3). The measurement of distances in the 10's of millimetres with sub-wavelength resolution is achievable with standard techniques, where nanometre resolution is possible with more advanced demodulation methods [30].

WLI carries similarities in the way a Michelson interferometer is configured whereby the output from two arms is combined, but an unpolarised light source with a broad optical bandwidth and hence low coherence is instead used [31]. This light source does not necessarily need to operate in the visible spectrum to truly form white light but can instead, for example, operate in the near-IR [32]. Where WLI is implemented as a distance or displacement sensor [33] [34], the target position is deduced by scanning the reference mirror to reveal the interference spectrum envelope, where the interference fringe with maximum contrast (which represents the target position) can be identified.

Where there are multiple target surfaces in the direction of light propagation, the reference mirror position is scanned accordingly to reveal multiple interference envelopes for each corresponding target (see Figure 2.7). WLI-based distance measurements can be achieved with nanometre and sub-nanometre resolutions over a measurement range of a couple of millimetres [35] [36].

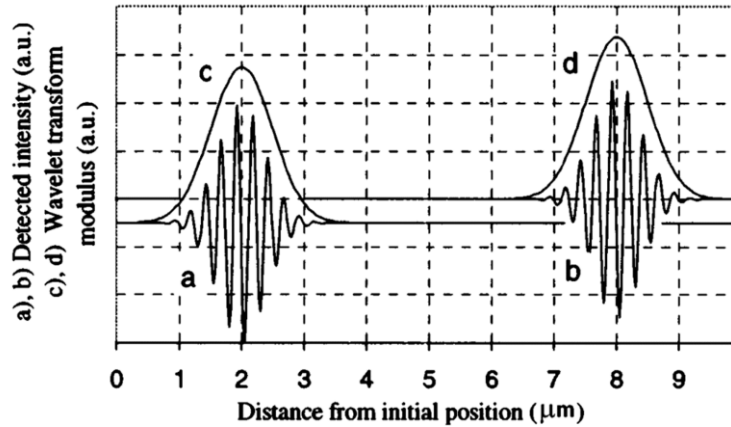


Figure 2.7: Example of signal recorded from white-light interferometry to determine component position. Adapted from [37].

Although the illumination light for WLI can be delivered by optical fibre, there is still the requirement for additional optics at the end of the fibre that form the head of the sensor [38], thereby increasing its overall size and potentially rendering it inapplicable to the measurement problem outlined in § 1.4. Sub-mm probe designs exist [39], but this is nonetheless many times larger than a bare fibre sensor capable with FPI.

2.2.3 Other devices

Beyond mechanical and optical devices there are, of course, other means by which distance can be measured which do not particularly fit in either category yet are still noteworthy.

Ultrasonic techniques offer similar operating principles to that of certain optical techniques, such as TOF. A transmitter and receiver module can be configured in this case to measure the TOF of ultrasonic waves in the kHz regime in air, although other signal processing techniques can be combined to provide improved performance [40]. Commercial ultrasonic distance measurement devices typically offer measurement ranges of <10 m with millimetre or sub-millimetre resolution [41]. Ultrasonic TOF, although

capable of measuring shorter distances than optical TOF, fails yet to meet the specification criteria as it does not display sub- μm resolution capabilities, similarly to that of optical TOF.

Capacitive sensors can also be used to determine distance, where the change in spacing between two electrodes induces a change in capacitance. Where the change in electrode spacing is controlled by some external mechanical movement, a sensor is realised. The capacitance value is directly related to the size of the capacitor, where a small capacitor is more susceptible to noise, therefore meaning that the capacitive sensors should be as large as possible [42]. Capacitive distance measurement devices are typically capable of measurement ranges of <10 mm with sub- μm , nm [43], or sub-nm resolution [44]. The offering of capacitive sensors therefore meet many of the specification criteria. It's main limitation, however, is that it is an electrical means of measurement acquisition and is thereby cause for concern if deployed in the sensing environment, as is outlined in § 1.4.

2.2.4 Conclusions

Given the measurement problem at hand, which is the sensing and monitoring of distance over a small range (i.e., millimetres) within a confined space, with accuracy and sensitivity in the nm regime, where electromagnetic interference and radiation may be of concern, few techniques inherently demonstrate candidate properties. For example, mechanical devices are bulky and comparatively demonstrate insufficient accuracy and resolution (in exchange for ease-of-use) and capacitive sensors are incompatible with the sensing environment. Further regarding the capacitive sensors, although they demonstrate sufficient accuracy and resolution suitable for the measurement problem, they are simply limited by their operating principle, rendering them incompatible with the sensing environment. This is observed with many of the distance measurement techniques reviewed, where the sensing performance meets requirements, but some other design aspect restricts its compatibility. Note that 'performance' in this instance is considered as the measurement accuracy and resolution. Exceptions to this are namely ultrasonic and optical TOF techniques, where the former offers insufficient performance, and the latter is better suited for long range measurements. Table 2.1 summarises the evaluation of the different distance measurement devices and sensing techniques covered in this section against the specification criteria.

Table 2.1: Summary of distance measurement devices and sensing techniques considered against specification criteria. Where appropriate, some devices and sensing technologies are referred to collectively, e.g., ‘Vernier calliper’ and ‘Digital calliper’ are collectively referred to as ‘Callipers’ for concision.

| Device/Sensor | Accuracy in nm regime | Resolution in nm regime | Sub-mm to mm range | Deployable in mm-scale spaces | Compatible with sensing environment |
|----------------------------|-----------------------|-------------------------|--------------------|-------------------------------|-------------------------------------|
| Callipers | X | X | ✓ | X | ✓ |
| Micrometer | ✓ | ✓ | ✓ | X | ✓ |
| Optical triangulation | ✓ | ✓ | X | X | ✓ |
| Confocal | ✓ | ✓ | ✓ | X | ✓ |
| Time-of-flight | X | X | X | X | ✓ |
| Fabry-Pérot interferometry | ✓ | ✓ | ✓ | ✓ | ✓ |
| White-light interferometry | ✓ | ✓ | ✓ | X | ✓ |
| Ultrasonic | X | X | X | X | ✓ |
| Capacitive | ✓ | ✓ | ✓ | X | X |

Overall, of the distance measurement techniques reviewed, optical techniques appear to offer the most appropriate solution and comparatively offer acceptable performance in relation to other techniques, regardless of compatibility issues. Yet even among themselves, optical techniques differ greatly in operation and configuration. The most significant limiting factor and differentiator is the capability to operate within a confined space, for example, its capability to integrate fibre technology. As such, techniques which require the use of bulk optics are unsuitable.

As a result, Fabry-Pérot interferometry offers an elegant solution where it can easily operate within confined spaces, demonstrates sensing performance which meets the specification requirements outlined in § 1.4, is compatible with the sensing environment, and (as a supplementary benefit) is capable of measuring absolute distance as opposed to displacement as with other interferometric techniques.

2.3 Gas sensing

Gas sensor technology has become an essential component in the monitoring, control, and analysis of systems with its integration in fields consisting of, but not limited to, scientific, medical, and environmental applications. More specifically, such applications range from: automotive and aircraft regarding the control of gas concentration in engines to establish optimal engine performance [45]; domestic and work safety regarding the detection of poisonous gases and air quality control [46]; city traffic control management regarding air quality monitoring in tunnels or in underground parking garages [47]; medical/clinical regarding diagnostics (breath analysis, disease detection) and drug monitoring [48]; food quality control regarding the detection of certain molecules which are formed when food is no longer consumable [49]; defence/military regarding the detection of chemical, biological and toxin warfare agents [50].

Optical gas sensor technologies in particular may provide important data that can be used to infer the presence of chemical ageing processes that can occur within hermetically sealed systems. The purpose of this literature review is to evaluate the suitability of optical gas sensing technologies for such an application, where it is important that the gas measurement is taken without affecting the chemical equilibria or changing the chemical composition in order to retain the integrity of these systems (i.e. needs to be non-extractive and non-consuming). Alongside this criterion, there is also a requirement to achieve sensitive and selective gas speciation measurements for gases including CO_x , NO_x , H_2O and O_2 . In addition, the sensor technology will need to be chemically and physically compatible with the system in which it is located, the sensor itself be of fibre-size dimensions and to display a long-term stability that extends to multiple years.

A comparison between the different gas detection techniques is attempted, however it is evident that the figures of merit are not consistent. Inevitably, a performance metric that is appropriate in one application may be of limited value in another or challenging to quantify. There are many metrics by which sensor performance can be evaluated, such as accuracy, sensitivity, resolution, response time, recovery time, etc., not to mention metrics such as sensitivity are often defined differently where $\text{kHz}/\%$ [51], $\mu\text{A}/\%$ [52], concentration (e.g., ppm) [53], and unitless values (i.e., a ratio of variables) [54] have been used, exacerbating the challenge for direct comparison. One metric which most consistently appears is that of the detection limit, and as such this metric is used when

drawing comparisons. Other noteworthy sensor properties are then considered when drawing conclusions.

2.3.1 Electrochemical gas sensors

Electrochemical gas sensors typically consist of a number of electrodes (often two, three, or occasionally four) that are in contact with an electrolyte. The functionality of an electrochemical sensor depends on an induced measurable outcome as a result of an electrochemical reaction upon the introduction of the gas desired to be detected. This measurable outcome may be in the form of the generation of a current (Amperometric), a potential difference between two electrodes (potentiometric), or change in electric conductivity at a series of frequencies (conductometric) [55].

Amperometric

Amperometric electrochemical sensors operate on the principle of diffusion of the gas in question into the sensor through the porous membrane to the working electrolyte which then undergoes electrolysis (either oxidation or reduction). This electrochemical reaction then induces a transfer of charge between the working electrode and counter electrode, where the measured current is proportional to the gas concentration [55]. For example, commercial devices for O₂ detection offer a detection limit of 5 ppm [56], while state-of-the-art amperometric sensors are capable of detection limits in the ppb regime [57], where 44 ppb has been achieved for NO₂ detection [58].

Potentiometric

A precondition that must be met for a potentiometric method to be applied successfully is that the potential measurement must be done with essentially zero current. A typical potentiometric sensor is the ion selective electrode (ISE) whose configuration can consist of two electrodes: The first is the working (indicator) electrode which has a potential that is determined by its environment; the second is a reference electrode which has a potential that is fixed by a solution containing the analyte of interest at a constant activity [59]. A particular analyte ion is measured selectively by the indicator electrode, at the tip of which is placed an ion-selective membrane, designed to generate a potential signal for the target ion. The detailed theory regarding the processes which take place at the membrane interface which generate the potential is available elsewhere [60]. Since the reference electrode potential is constant, the measured potential difference can be related to the

concentration of the dissolved ion, i.e. the indicator electrode response is governed by the Nernst equation [55]:

$$E = E^O + \frac{\mathcal{R}\mathcal{T}}{\eta F} \ln \frac{a^O}{a^R}, \quad (1)$$

where E is the measured electrode potential, E^O is the standard electrode potential, \mathcal{R} is the universal gas constant, \mathcal{T} is the absolute temperature, η is the number of moles of electrons exchanged in the electrochemical reaction, F is the Faraday constant, and a^O and a^R are the activities of the oxidised and reduced species respectively [55]. Commercial O₂ potentiometric sensor devices have detection limits in the low-ppm regime (1 ppm) [61]. Laboratory-developed potentiometric sensors for the detection of CO₂ and NO₂ have also demonstrated similar performance [62].

Conductometric

Conductometric sensors operate on the principle of variations in electrolyte conductivity which occur when an analyte is present, which effectively changes the number of mobile charge carriers in the electrolyte. As opposed to a voltage measurement, a sinusoidal voltage is applied and the resulting current is measured, upon which the conductance can be determined in the frequency domain [63], where the conductivity is a linear function of the ion concentration [55]. The detection of NO₂ by means of conductometric sensing has been achieved with detection limits of 0.4 ppm [64].

2.3.2 Mass-Sensitive gas sensors

Mass sensitive gas sensors operate on the principle of changes and disturbances to the mass of the sensor surface upon interacting with the analyte. This interaction can come in the form of mass adsorption on the micro system which induces a measurable resonant frequency shift [65] as illustrated below in Figure 2.8, where a schematic for such a device can be seen in Figure 2.9(d):

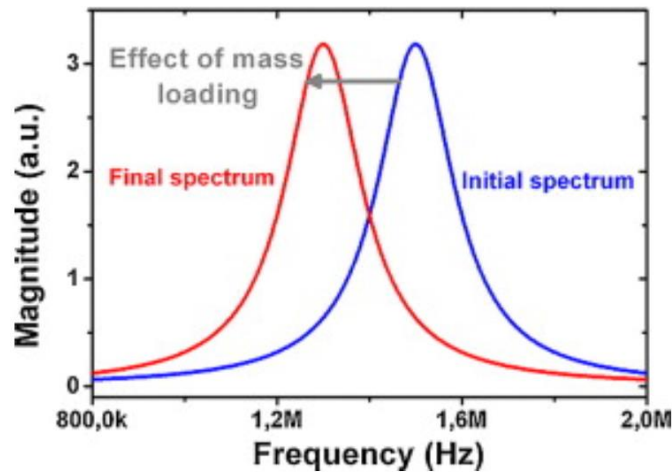


Figure 2.8: Principle of operation of mass sensors by frequency shift measurement. Adapted from [65].

Detecting the stress changes due to micromechanical structure deflection can also be used to monitor changes in mass by utilising a microcantilever where the analyte sensitivity and selectivity is dependent on the corresponding coating applied to the active surface [66]. Quartz crystal microbalance (QCM) and surface acoustic wave (SAW) are other common variations of mass sensitive gas sensor technologies. QCM operates on the inherent property of piezoelectricity, where an oscillating piezoelectric is used to generate acoustic waves and a single crystal quartz is used to measure mass [67]. QCMs typically consist of a circular quartz disc situated between two metal electrodes, where the application of an alternating electric field to the quartz induces alternating contraction and expansion of the crystal lattice and a resonant condition can be reached [67]. The change in frequency of the oscillating crystal as mass adsorption on the surface occurs can then be determined, as was first demonstrated by Sauerbrey in 1959 [68], where the frequency shift can be used to determine the gas concentration. This approach is commonly used in vacuum thin film deposition thickness monitoring.

SAW devices, similar to QCM devices, also generate acoustic waves through the utilisation of piezoelectric crystal resonators. Through the process of photolithography, periodic comb-shaped interdigital transducer (IDT) patterns are developed on the piezoelectric material where under the application of an AC voltage, acoustic waves are generated in the direction from the transmitter IDTs (input electrodes) to the receiver IDTs (output electrodes). The signal which is obtained at the receiver IDTs is then converted back to an electrical signal and is processed. The distance between the two IDTs (the chemical recognition layer) determines the selectivity of the device and is

dependent on the applied coating material which can establish interaction with a specific analyte and can distinguish between diverse molecules [69]. A schematic representation of these devices can be seen below in Figure 2.9:

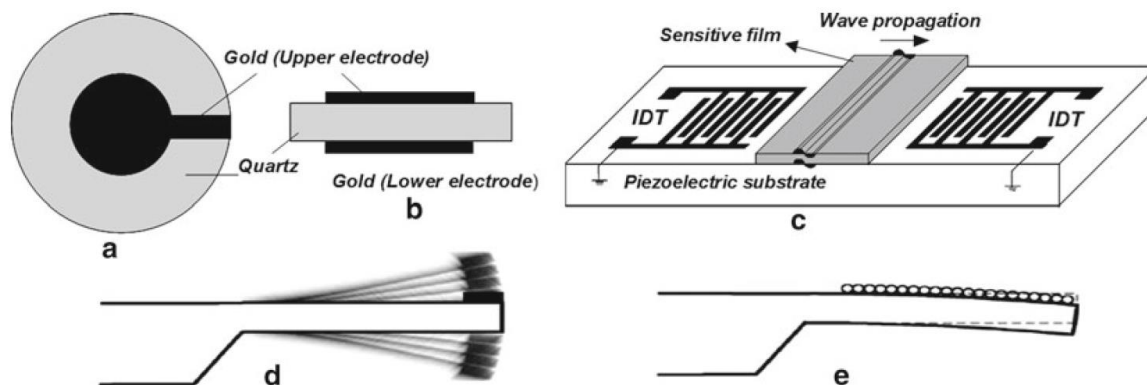


Figure 2.9: Schematic diagrams of mass-sensitive gas sensors: (a, b) quartz crystal microbalance (QCM device); (c) surface acoustic wave (SAW) device; (d, e) microcantilever – (d) dynamic mode: adsorption of analyte molecules in a sensor layer leads to shift in resonance frequency, and (e) static mode: the cantilever bends owing to adsorption of analyte molecules and change of surface stress at the cantilever surface. Adapted from [66].

Exemplary research of QCM and SAW devices for the detection of H₂O and H₂ respectively have yielded detection limits of 2 ppm [70] and 7 ppm [51].

2.3.3 Magnetic gas sensors

The functionality of magnetic gas sensors is dependent on the paramagnetic properties of the analyte. Oxygen has relatively high magnetic susceptibility in comparison to other gases as can be seen below in Table 2.2, making oxygen the most suitable gas to be detected utilising this method. Nitric oxide is also typically suitable, but other common gases (particularly the ones listed in Table 2.2) will fail to be detected at any acceptable degree of sensitivity due to their weak paramagnetic properties. Paramagnetic oxygen sensors typically consist of a cylindrical container within which is suspended a small glass dumbbell in a strong, nonuniform magnetic field, a schematic of which can be seen in Figure 2.10:

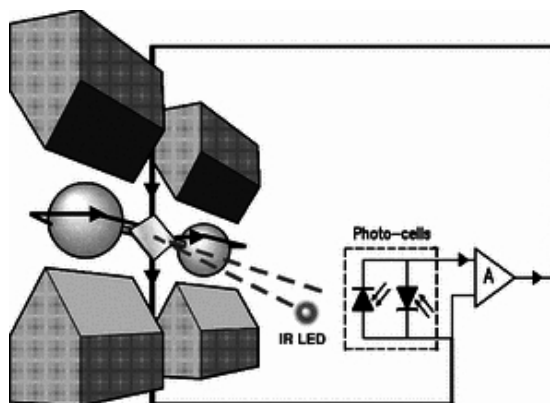


Figure 2.10: Schematic diagram of a dumbbell type paramagnetic oxygen sensor. Adapted from [71].

Oxygen molecules introduced into the container will be attracted to areas of higher magnetic field and tend to align their magnetic moments with the field due to their high magnetic susceptibility. This results in an air pressure gradient forming within the container causing the suspended dumbbell to rotate. The rate of rotation is monitored and a counter electromagnetic torque is applied accordingly to restore the dumbbell to its original position by regulating an electric current through a wire wrapped around the dumbbell. The current required to generate the restoring counter torque is then proportional the amount of partial pressure oxygen, which can then be displayed as a percentage of oxygen [72].

Table 2.2: Molar magnetic susceptibility (χ_m) of common gases. All values refer to nominal room temperature (285K to 300K) unless otherwise stated. Positive and negative values represent paramagnetism and diamagnetism respectively. Data taken from the CRC Handbook of Chem. and Phys. [73].

| Name | Formula | $\chi_m / 10^{-6} \text{ cm}^3 \text{ mol}^{-1}$ |
|--------------------------|-----------------|--|
| Oxygen | O ₂ | 3449 |
| Nitric oxide | NO | 1461 |
| Nitrogen dioxide (408 K) | NO ₂ | 150 |
| Nitrogen | N ₂ | -12.0 |
| Hydrogen | H ₂ | -3.99 |
| Carbon monoxide | CO | -11.8 |
| Carbon dioxide | CO ₂ | -21.0 |
| Methane | CH ₄ | 17.4 |

Paramagnetic oxygen sensors are limited by the moving parts within the design, restricting applicability in high temperature, humid, and vibrating environments. The magnetic nature of oxygen also typically results in detecting oxygen concentrations of >100 ppm [53].

2.3.4 Thermometric gas sensor

Thermometric (also known as calorimetric) devices operate by detecting changes in temperature caused by chemical reactions which then result in measurable electrical signals such as changes in resistance, current or voltage.

One type of thermometric sensor can be set up by simply coating a thermistor with a catalytic layer. Thermistors mainly consist of a semiconductor body which have temperature dependant conductivity. A hydrogen sensor, for example, can be created by coating a thermistor with black platinum, where traces of hydrogen in the air burn in the catalytic area resulting in a rise in temperature [74]. The temperature difference with the ambient temperature can then be measured in terms of resistance change which is then directly related to the concentration of hydrogen in the air. Note that this methodology is only applicable with combustible gases, which means that gases such as hydrogen sulphide or carbon monoxide can also be detected with this arrangement (but using their suitable corresponding catalysts) [74].

Another type of thermometric gas sensor is the pellet resistor sensor called the pellistor, which consists of a similar arrangement to the thermistor such that there is a thin catalytic coating, but the coating is applied to an inert ceramic bead within which there is a thin platinum coil [75]. In operation, a current is passed through the coil that heats up the catalyst layer which allows oxidation to occur in the presence of a flammable gas or vapour [76]. Similar to combustion, the oxidation that occurs is exothermic, and increases the temperature of the catalytic layer and coil. This rise in temperature changes the electrical resistance of the coil. By incorporating the sensing element in a Wheatstone Bridge circuit, the sensing element temperature rise can be determined [76], which can then relate directly with the gas concentration in the surrounding atmosphere. Figure 2.11 below illustrates a schematic representation of a thermistor and pellistor sensor:

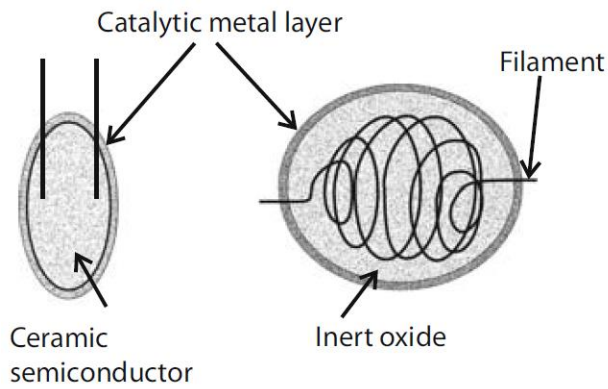


Figure 2.11: Thermometric (calorimetric) sensors. Left: thermistor, right: pellistor. Adapted from [74].

The detectability of combustible gases using pellistors are typically in a concentration range of ~ 1000 ppm to 10^3 's of percent, while the detection of volatile organic compounds (VOC) has been demonstrated at 20-200 ppm [75].

Thermal conductivity sensors (sometimes referred to as katharometers) operate by drawing a comparison between the sample gas and a reference gas. In the sensor a sensing element (either a heated thermistor or platinum filament) is exposed to the sample gas and another, used as a reference, is placed in a sealed compartment. If the sample gas has a thermal conductivity which is higher than that of the reference, then the exposed element loses heat and its temperature decreases. On the other hand, if the sample gas has a lower thermal conductivity than the reference, then the temperature of the exposed element increases. These changes in temperature are proportional to the concentration of the sample gas and alter the electrical resistance which is measured as an imbalance in a Wheatstone Bridge [75]. A schematic representation of this device can be seen in Figure 2.12:

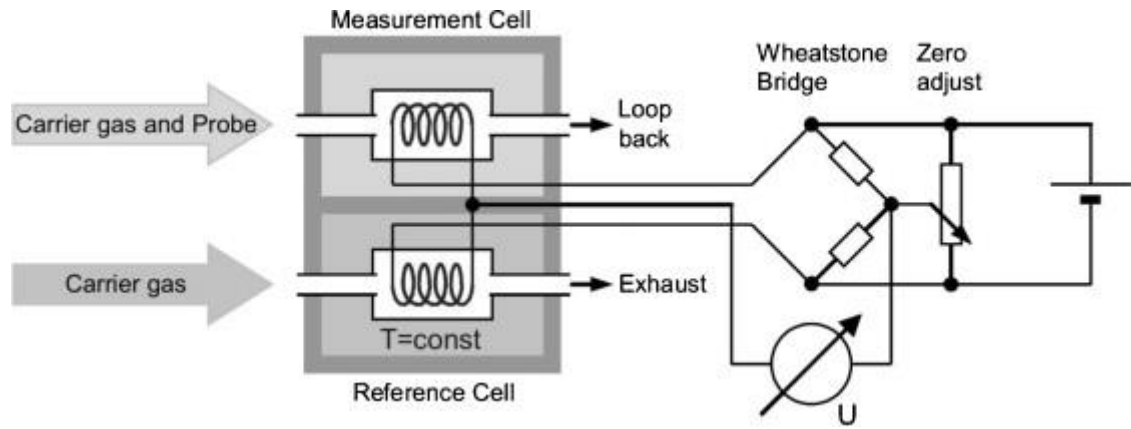


Figure 2.12: Measurement and reference cell of a thermal conductivity sensor connected in a Wheatstone bridge circuit. Adapted from [77].

It is important to note that this method is primarily implemented to detect gases which have a thermal conductivity greater than air (i.e., greater than 1). Higher thermal conductivities allow for lower concentrations to be measured [75]. Issues arise when attempting to detect gases which have a thermal conductivity <1 due to potential interference of water vapour. Using thermal conductivity sensors, the detection of NO has been achieved with a detection limit of 2-5 ppm [54].

2.3.5 Optical gas sensors

The key operating principles of optical sensors are based on classical spectroscopy, where deviation only occurs regarding the elements of the experiment and their arrangement. Generally speaking, optical gas sensors operate by allowing visible light or other electromagnetic waves to interact with the analyte, where the resulting change in optical phenomena are detected. This interaction with the analyte is evaluated and the corresponding change in some optical parameter is then related to the concentration of the analyte.

Various optical gas sensing techniques are outlined below, such as absorption-based and fluorescence-based sensors, but first an overview regarding the implementation of optical fibres in sensors is covered.

Optical Fibres

The implementation of optical fibres in sensors has introduced a wide range of advantages consisting of the capability of remote sensing, immunity to electromagnetic interference,

high sensitivity, and possibility of point or multipoint detection, to name a few. Their geometrical flexibility and material properties allow for applications in medicine [78] [79] since accessibility to all parts of the human body is feasible, explosives detection [80] as fibre probes do not carry the risk of overheating or creating a spark, and operation in high-voltage environments [81] due to their dielectric characteristic. However, optical fibres also introduce their own set of limitations such as limited performance in dusty environments or other harsh conditions, and the occurrence of parasitic loss due to scattering in the medium.

The diversity of the various optical sensing principles is substantial, yet the fundamental components which comprises a fibre optic sensor, i.e. the optical hardware, remains unchanged: a source, an optical sensing element and a photodetector (with a recording device). The determination of the optical hardware allows for the selectivity, sensitivity, and time response of the sensor to be tailored.

Absorption

Absorption-based fibre-optic sensors were the first fibre-optic chemical sensor to be described in literature [82]. With this methodology, the substance property which is used to quantify the change in light is the absorbance, which is directly proportional to the path length, l , and the concentration, c , of the absorbing species, such that according to Beer's Law:

$$A = \epsilon cl \quad (2)$$

where A is the absorbance and ϵ is a constant of proportionality, called the absorptivity [83]. As light is passed through a substance with arbitrary absorbance, the corresponding reduction in light intensity can be quantified and related to the substance's concentration. The principles of absorption spectroscopy is elaborated upon in further detail in § 6.2.

Absorbance can be used to identify certain molecules in a medium due to each having a specific absorption spectrum, i.e. different molecules absorb EM radiation of different corresponding wavelengths. This identification procedure can prove to be very complex when attempting to do so in any arbitrary environment as there will be many different chemical specimens in the medium. However, absorption-based optical sensors are commonly used for specific analysis in a controlled medium. Thus, a small number of wavelengths are used to quantify the change in light intensity when the incident light is passed through the sample [84]. This limitation, however, can often be circumvented by

the adoption of broadband techniques. Many absorption-based gas detection techniques exist, too many to exhaustively list here. Some examples consist of multi-pass techniques such as the Herriott cell [85] and White cell [86], and cavity enhanced techniques such as cavity ringdown spectroscopy (CRDS) [87] and cavity-enhanced absorption spectroscopy (CEAS) [88]. By means of absorption, detection limits in the ppm, ppb, and even ppt regime have been achieved [89].

A comprehensive study on the various absorption-based optical gas detection techniques can be found in [89].

Fluorescence

Fluorimetry, the utilisation of fluorescent measurements, is a fundamentally sensitive and simple technique. The intrinsic fluorescence of an analyte may be measured, or a sensor may be designed which utilises an indicator dye, where the variation of the fluorescence is measured with the determinant concentration [90].

The relationship between the luminophore (which is the atom or atomic grouping in a substance responsible for its luminescent properties) concentration and the intensity of its emission is governed by:

$$I_L = \Phi_L I_0 \kappa \varepsilon_\lambda l c \quad (3)$$

where Φ_L is the luminescence quantum yield, I_0 is the excitation light intensity, κ is an instrumental parameter (i.e. the emission collection efficiency), ε_λ is the luminophore absorption coefficient at the excitation wavelength, l is the optical pathlength and c is the luminophore concentration [91].

By means of fluorescence, a detection limit for VOCs of 15.4 ppm has been achieved [92]. Further studies for the detection of other analytes have resulted in similar detection limits in the ppm regime [93] [94].

Chemiluminescence

Chemiluminescence, similar to fluorescence, is another type of luminescence, which is the emission of photons as a result of an electronically excited compound returning to its ground state. The classification of different types of luminescence arises when considering the different sources of excitation energy, where in the case for chemiluminescence, photon emission is produced due to some chemical reaction.

The measurements involved with chemiluminescence consists of monitoring the rate of photon emission, where the light intensity is dependent on the luminescent reaction rate. Due to this, the intensity of light is directly proportional to the concentration of the reactant involved in the luminescent reaction [95]. Chemiluminescence-based gas sensors have demonstrated detection limits of 0.3 ppb for analytes such as NO, and 40 ppt for O₃ [96].

Surface-Enhanced Raman Scattering

Where light is scattered after being incident upon a material, almost all photons are elastically scattered (Rayleigh scattering), meaning they have the same energy, frequency, and wavelength as the incident photons. Inelastic scattering is when the energy of the scattered photons differs from the incident photons, commonly known as the Raman effect (or Raman scattering), which occurs approximately in one photon out of a million [97]. Since vibrational information is specific to the molecular symmetry and the chemical bonds, the acquisition of this vibrational information using Raman spectroscopy offers the detection of what is commonly considered to be the chemical “fingerprint” of the molecules and in turn the substance at hand.

The surface-enhanced Raman scattering (SERS) effect is a variation of Raman spectroscopy which arises from the adsorption of molecules on specially textured metallic surfaces [97]. The introduction of SERS alleviated the need for high-power, multiple-wavelength excitation sources that were required for other Raman techniques such as coherent anti-Stokes Raman scattering and increased the viability of Raman spectroscopy as an analytical technique.

The detection of NO₂ by SERS has been achieved with a detection limit of 0.5 ppm, however the SERS technique lends itself to detection limits in the ppb regime depending on the analyte in question [98].

2.3.6 Conclusions

To reiterate the criteria associated with detecting gases in hermetically sealed systems: the sensing technology must be non-consuming, selective towards CO_x, NO_x, H₂O and O₂, have detection limit in the ppm regime, the sensing device must be fibre-sized and must exhibit long-term stability. Optical gas sensing methods cover all of these criteria, whereas other sensing methods fall short in one way or another: Electrochemical gas

sensors can be irreversible, and the operating temperature of the analyte is often required to be 200-500 C° for sufficient selectivity depending on the specific sensing method; mass-sensitive gas sensors require specific preparation (e.g. coatings) in order to detect certain gases and thus the device will require replacement depending on the desired gas to be detected, which is not feasible to do for hermetically sealed systems; magnetic gas sensors are primarily used for sensing O₂ due to their fundamental operating principles; some thermometric gas sensors (thermistors and pellistors) are only applicable to combustible gases and operate on exothermic reactions while others (thermal conductivity gas sensors) are inefficient at detecting gases which have similar thermal conductivity to their reference. Table 2.3 summarises the evaluation of the different distance measurement devices and sensing techniques covered in this section against the specification criteria.

Table 2.3: Summary of gas sensing techniques considered against specification criteria.

The sensing techniques are categorically listed for concision. Note that 'Multi-purpose' refers to the capability in measuring each of the gases of interest with a single device.

| Sensing technique | Detection limit | Multi-purpose | Non-consuming | Selective | Compatible with sensing environment |
|-------------------|-----------------|---------------|---------------|-----------|-------------------------------------|
| Electrochemical | ✓ | × | × | ✓ | × |
| Mass-sensitive | ✓ | × | × | ✓ | × |
| Magnetic | ✓ | × | ✓ | ✓ | × |
| Thermometric | ✓ | × | × | ✓ | × |
| Optical | ✓ | ✓ | ✓ | ✓ | ✓ |

In conclusion, among the gas sensor technologies reviewed and considered, optical gas sensor technologies demonstrate the most potential with the implementation of optical fibres which introduce flexibility, reliability and remote monitoring to a methodology which is sensitive, selective, and stable – properties which make this technology favourable in its application to hermetically sealed, inaccessible systems.

Chapter 3

Fabry-Pérot interferometry and cavity demodulation

3.1 Introduction

Fabry-Pérot interferometry is one of the many ways in which one can measure distance using light, as was outlined in § 2.4.2. In the context of the sensor to be developed here, i.e., a distance measurement sensor for structural health monitoring, the properties of Fabry-Pérot interferometry align well with the solution required to address the measurement problem. Namely, a technique that can provide high resolution measurements over a short distance and is compatible with optical fibre technology.

This chapter covers the principles of Fabry-Pérot interferometry in further depth than § 2.4.2. Its implementation using optical fibres and the different signal demodulation methods are discussed, after which sensor performance is evaluated by both simulation and experiment using conventional single core fibres (SMF28) to demonstrate benchmark performance.

3.2 Principles of Fabry-Pérot interferometry

3.2.1 *Mathematical model*

The Fabry-Pérot interferometer (FPI) relies upon the interference that arises from beams formed by the reflection that occurs at two parallel surfaces as illustrated in Figure 3.1.

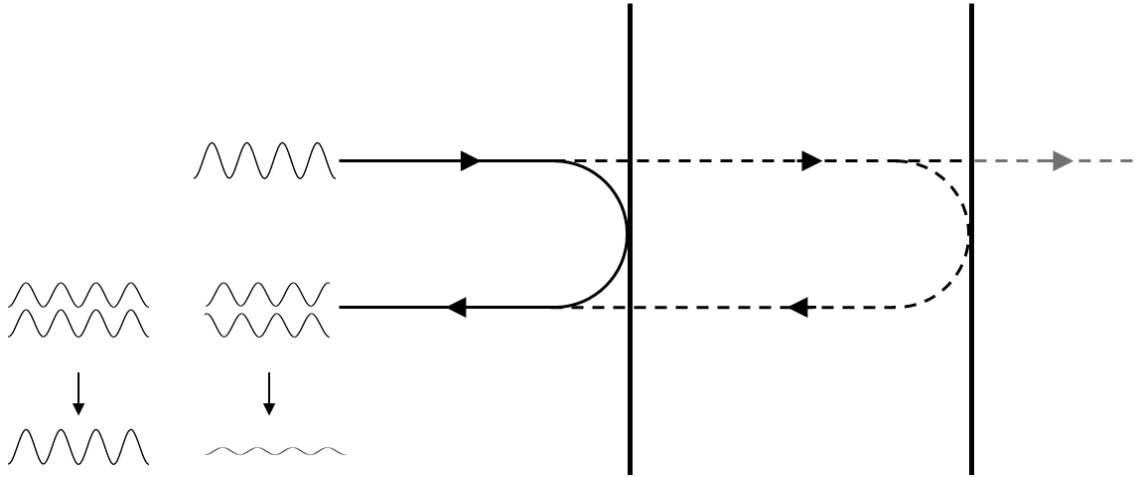


Figure 3.1: Illustration of constructive or deconstructive interference arising from the beam reflection that occurs when incident upon two partially reflective/transmissive parallel surfaces.

The corresponding model that adequately describes the reflected (or transmitted) intensities is dependent on properties of these reflecting surfaces. This is typically captured via the definition of the cavity finesse, typically denoted as F , of the Fabry-Pérot cavity that is formed. Finesse is evaluated as the ratio of the free spectral range (FSR) of the optical resonator (cavity) and the full-width at half-max (FWHM) linewidth of its resonances [99]. Generally speaking, if the cavity is formed by highly reflective surfaces (i.e., $>90\%$ reflectivity), the resonance linewidth is narrow, and the finesse is subsequently high. The opposite is true, whereby a cavity which is formed by low reflectivity surfaces has resonances with broader linewidths, and the finesse is low. Although the work in this thesis is concerned with the reflected intensity of low finesse cavities, as will be elaborated upon further in the next section, expressions for both reflected and transmitted intensities of low and high finesse cavities are covered for completeness.

In the context of a high finesse optical cavity, a multiple beam interference model is employed. An idealised model may only be relevant if the following assumptions can be made: (i) Diffraction effects are negligible; and (ii) the losses due to the cavity medium and surfaces are negligible. Multiple beam interference is illustrated in Figure 3.2, where two surfaces with reflection and transmission coefficients, r and t , are separated by thickness, d , consisting of a medium with refractive index, n .

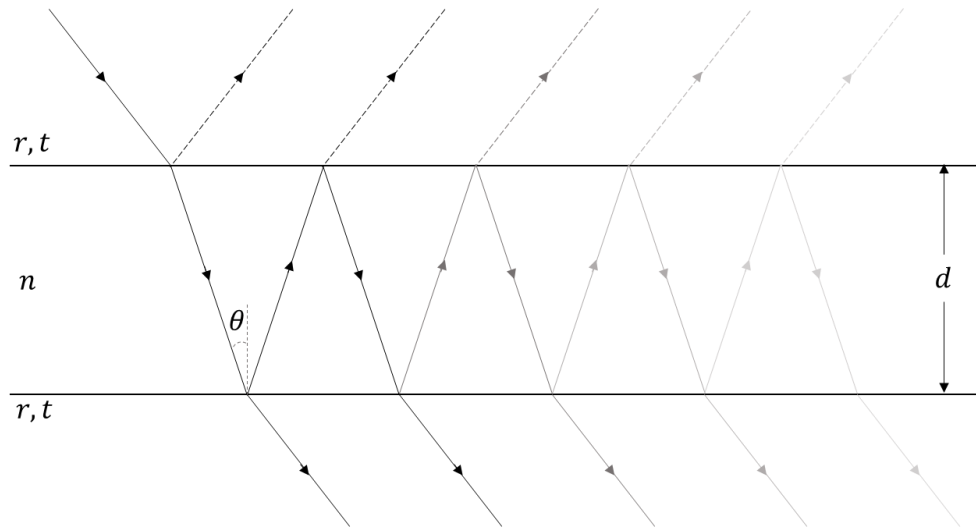


Figure 3.2: Illustration of multiple beam interference. Note that in many cases beams will be normally incident on the surfaces, however a non-zero θ improves clarity and allows the more general solution to be considered.

The beam incident on the first surface partially reflects, while the remainder transmits and refracts, in turn becoming incident on the second surface at an angle θ to the normal. The interaction at the second surface is similar, where the beam partially reflects and the remainder transmits. The interference condition that governs the reflected and transmitted intensity is the phase difference, δ , between any two adjacent emerging rays, which is given by equation (3.1):

$$\delta = \frac{2\pi}{\lambda} \times OPD = \frac{4\pi n d \cos \theta}{\lambda} \quad (3.1)$$

Where OPD is the optical path difference, and λ is the wavelength of incident illumination. Note that a π radians phase shift occurs upon reflection if the light is transitioning from a low-to-high refractive index medium. A phase discrepancy may arise that is not expressed in equation (3.1) whereby the π radians phase shift occurs only at one of the two surfaces depicted in Figure 3.2. This is, however, inconsequential to the analysis covered in § 3.3 which is based on the frequency of the interference spectrum and not the absolute phase.

The reflected and transmitted intensities, I_r and I_t respectively, can therefore be described using equations (3.2) and (3.3) [100]:

$$I_r = I_i \frac{2R(1 - \cos \delta)}{1 + R^2 - 2R \cos \delta} \quad (3.2)$$

$$I_t = I_i \frac{1 - R}{1 + R^2 - 2R \cos \delta} \quad (3.3)$$

where I_i is the incident intensity, and $R = r^2$.

When a low finesse optical cavity is evaluated, i.e. by low reflectivity surfaces, then a two-beam interference model is often sufficient to describe the cavity performance. This is valid where the surface reflectivities are sufficiently low such that multiple cavity reflections are negligible (cavities of reflectivity <5% can be considered to be low in the context of the approximation [101]). This is illustrated in Figure 3.3.

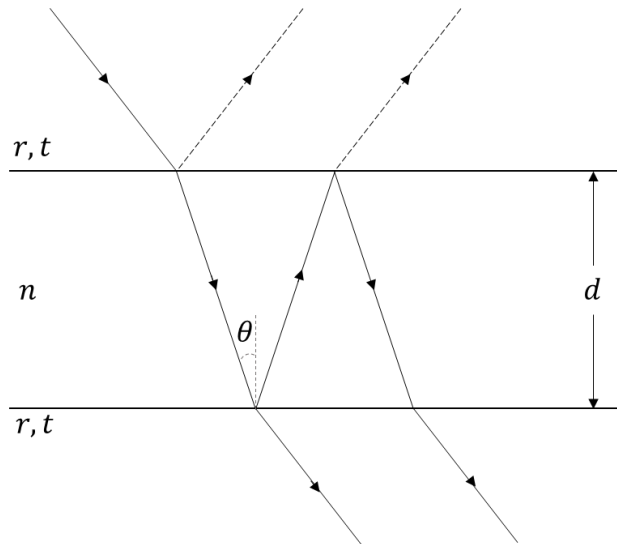


Figure 3.3: Illustration of two-beam interference.

As the surface reflectivities are low in this context, a practical simplification can be implemented in equations (3.2) and (3.3) where the denominator tends to unity. Equations (3.4) and (3.5) therefore represent the reflected and transmitted intensities where multiple reflections are assumed negligible.

$$I_r = 2RI_i(1 - \cos \delta) \quad (3.4)$$

$$I_t = I_i(1 - R) \quad (3.5)$$

A close approximation carries the benefit of allowing the adoption of simplified models for simulation purposes, which in turn minimises the computational requirement for modelling and/or experimental data post-processing. These concepts are covered in detail in § 3.3.

It is important to note that when light enters a FPI at an oblique angle, its reflected and transmitted polarisation states alter as a function of the angle of incidence, where both the reflected and transmitted beams are partially polarised except for when the angle of incidence and angle of transmission are orthogonal, at which point the reflected beam polarisation is entirely perpendicular to the plane of incidence [102]. As will be seen in the following section, only configurations where the incident beam is normal to the target surface are considered, and so the aforementioned polarisation effects are negligible. Where there may be some slight misalignment, the partial polarisation would result in very limited change to fringe visibility.

3.2.2 Fabry-Pérot interferometry using optical fibres

There are primarily two types of fibre FPI's: Intrinsic FPI (IFPI), where the optical cavity is situated within the fibre such that the fibre region located between two partially reflective mirrors is both the sensing element and the waveguide; and extrinsic FPI (EFPI), where the cleaved fibre end acts as a partially reflective mirror and the FP cavity is formed between the fibre end and some external reflector. To address the problem at hand, which is concerned with detecting the displacement of component parts within a physically constrained system, EFPI devices are of interest due to their accuracy and potential for miniaturisation. A schematic representation of a standard EFPI using a normal cleaved optical fibre is shown in Figure 3.4.

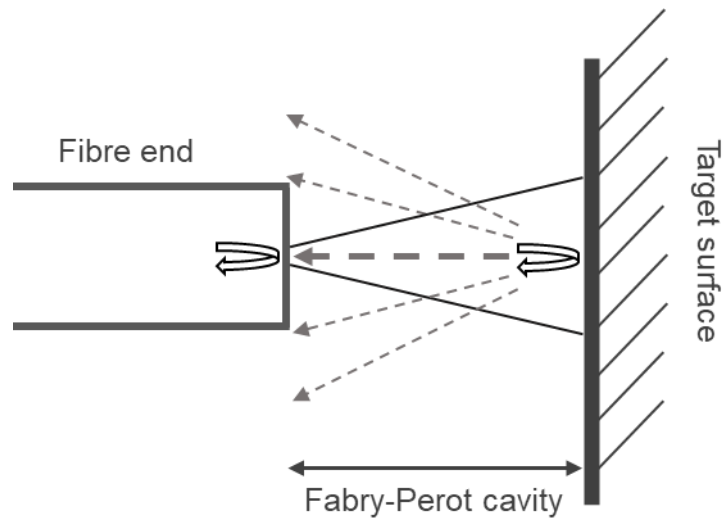


Figure 3.4: Standard external Fabry-Pérot interferometer using a normal cleaved optical fibre. For simplicity the fibre core is not illustrated.

The light that is guided by the fibre is partially reflected at the silica-air interface which approximately accounts for 3.5% of the incident light. This is commonly known as the Fresnel reflection [103]. The remaining light will then interact with the target surface and, depending on its surface properties, some portion will be reflected and couple back into the fibre core. The amount of light that couples back into the fibre is also dependant on any angular misalignment that is present, as well as the length of the air gap between the fibre and the target surface. i.e., The greater the gap, the greater the coupling losses. In a practical sense, it is safe to assume that some degree of misalignment will exist. All of these factors combined typically results in a small amount of light coupling back into the fibre. If the target surface is assumed to be a perfect mirror, then by symmetry Figure 3.4 can be adapted to Figure 3.5, which is the equivalent of two fibres facing each other spaced twice as far apart. This is a convenient model, as it is extensively considered in the literature [104].

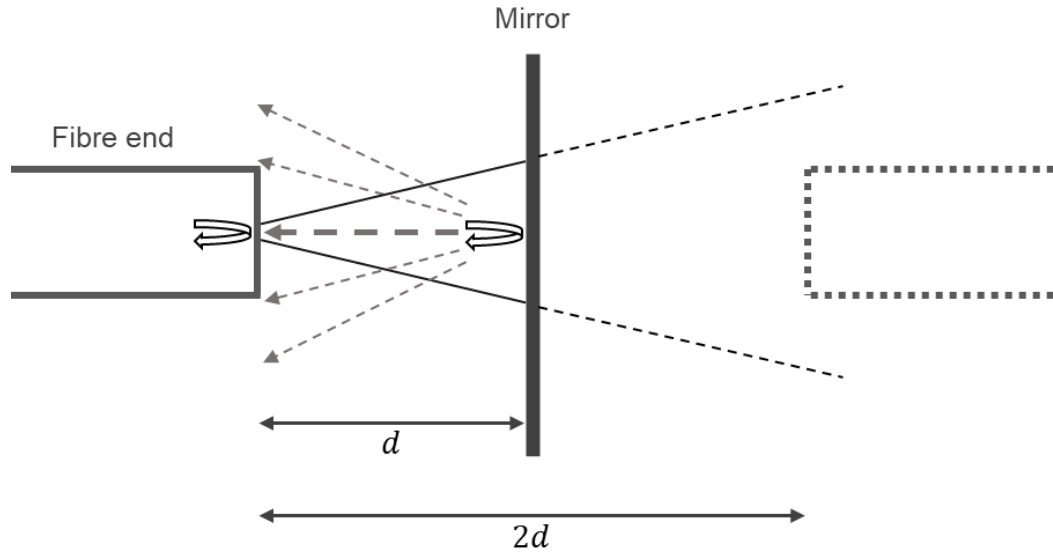


Figure 3.5: Equivalence illustration of fibre-to-mirror and fibre-to-fibre setup.

By applying the Gaussian approximation, the coupling losses that would occur from one fibre to another spaced apart by $2d$ can be estimated. In other words, the losses that would occur from the reflected light from a perfect mirror spaced d away from the fibre can be estimated. This loss is given by equation (3.6) [104]:

$$\alpha_l(dB) = 10 \log \left(1 + \left(\frac{2d\lambda}{2\pi n \left(\frac{MFD}{2}\right)^2} \right)^2 \right), \quad (3.6)$$

where MFD is the mode field diameter, which for a standard singlemode fibre (SMF28 at 1550nm) is $10.4 \mu\text{m}$ [105], and n is the refractive index of the medium, which in this application is air. For a wavelength of 1550 nm, Figure 3.6 illustrates the change in coupling loss with changing cavity length.

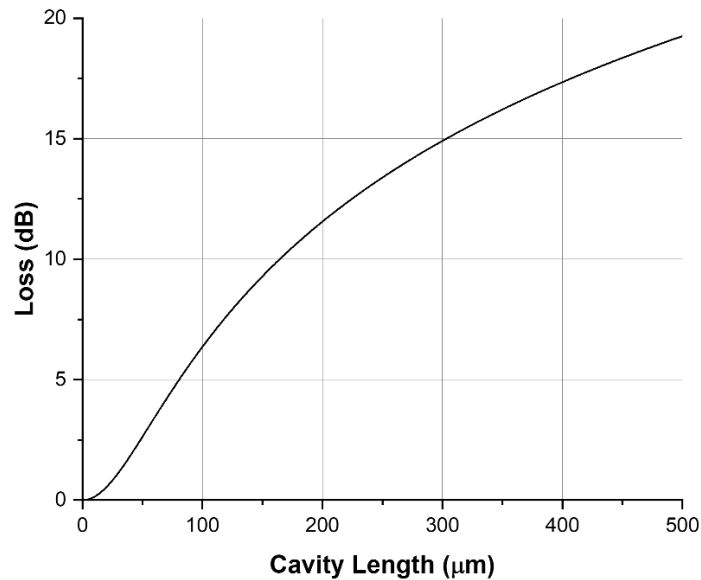


Figure 3.6: Modelled coupling loss as a function of cavity length.

It can therefore be concluded that the signal attenuation quickly becomes significant with increasing cavity length, where 6.4 dB loss is reached at 100 μm , assuming no other sources of loss (i.e., a perfect mirror with perfect alignment). Note that the reflectivity of the first interface of the optical cavity is defined by the Fresnel reflection which occurs, and the effective reflectivity of the second interface is a function of the cavity length as outlined in Figure 3.6. As will be shown later, cavity lengths of $>100 \mu\text{m}$ are used during experimentation, extending to several millimetres. The corresponding high loss that is experienced at the second interface at these cavity lengths, coupled with the high loss due to the Fresnel reflection at the first interface, results in high round-trip losses and thereby validates the formation of a low-finesse optical cavity. As such, the light intensity, which is measured in reflection in the presence of a low-finesse optical cavity, can be described by equation (3.4).

In order for this rudimentary configuration to be a viable solution, there must be sufficient space in front of the target surface to position the fibre without excessive bending of the connecting fibre. Otherwise, the fibre must be embedded within one of the components of interest, with the cleaved fibre end protruding towards the target surface. For engineering reasons this may not be possible or advisable. To compound this, where there may be multiple layers of restriction, the embedding design quickly becomes significantly more complex. Besides this, there is also the inherent limitation that this configuration will simply measure the distance between the fibre and the target surface, whereas the desired functionality is to measure the distance between *two* component parts. These

challenges are addressed by incorporating turning mirrors onto the end of a multi-core fibre, as shown in Figure 3.7.

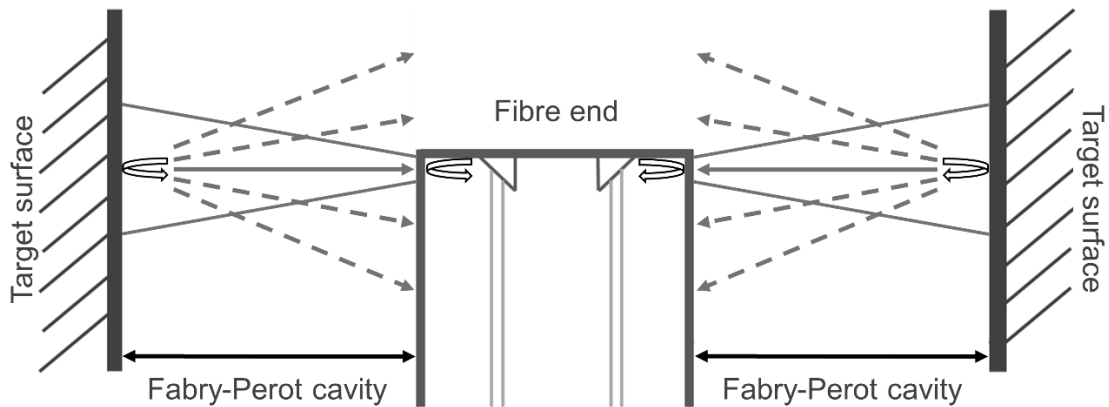


Figure 3.7: Schematic of multi-core fibre Fabry-Pérot interferometer with turning mirrors to redirect light perpendicular to fibre axis.

The incorporation of turning mirrors allows for the deployment of optical fibres in regions that are otherwise inaccessible without significant (undesirable) modification to the surrounding structure. The light is redirected perpendicular to the fibre axis via total internal reflection (the effects of which are comprehensively discussed in § 5.3.2), and the Fabry-Pérot cavity is formed between the circumferential edge of the fibre (as opposed to the cleaved fibre end) and the target surface. In the case of a multicore fibre optical cavities are formed on both sides of the fibre, allowing for simultaneous measurement acquisition. Given a known fibre core spacing, the total distance between two parallel surfaces can therefore be determined.

The turning mirror design, the fabrication approaches investigated, and further discussion regarding the limitations of different fibre types are covered in Chapter 4.

3.3 Demodulation methods

In the application of EFPI's that are discussed here, it can be assumed that the incident light from the fibre is normal to the target surface and that the cavity media is air. By illuminating the cavity with a swept wavelength source, interference fringes are generated in the reflected optical spectrum which, to a first order (as per equation (3.4)), can be expressed as:

$$I(\lambda) = 2RI_0 \left[1 - \cos\left(\frac{4\pi d}{\lambda}\right) \right] \quad (3.7)$$

Where $I(\lambda)$ is the wavelength dependent intensity, and I_0 is the light source intensity. The optical fringe spacing that emerges from the interference spectrum is a function of the cavity length, d .

In other words, when the cavity length is fixed and the light source is swept across a wavelength range, the reflected signal transitions between constructive and destructive interference. When the cavity length varies, the rate at which the transition between constructive and destructive interference occurs also varies. i.e., the periodic spacing between interference fringes changes. Therefore, a common approach to determine the cavity length from a FPI measurement is by its correspondence to the spectral periodicity, or the free spectral range (FSR), by equation (3.8).

$$d = \frac{c}{2n\Delta\nu} = \frac{\lambda^2}{2n\Delta\lambda} \quad (3.8)$$

Where c is the speed of light in free space, $\Delta\nu$ is the periodicity in the frequency domain (i.e., the FSR), and $\Delta\lambda$ is the periodicity in the wavelength domain.

This approach relies simply on data acquired at two points on the reflected spectrum to obtain a value for $\Delta\lambda$ (or $\Delta\nu$) – the broader the spectral spacing between interference fringes, the larger $\Delta\lambda$ becomes, which correlates to a shorter cavity length. Similarly, the narrower the spectral spacing between interference fringes, the smaller $\Delta\lambda$ becomes, which correlates to a longer cavity length.

Although there is a certain elegance to the simplicity of this approach, its reliance on only two data points is its limitation, where all other data within the recorded spectrum are unused. As such, the accuracy of its results comes into question – how accurately can one define the precise wavelength band of the reflected spectrum's FSR? Perhaps the implementation of a peak-detection algorithm to identify the exact spectral position of the interference fringes may be the solution. What if, however, there are multiple optical cavities present, and each cavity's corresponding interference fringes overlap with one another? Additionally, what if the signal strength is so low that it is unclear where the interference fringe peaks spectrally reside?

In this section, alternative methods of demodulating the reflected spectrum that utilise all of the acquired data will be discussed which overcome these issues to successfully yield cavity length information.

3.3.1 Fast-Fourier transform

The Fourier transform is a mathematical technique that transforms a signal that is represented in the ‘time’ domain to the ‘frequency’ domain, and vice versa. It can be thought of as a deconstruction of the input time-dependent signal to its constituent frequencies in terms of amplitude and phase. For a given function, $f(t)$, the forward and inverse Fourier transform can be defined by equations (3.9) and (3.10) respectively [106].

$$\mathcal{F}(\omega) = \int_{-\infty}^{\infty} f(t)e^{-i2\pi\omega t} dt \quad (3.9)$$

$$f(t) = \int_{-\infty}^{\infty} \mathcal{F}(\omega)e^{i2\pi\omega t} d\omega \quad (3.10)$$

The Fourier transform in this form, however, is only applicable where the input function can be solved analytically. This is typically not the case for physical measurements consisting of finite data sets. Therefore, a discrete Fourier transform (DFT) may be applied to a finite sequence $f(n)$ with N terms as defined by equations (3.11) and (3.12) [107].

$$\mathcal{F}(k) = \sum_{n=0}^{N-1} f(n)e^{-\frac{i2\pi}{N}kn} \quad (3.11)$$

$$f(n) = \sum_{k=0}^{N-1} \mathcal{F}(k)e^{\frac{i2\pi}{N}kn} \quad (3.12)$$

Although the DFT overcomes the challenge associated with analysing real-world data sets, it may not always be practical due to the large quantity of computations required to complete the transform for very large data sets. This can be bypassed by using a fast Fourier transform (FFT), which is an efficient algorithm for calculating the DFT and can greatly reduce computation times. Evaluating equation (3.11) directly requires N^2 operations – there are N outputs of $\mathcal{F}(k)$, each requiring a sum of N terms. In comparison, a FFT can compute the same data set in $N \log N$ operations [108]. Depending on the size

of the data set in question, for a typical computer, this can reduce the processing time from hours or days down to seconds.

A FFT can therefore be applied to the reflected optical spectrum to extract fringes per spectral unit, or the fringe frequency. In a practical implementation, some pre-processing steps are required for this to be achievable, as highlighted in Figure 3.8. The interferogram is converted into the *optical* frequency domain (wavenumber) by simply reciprocating what was initially recorded in the wavelength domain. This data set is then resampled to provide a linear sample spacing with sampling frequency f_s , and a FFT is applied to yield cavity length information.

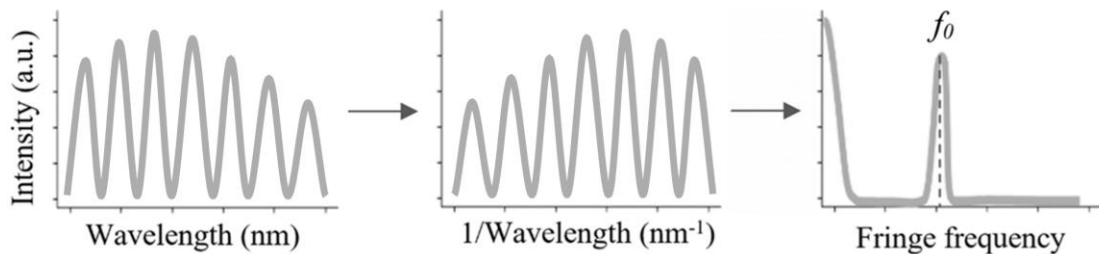


Figure 3.8: Data processing for cavity length acquisition from reflected optical spectrum.

The main frequency, f_0 , is defined as [109]:

$$f_0 = \frac{2d}{\lambda^2} \quad (3.13)$$

After the spectrum has been resampled, the true position of f_0 is determined by its initial position divided by C , where $C = f_s/N$, and N is the total number of points in the resampled spectrum dataset. Therefore, once peak position f_0 is detected, the cavity length can be calculated from equation (3.13). Many peak detection algorithms exist, such as a gaussian fit, quadratic fit, interpolated maximum search, centroid (where the algorithm outputs the dataset's geometric centre), and linear phase operator, to name a few [110]. These peak detection algorithms have been applied to a fibre Bragg grating system and compared in [110], which concludes that four of the five peak detection algorithm yield comparable output resolution, with the exception of the centroid algorithm, which performed noticeably worse. Therefore, in this work, the peak detection algorithm that is used is that of a quadratic fit implemented within LabVIEW virtual

instruments. The input parameter of primary importance for this peak detection algorithm is the width, which refers to the number of consecutive data points implemented in the quadratic fit. In this instance, the minimum possible width of 3 is used, which corresponds to an exact fit, whereas a larger number will inherently introduce with it smoothing of high frequency noise [111].

The cavity length reading using solely a FFT inherently carries with it certain inaccuracies. For example, small fluctuations or drifting of the cavity length during a scan of the swept laser source will result in a non-uniform fringe spacing, which is detrimental to the accuracy of the FFT measurement (i.e., results in peak broadening which may occur symmetrically or otherwise). A rectification method in the form of a function-fitting algorithm is discussed in the following section.

3.3.2 *Function-fitting algorithm*

The implementation of a function-fitting algorithm (FFA) offers a solution to the shortcomings of FFT analysis described above. The fitting function is of the form:

$$I(\lambda) = A(\lambda) + B(\lambda) \cos\left(\frac{4\pi d}{\lambda}\right) \quad (3.14)$$

Where $A(\lambda)$ and $B(\lambda)$ are the average and the peak-to-peak amplitude of the signal respectively. Let us assume that the measurement signal is normalised and contains the sequence of data

$$I_1, I_2, \dots, I_N \quad (3.15)$$

at corresponding wavelengths $\lambda_1, \lambda_2, \dots, \lambda_N$. If the cavity length is known, this dataset can be modelled using equation (3.14), so that:

$$I_i = A_i + B_i \cos\left(\frac{4\pi d}{\lambda_i}\right), \quad i = 1, 2, \dots, N \quad (3.16)$$

Although the cavity length is, in fact, not known, it can be estimated. The closer the estimate to the true cavity length, the smaller the error becomes, where the error is defined as:

$$Error_i = I_i - \left(A_i + B_i \cos\left(\frac{4\pi d}{\lambda_i}\right) \right), \quad i = 1, 2, \dots, N \quad (3.17)$$

Note that in equation (3.17), I_i is the i^{th} measured signal intensity, and $A_i + B_i \cos\left(\frac{4\pi d}{\lambda_i}\right)$ is the fitted function intensity of equal index. More comprehensively, an appropriate value of d is searched for that minimises the sum of squares error (SSE) which can be described as:

$$\min_d \sum_{i=1}^N \left(I_i - A - B \cos\left(\frac{4\pi d}{\lambda_i}\right) \right)^2 \quad (3.18)$$

Computationally speaking, it is impractical to search through an unnecessarily large range of candidate cavity lengths. The cavity length reading that is obtained via the FFT analysis can be used as an initial estimate, and a grid search with a defined increment resolution can thusly be conducted. The process is demonstrated in Figure 3.9 & 3.10, where a grid search between 340 – 360 μm with a 5 nm increment is applied to a simulated optical cavity using a swept source between 1510 – 1590 nm wavelengths.

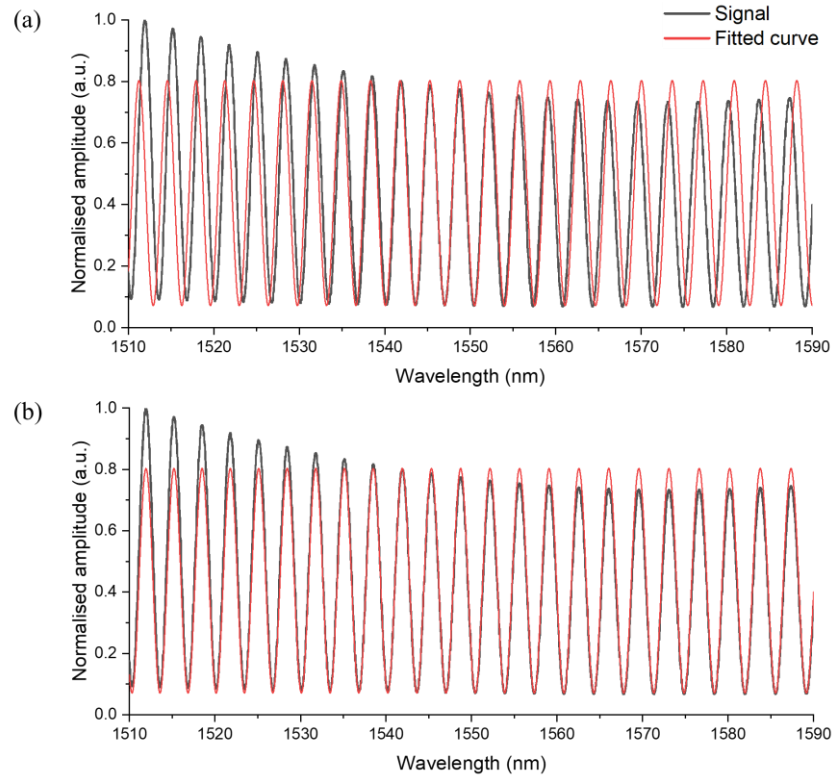


Figure 3.9: Simulated input signal with arbitrary amplitude envelope to replicate possible real signal for demonstration purposes. (a) Poor cavity length estimate of

$d=343 \mu\text{m}$ resulting in a large error fit. (b) Good cavity length estimate of $d=350 \mu\text{m}$ resulting in a minimal error fit.

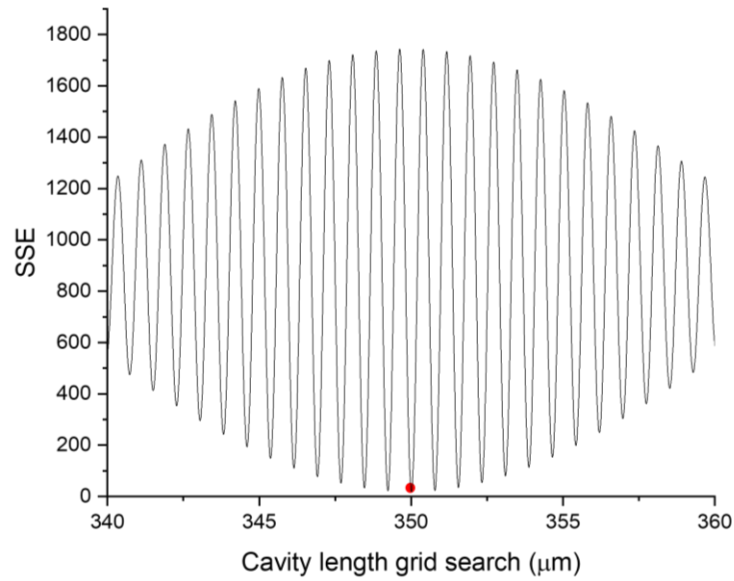


Figure 3.10: Example of sum of squares error (SSE) graph across a range of cavity length inputs during grid search. The red dot indicates the global minimum.

The true cavity length in this exemplary case is considered to be $350 \mu\text{m}$ as this cavity length value results in the lowest SSE. The range and resolution of the grid should ideally be tailored to the hardware capabilities and the application in question to ensure a real-time measurement readout is preserved. Table 3.1 summarises the steps undertaken to perform the FFA.

Table 3.1: Function-fitting algorithm and grid search summary.

- 1) Acquire a cavity length reading from the FFT analysis as an initial estimate
- 2) Generate a cavity length grid. E.g.

$$d_{grid} = \begin{pmatrix} d_{initial - N/2} \\ \vdots \\ d_{initial - 2} \\ d_{initial - 1} \\ d_{initial} \\ d_{initial + 1} \\ d_{initial + 2} \\ \vdots \\ d_{initial + N/2} \end{pmatrix}$$

-
- 3) Fit the function described by equation (3.16)
 - 4) Apply SSE analysis described by (3.18)
 - 5) The value of d which minimises the SSE is considered the true cavity length.
-

In the presence of slow cavity length drift or fluctuation during a wavelength scan of the swept laser source, where there is non-uniform fringe spacing, the FFA output is effectively the average cavity length among the range of cavity lengths which are input during the period of a single scan. With increased temporal resolution, i.e., faster scan speed, fewer different cavity lengths are input at any given linear drift/fluctuation rate, which will improve the SSE. Conversely, at any fixed scan speed, slower cavity length drift or fluctuation will also result in fewer different cavity lengths being input, also improving the SSE. For a configuration where the scan speed is slow and fixed (as is the case outlined in § 3.5) it is desirable to have a measurement environment where the target surface is not prone to significant drift or fluctuations. In applications where this is not possible, the appropriate interrogation system with sufficient scan speed may be implemented, e.g., where 1 kHz vibration is present, a 2 kHz interrogation system or better (as per the Nyquist limit) may be appropriate.

3.4 Evaluation of demodulation methods using LabVIEW virtual instruments (VI)

In order to quantifiably assess the performance of the FFT and FFA analysis both individually and comparatively, a simulated optical cavity signal is generated using LabVIEW with easily controllable input parameters. The simulated signal largely follows equation (3.14), with an introduced *Noise* parameter as outlined in equation (3.19).

$$I(\lambda) = A(\lambda) + B(\lambda) \cos\left(\frac{4\pi d}{\lambda} (1 + \text{Noise} \times \text{RNG})\right) \quad (3.19)$$

Where *RNG* is a random number generator between 0 – 1 with a uniform distribution, and *Noise* is an arbitrary scalar. A positive noise is applied to avoid logical errors where the amplitude could be <0. The introduction of a noise parameter allows for the controlled deterioration of the signal-to-noise ratio (SNR) of the simulated spectrum. Examples of low and high noise simulated signals with a defined cavity length of $d = 350.000 \mu\text{m}$ are shown in Figure 3.11.

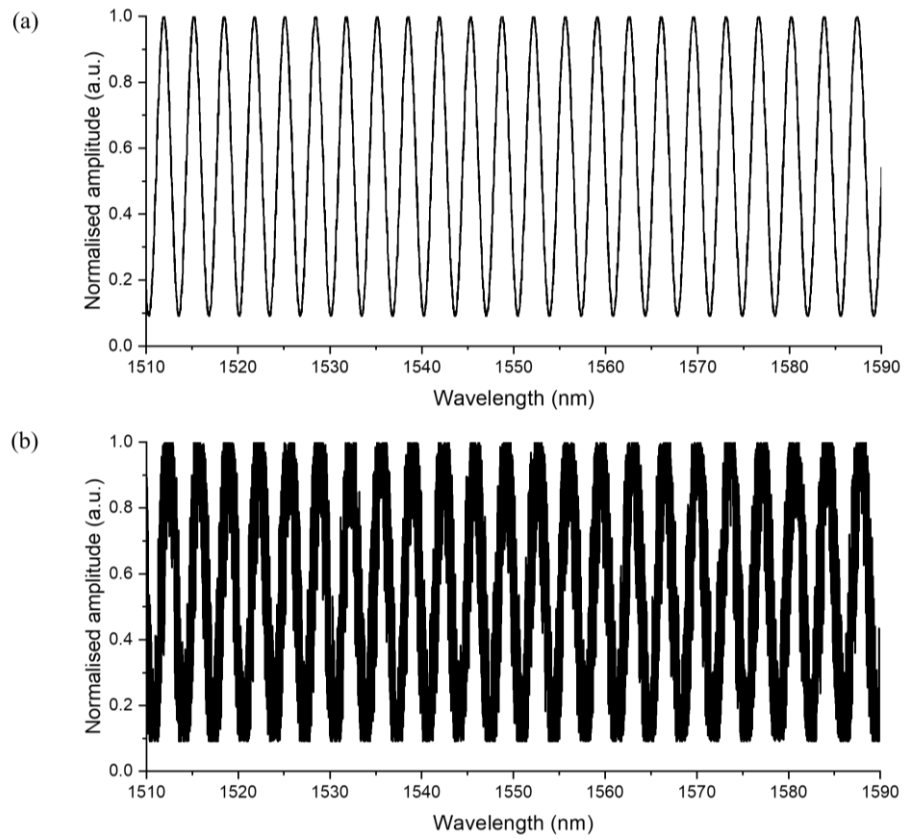


Figure 3.11: (a) Low noise simulated optical cavity signal. (b) High noise simulated optical cavity signal.

A direct comparison can be drawn between both cavity length measurement approaches (FFT and FFA) by applying them to both the low and high noise signals (see Figure 3.12). By measuring the cavity length over a period of time, the mean reading is indicative of the measurement's accuracy – the closer to the true cavity length (which in this case is defined as $d = 350.000 \mu m$ for both simulated signals), the more accurate the reading. In addition to this, the standard deviation (σ) of the measurement fluctuations assesses the measurement's sensitivity. Plus-or-minus two standard deviations (2σ) correlate to approximately a 95% confidence interval, so two standard deviations is used to assess sensitivity.

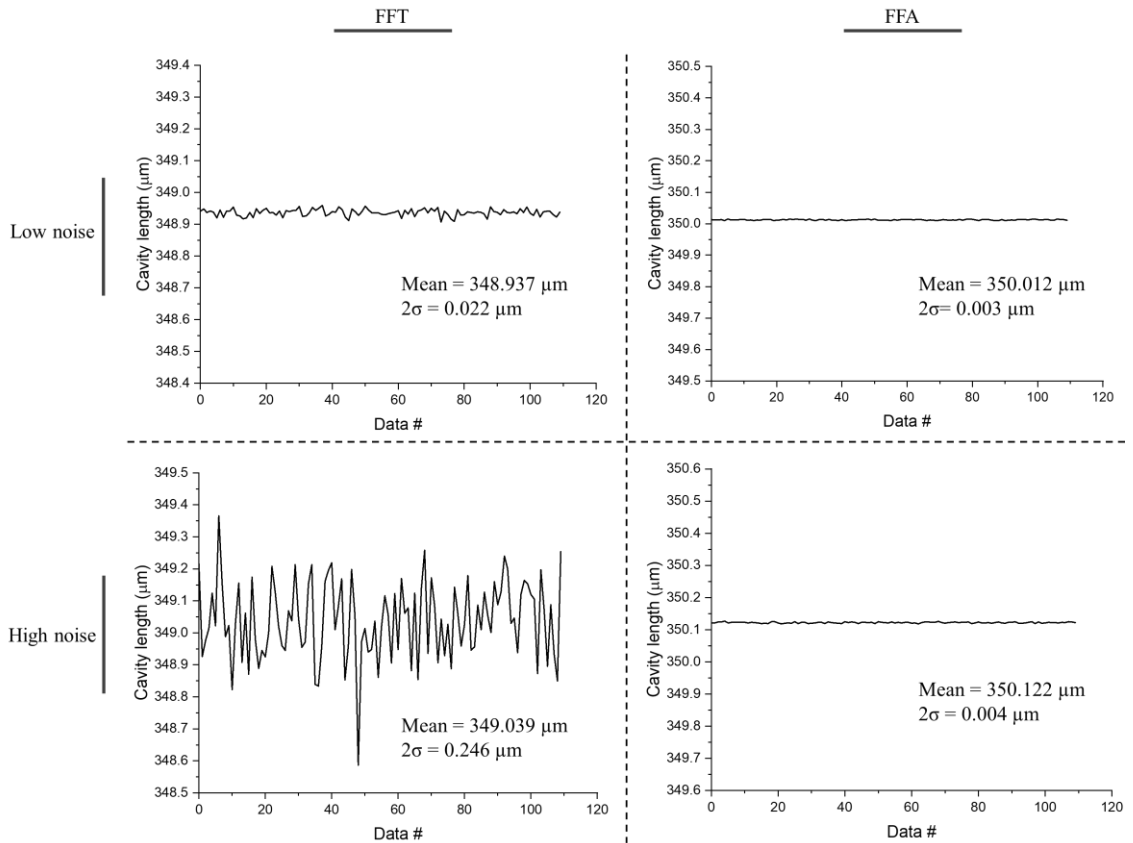


Figure 3.12: FFT and FFA cavity length measurement approaches applied to both low and high noise simulated signals.

Note that in Figure 3.12, the cavity length axis (vertical axis) on each graph has the same range of 1 μm to easily draw direct comparisons. Regarding the low noise signal, the FFA reading displays better accuracy and sensitivity compared to the FFT reading. When the high noise signal is considered, not only does the FFA reading still display better accuracy, but the sensitivity remains relatively unchanged, whereas the FFT reading experiences significantly worse sensitivity.

The cavity length grid search performed on both low and high noise signals generates the SSE graph in Figure 3.13:

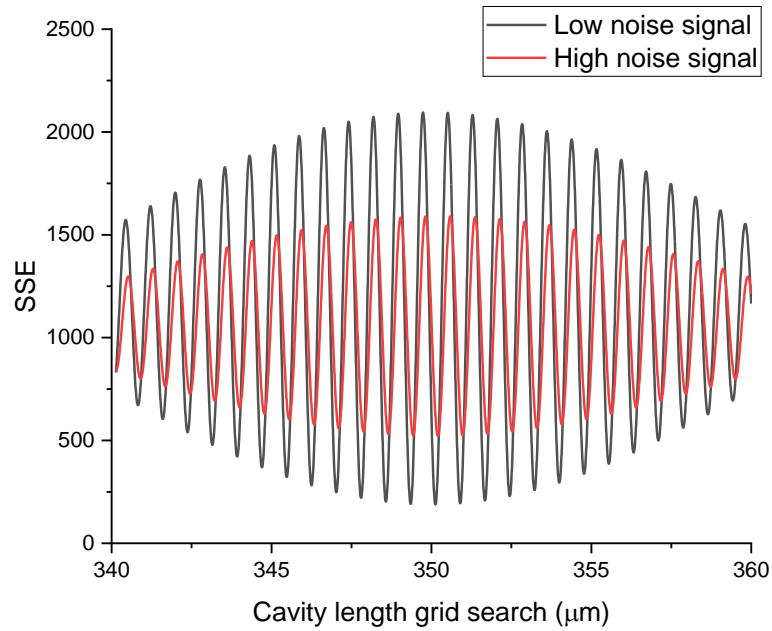


Figure 3.13: SSE graph of simulated arbitrary low and high noise signals.

It is clear that with degrading SNR of the reflected optical spectrum, the corresponding SSE analysis of the cavity length grid search will result in valleys with larger amounts of error across the grid. As long as an appropriate peak-detection (or in this case, valley-detection) algorithm can reliably converge to the cavity length of least error, the poor SNR appears to be not problematic, where the FFA reading will demonstrate better accuracy and sensitivity compared to the FFT reading. However, as the SNR degrades further, there comes a threshold where the SSE analysis no longer reliably converges to a single solution – cavity lengths in the vicinity of the true cavity length will compete for having the lowest error, and the convergence will jump back-and-forth. The spacing between valleys is approximately $0.8 \mu\text{m}$, many orders of magnitude greater than the sensitivity of any one solution. Therefore, once this occurs, the limit of FFA applicability is reached and should no longer be considered reliable for accurate and sensitive cavity length measurements.

3.5 Experimental evaluation of demodulation methods

An experimental evaluation is conducted following the simulated performance assessment of the FFT and FFA cavity measurement techniques. This is performed using a normal cleaved and a 45° angle cleaved single-core fibre. These behave as both precursors leading to the implementation of multi-core fibre, as well as a frame of reference for what can optimally be achieved experimentally.

3.5.1 Experimental configuration

The experimental configuration is shown in Figure 3.14. An optical sensing interrogator (SM125-700, MicronOptics) is employed as both the light source and the detector. This consists of a swept laser source with a wavelength range of 1510 – 1590 nm and a data acquisition rate of 5 Hz. The wavelength is swept at a resolution of 0.0125 nm. The theoretical maximum resolvable cavity length corresponds to an interference fringe consisting of at least two points, as described by the Nyquist limit. Given the scan resolution, the FSR at the maximum cavity length is defined by a wavelength gap of 0.025 nm, which corresponds to a maximum resolvable cavity length is $\sim 48,000 \mu\text{m}$ as calculated from equation (3.8).

SMF28 fibre is connected to the optical interrogator. Depending on the type of fibre sensor (i.e., with or without turning mirrors), the fibre is oriented either parallel or perpendicular to the target surface, where the target surface is a mirror mounted to a moveable platform. The interference spectrum generated from this configuration is recorded and sent to a computer for data processing. The moveable platform is also fitted with a retroreflector which is used in conjunction with a commercial laser interferometer (633 nm, 1nm resolution, $\pm 0.0001\%$ accuracy) to assess the accuracy of the fibre measurement system.

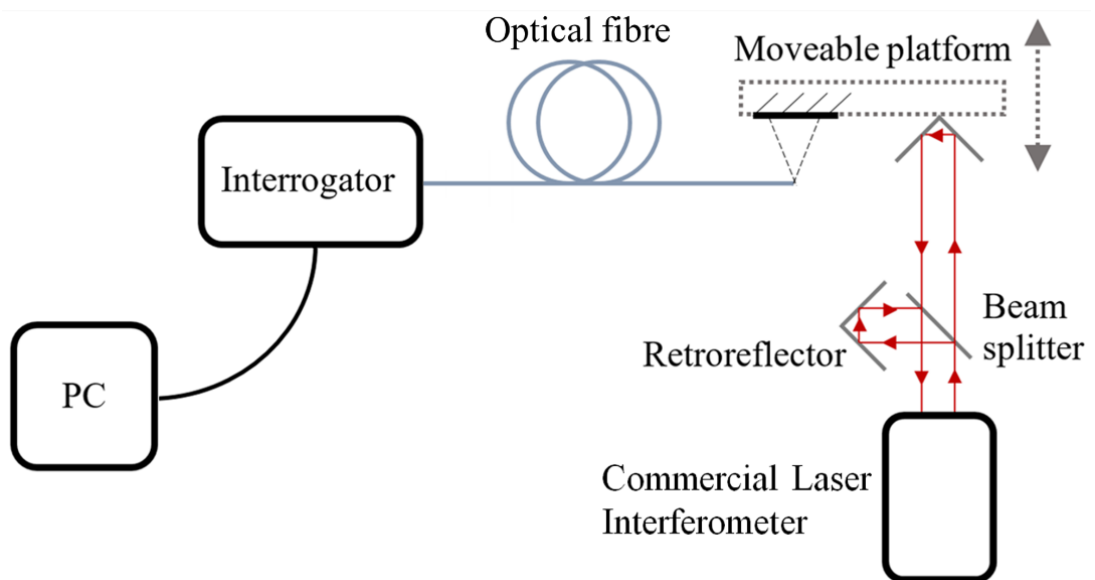


Figure 3.14: Experimental configuration for fibre optic Fabry-Pérot sensor accuracy assessment.

3.5.2 Normal cleaved fibre

The sensor performance metrics are defined here to be the sensor's accuracy, sensitivity, and range. The sensor accuracy is assessed by measuring the displacement of a target surface in conjunction with a highly accurate laser interferometer and the resulting data sets are compared. A linear fit is then applied and the residuals, which are the differences between each data point and the fitted line, are evaluated. In the absence of noise or systematic errors it is expected that the intercept of the fitted line is the origin, and the gradient is 1. Any deviation from this is likely due to minor misalignment of the optics involved in the experiment. This assessment, which is conducted with a normal cleaved single-mode, single-core fibre (SMF28) is repeated using both FFT and FFA cavity length measurement techniques (see Figure 3.15).

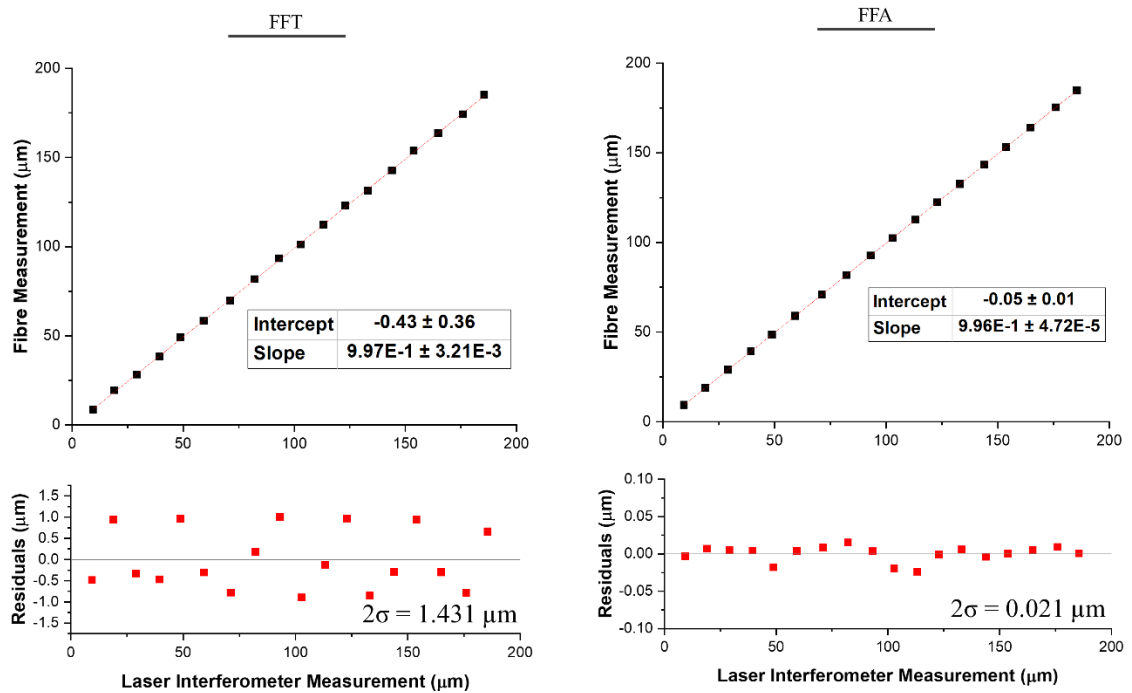


Figure 3.15: Normal cleaved fibre sensor and laser interferometer measurements using FFT (left) and FFA (right) cavity length measurement techniques to assess sensor accuracy, consisting of cavity lengths $\sim 300 - 500 \mu\text{m}$. Note that the horizontal axes are of displacement and the residuals vertical axes are of different scales.

The sensor accuracy can be quantified by taking the standard deviation of the residuals. Two standard deviations correlate to approximately a 95% confidence interval, allowing for a more comprehensive assessment. Therefore, it can be concluded that the normal

cleaved fibre sensor accuracy using a FFT and FFA method result in accuracies of $\pm 1.431 \mu\text{m}$ and $\pm 0.021 \mu\text{m}$ respectively.

With regards to assessing the sensor sensitivity, a fixed cavity length is measured continually for a period of time, and the measurement fluctuations that occur are representative of the measurement sensitivity. Similarly as with the accuracy assessment, the sensitivity is defined as two standard deviations of the fluctuating measurements at each fixed cavity length. This process is repeated up until a cavity length where the FFA fails to reliably converge to a single solution, in turn, identifying the range of the sensor as well. An example of the fluctuations measured at a fixed cavity length is shown in Figure 3.16, and the sensitivity across the operable range of the sensor is shown in Figure 3.17.

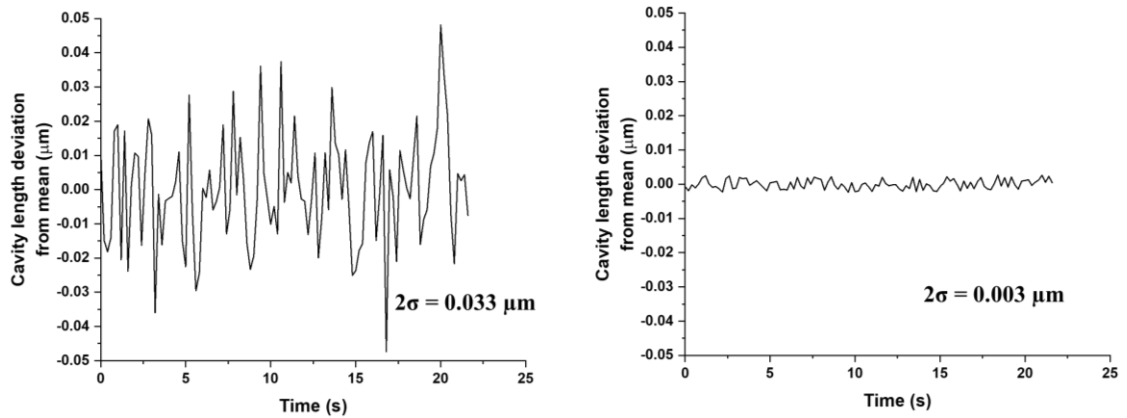


Figure 3.16: Fluctuations measured using FFT (left) and FFA (right) at a fixed cavity length of $\sim 2000 \mu\text{m}$.

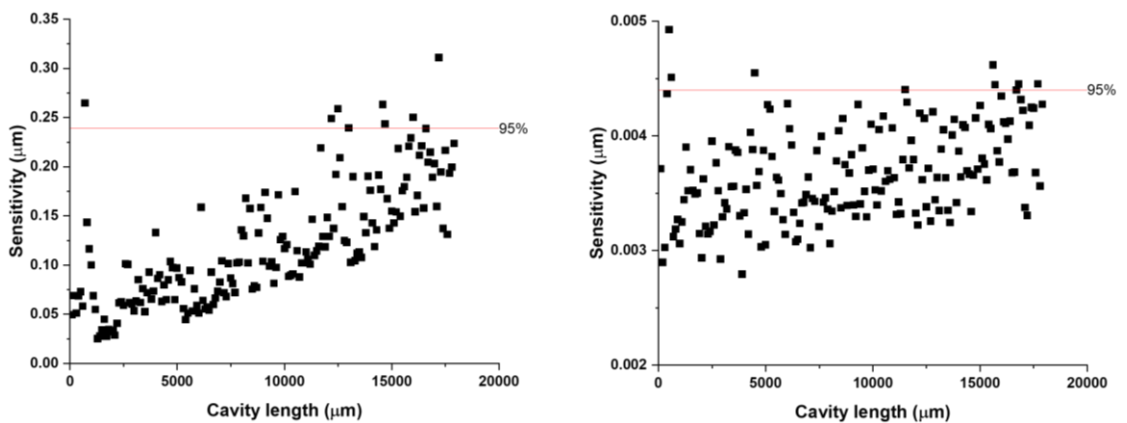


Figure 3.17: Sensitivity measurements of normal cleaved fibre using FFT (left) and FFA (right) taken in increments of $\sim 100 \mu\text{m}$ up to the maximum sensor range. The red line corresponds to the sensitivity within which 95% of data points fall under. Note that the vertical axes are of different scales.

Regarding the cavity length measurements acquired using the FFT, there is a clear trend that shows the sensitivity deteriorates as the cavity length increases. Such a trend is not so clear regarding the dataset acquired using the FFA. Adhering to the concept of 95% confidence, a line is drawn in Figure 3.17 at the sensitivity value within which 95% of the remaining data points fall under. Although this approach may not be the most appropriate for the dataset acquired using the FFT, as there is a distinct gradient trend at different cavity lengths, this 95% sensitivity value allows for an assessment in the worst case (i.e., the longest achievable cavity length) that can be used to draw direct comparisons between FFT and FFA results. It can therefore be concluded that sensitivities of $\pm 0.239 \mu\text{m}$ and $\pm 0.0044 \mu\text{m}$ (or $\pm 0.004 \mu\text{m}$, rounded to the nearest nm), using FFT and FFA respectively, over a range of $\sim 18 \text{ mm}$ are achieved.

When all results acquired using a normal cleaved fibre are considered, it is clear that the FFA offers a significantly improved cavity length measurement approach. When comparing the accuracies achieved, the FFA results in an improvement of 68 times that of the FFT measurement. A similar improvement is also seen regarding the sensitivity assessment, where an improvement of 54 times that of the FFT measurement is observed across the total range.

3.5.3 45° angle cleaved fibre

The metrics used to assess sensor performance using a normal cleaved fibre are also applied to a fibre cleaved at 45° (Figure 3.18). It is desired to garner an understanding of how the sensor will perform without any additional processes to the fibre, i.e., without any reflective coating on the 45° facet and leaving the circular circumference intact. Although not all of the guided light will satisfy the condition for total internal reflection at the 45° facet due to the numerical aperture of the fibre core (the effects of this are explored in detail in § 4.2.3), the reduction in light intensity may be compensated for by the circumferential edge of the fibre behaving as a lens – the divergent beam may be narrowed enough to improve the signal return from the target surface.

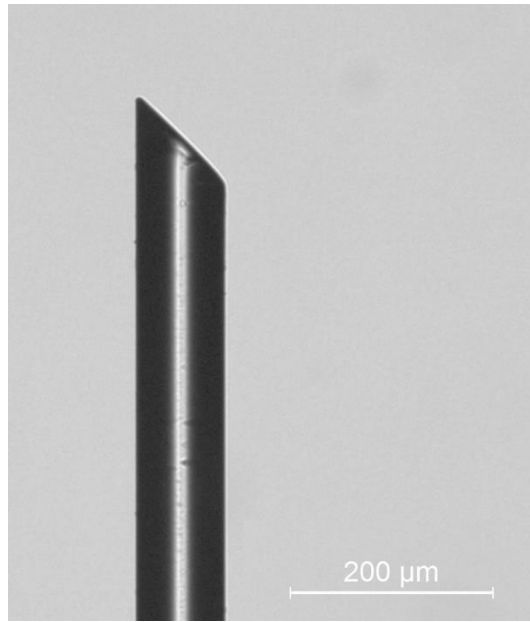


Figure 3.18: SMF28 optical fibre cleaved at 45° to the fibre axis

The same configuration is used as with the normal cleaved fibre to assess accuracy (Figure 3.19), sensitivity and range (Figure 3.20) of the 45° angle cleaved fibre.

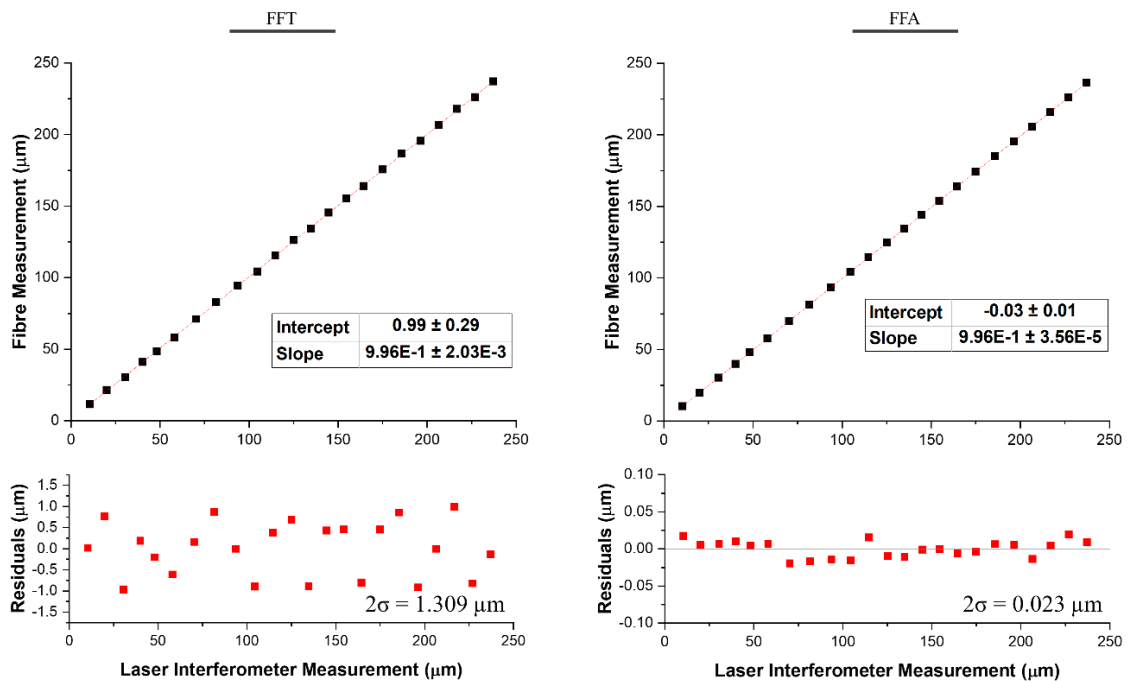


Figure 3.19: 45° angle cleaved fibre sensor and laser interferometer measurements using FFT (left) and FFA (right) cavity length measurements techniques to assess sensor accuracy, consisting of cavity lengths ~300 – 500 μm. Note that the horizontal axes are of displacement and the residuals vertical axes are of different scales.

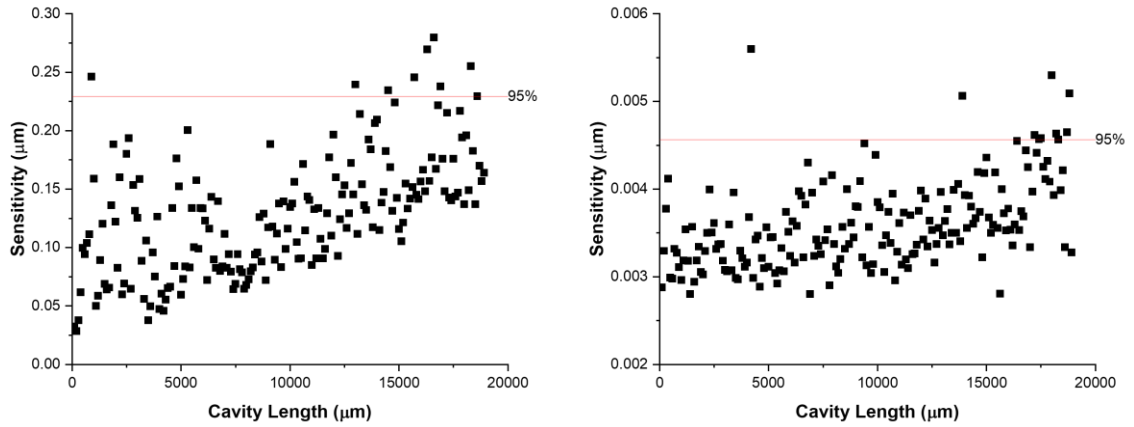


Figure 3.20: Sensitivity measurements of 45° angle cleaved fibre using FFT (left) and FFA (right) taken in increments of ~100 μm up to the maximum sensor range. The red line corresponds to the sensitivity within which 95% of data points fall under. Note that the vertical axes are of different scales.

By once again considering results that fall within a 95% confidence interval, the accuracy of the sensor using the FFT and FFA is $\pm 1.309 \mu\text{m}$ and $\pm 0.023 \mu\text{m}$ respectively. The FFA measurement therefore corresponds to an improvement of 57 times that of the FFT measurement in the context of accuracy. According to Figure 3.17, the sensor sensitivity using the FFT and FFA measurements is $\pm 0.230 \mu\text{m}$ and $\pm 0.0046 \mu\text{m}$ (or $\pm 0.005 \mu\text{m}$, rounded to the nearest nm) respectively, across a range of ~19 mm. The FFA measurement therefore corresponds to an improvement of 50 times that of the FFT measurement in the context of sensitivity.

When comparing the results obtained using the normal cleave fibre and the 45° angle cleaved fibre, many similarities can be observed. The sensitivity measurements obtained using the FFT for both fibres indicate a clear deterioration of sensitivity with increasing cavity length at similar rates, whereas with the FFA equivalent, not only is the sensitivity significantly improved, but it is also considerably more uniform across the operable range of each sensor. The accuracies of both fibres are also very similar, where accuracies of $\pm 0.021 \mu\text{m}$ and $\pm 0.023 \mu\text{m}$ are obtained for the normal cleaved fibre and the 45° angle cleaved fibre respectively using the FFA, both of which represent a significant improvement over their FFT measurement counterpart.

One performance comparison that is particularly interesting is the operable range of each sensor, where ranges of ~18 mm and ~19 mm were obtained for the normal cleaved fibre and the 45° angle cleaved fibre respectively. Firstly, it is important to note that the sensor

ranges are approximated to the nearest mm as it is challenging to identify a range cut-off with any higher resolution. This is primarily due to the semi-quantitative nature of the approach used in assessing the operable range coupled with the uncontrollable and unpredictable external influencers of the practical configuration. The “practical configuration” here refers to the small misalignments that are likely present to some extent with each fibre sensor during the experimental process, and its “external influencers” refers to anything which may be undetectable to humans but impactful enough to influence the fibre measurement (e.g., vibrations due to a door closing quickly elsewhere in the building, very small temperature changes which may expand/contract the mirror/fibre mounts, etc.). The assessment approach is considered semi-quantitative as it relies on identifying the point at which the FFA no longer reliably converges to a single solution. If, for example, 100 data points are acquired using the FFA and all 100 of them converge to a single solution then it is clear that the FFA reading has reliably converged to a solution. If, however, 99 out of 100 data points are of one solution, and there exists 1 data point where the FFA has converged to another solution, then there is still a strong argument to made that the FFA has reliably converged to a solution, and perhaps there was some external influencer which momentarily disturbed the measurement. Furthering this analogy, if 80 out of 100 data points were of one solution, and the remaining 20 were of another, then assessing the reliability of the convergence becomes more challenging: If these 20 data points are sporadically spread out across the data set, then one may still claim that the FFA has reliably converged to a solution which accounts for 80 out of the 100 data points. If, however, all 20 data points were at the end of the data set, this sudden transition may lead to the conclusion that the FFA has not reliably converged to a solution. All of these factors described contributes towards the challenge of measuring the sensor range with high resolution.

With this in mind, it can be seen that both the normal cleaved fibre and the 45° angle cleaved fibre demonstrate very similar ranges. This is indicative that the circumferential edge of the fibre sufficiently compensates for the loss of the light that occurs at the 45° facet. Although applying a reflective coating to the facet may improve this further, it is clear that this is not a requirement for sufficient sensor functionality.

3.6 Conclusions

The principles of Fabry-Pérot interferometry, regarding its mathematical model and its implementation with optical fibres, is discussed. To overcome the limitations of

accessing spatially confined regions for sensor deployment, as well as achieving the capability of measuring absolute distance between two surfaces, turning mirrors fabricated onto multi-core fibre will be explored.

The signal that is recorded from the Fabry-Pérot cavity that is formed between the fibre and the target surface can be demodulated in a number of ways. The most rudimentary of which consists of identifying the free spectral range from two points on the reflected spectrum. This approach, although elegant in its simplicity, disregards the remaining unused data points. A fast-Fourier transform (FFT) circumvents this issue, where the cavity length information is extracted from the fringe frequency of the reflected spectrum. This approach is further improved by incorporating a function-fitting algorithm (FFA).

Evaluating the amount of improvement the FFA introduces in comparison to solely using the FFT approach is at first conducted by simulation, and then experimentally using a normal cleaved fibre and a 45° angle cleaved fibre. It was revealed that the FFA consistently provides better accuracy and sensitivity compared to the FFT measurement datasets. The experimental results are summarised in Table 3.1.

Table 3.1: Summary of experimental results using normal cleaved fibre and 45° angle cleaved fibre to assess FFT and FFA cavity length measurement techniques.

| | | Accuracy (μm) | Sensitivity (μm) | Range (mm) |
|-------------------------|-----|----------------------------|-------------------------------|------------|
| Normal cleaved fibre | FFT | 1.431 | 0.239 | ~18 |
| | FFA | 0.021 | 0.004 | |
| 45° angle cleaved fibre | FFT | 1.309 | 0.230 | ~19 |
| | FFA | 0.023 | 0.005 | |

Regarding the 45° angle cleaved fibre, a portion of the guided light will not satisfy the condition for total internal reflection and will therefore be lost. Despite this, the 45° angle cleaved fibre demonstrates very similar operable range than that of the normal cleaved fibre. This may be indicative that the circumferential edge of the fibre behaves as a lens and sufficiently compensates for this loss.

Chapter 4

Fibre optic probes for distance measurements

4.1 Introduction

Typically, when light is coupled into the fibre core, it remains there. This is achieved by the total internal reflection (TIR)* that occurs within the structure of an optical fibre. Fundamentally, a typical optical fibre is comprised of a light guiding core and an outer cladding, both made from fused-silica, where a dopant is commonly introduced to one to induce a step change in refractive index. Although it is far more common for applications to consist of fibres with only a single core, the novelty of fibre consisting of multiple cores, or multi-core fibre (MCF), will prove itself crucially valuable in this work. MCF is typically considered to be a specialty fibre, and so its commercial availability is incomparable to that of single-core fibre (SCF). Although off-the-shelf solutions exist [112], it is common for bespoke MCF solutions to be required depending on the application.

In order to measure the absolute distance between two close parallel surfaces, turning mirrors are fabricated onto a MCF to redirect the guided light perpendicular to the fibre axis (this concept is illustrated in § 3.2.2, Figure 3.7). When such a MCF is positioned between parallel component surfaces of interest, Fabry-Pérot cavities are formed on either side of the fibre. In addition to the known core spacing, the total distance between components can be determined.

* The comprehensive solution to guided light within a waveguide is described by Maxwell equations, but TIR is sufficient as a first order approximation with regards to the work conducted in this thesis.

In this thesis, there are three turning mirror fabrication processes explored to assess the applicability of different technologies in fibre sensor fabrication. One consists of using a focused ion beam (FIB) to mill the desired feature directly onto the cleaved fibre end; another involves an ultrafast laser inscription process followed by chemical etching using potassium hydroxide (KOH) to remove the inscribed feature from the fibre; and the last uses the same laser inscription and chemical etching process but applied to a fused-silica wafer to produce a small component that is attached to the fibre. In this chapter, the advantages and limitations of different fibre types are discussed, and the effectiveness of different turning mirror designs and fabrication approaches are investigated.

4.2 Fibre characteristics and limitations

There are more characteristics that define optical fibre behaviour beyond the number of cores present. In this section, the relevant characteristics that contribute towards its beneficial or detrimental properties in the context of distance measurement applications are discussed.

4.2.1 *Single-core fibre*

Although it has already been established that MCF is a potential solution for a miniature gap sensing probe, SCF has a crucial role regarding the chronological development of the final sensor to be deployed. As the measurement technique is interferometric and based upon a scanning wavelength interrogation, both fibre types (SCF and MCF) will be single mode at the operating wavelengths. In some circumstances, the size of the cladding may differ, but this will be elaborated upon in the next section.

Some of the most significant differentiators between the SCF and MCF used here reside with the splicing capabilities and requirements, and interfacing with the fibre to couple light into and out of the core(s). Regarding SCF, both of these processes are highly developed and relatively straightforward. Standardised SCF connectors are well established and offer a low-loss, plug-and-play solution for interfacing the light source with a compatible connector to the fibre. Some commonly used fibre connectors are FC/PC[†] and FC/APC[‡] connectors which feature typical connector-to-connector losses of ~0.25 dB [113].

[†] Ferrule connector / physical contact

[‡] Ferrule connector / angled physical contact

Similarly, the splicing of SCF to SCF can be achieved using standard, commercially available splicers: SCF requires no rotational alignment, and the precise transverse and angular alignment that is required can be easily achieved by automatic motor adjustment present in modern commercial fibre splicers. This typically results in low-loss splices of the optical fibre, often in the range of 0.01 dB loss.

With this in mind, SCF is justifiably an excellent stepping-stone towards the development of an absolute distance measurement fibre sensor which will eventually utilise MCF. By implementing a turning mirror onto SCF using the fabrication approaches investigated, this provides a simpler fibre for process optimisation and a near-‘ideal’ sensor can be established as a benchmark, where any deviation in performance of the MCF sensor equivalent can be evaluated accordingly.

4.2.2 Multi-core fibre

The material composition of the fibre cores turns out to be significant with regards to its interaction with the different turning mirror fabrication processes, as was discovered experimentally. There are two readily accessible MCF used in this work, where the cross-sections of each are illustrated in Figure 4.1.

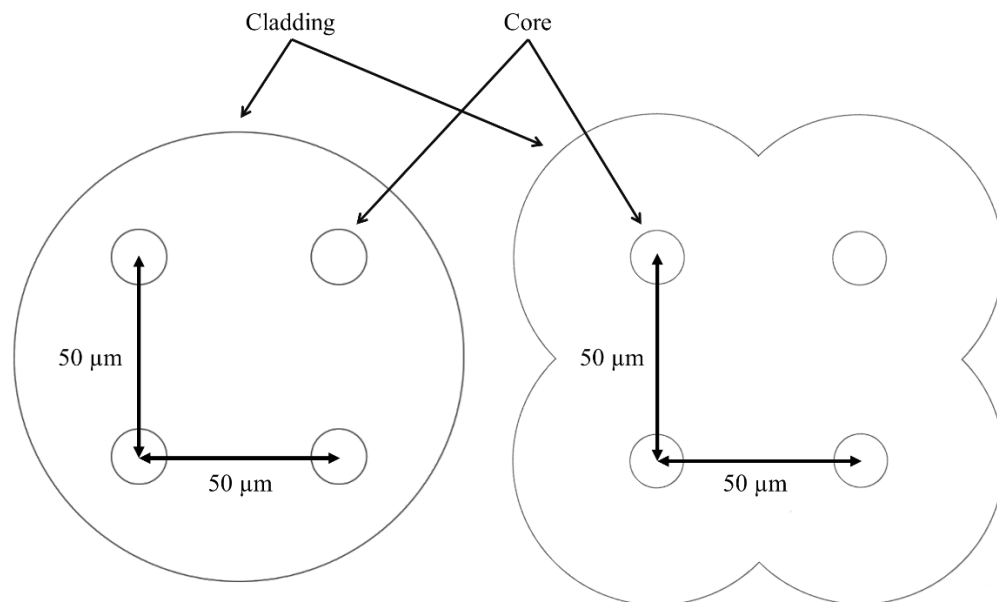


Figure 4.1: Cross-sectional illustration of (left) circular MCF and (right) “clover” MCF.

Due to the cross-sectional shapes, they are aptly labelled as *circular* MCF, and *clover* MCF, appropriate to the latter's resemblance to a four-leaf clover. Both MCF consist of four cores in a square lattice, with a 50 μm pitch (verified under microscope to $\pm 1 \mu\text{m}$) and are single mode at 1550 nm. The circular MCF contains a standard fused-silica 125 μm ($\pm 1 \mu\text{m}$) diameter cladding with boron co-doped germanosilicate cores. This was originally produced with fibre Bragg grating applications in mind and so is photosensitive. The boron co-doped germanosilicate cores are selectively etched by KOH (see Figure 4.2), and therefore are unsuitable for some designs.

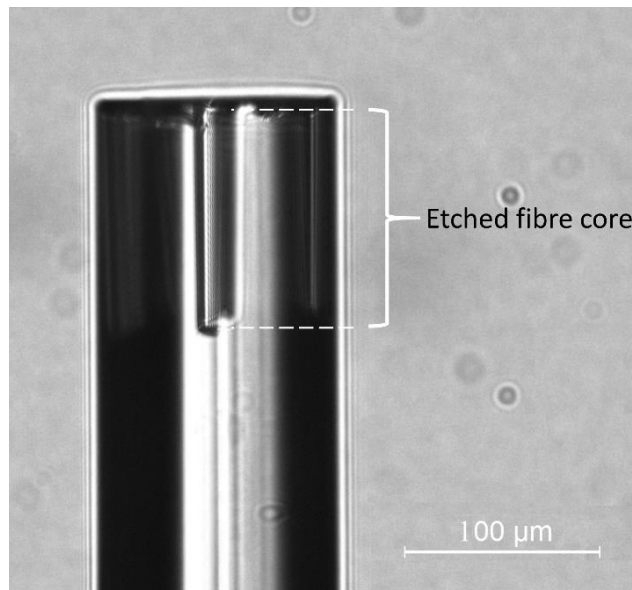


Figure 4.2: Microscope image of circular MCF cores selectively etched by KOH.

This unintended selective etching behaviour renders the circular MCF incompatible with the turning mirror fabrication approach consisting of laser inscription and chemical etching using KOH. Although any inscribed feature on the fibre end may be fabricated as designed, the cores would etch from underneath said feature, leading to unguided and scattered light, resulting in severe signal loss. This unintended selective etching behaviour was not observed with the clover MCF, and as such provided a suitable substitute regarding the fabrication process involving chemical etching. This suggests that the clover MCF cores are fused-silica, but it is unclear and unknown as to what specific dopant is present in the cladding. Regardless, it is observed to be inconsequential in its application. Regarding fabrication processes where the fibre is not chemically etched, the circular MCF is still desirable due to its conventional cross-sectional shape

(consequences of the clover MCF's cross-sectional shape are discussed later in this section).

Generally speaking, there are further limitations that are inherent within MCF that must be taken into consideration. Addressing each core individually requires interfacing of SCF's to MCF. This interface is commonly referred to as a fanout, which is achieved via laser inscribed 3D waveguides. In such systems, the subsequent insertion losses can be significant, where losses up to 3 dB per core are not uncommon. Further details regarding the specific fan-out system used is described in § 4.2.3.

The fanout can be thought of as a self-contained system consisting of SCF inputs and one MCF output. The MCF output from the fanout is also circular in cross-section, with the same dimensions and core spacing to that of the circular MCF illustrated in Figure 4.1. Ideally, the fabrication of turning mirrors would be undertaken on the output MCF of the fanout to avoid any additional insertion loss, but certain practical restrictions can prevent this from taking place. For example, the SCF to MCF waveguide interface is typically fragile and handling the fanout during each stage of the different fabrication processes introduces increased risk of damaging the system permanently, possibly to such an extent where it is no longer functional. Additionally, the length of the output MCF may not be sufficient for the practical implementation in the different fabrication systems. It is also unclear how the fanout would be influenced when under a vacuum (in the case of attempting to situate the fanout as a whole within the FIB machine). It is therefore necessary to utilise additional lengths of MCF which can then be spliced onto the fanout.

MCF to MCF splices are more challenging due to the need for precise rotational alignment. Losses from a fibre-to-fibre connection can arise in many ways [104]. In order to achieve a low-loss connection in a MCF, the alignment of all cores must be considered. Figure 4.3 illustrates the common types of misalignment that significantly affect the signal loss in a fibre-to-fibre connection.

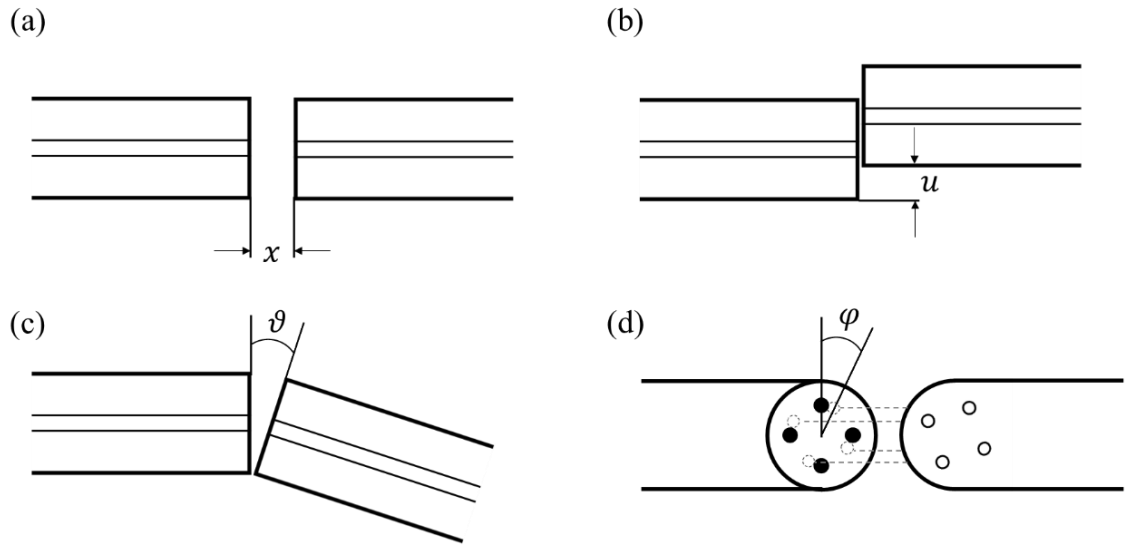


Figure 4.3: Misalignment types between fibre connections. (a) Longitudinal misalignment, (b) transverse misalignment, (c) angular misalignment, (d) rotational misalignment.

Assuming a straight cleave is achieved, misalignment types (b) and (d) are of most significance regarding MCF-MCF splices. As the rotational misalignment is the core-to-core transverse offset rotated about the fibre axis, this can be considered as another form of transverse misalignment. As such, to estimate the losses due to rotational misalignment, the Gaussian approximation for singlemode circular waveguides can be utilised [104], where the loss is given by

$$L(\text{dB}) = 4.34 \left(\frac{u}{\text{MFD}/2} \right)^2, \quad (4.1)$$

where u is the transverse offset between cores and MFD is the mode field diameter, which for standard singlemode fibres has a value of $10.4 \mu\text{m}$ [105]. As illustrated in Figure 4.4, a relationship between the transverse offset and the core rotational offset, φ , is derived in equation (4.2):

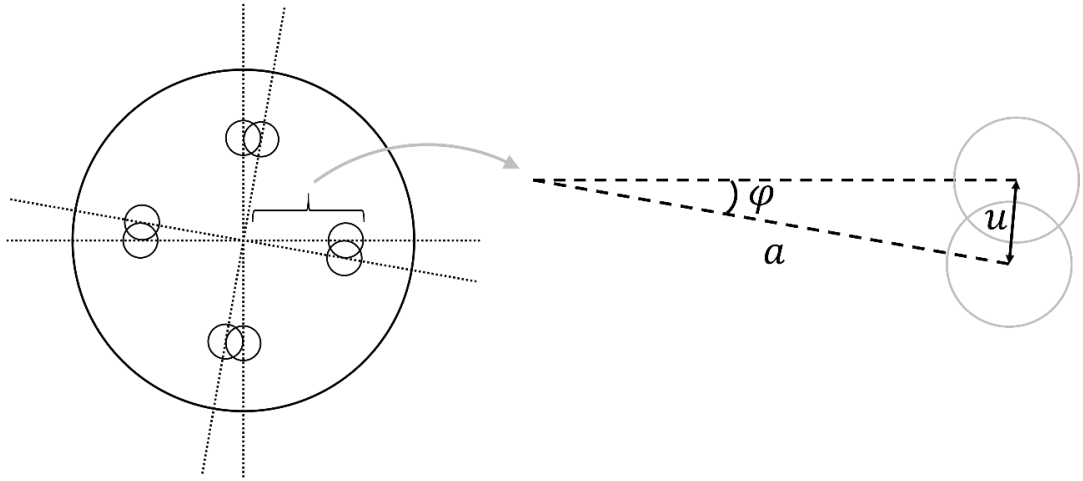


Figure 4.4: Diagrammatic representation of relationship between transverse offset and rotational offset for multi-core fibre.

$$u = 2a \sin(\varphi/2), \quad (4.2)$$

where a is the core distance from the fibre centre. By substituting equation (4.2) into (4.1), an expression for the splice loss as a function of rotational misalignment is obtained.

$$L_r(\text{dB}) = 69.44 \left(\frac{a \sin(\varphi/2)}{\text{MFD}} \right)^2 \quad (4.3)$$

The plot of this function is shown in Figure 4.5. From this it can be concluded that a slight rotational misalignment can result in an appreciable loss. To achieve a splice loss of <1 dB per core would require rotational alignment better than $\pm 4^\circ$. This is only true assuming that the rotational misalignment is the only source of loss, i.e., the fibre end is perfectly cleaved and aligned, (longitudinally, transversely, and angularly).

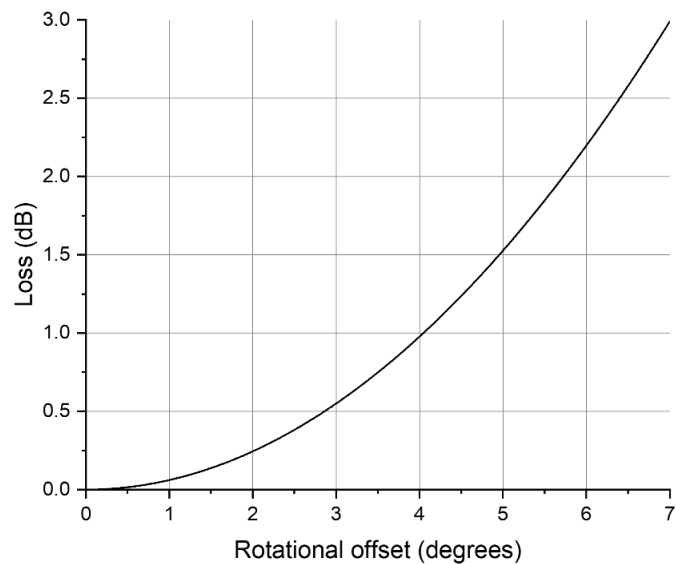


Figure 4.5: Modelled loss due to rotational misalignment between two MCFs.

Further considering splicing limitations, the unique cross-sectional shape of the clover MCF may also introduce complications to the splicing procedure. The maximum diameter of the clover MCF is 150 μm , compared to the circular MCF diameter of 125 μm . The mismatched cross-sectional shape introduces yet another source of insertion loss, where even though the core size and spacing is the same, the cladding overhang results in overflow and distorts the splice, as shown in Figure 4.6.

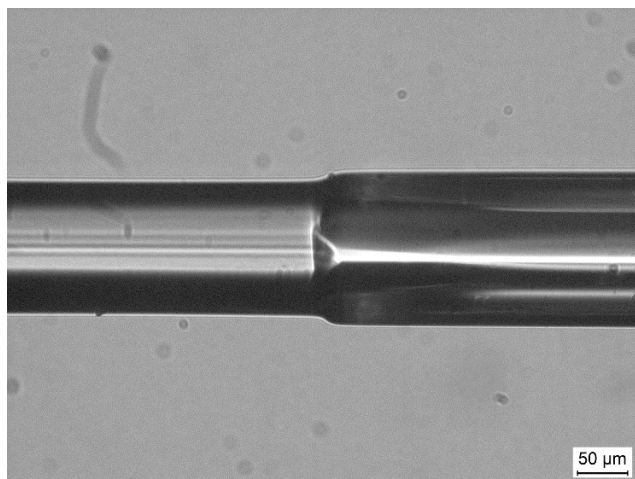


Figure 4.6: Fusion splice between (left) Circular MCF and (right) clover MCF resulting in a distorted splice with typical splice losses in the vicinity of 3 dB.

4.2.3 Fan-out system and insertion losses

The implemented fan-out system was acquired from Chiral Photonics. The schematic diagram is illustrated in Figure 4.7.

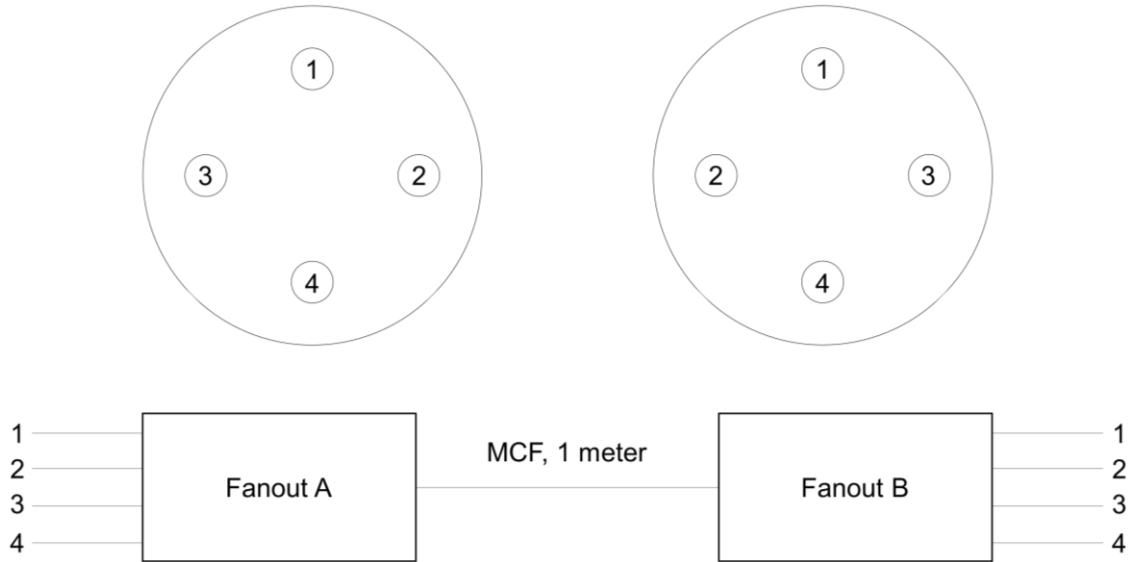


Figure 4.7: Schematic diagram of fanout systems and channel configuration.

This system is a collective of two fanouts, labelled *Fanout A* and *Fanout B*. The accompanying specifications provided by Chiral Photonics are outlined in Table 4.1.

Table 4.1: Fanout specifications measured by Chiral Photonics at 1550 nm.

| | | Fanout B | | | |
|----------|-------|----------|-------|-------|-------|
| | | 1 | 2 | 3 | 4 |
| Fanout A | Ch. # | | | | |
| | 1 | -0.9 | < -55 | -50.8 | -50.0 |
| | 2 | -49.8 | -0.6 | -49.3 | < -55 |
| | 3 | < -55 | -49.3 | -1.3 | < -55 |
| 4 | -51.1 | < -55 | < -55 | -1.5 | |

| | |
|--|---------------------|
| | Insertion Loss (dB) |
| | Crosstalk (dB) |

In order to fabricate a sensor capable of measuring the absolute distance between two surfaces, opposite facing cores are selected such that the beam exiting the fibre exits perpendicular to the circumferential edge. Therefore, as per Figure 4.7, channels 1 & 4 or 2 & 3 must be selected to satisfy this condition. Among these two channel pairs, the specifications supplied in Table 4.1 indicate channels 2 & 3 result in the least amount of

insertion loss. It is important to note that the losses outlined in Table 4.1 are the total losses through both fanouts. The MCF connecting both fanouts to each other is cut so that each fanout can be used independently. It is therefore necessary to reassess the insertion losses of channels 2 & 3 for both fanouts separately. The specification provided by Chiral Photonics also indicates crosstalk between channels is sufficiently low to be considered negligible. Figure 4.8 illustrates the configuration used in-house to assess the insertion loss of fanouts A and B individually.

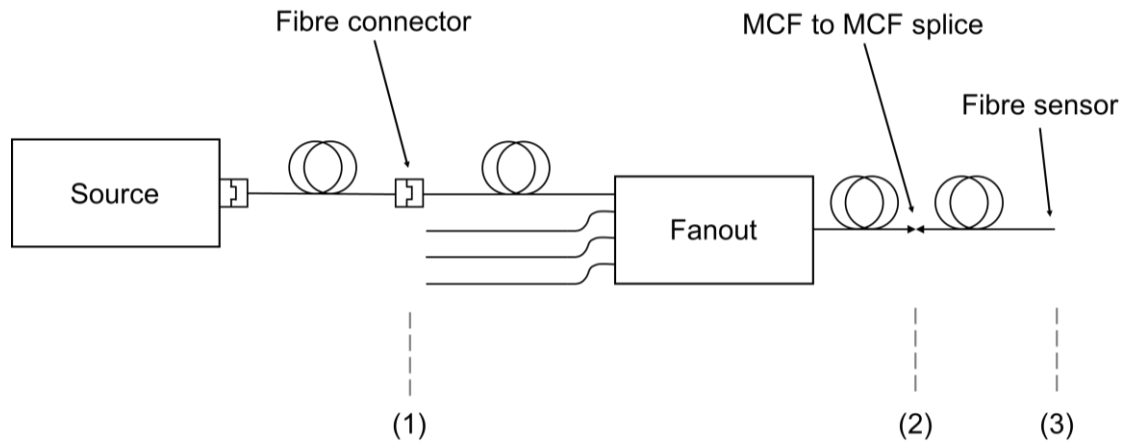


Figure 4.8: Configuration used in-house to assess fanout insertion loss where positions (1), (2) and (3) indicate where measurements are taken.

The equipment used consists of a 10 mW 1550 nm broadband source (FWHM 100 nm, AMPAQ), an optical power meter (PM100D, Thorlabs), and a standard photodiode (S122C, Thorlabs). Power measurements are taken at positions (1), (2), and (3) as indicated in Figure 4.8. The reading obtained at position (1), when the fanout is not connected to the source, is considered the reference signal. The reading obtained at position (2), with the fanout connected to the source, therefore allows for the assessment of the subsequent signal drop. This is repeated for channels 2 & 3 for both fanouts. By taking a measurement at position (3) after the MCF sensor has been spliced to the fanout, the corresponding splice loss can also be quantified. Due to the limited length of fibre available from each fanout, both fanouts are fully utilised.

When a MCF with turning mirrors is spliced to the fanout, a source of loss will also arise from the turning mirror interface due to the surface finish of the facet, as well as the limitation by which the light is reflected via total internal reflection. Due to the divergent beam profile from the fibre cores, some portion of the light will not satisfy the condition for total internal reflection and will continue its propagation trajectory by refraction

through the front face of the fibre. The amount of light that is not reflected will vary between each fibre core as the fabricated turning mirror is unlikely to be at exactly 45° as designed. The turning mirror loss can therefore be quantified by simply measuring the light that exits the fibre both from the front and from the side.

Table 4.2 summarises the losses measured for all MCF sensors and the corresponding fanouts. The MCF sensor fabricated via FIB milling is allocated to Fanout A, and the laser inscribed clover MCF is allocated to Fanout B. Once all experiments conducted with the laser inscribed clover MCF are complete, this splice is broken and the fused-silica component circular MCF is allocated to Fanout B.

Table 4.2: Losses measured for each MCF sensor and corresponding fanouts.

| | | Fanout loss (dB) | Splice loss (dB) | Turning mirror loss (dB) | Total loss (dB) |
|---|-----------|------------------|------------------|--------------------------|-----------------|
| Fanout A (FIB milled circular MCF) | Channel 2 | -0.34 | -1.58 | -1.72 | -3.64 |
| | Channel 3 | -0.42 | -2.03 | -1.23 | -3.68 |
| Fanout B (Laser inscribed clover MCF) | Channel 2 | -0.54 | -2.83 | -2.16 | -5.53 |
| | Channel 3 | -1.05 | -3.63 | -2.09 | -6.77 |
| Fanout B (Fused-silica component circular MCF) | Channel 2 | -0.54 | -1.51 | -1.20 | -3.25 |
| | Channel 3 | -1.05 | -1.65 | -1.39 | -4.09 |

It is worth highlighting that the higher splice loss of *Fanout B (Laser inscribed clover MCF)* is suspected to have arisen from the differing cross-sectional shapes of the spliced fibres in question (i.e., a clover-shaped fibre spliced onto a circular-shaped fibre). Additionally, the higher turning mirror loss suggests a poorer surface finish as a result of the chemical etching process.

4.3 Focused-ion beam milling

Here, the turning mirrors are fabricated using a focused-ion beam (FIB) (Quanta 3D FEG, FEI). FIB systems use a focused beam of ions, in this case positively charged gallium ions that, when operated at high beam currents, allows for the controlled removal of material (milling). Prior to milling, the fibre end is gold coated to prevent charge accumulation effects. An example of the occurrence of charge accumulation effects during imaging using a scanning electron microscope (SEM) is shown in Figure 4.9, where the imaged circular MCF is significantly distorted.

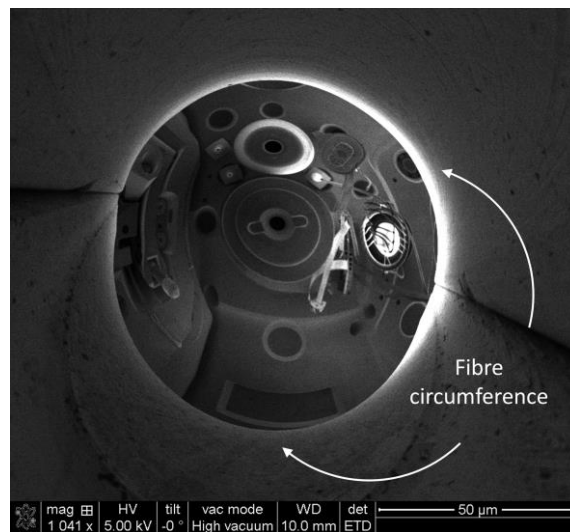


Figure 4.9: Charge accumulation effects demonstrated by uncoated circular MCF imaged by scanning electron microscope. The fibre dimensions are distorted and the chamber interior is reflected on the end of the fibre.

A FIB milled turning mirror fabricated onto SMF28 SCF is imaged using a SEM as seen in Figure 4.10, where a 7 nA acceleration current is used to mill a $20 \times 12 \mu\text{m}$ feature $35 \mu\text{m}$ deep, tilted at 45° with respect to the fibre axis. Typically, a larger acceleration current is applied to mill with a fast and coarse surface finish, after which a refined slow pass is applied with a low acceleration current. However, due to the small dimensions involved here, a single refined pass proved sufficient. This process, with the milling parameter stated, takes approximately 3 hours to complete.

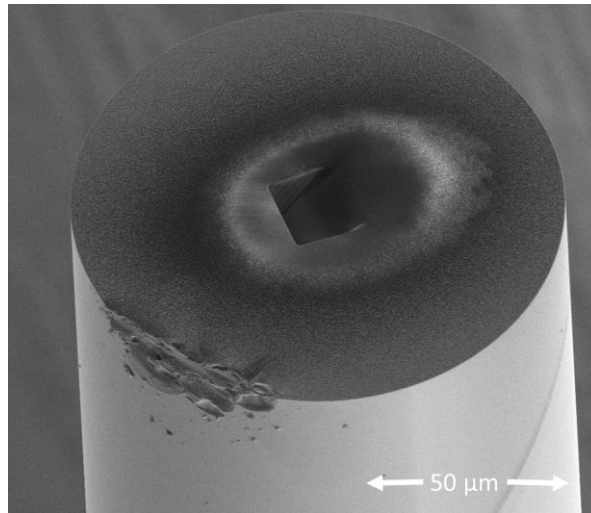


Figure 4.10: SEM image of turning mirror fabricated by FIB milling onto SMF28 fibre.

Aligning the turning mirror to the SCF is simple, as there is no specific orientation to consider, and the facet is positioned at the centre of the cleaved fibre cross-section. The alignment process is more challenging with regards to MCF, as the core locations must be identifiable in order to correctly position the turning mirrors. As demonstrated in Figure 4.11(left), the gold coated fibre does not have distinguishable cores (or other features) to assist with alignment. However the selective etching behaviour of the circular MCF with KOH (discussed in § 4.2.2 above) can be exploited to circumvent this: The MCF is submerged in a KOH solution heated to 85 °C for approximately 10 minutes which selectively etches the cores such that after gold coating, small dimples become distinguishable which are used to identify the core locations using the SEM (Figure 4.11(right)). The dimples have a depth of $\sim 1 \mu\text{m}$ which is comparatively small to the milled feature depth of $35 \mu\text{m}$, and therefore does not affect the milling process.

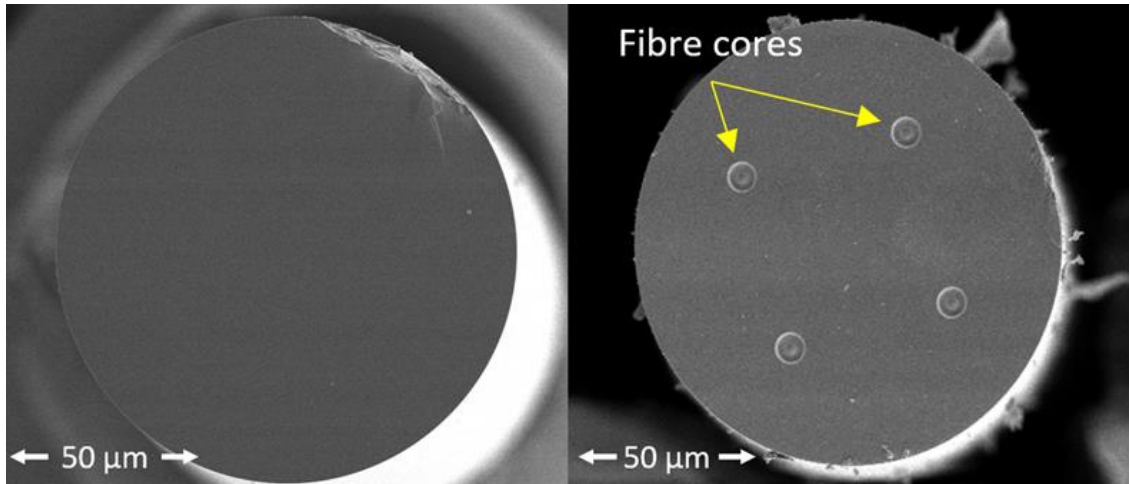


Figure 4.11: (left) SEM image of gold coated MCF, (right) SEM image of gold coated MCF that was pre etched using KOH etching for ~10 minutes before gold coating and imaging.

The circular MCF is FIB milled using the same parameters as that of the SCF. Figure 4.12 displays the SEM image captured of the FIB milled MCF, where on-screen markers are used to verify the turning mirror angle with respect to the fibre end face. Note that the on-screen markers are simply for verification, and not purposed for high accuracy measurement.

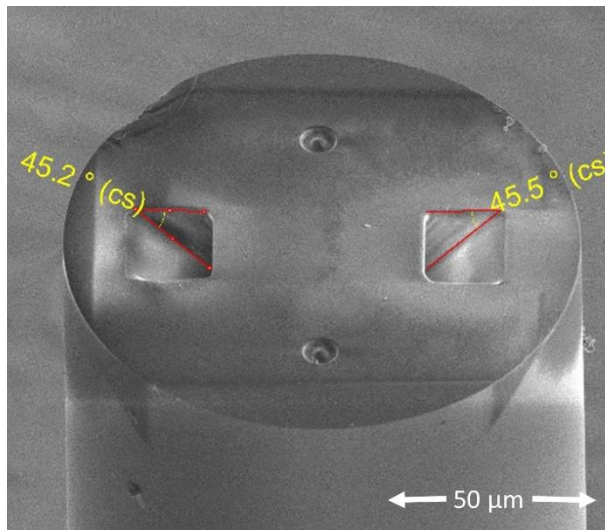


Figure 4.12: SEM image of circular MCF with turning mirrors fabricated using a FIB. The uncertainty of the on-screen angle markers are limited by the screen pixel density, leading to an uncertainty of $\pm 0.3^\circ$.

4.4 Femtosecond laser inscription and selective chemical etching

Femtosecond laser inscription and selective chemical etching has also been referred to as ultrafast laser assisted etching (ULAE), selective laser-induced etching (SLE) [114], and femtosecond laser induced selective etching (FLISE) [115]. The abbreviation “ULAE” will be adopted when referring to this fabrication process here. ULAE is a two-step process consisting of ultrafast laser inscription (ULI) and chemical etching. The ULI process does not remove any of the substrate material, but instead modifies it to enhance its sensitivity to selective etching, after which KOH is introduced to remove the inscribed feature.

Two approaches are investigated using ULAE to fabricate turning mirrors. In one approach, ULAE is applied directly to the cleaved end of the fibre (referred to here as *subtractive modification*), and the other consists of a component that is fabricated from a fused-silica wafer that is then attached to the fibre.

4.4.1 *Subtractive modification*

A femtosecond pulsed fibre laser (BlueCut, Menlo Systems) operating at 1030 nm with a pulse duration of 360 fs and a pulse repetition rate of 250 kHz is used in the ULI process. A pulse energy of 160 nJ produces the desired features with sufficient selectivity of ~650, i.e., the laser processed material chemically etches at a rate ~650 times faster than the surrounding material. These parameters are determined according to the process described in [116]. The following work is the result of a collaboration with Calum Ross, who developed the system for the machining of non-fibre samples [116]. Figure 4.13 illustrates a simplified configuration used for ULI.

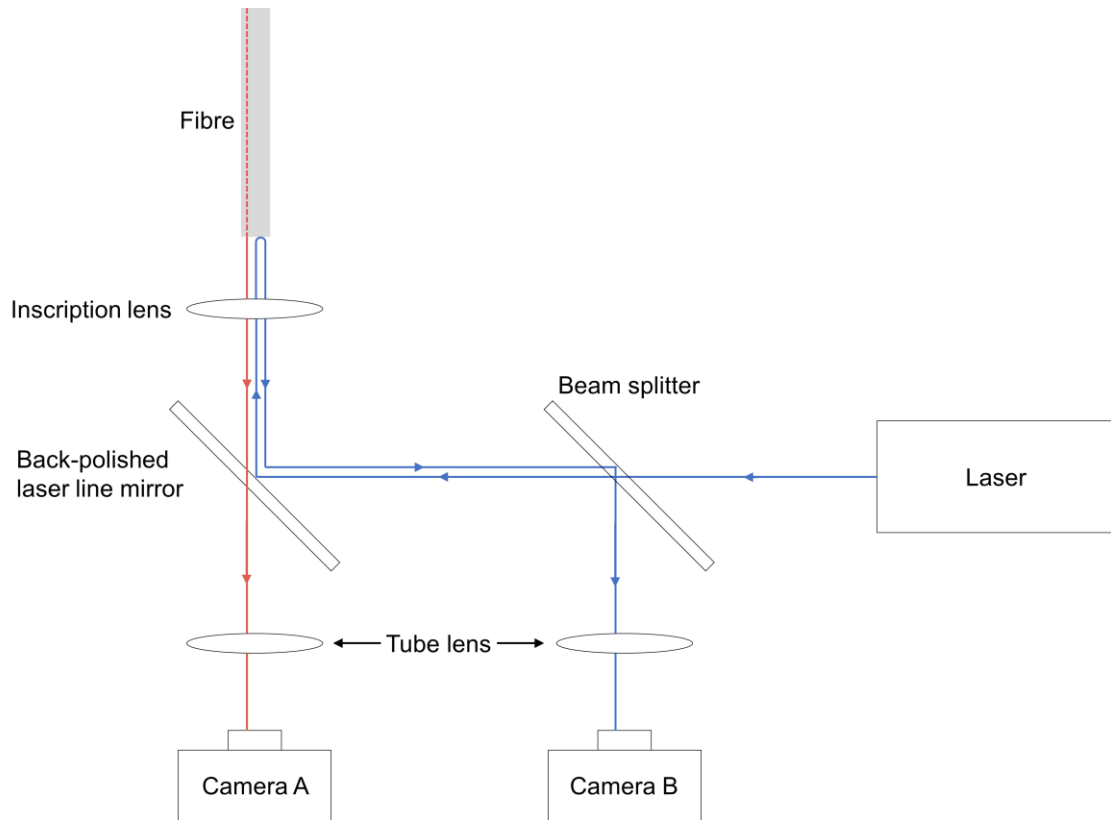


Figure 4.13: Illustration of apparatus configuration used in laser inscription process.

The red line represents light from the fibre, and the blue line(s) represents the laser light. All ray paths are offset to clarify direction of propagation.

The blue lines in Figure 4.13 represent the 1030 nm wavelength light used during the inscription process, and the red line represents the visible red light used for the fibre alignment process. Initially, once the fibre is situated onto the translation stage, red light is coupled into all cores of the fibre arbitrarily such that the fibre and the core locations are visible when imaged by a camera (Camera A). The fibre is then rotated such that the square lattice cores are rotationally oriented to align with the stage's linear axes (where single-core fibre is concerned, this step is disregarded). The back-polished laser line mirror is highly reflective at the laser wavelength, and so the red light from the fibre is transmitted to the first camera optics while reflecting (almost) all laser light to the fibre end face. A second camera (Camera B) is used in conjunction with a beam splitter to assist with aligning the fibre to the laser beam. This is achieved by monitoring the back reflection from the fibre end face while the laser is operating at low power. Note that this camera images the laser light and not the fibre end face, and so alignment is achieved by first locating the bounds of the fibre circumference, in turn identifying the centre of the fibre end, after which the core locations can be determined by relative positioning.

Once all alignment is complete, the inscription process is commenced using the laser parameters outlined above.

After inscription, etching requires a two-hour immersion in a 8 mol/L KOH solution, heated to 85 °C, after which the fibre end is cleaned in an ultrasonic bath and allowed to dry. Figures 4.15 and 4.16 show turning mirrors fabricated by ULAE on SCF and clover MCF respectively. A rendered model of the turning mirror on SCF is first shown in Figure 4.14 for clarity of the inscribed feature geometry and the inscription pattern. This pattern is used to prevent a ‘staircase’ facet from forming that would otherwise arise if a pattern in the perpendicular direction were adopted, which would be detrimental to the reflected beam profile.

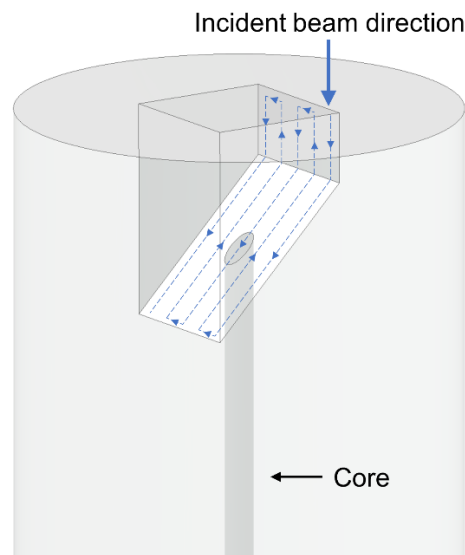


Figure 4.14: Rendered image of turning mirror on single-core fibre. The dotted blue lines represent the inscription pattern used.

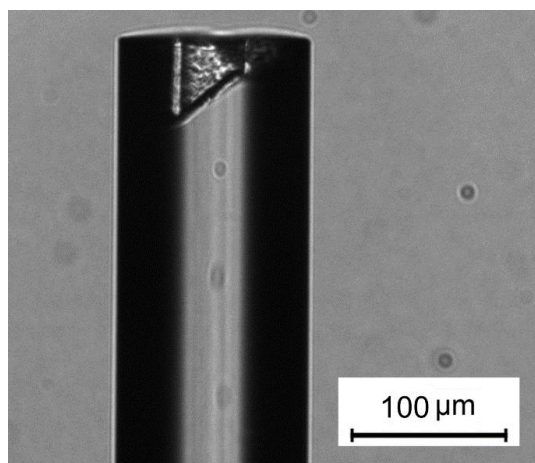


Figure 4.15: Microscope image of turning mirror fabricated by ULAE onto SMF28.

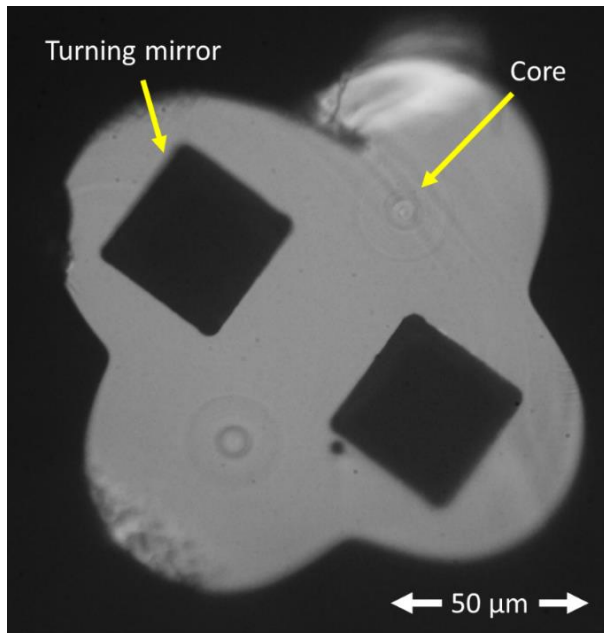


Figure 4.16: Microscope image of turning mirrors fabricated by ULAE onto clover MCF.

Turning mirror alignment for SCF simply requires centre positioning of the turning mirror facet to the fibre cleaved end and rotational alignment is unimportant. For the clover MCF, unlike the FIB milling fabrication process, ULAE does not require gold coating of the fibre, and therefore the cores are distinguishable by simply coupling visible light into them without the need for any pre-processing. The turning mirrors are positioned directly above the cores of interest, the alignment of which is also assisted by the distinct cross-sectional shape of the fibre to ensure the beams are directed ‘radially’ outwards. In Figure 4.16 the mirrors are shown end-on: the cross-sectional shape becomes a hinderance as it distorts the image when a side-view is attempted.

4.4.2 Fabrication of fused-silica component

The turning mirrors fabricated here undergo the same ULAE process as with the subtractive modification approach but are instead fabricated onto components from a fused-silica wafer that are adhered to the fibre. The wafers are 1 mm thick and have lateral dimensions larger than the dimensions of the geometry that is inscribed. The component design, the inscription patterns, and its adhesion onto SMF28 fibre are shown in Figure 4.17 and Figure 4.18. The component’s largest external dimensions are $1 \times 1 \times 0.25$ mm.

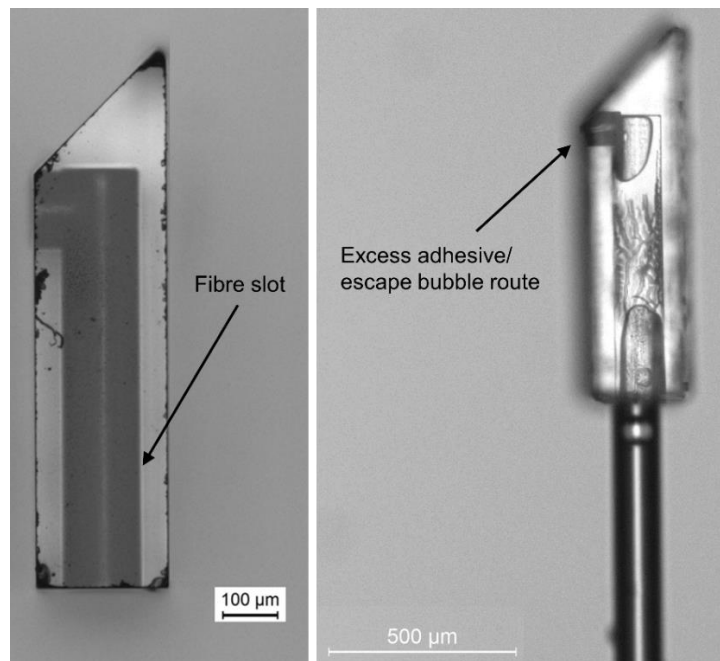


Figure 4.17: (left) Turning mirror fused-silica component fabricated by ULAE for SCF. (right) Fused-silica component adhered to SMF28 fibre using Norland Optics UV curing optical adhesive.

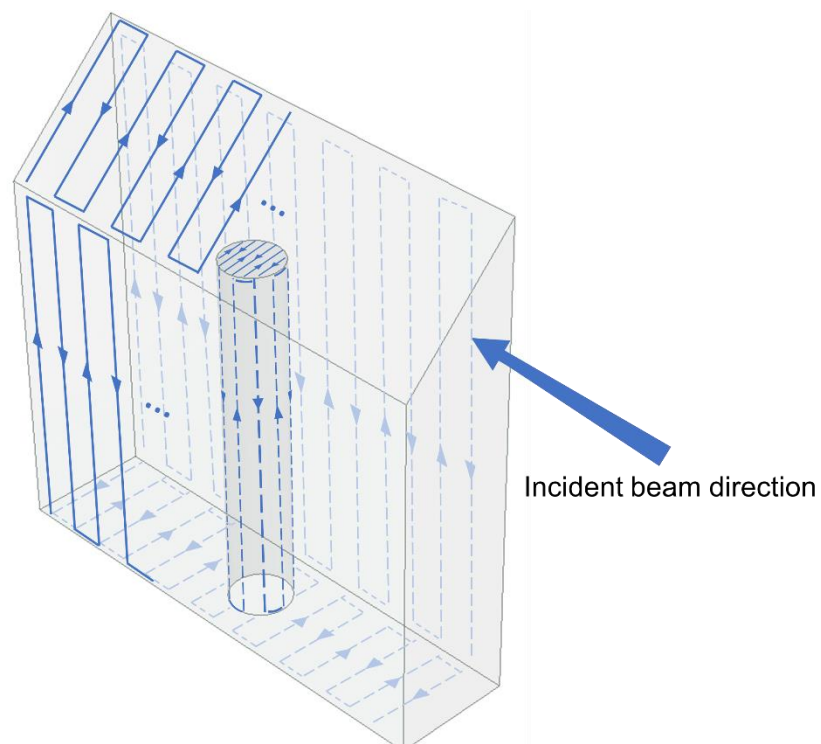


Figure 4.18: Fused-silica component model. The blue lines represent the inscription pattern. To improve clarity: the escape bubble route is omitted; only a portion of the inscription pattern is displayed on some surfaces; and a combination of solid and dotted lines are used with different shading.

The adhesive used is Norland Optics NOA 61. This optical adhesive is applied as a liquid and is then cured by ultraviolet (UV) light. Once the adhesive-coated fibre is situated within the component, it is exposed to UV light for 1 hour and allowed to cure.

The process of aligning the fibre to the fused-silica component is illustrated in Figure 4.19. The fibre is mounted to a 3-axis flexure stage and a camera images the position of the cleaved fibre with an imaging axis tilted approximately 45° to the fibre axis. This configuration allows for precise alignment in all three linear axes. The fibre slot in the fused-silica component has a diameter of $130\ \mu\text{m}$ which is oversized compared to the fibre diameter (c.f. SMF28 cladding $\varnothing 125\ \mu\text{m} \pm 0.7\ \mu\text{m}$) to allow for any machining uncertainty and to allow for sufficient adhesive to enter during the alignment process. Considering the fibre slot has a length of $750\ \mu\text{m}$ (and no significant taper is noted with respect to its length), this corresponds to a maximum possible angular misalignment of the fibre to the fibre slot of approximately 0.1° , assuming no buckling or bending of the fibre. Final assemblies of the fused-silica component adhered onto the fibre are inspected under a high magnification optical microscope to verify that no discernible misalignment has occurred, and so such misalignment is considered negligible for the purposes of sensor evaluation.

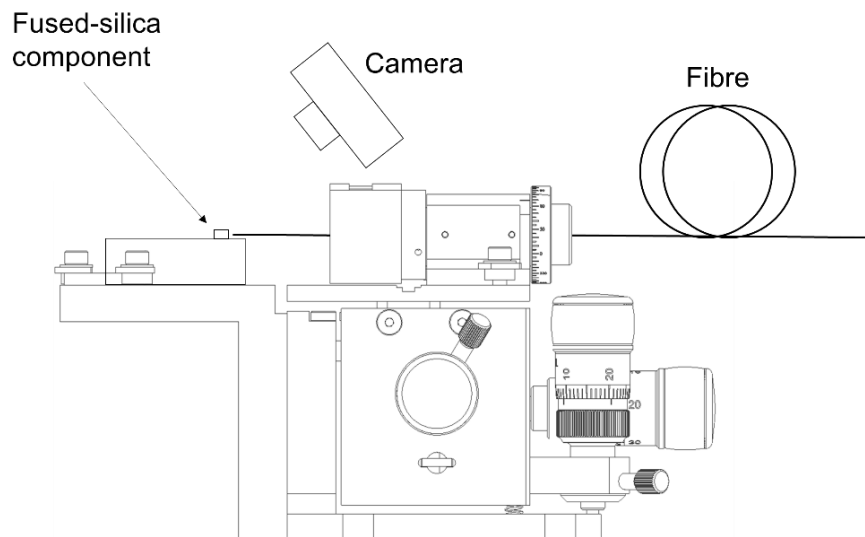


Figure 4.19: Schematic illustration of fibre alignment process to fused-silica component.

The effects of the parasitic optical cavities which are prone to arise either due to misalignment or air-bubble formation are discussed in § 5.3.3. Note that when sensor performance is evaluated in the following section, sensors which do not exhibit any

notable misalignment or air-bubble formation are used, and so there are no parasitic cavities present which may influence the evaluation outcome.

The fused-silica component design changes slightly to accommodate compatibility with MCF, as seen in Figure 4.20. In this design, the largest external dimensions are $1 \times 1 \times 0.5$ mm. The inscription orientation and patterns used are the same as that illustrated in Figure 4.18.

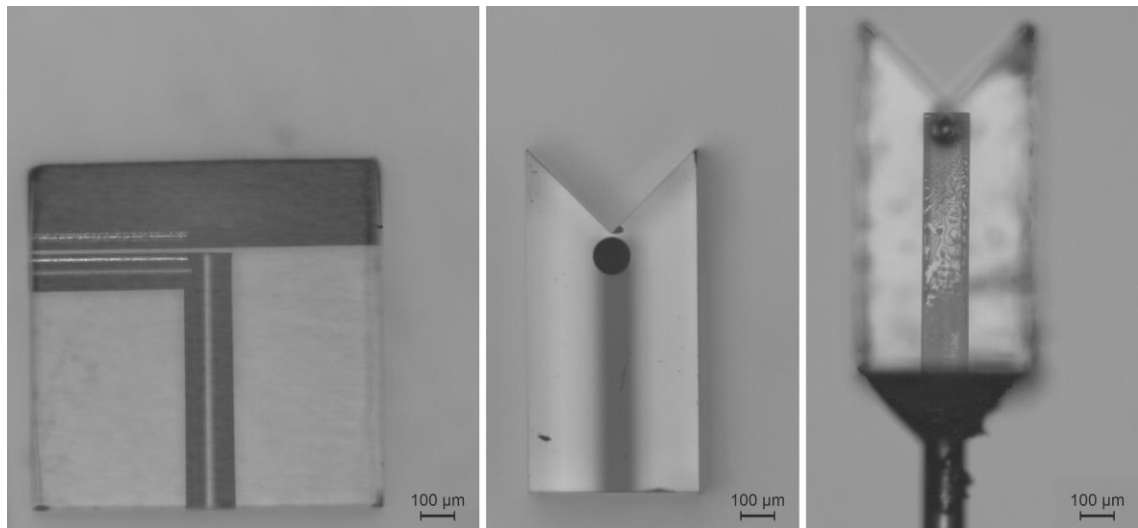


Figure 4.20: (left and centre) Turning mirror fused-silica component fabricated by ULAE for MCF. (right) Fused-silica component adhered to circular MCF using Norland Optics UV curing optical adhesive.

Aligning the fibre to the component is much of the same as with SCF (Figure 4.19), but in this case precise rotational alignment is important. Once situated within the fused-silica component, this can be achieved by coupling visible light to all cores of the MCF and rotating the fibre until two of the cores can be seen emitting light at the facet intersection. Figure 4.21(a) highlights the difference between correct rotational alignment and misalignment of the fibre with respect to the fused-silica component, and Figure 4.21(b) illustrates the potential consequences of rotational misalignment.

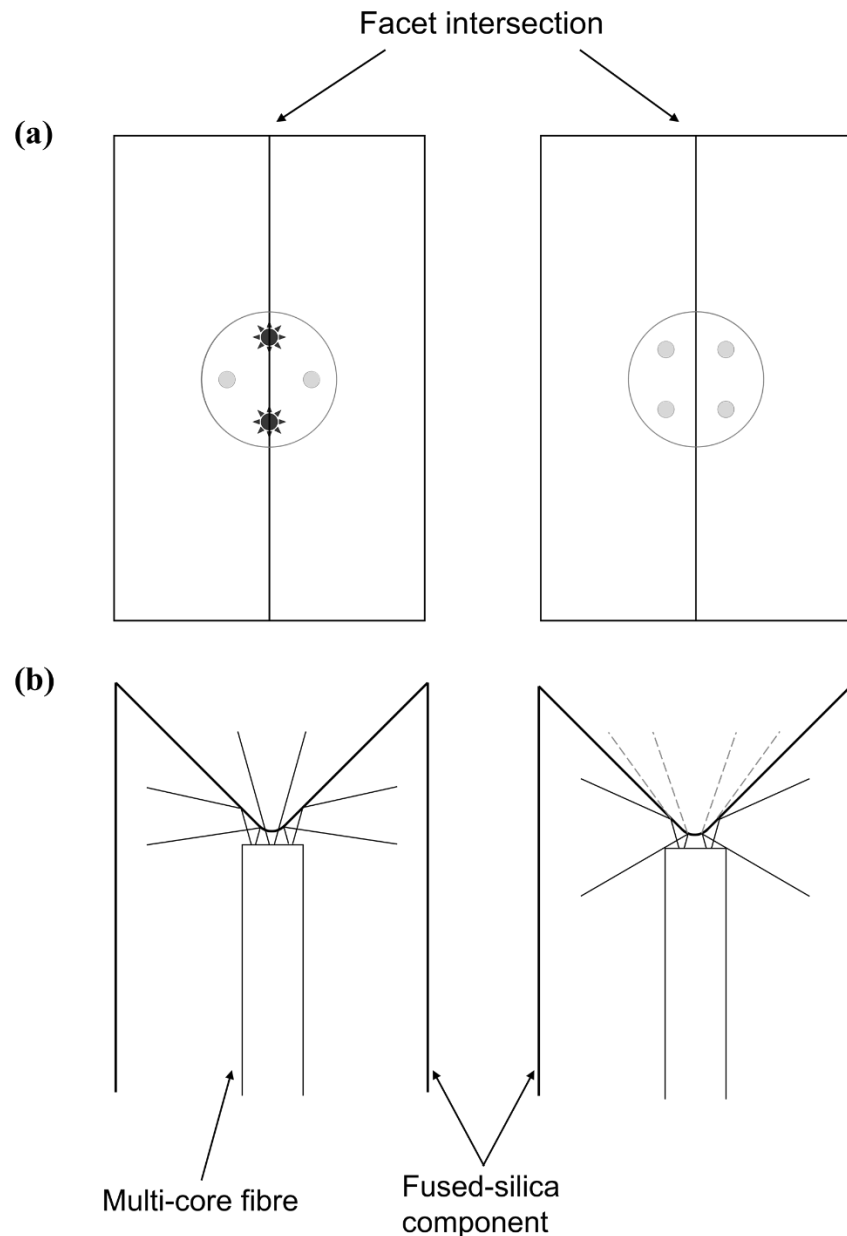


Figure 4.21: (a) End-on view and (b) side-view illustration of a fused-silica component attached to MCF: (left) Correct rotational alignment leading to illuminated fibre cores brightly visible along the fused-silica component facet intersection; (right) Rotational misalignment indicated by dimly visible cores. Features and proportions are exaggerated for clarity.

Although it is designed for the facets to be perpendicular to one another (i.e. both are 45° to the fibre axis), the chemical etching process can typically result in slightly rounded corners. This effect contributes to increased losses at the reflection interface if the fibre is rotationally misaligned. Figure 4.22 shows that the MCF sensor used in experimentation has been correctly rotationally aligned to its corresponding fused-silica component.

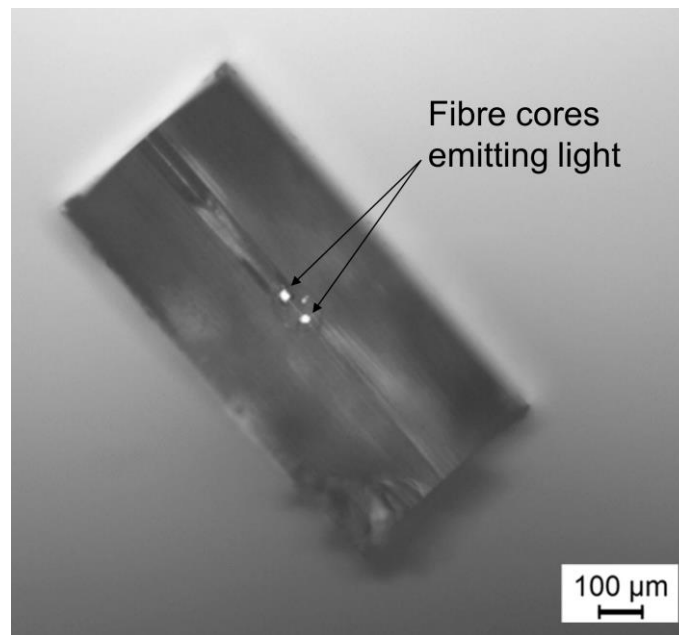


Figure 4.22: Demonstration of correct rotational alignment of MCF with respect to fused-silica component.

4.5 Sensor performance analysis

The performance of each fibre sensor is assessed using the experimental configuration described in § 3.5.1. The same performance metrics are evaluated to that of the normal cleaved and 45° angle cleaved fibre sensors outlined in § 3.5.2. These being accuracy, sensitivity, and range. Here, the results displayed for the SCF sensors are obtained by both the FFT and FFA measurements, whereas the MCF sensor results are displayed by focussing on the FFA measurements only. As will be seen, the improvement observed by the incorporation of the FFA in Chapter 3 is also present here. This therefore further justifies abandoning the FFT measurement when assessing MCF sensor performance. Figure 4.23 and Figure 4.24 shows the assessment results for SCF sensor accuracy and sensitivity/range respectively.

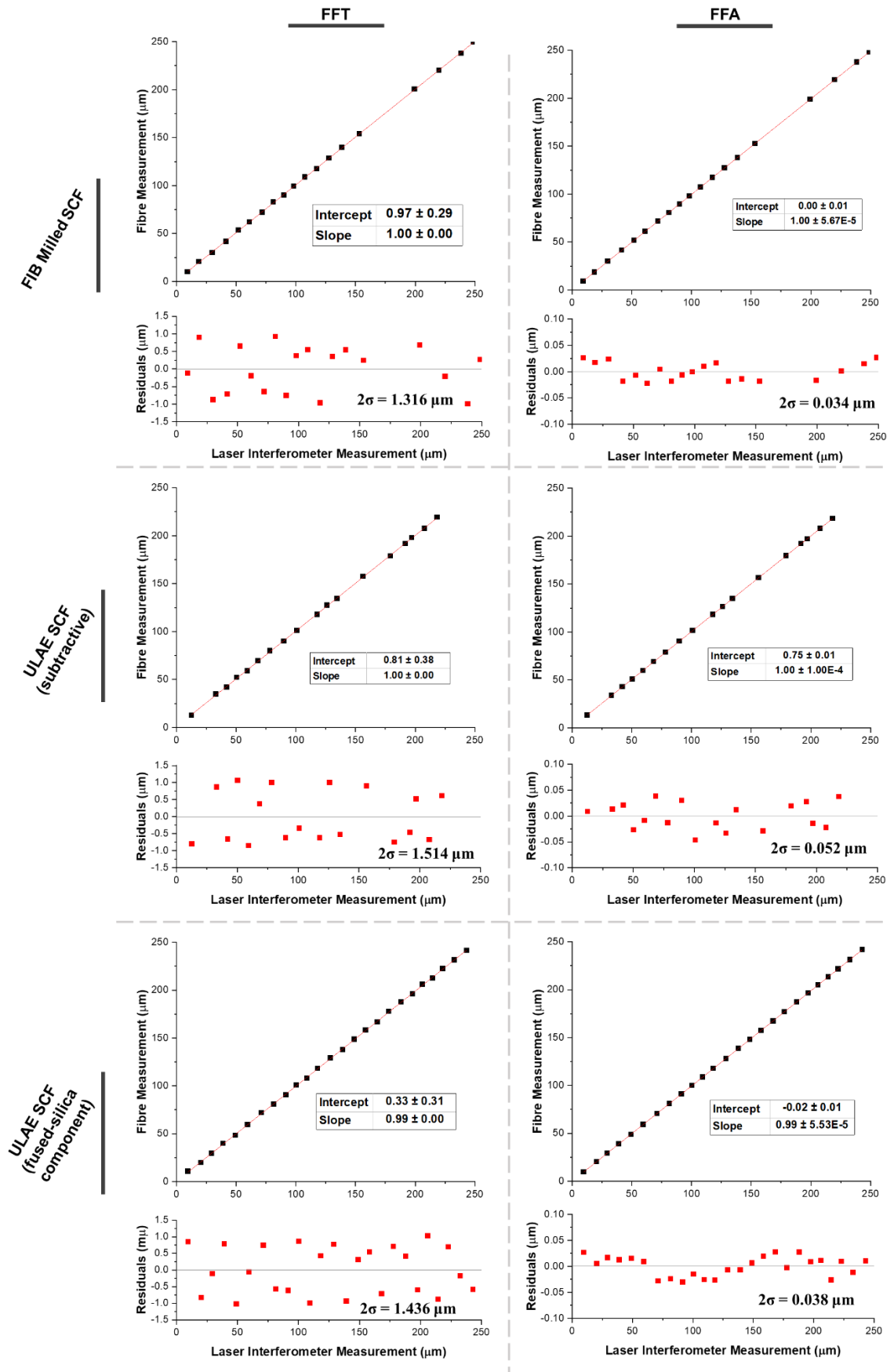


Figure 4.22: SCF sensor and laser interferometer measurements using FFT and FFA cavity length measurements techniques to assess sensor accuracy, consisting of cavity lengths $\sim 300 - 500 \mu\text{m}$.

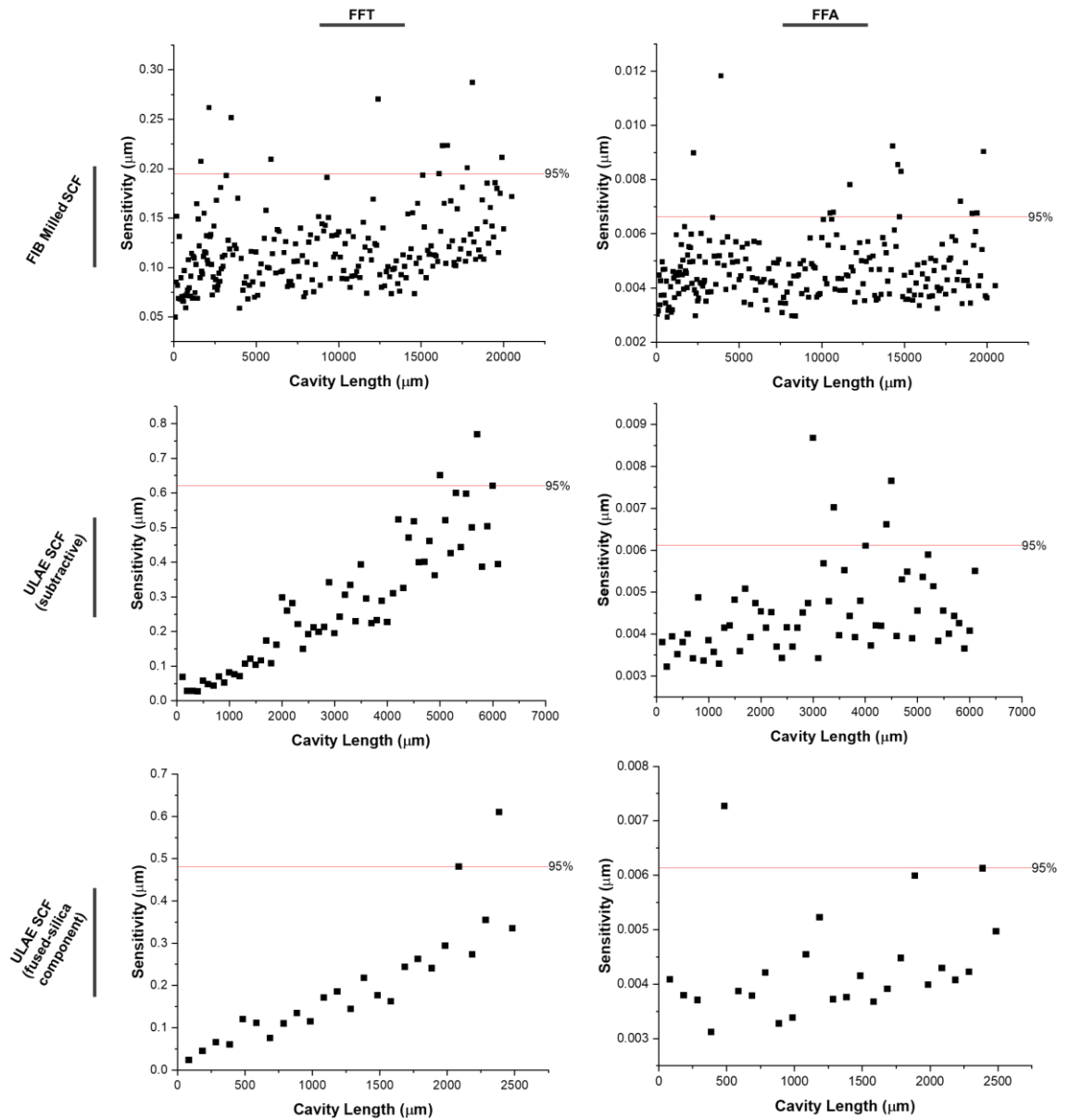


Figure 4.24: Sensitivity assessment measured via FFT and FFA of the SCF sensors taken in increments of $\sim 100 \mu\text{m}$ up to the maximum sensor range. The red line corresponds to the sensitivity within which 95% of data points fall under.

Regarding Figure 4.23, the accuracies achieved by the FFT measurements are quite comparable to the accuracies achieved with the normal cleaved and 45° angle cleaved fibre sensors in § 3.5.2 and § 3.5.3 (c.f. normal cleaved and 45° angle cleaved fibre accuracies of $\pm 1.431 \mu\text{m}$ and $\pm 1.309 \mu\text{m}$ respectively). Considering the FFA measurements, however, the comparative difference is more noticeable, but not necessarily substantial (c.f. normal cleaved and 45° angle cleaved fibre accuracies of $\pm 0.021 \mu\text{m}$ and $\pm 0.023 \mu\text{m}$ respectively). It is unclear what has explicitly caused this discrepancy: it is possible that many more repeat assessments are required to evaluate

refined accuracy values, but it is also hypothesised that increased losses that occur as a result of the processes applied to the fibre during turning mirror fabrication may have led to diminished accuracies. In either case, it is clear that the FFA measurement significantly improves the sensor accuracy compared to the FFT equivalent in all SCF sensors.

Regarding Figure 4.24, both ULAE SCF sensors demonstrate a clear trend where the sensitivity deteriorates with increasing cavity length, as far as the FFT measurement is concerned. This trend was also observed with the normal cleaved and 45° angle cleaved SCF sensors in § 3.5.2 and § 3.5.3. A similar trend could possibly be observed also with the FIB milled SCF sensor, but to a lesser extent. The FFA measurement once again offers a significant improvement compared to the FFT equivalent, where no such sensitivity deterioration is observed. It appears that once the FFA is successful in converging to a single solution reliably, then the corresponding sensitivity of the measurement is consistent across the range of the sensor, which is in this case is ~0.006 µm for all three SCF sensors outlined in Figure 4.24.

Regarding the sensor range, the FIB milled SCF sensor portrays the longest operable range of ~20 mm. This is very similar to the normal cleaved and 45° angle cleaved fibre sensors (c.f. ~18 mm and ~19 mm). There is no clear reason for why the FIB milled SCF sensor should inherently operate over a longer range compared to the 45° angle cleaved fibre. It is therefore suspected that the small discrepancy here is likely due to small variations in alignment that have allowed for slightly longer cavities to function with the FFA at the time of measurement. Regarding the ULAE SCF sensors (subtractive and fused-silica component), the operable ranges are ~6 mm and ~2.5 mm respectively. This noteworthy reduction in operable range is likely due to the increased signal loss which arises from the poorer surface finish obtained after the chemical etching process. The ULAE SCF sensor using the fused-silica component may experience further losses yet from the adhesive layer that can accumulate non-uniformly between the cleaved fibre end and the fused-silica component. The combination of these effects has likely contributed to the reduced range observed in Figure 4.24. To verify this, surface profile measurements are taken of the fused-silica component and compared to that of a cleaved fibre end using white light interferometry (WLI) (Sensofar S neox), as shown in Figure 4.25. This is undertaken to assess the surface roughness introduced by the chemical etching process.

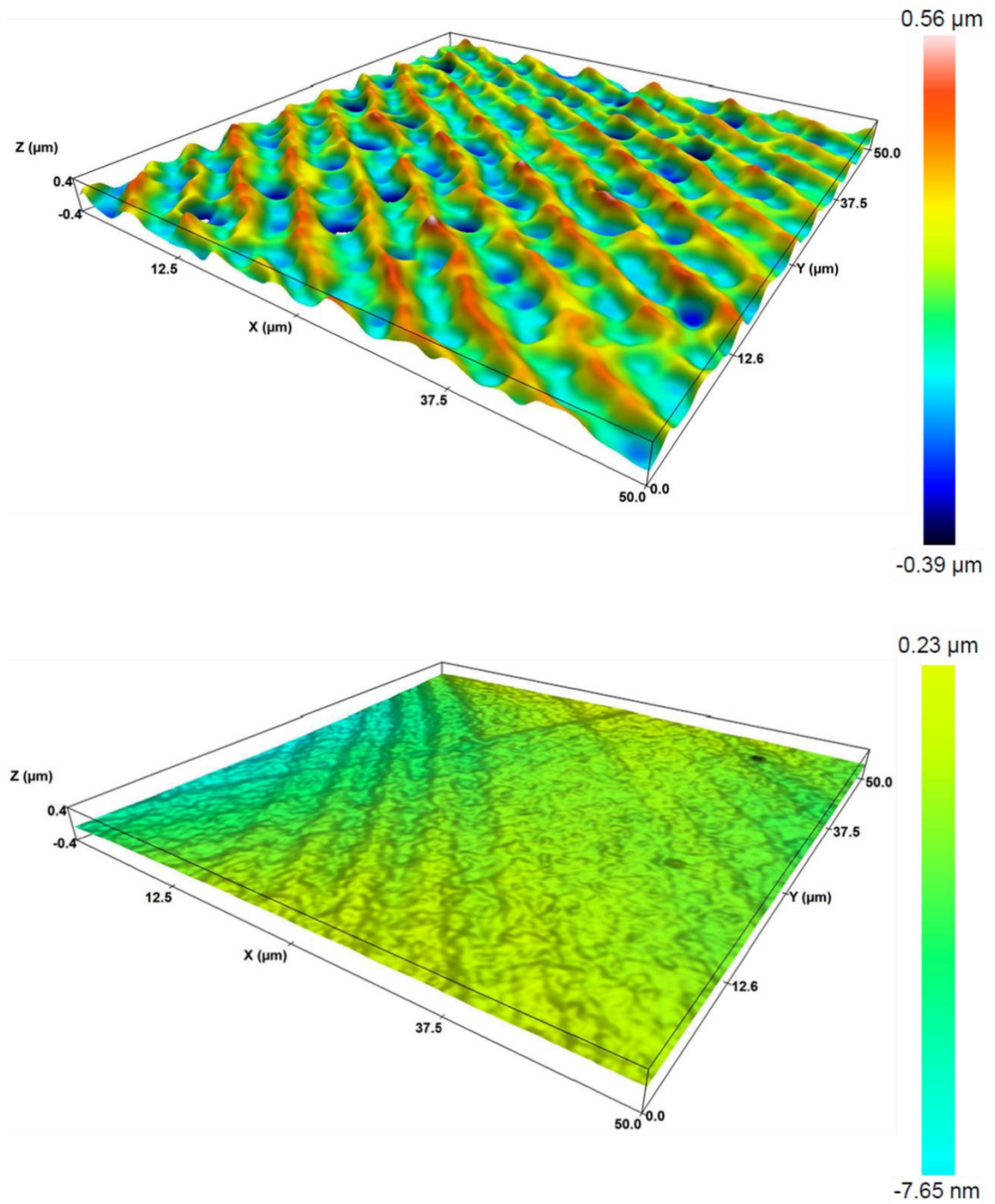


Figure 4.25: Surface profile images taken by WLI of (top) fused-silica component and (bottom) cleaved fibre end, resulting in surface roughnesses of $S_a = 108 \text{ nm}$ and $S_a = 35 \text{ nm}$ respectively over a $50 \times 50 \text{ μm}$ area. Both images are displayed with the same xyz scale to facilitate direct visual comparison.

The surface profile measurements taken over an area of 50 μm^2 demonstrate roughnesses of $S_a = 108 \text{ nm}$ and $S_a = 35 \text{ nm}$ for the fused-silica component and the cleaved fibre end respectively, the results of which are indicative of the diminished sensing range experienced by the KOH etched fibre sensors. The periodic structure observed on the

surface of the fused-silica component is not believed to be due to the laser raster pattern, but instead due to the polarisation dependant nanogratings which subsequently cause the emergent effect displayed in Figure 4.25. Detailed elaboration on this subject matter is beyond the scope of work presented in this thesis – further reading on the influence of polarisation on surface structure for ULAE can be found in [116] and [117]. The scattering due to the increased surface roughness observed on the fused-silica component is believed to be the primary cause for the diminished sensor range displayed in Figure 4.24. Although the geometry of the periodic structure may invoke concern that transmitted light is susceptible to phase changes, the measured surface roughness of $S_a = 108 \text{ nm}$, approximately equivalent to $\lambda/15$, is comparable to surface finishes on commercially available off-the-shelf optics, and so any phase effects are deemed largely negligible.

Figure 4.26 and Figure 4.27 shows the assessment results for MCF sensor accuracy and sensitivity/range respectively.

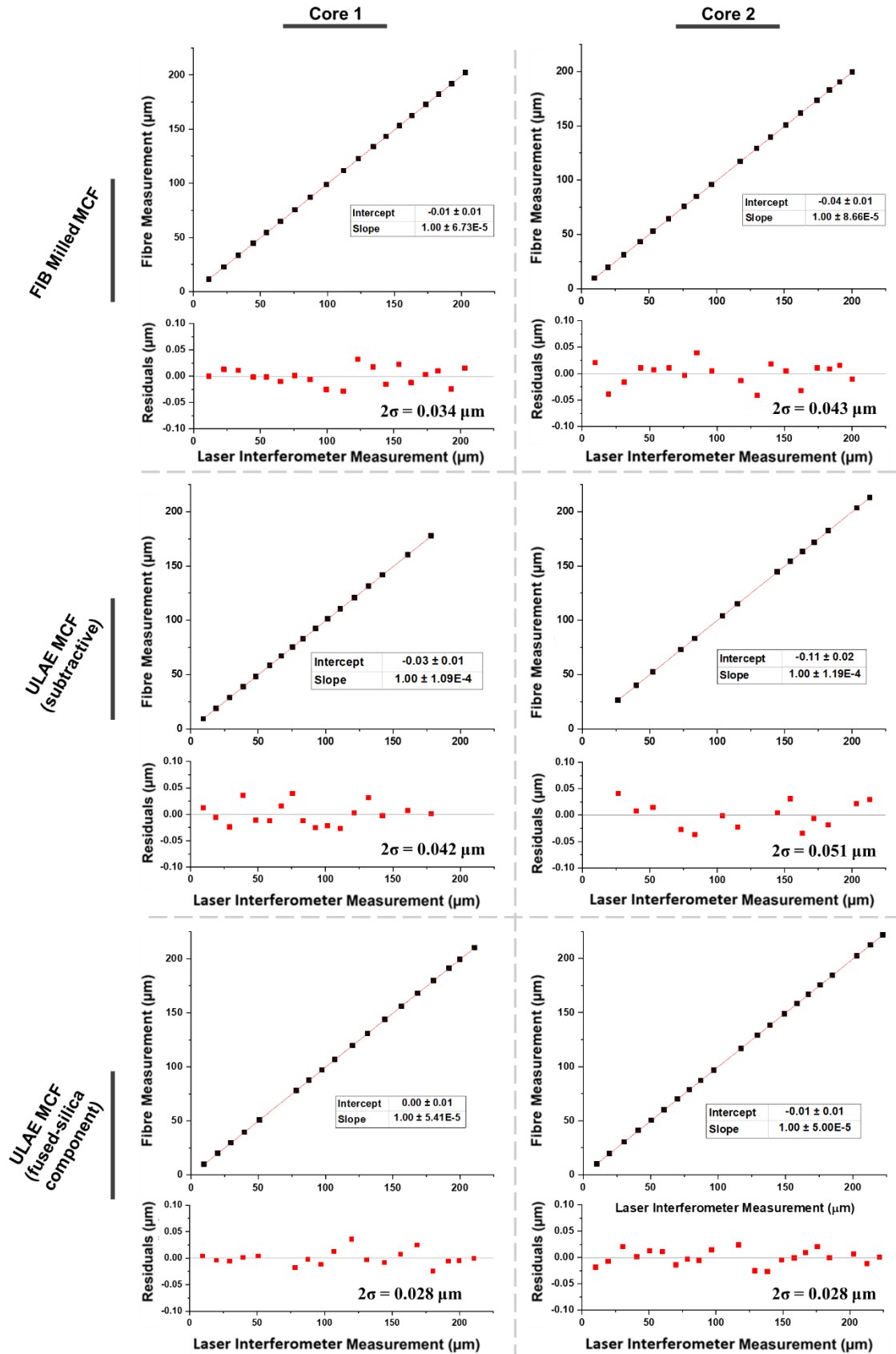


Figure 4.26: MCF sensor and laser interferometer measurements using the FFA cavity length measurements technique to assess sensor accuracy for both cores of each sensor, consisting of cavity lengths $\sim 300 - 500 \mu\text{m}$.

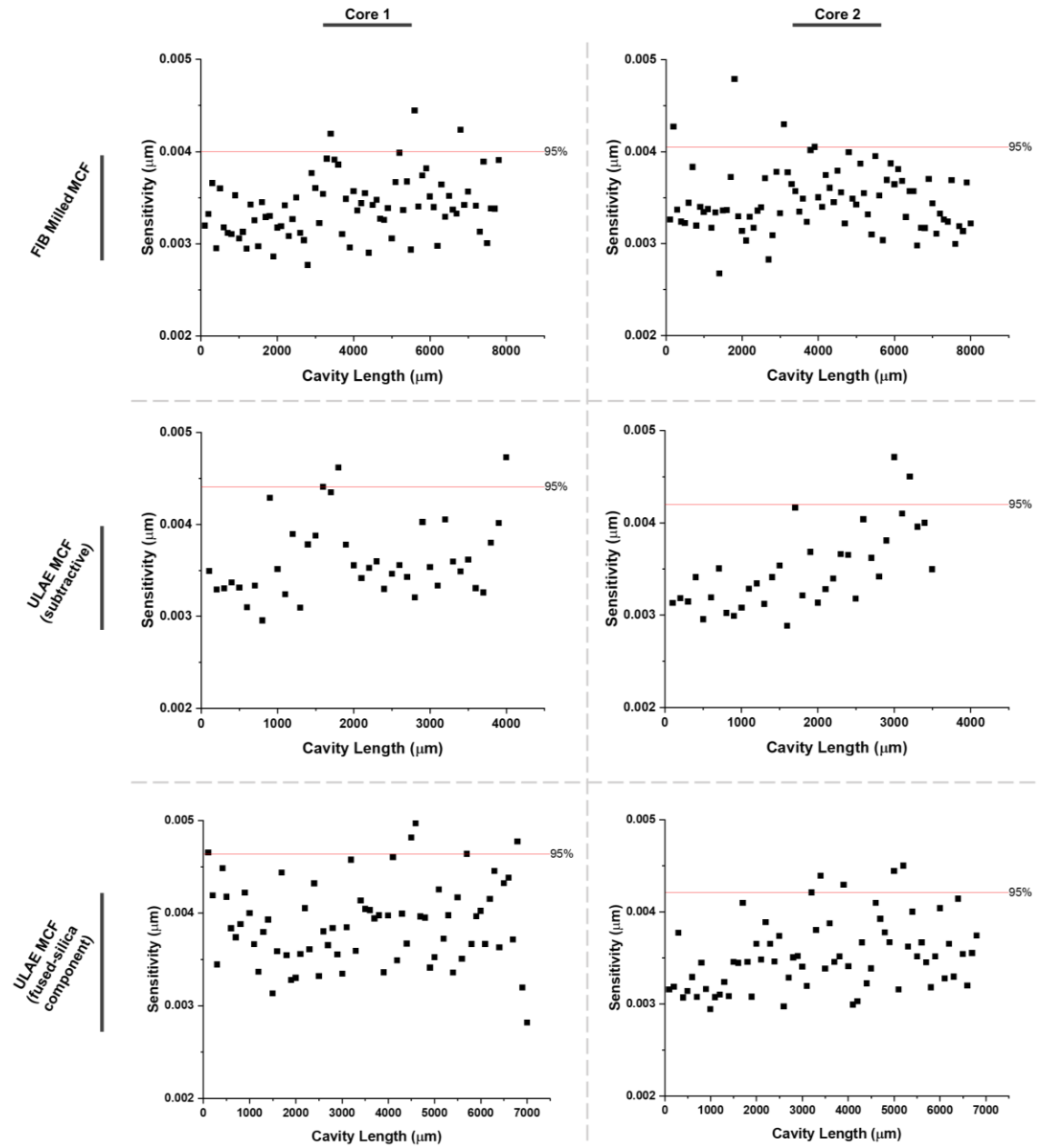


Figure 4.27: Sensitivity assessment of both cores of each MCF sensor using the FFA measurements taken in increments of $\sim 100 \mu\text{m}$ up to the maximum sensor range. The red line corresponds to the sensitivity within which 95% of data points fall under.

From Figure 4.26, it can be seen that the accuracy values obtained from either core of each MCF sensor compares very well with their SCF sensor equivalent. In the case for the MCF sensors, however, as two cores are taking simultaneous measurements, the total accuracy requires additional evaluation. Equation (4.4) describes the total accuracy achieved with each MCF sensor:

$$2\sigma_{Total} = \sqrt{(2\sigma_{core\ 1})^2 + (2\sigma_{core\ 2})^2}, \quad (4.4)$$

where $2\sigma_{core\ 1}$ and $2\sigma_{core\ 2}$ refer to the accuracy values obtained for core 1 and core 2 respectively. Table 4.3 summarises the total accuracy achieved with each MCF sensor.

Table 4.3: Summary of total accuracy values obtained for each MCF sensor.

| MCF Sensor | Total accuracy (μm) |
|-------------------------------|----------------------------------|
| FIB Milled | ± 0.055 |
| ULAE (Subtractive) | ± 0.066 |
| ULAE (Fused-Silica Component) | ± 0.040 |

From Figure 4.27, the sensitivities achieved are also consistent with those measured for the SCF sensors. When rounded to the nearest nm, each core of each MCF sensor demonstrates sensitivities of $0.004\ \mu\text{m}$ (with the exception of Core 1 of the ULAE fused-silica component MCF sensor, which demonstrates a sensitivity of $0.005\ \mu\text{m}$). Similarly to the accuracy assessment, as both cores of each MCF sensor operate simultaneously, a value for total sensitivity is evaluated which follows the same expression as equation (4.4). For each MCF sensor, the sensitivity values for both cores are squared and the square root is taken of the summation. This results in all MCF sensors obtaining total sensitivities of $0.006\ \mu\text{m}$.

Regarding the assessment of the sensor range, each core of the FIB milled and ULAE (subtractive) MCF sensor demonstrate diminished ranges compared to their SCF sensor equivalent. This is likely due to the increased losses that are experienced as a result of using a fanout and the subsequent MCF-to-MCF splice. Interestingly, this is not the case for the ULAE (fused-silica component) MCF sensor, where each core individually demonstrates much better range compared to the SCF equivalent (c.f. $\sim 2,500\ \mu\text{m}$). It is not entirely clear why this is, but it is speculated that the adhesive layer between the cleaved fibre end and the fused-silica component cured in a fashion less disruptive to the signal in the case for the MCF sensor. Although it is certain that no large air bubbles were formed, as would have been immediately apparent in the measurement signal, microbubbles may be the culprit which may not be explicitly clear during visual inspection under a microscope. The total ranges for the FIB milled, ULAE (subtractive),

and ULAE (fused-silica component) MCF sensors is therefore $\sim 16,000 \mu\text{m}$, $\sim 7,500 \mu\text{m}$, and $\sim 14,000 \mu\text{m}$ respectively.

Although all sensor accuracies have been assessed, it is worth noting that these assessments were undertaken within cavity length ranges of $\sim 300\text{-}500 \mu\text{m}$. The purpose of this was to establish a consistent method to draw comparisons between each sensor. However, the question remains whether the obtained accuracies are also true at longer cavity lengths. To answer this, further accuracy assessments are carried out for Core 2 of the FIB milled MCF sensor throughout the range of its operability (Table 4.4).

Table 4.4: Summary of accuracy measurements taken for Core 2 of the FIB milled MCF at different cavity length ranges, rounded to the nearest nm.

| Measurement range (μm) | Accuracy (μm) |
|-------------------------------------|----------------------------|
| $\sim 300\text{-}500$ | ± 0.043 |
| $\sim 1000\text{-}1200$ | ± 0.046 |
| $\sim 1800\text{-}2000$ | ± 0.030 |
| $\sim 2800\text{-}3000$ | ± 0.020 |
| $\sim 3800\text{-}4000$ | ± 0.044 |
| $\sim 4800\text{-}5000$ | ± 0.052 |
| $\sim 5800\text{-}6000$ | ± 0.030 |
| $\sim 6800\text{-}7000$ | ± 0.038 |

Due to the time-consuming nature of this assessment, it is unfeasible at the time of measurement to repeat this assessment for all sensors across each of their respective operable ranges. As can be seen from Table 4.4, there is no clear upward or downward trend in the accuracy value that is obtained at different cavity lengths. As the fundamental operating principle is the same for all sensors, this provides merit to assume that the accuracy value assessed at cavity lengths $\sim 300\text{-}500 \mu\text{m}$ does not predictably improve or deteriorate at increased cavity lengths.

4.6 Conclusions

It is required to measure the absolute distance between component parts situated within spatially confined regions. This challenge is overcome by fabricating turning mirrors on multi-core fibre (MCF) to redirect the guided light perpendicular to the fibre axis in

opposite directions. Three different turning mirror fabrication processes are investigated (focused-ion beam (FIB) milling, ultrafast laser assisted etching (ULAE) applied directly to the fibre cleaved end, and ULAE of a fused-silica component attached to the fibre) and their performance are evaluated.

The relevant characteristics of single-core fibre (SCF) and MCF and their limitations are discussed. Each turning mirror fabrication approach is first applied to SCF to establish a dataset benchmark, which is then used as comparison for the dataset obtained by the MCF sensor equivalent. It is revealed that the function-fitting algorithm (FFA) measurement approach offers significantly improved accuracy and sensitivity compared to fast-Fourier transform (FFT) measurement for all fibre sensors assessed in this chapter. These findings are consistent with the conclusions drawn in Chapter 3. Table 4.5 provides a summary of results obtained for both SCF and MCF sensors assessed in this chapter.

Table 4.5: Summary of all sensor performance results acquired using the FFA for all fibre sensors. Accuracy and sensitivity rounded to the nearest nm.

| | | Accuracy (μm) | Sensitivity (μm) | Range (mm) |
|-------------------------------|-----|----------------------------|-------------------------------|------------|
| FIB Milled | SCF | 0.034 | 0.007 | ~20 |
| | MCF | 0.055 | 0.006 | ~16 |
| ULAE Subtractive Modification | SCF | 0.052 | 0.006 | ~6 |
| | MCF | 0.066 | 0.006 | ~7.5 |
| ULAE Fused-Silica Component | SCF | 0.038 | 0.006 | ~2.5 |
| | MCF | 0.040 | 0.006 | ~14 |

With consideration of the previous and current chapters' findings, highly accurate and sensitive fibre gap sensors have been realised based on single-point measurements. Where the fused-silica component is concerned, altered design approaches carry the potential for multi-point measurements, establishing a possible capability for different measurands for structural health monitoring.

Chapter 5

Fibre optic probes for tilt measurements

5.1 Introduction

In the past two chapters, the principles of Fabry-Pérot interferometry (FPI), its integration with optical fibre technology, and the development of fibre optic distance measurement sensors have been discussed and demonstrated. These concepts are built upon and expanded further in this chapter. The fibre distance measurement sensor covered in Chapter 4 provides excellent accuracy and sensitivity while maintaining small physical dimensions (largest dimension is 1 mm) so that deployment into confined spaces is possible. For structural health monitoring (SHM) purposes, the usefulness of such single-point measurement sensors would largely be dependent on the specific application at hand and the amount of information regarding the structure that is desired. If the structure's components that are to be monitored are susceptible to positional drift in a particular linear direction (e.g., a bolt fitting loosening over time), then a single-point monitoring solution may be sufficient. If, however, the deterioration of a structure leads to unpredictable misalignment (e.g., one side of a gasket drifting more than the other as a consequence of sealant outgassing), then the extraction of further information regarding such components may be desired.

The deployment of an array of sensors would be possible, which could provide the comprehensive information required. However, if the desired information is simply by how much one side of said component has drifted in relation to the other (i.e., tilt), then the measurement problem can be simplified to a two-point measurement system.

In this chapter, a fibre sensor based on differential FPI is developed which retains the small overall physical dimensions required for access within confined spaces.

5.2 Differential Fabry-Pérot interferometry

The mathematical model of FPI and its integration with optical fibres are outlined in § 3.2.1 and § 3.2.2 respectively. Here, a fused-silica component is fabricated by ultrafast laser assisted etching (ULAE) which incorporates a 45° turning mirror such that once the component is adhered to the fibre, the fibre guided light is redirected perpendicular to the fibre axis by total internal reflection (TIR). This is the same process as used for the fibres in § 4.4 and is illustrated in Figure 5.1. The redirection of light in this manner allows for sensor deployment into confined spaces without the need for significant modification to the structure in question.

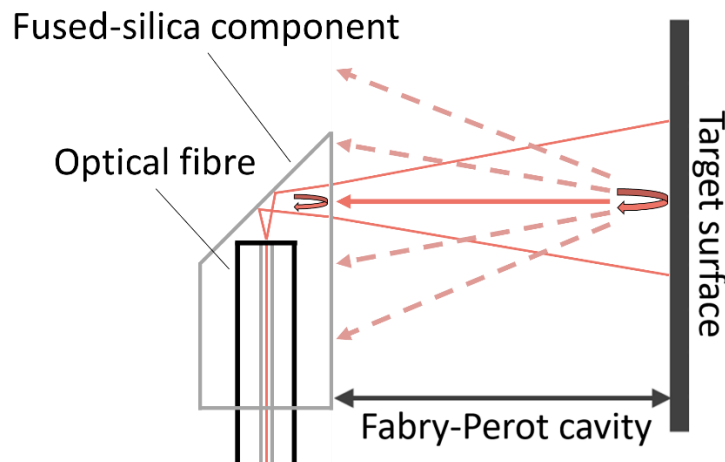


Figure 5.1: Schematic illustration of the designed functionality of Fabry-Pérot interferometry using a fused-silica component adhered to optical fibre to redirect light perpendicular to the fibre axis.

Due to Fresnel reflections, a small portion of light ($\sim 3.5\%$) will back-reflect from the edge of the fused-silica component at the fused-silica-air interface, and the remaining light will continue to propagate and interact with the target surface. Depending on the properties of the target surface, some amount of the propagating light will reflect from the target surface back towards the fused-silica component. The subsequent interference that occurs as the beams recombine at the edge of the fused-silica component define the length of the Fabry-Pérot cavity. The fused-silica component can be adapted to

accommodate the use of a two-fibre bundle, where two simultaneous Fabry-Pérot cavities are formed that are spatially offset from one another.

Each fibre measures optical cavities of equal length when the target surface is perfectly parallel to the fused-silica component, as depicted in Figure 5.2 (a).

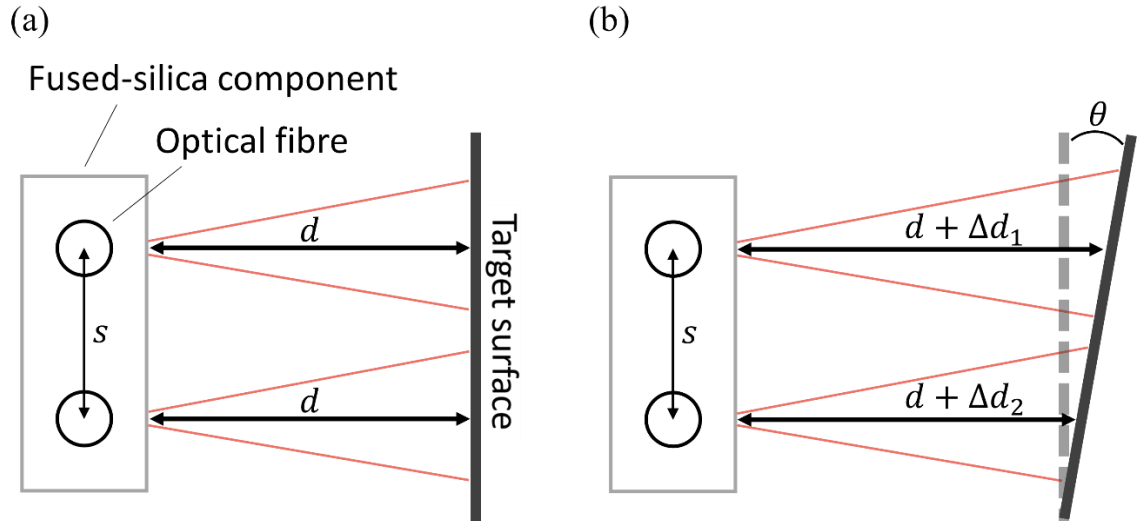


Figure 5.2: (a) Illustration of parallel configuration resulting in optical cavities of equal length measured by each fibre. (b) Illustration of target surface deviating by angle θ with respect to the fused-silica component.

Each fibre measures optical cavities of different lengths when the target surface experiences some angular deviation, θ , with respect to the reference plane defined by the fused-silica component, where Δd_1 and Δd_2 are the linear deviations of the first and second fibre measurement respectively. The angular deviation, or tilt, of the target surface can therefore be determined using equation (5.1):

$$\theta = \tan^{-1} \left(\frac{\Delta d_1 - \Delta d_2}{s} \right) \equiv \tan^{-1} \left(\frac{D_1 - D_2}{s} \right), \quad (5.1)$$

where s is the spacing between each fibre, and D_1 and D_2 are the cavity lengths measured by the first and second fibre respectively.

5.3 Sensor design and considerations

5.3.1 Component fabrication

A fused-silica wafer with dimensions $10 \times 10 \times 0.25$ mm first undergoes ultrafast laser inscription (ULI) which modifies the substrate material to enhance its susceptibility to selective chemical etching. A femtosecond pulsed fibre laser (BlueCut Menlo Systems) operating at 1030 nm with a pulse duration of 360 fs, a pulse repetition rate of 250 kHz, and a pulse energy of 200 nJ is used for ULI. These parameters are determined according to [116]. The inscription orientation and pattern used is the same as that described in § 4.4.2. After ULI, the fused-silica wafer is submerged in an 8 mol/L KOH solution heated to 85 °C to commence the chemical etching process, which selectively removes the laser inscribed features. Alongside the excess unused wafer substrate, what remains are the desired fused-silica components (Figure 5.3). The fused-silica components are then cleaned in an ultrasonic bath and allowed to dry. The design has maximum external dimensions of $1 \times 1 \times 0.25$ mm and incorporates two fibre slots spaced 0.75 mm apart from each centre axis. There is a cylindrical extrusion at the top of each fibre slot to allow for excess adhesive and/or air bubbles to escape during fibre mounting.

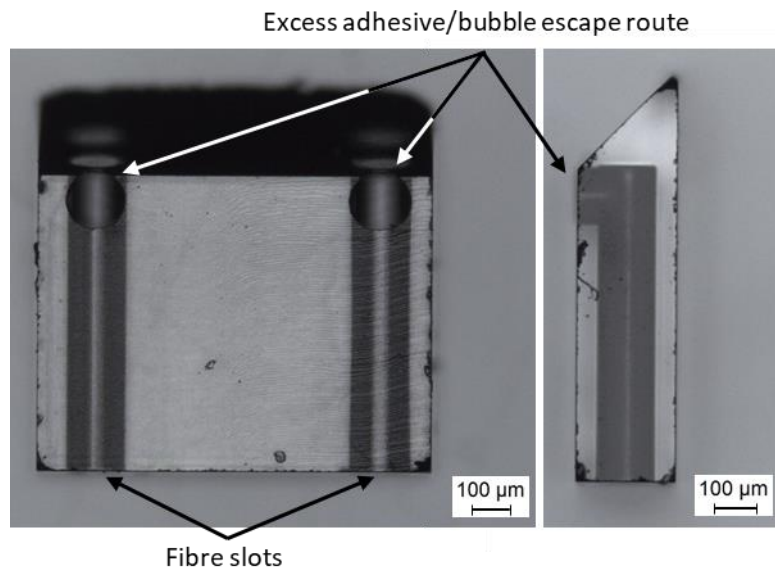


Figure 5.3: Micrograph of fused-silica component fabricated by ULAE.

The same configuration as outlined in § 4.4.2 is used to mount the fused-silica component to the fibres. The fibres used (SMF28) are single-core and single mode at 1550 nm

wavelength. Each fibre is first stripped, cleaved, and dipped in Norland Optics NOA 61 optical adhesive to establish a liquid coating which is then cured by UV exposure for one hour after mounting of the fused-silica component. The fused-silica component mounted to the two-fibre bundle is shown in Figure 5.4.

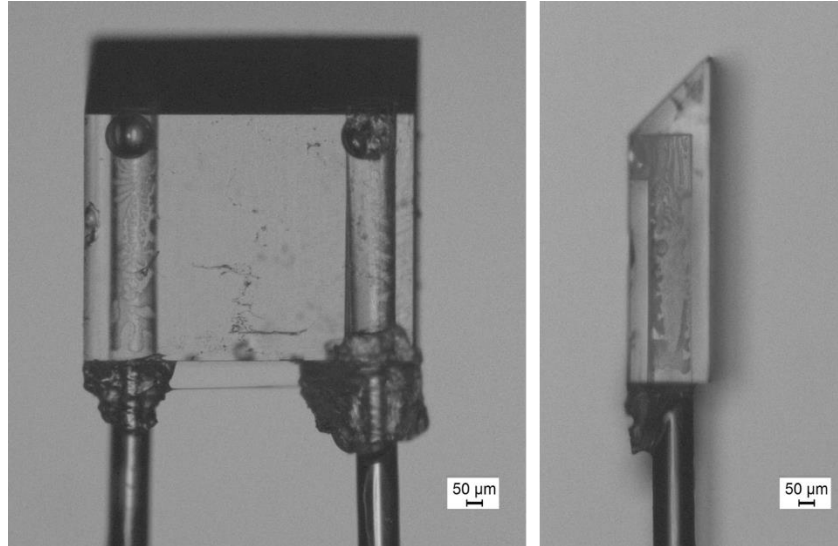


Figure 5.4: Micrograph of fused-silica component mounted to two SMF28 fibres.

5.3.2 Total internal reflection considerations

As mentioned earlier, the redirection of light at the turning mirror interface is achieved by TIR. The condition for TIR to be satisfied is governed by Snell's Law (equation (5.2)), which leads to an expression for the critical angle (equation (5.3)):

$$n_1 \sin \theta_1 = n_2 \sin \theta_2 \quad (5.2)$$

$$\theta_c = \sin^{-1} \left(\frac{n_2}{n_1} \right) \quad (5.3)$$

Light within a higher refractive index medium, n_1 , incident upon a lower refractive index medium, n_2 , at an angle θ_1 , will refract at some angle, θ_2 . The smallest incident angle possible where the light will no longer refract is known as the critical angle, θ_c , where $\theta_2 = 90^\circ$. Given the operation of the fibre mounted fused-silica component at 1550 nm and in air ($n_1 = 1.45$ and $n_2 = 1$), the critical angle can be calculated:

$$\theta_c = \sin^{-1}\left(\frac{1}{1.45}\right) = 43.6^\circ \quad (5.4)$$

Therefore, any angle larger than 43.6° will result in TIR. If the incident beam were collimated, the 45° angle facet on the fused-silica component would totally internally reflect all incident light (assuming ideal conditions with no losses at the interface). However, the fibre (SMF28) that guides the light has a numerical aperture (NA) of ~ 0.14 [105], where NA is defined as:

$$NA = n \sin \alpha, \quad (5.5)$$

where α is the angle of the propagating beam cone with respect to the fibre axis (i.e., divergence angle) and 2α is commonly referred to as the acceptance angle. For singlemode fibre, however, using the Gaussian beam propagation model offers a better estimate of the divergence angle which, to a first order approximation and in the far field, is given by (in radians) [118]:

$$\alpha = \frac{\lambda}{\pi(MFD/2)}, \quad (5.6)$$

where the beam's waist diameter has been equated to the fibre's mode field diameter (MFD) [119], which for SMF28 fibre operating at 1550 nm is $10.4 \mu\text{m}$ [105].

The acceptance angle can therefore be calculated to be approximately 10.9° . Some portion of this diverging light will not satisfy the condition for TIR, which is a geometrical problem illustrated in Figure 5.5 and Figure 5.6.

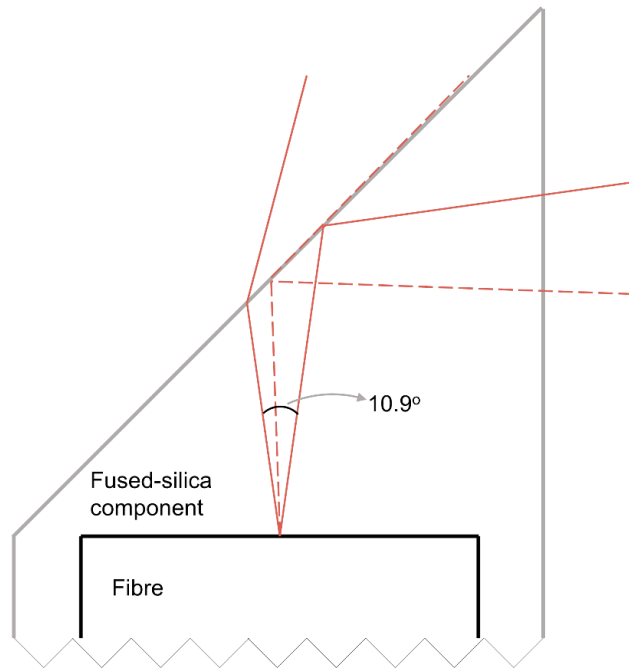


Figure 5.5: Illustration of beam propagation from fibre and its interaction with the fused-silica component angled facet interface.

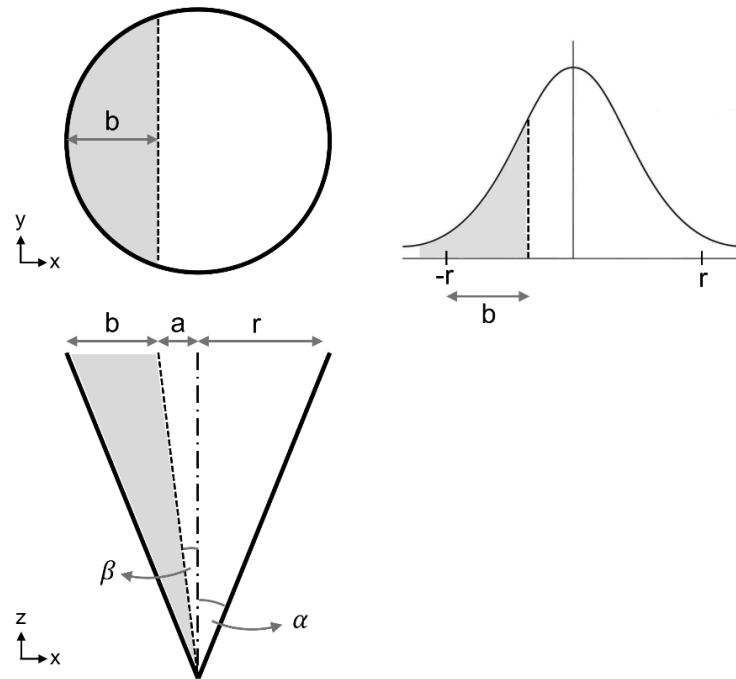


Figure 5.6: Illustration of the diverging beam profile where the shaded region represents the portion of light that does not totally internally reflect. Angles are exaggerated for clarity.

To model the proportion of light that is successfully reflected at the angled facet of the fused-silica component under ideal conditions (i.e., no scatter losses due to surface

roughness), a ray trace simulation using Zemax OpticStudio is developed, where detectors are appropriately positioned to monitor the reflected and refracted light through an imported model of the fused-silica component (see Figure 5.7 and Figure 5.8). The model is simulated using 1,000,000 analysis rays operating at a wavelength of 1550 nm with a Gaussian intensity profile.

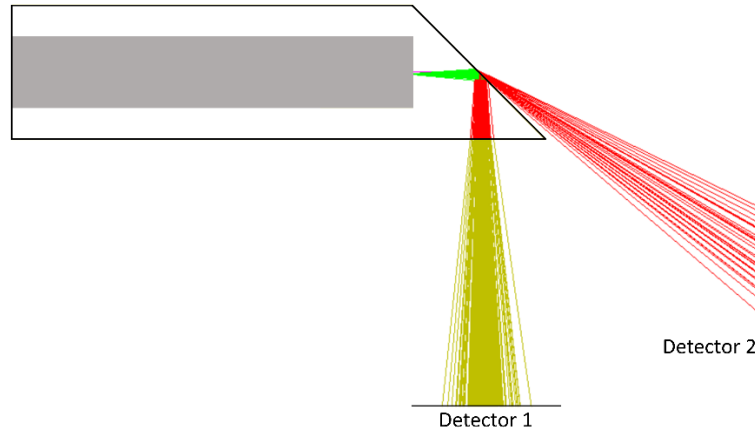


Figure 5.7: Zemax ray trace model of Gaussian beam propagation through fused-silica component. Detectors 1 & 2 determine the amount of light that is reflected and refracted by the angled facet respectively. Coloured rays represent the different ray segments. 1,000,000 analysis rays are used during simulation.

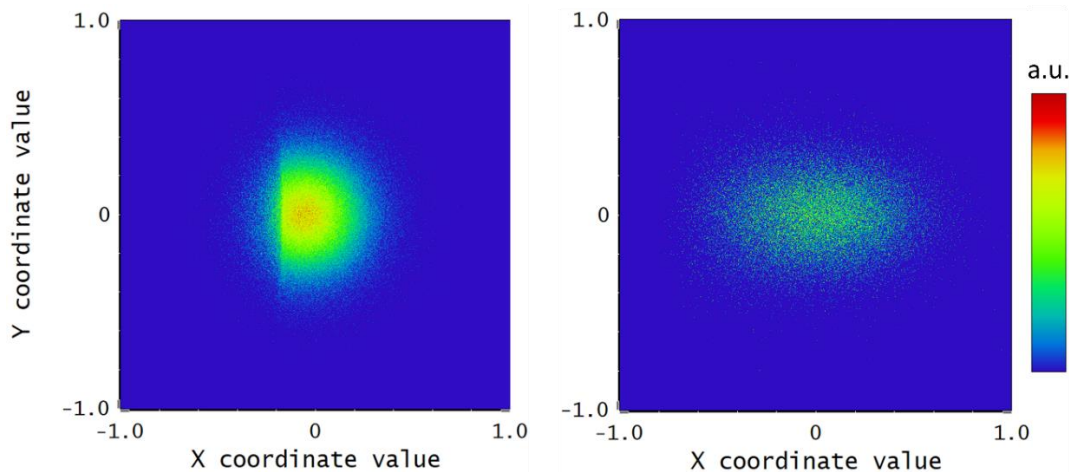


Figure 5.8: Simulation displays of (left) Detector 1 and (right) Detector 2.

The simulated output from both detectors suggests that $\sim 83.5\%$ ($\cong 0.8$ dB loss) of the light from the fibre is reflected at the angled facet of the fused-silica component. This ideal model can be compared to the turning mirror losses experimentally verified in § 4.2.3 (Table 4.2), where in the best-case, losses of ~ 1.2 dB are presented.

5.3.3 Parasitic optical cavities

Although the optical adhesive used with fused-silica component sensors is (closely) index matched (refractive index of the cured polymer is 1.56 [120]), it is still possible for secondary and tertiary optical cavities to form during measurement acquisition. These additional cavities are typically unwanted, and so are referred to as parasitic cavities. These parasitic cavities arise when back reflection occurs at any interface between two optical media, for example at the cleaved fibre end (via Fresnel reflection). Ideally, the index matched adhesive would prevent this, but residual reflections may still occur depending on the quality of the cured adhesive finish, e.g., if there is a thick adhesive layer with micro-bubbles between the cleaved fibre end and the fused-silica component, or if a single larger bubble is formed above the fibre core, leaving a trapped air gap that is too small to reasonably detect by means implemented in this work ($\sim 1 \mu\text{m}$). The different optical cavities that can typically form are illustrated in Figure 5.9.

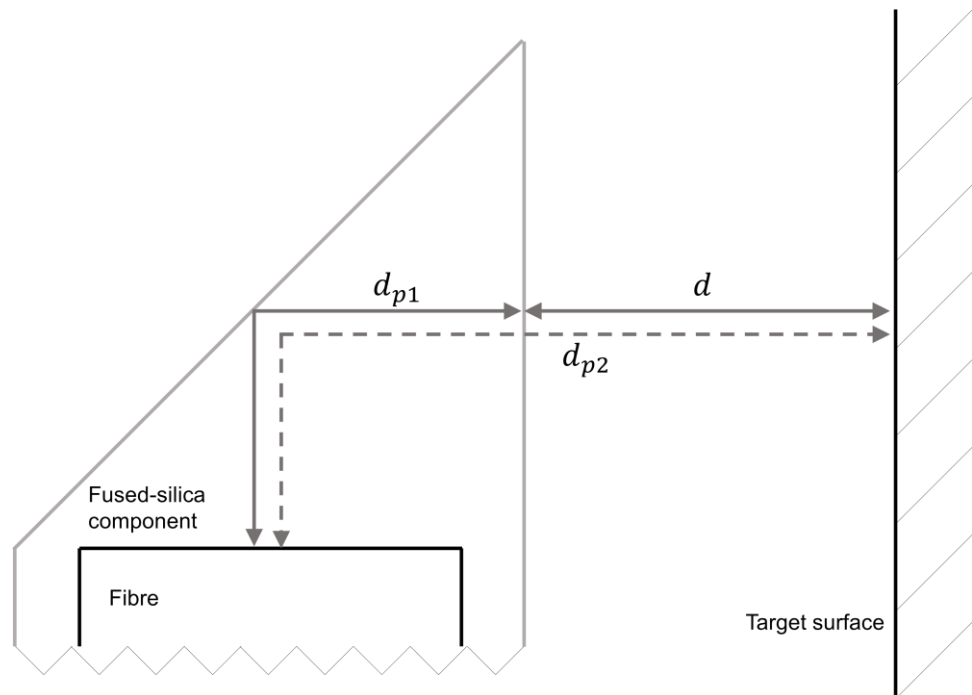


Figure 5.9: Schematic of the different optical cavities that can form with the fibre sensors that utilise the fused-silica component, where d_{p1} and d_{p2} are the parasitic cavities and d is the primary optical cavity of interest.

Referring to Figure 5.9, d_{p1} and d_{p2} are the parasitic optical cavities, and d is the primary optical cavity of interest. When acquiring a signal in the presence of parasitic cavities, although they are unwanted, it is easy to distinguish and identify each cavity (as long as

they are different in size from the cavity of interest), and therefore isolate the primary cavity of interest. The first parasitic cavity, d_{p1} , is of a constant value that is known by design, which in this case corresponds to an optical path length of $\sim 380 \mu\text{m}$. The other cavities, d and d_{p2} , can be expressed by the following relationship whereby:

$$d = d_{p2} - d_{p1}, \quad (5.7)$$

therefore the comparison $d < d_{p2}$ is always true. An example of the signal acquired using a fused-silica component mounted fibre sensor with parasitic cavities is shown in Figure 5.10.

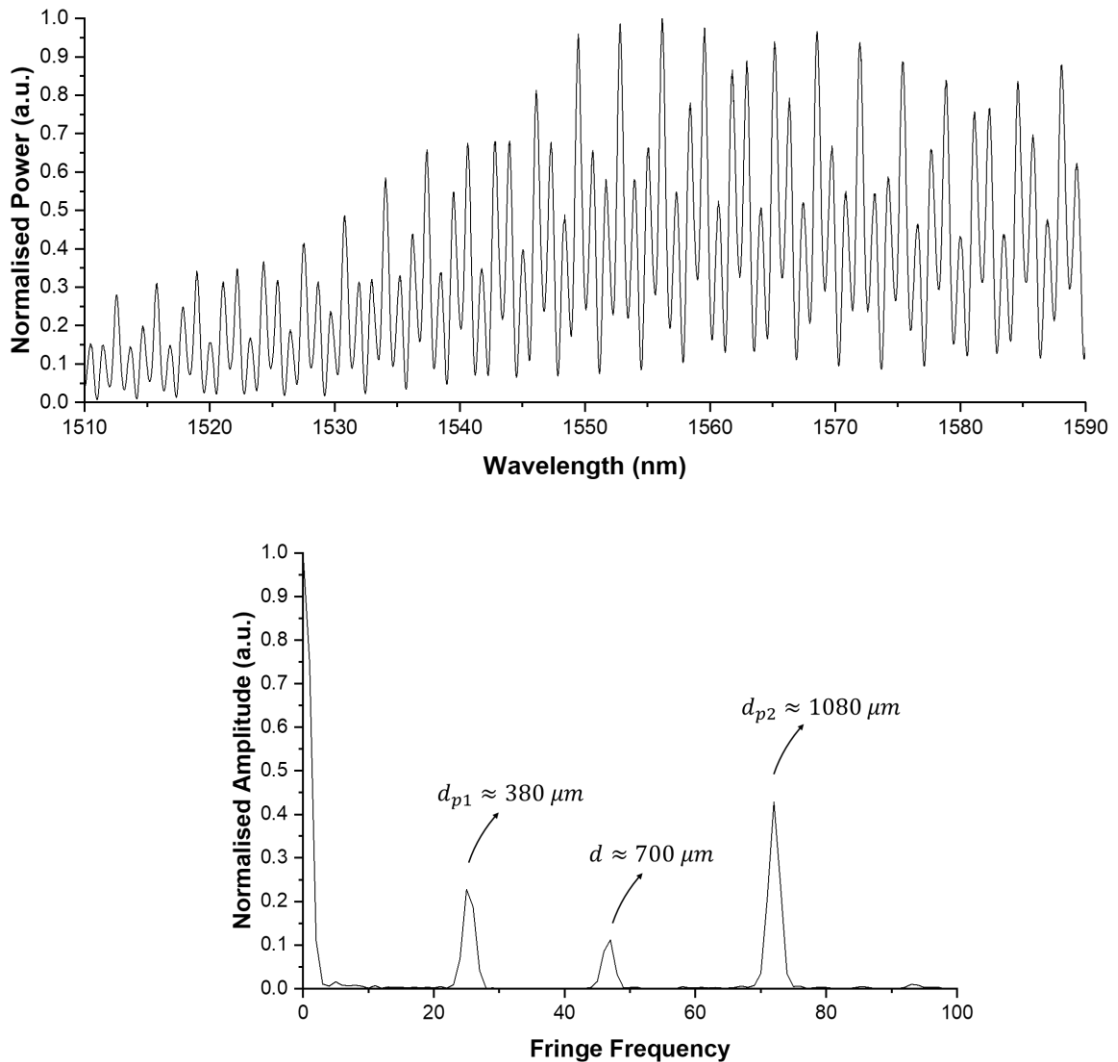


Figure 5.10: Signal acquired using a fused-silica component mounted fibre sensor with parasitic cavities, with a primary cavity length of $\sim 700 \mu\text{m}$. (top) Reflected interference spectrum, (bottom) Fourier transform of the reflected interference spectrum.

Note that in Figure 5.10, the first peak in the Fourier transform graph that has a normalised amplitude of 1 at zero frequency occurs due to the positive offset of the input spectrum. When parasitic cavities form, light is reflected at surfaces which, by definition, are of no interest. This leads to less light being reflected at the surfaces which form the primary cavity of interest, in turn resulting in a diminished amplitude of the corresponding Fourier transform peak. This subsequently results in greater error when applying the function-fitting algorithm (FFA) (see § 3.3.2). It is possible, although suboptimal, to determine the primary cavity length by using only the parasitic cavities (equation (5.7)). However, this doubles the computations required in post-processing of the data when using the FFA, as the FFA will need to be applied to each parasitic cavity simultaneously which, depending on the capabilities of the hardware undertaking the computations, could be extremely taxing. Additionally, this indirect approach for measuring the primary cavity length could potentially be less accurate, as small temperature fluctuations could result in drifting of the optical path length for d_{p1} regarding the adhesive layer, rendering equation (5.7) untrue. Attempting to measure the primary cavity length directly in the presence of parasitic cavities, as long as the signal strength is sufficient, should not lead to any complications with the acquired data. There is, however, a limitation present where cavity lengths in the vicinity of 380 μm (i.e., the first parasitic cavity) will not be measured accurately as the Fourier transform peak corresponding to the primary cavity will effectively be masked by the peak corresponding to d_{p1} . Therefore, in all accounts, parasitic cavities should be avoided for the sensor to be utilised to its full potential.

Figure 5.11 shows an example of measurement data acquired where no parasitic cavities are present. The success yield of mounting a fused-silica component to a fibre that has no parasitic cavities has some dependency on the skill and experience of the assembler. During the research conducted here, approximately 1 in 5 fused-silica component sensor assemblies yielded results free of parasitic cavities.

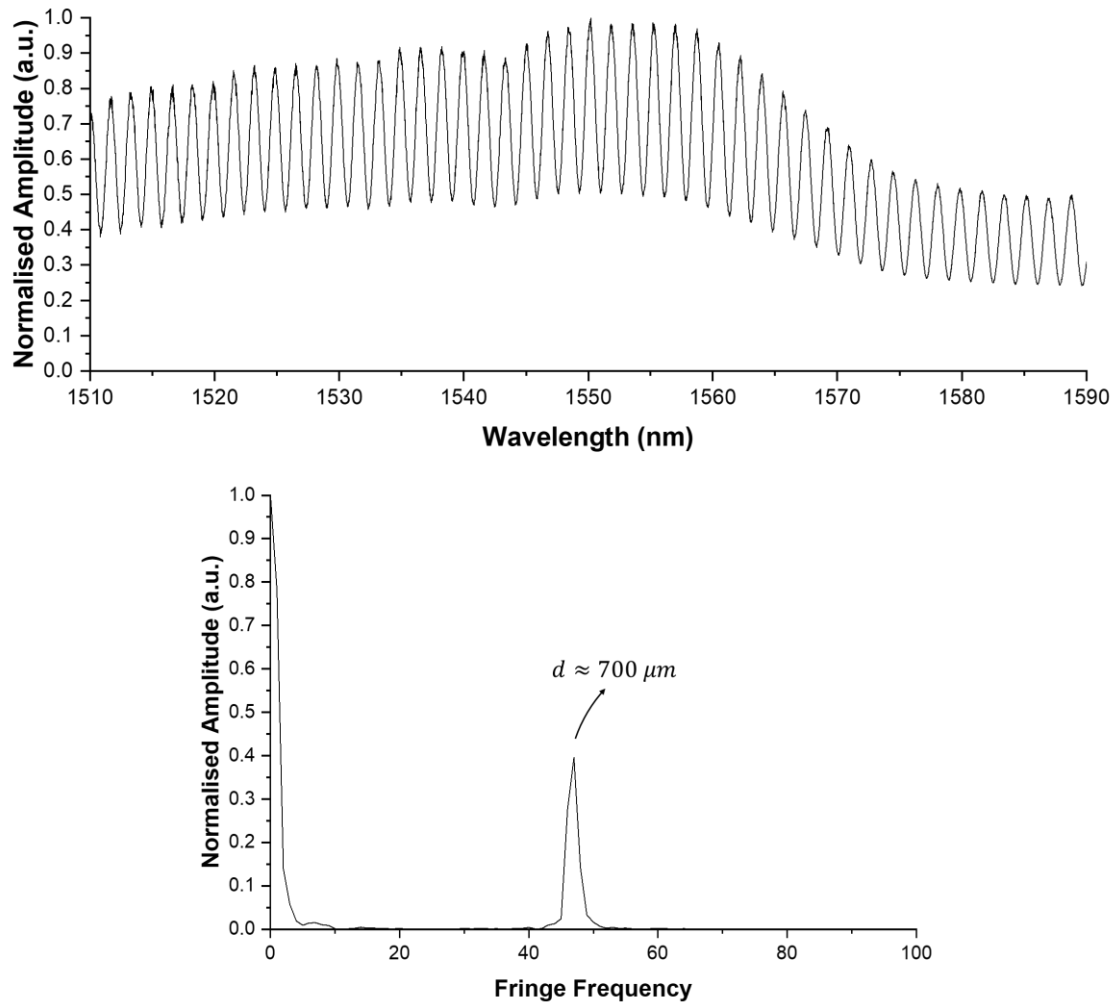


Figure 5.11: Signal acquired where no parasitic cavities are present, measured at a cavity length of $\sim 700 \mu\text{m}$. (top) Reflected interference spectrum, (bottom) Fourier transform of the reflected interference spectrum.

5.3.4 Tilt effects on return signal

When the target surface experiences some angular deviation with respect to the fused-silica component, each fibre will measure different cavity lengths. Beyond the absolute change in cavity length, there are other implications the tilted target surface has on the returned signal. One such implication is the changing perpendicular direction from the target surface with respect to the propagating beam and the corresponding cavity length for which light is most likely to reflect back into the fibre. This effect is illustrated in Figure 5.12.

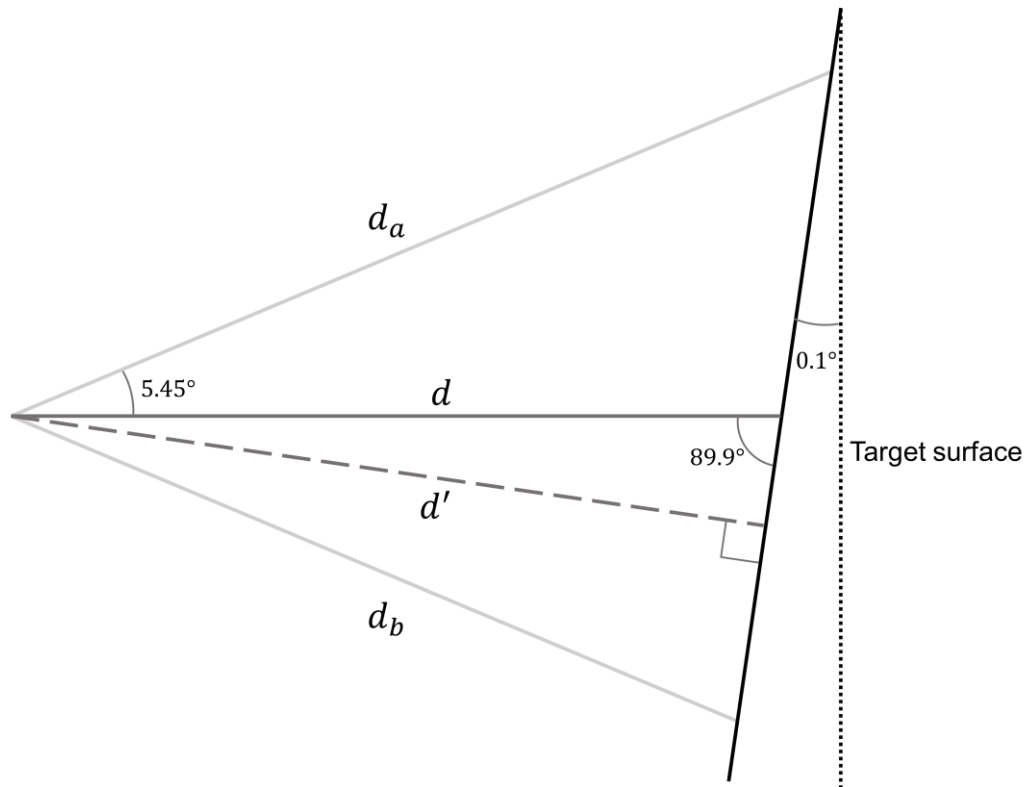


Figure 5.12: Schematic of diverging beam interaction with tilted target surface, where d_a and d_b are the outermost cavity lengths, d is the cavity length that is formed in the axis of propagation, and d' is the cavity length formed perpendicular to the target surface. Angles are exaggerated for clarity.

If the target surface were to deviate by an angle of 0.1° (the relevance of this value is revealed in § 5.4.2), the beam perpendicular to the target surface changes from that which corresponds to cavity length d to d' . Due to the Gaussian profile of the beam, the propagating portion of light along d' is of a lower power compared to the portion of light propagating along d . Depending on the distance between the fibre and the target surface, the amount of light that reflects back into the fibre that form both d and d' cavities could be equally significant. Subsequently, this could result in a broadening of the Fourier transform signal because in effect a spread of multiple cavities are now demodulated, as opposed to a single length cavity. To quantify this effect, an analytical approach is adopted to assess the amount of broadening that could occur.

In the worst-case scenario, the beam would have a uniform intensity profile (as opposed to a Gaussian profile), and the target surface would be retroreflecting. This means that light in all angles of propagation (within the bounds of the acceptance angle) would reflect back to the fibre by equal amounts. The corresponding cavity lengths that would arise

within the acceptance angle, at an exemplary central distance of $1000\ \mu\text{m}$, is depicted in Figure 5.13.

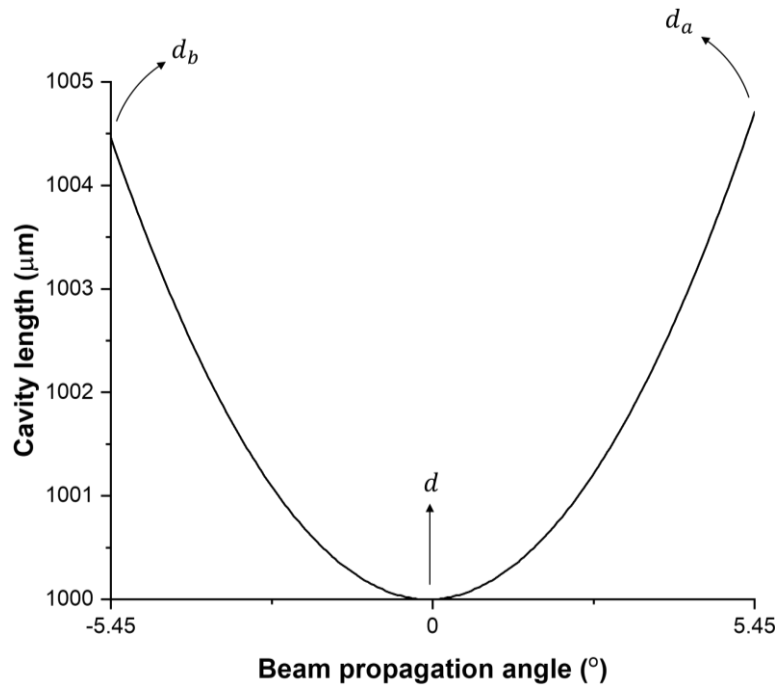


Figure 5.13: Cavity length as a function of beam propagation angle within the bounds of the acceptance angle, where d_a and d_b are the outermost cavity lengths, and d is the central cavity length.

The multiple cavity lengths used in the analytical approach are defined using an angular resolution of 0.05° within the bounds of the acceptance angle (i.e., from -5.45° to $+5.45^\circ$ in increments of 0.05° , which corresponds to 219 data points). The reflected signal that would be generated when comprised of the many cavity lengths defined here is modelled using equation (3.13) (see § 3.3.2). The Fourier transform of the modelled reflected signal that is comprised of a single cavity length ($d = 1000\ \mu\text{m}$) and multiple cavity lengths is shown in Figure 5.14.

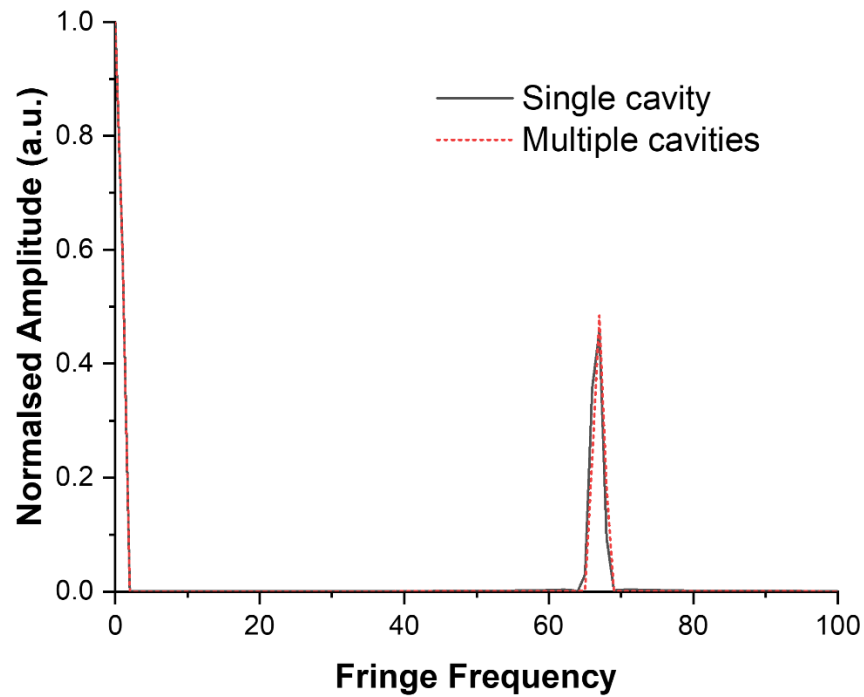


Figure 5.14: Fourier transform of modelled reflected Fabry-Pérot signal which comprises of a single cavity at $d = 1000 \mu\text{m}$ (black solid line) and multiple cavities across the propagating beam acceptance angle (red dotted line).

As can be seen from Figure 5.14, the amount of broadening that occurs in the Fourier transform is insignificant in the worst-case scenario (FWHM ~ 1.7 for both). It is therefore reasonable to conclude that the broadening that may occur given a Gaussian beam profile incident upon a mirror target surface is also insignificant. What may be of more significance, however, is the shift that is observed of the Fourier transform peak. In Figure 5.14, this shift corresponds to a cavity length change of $\sim 4 \mu\text{m}$, which would likely be less given a Gaussian beam profile incident upon a mirror. The influence this has on sensor accuracy is experimentally assessed in § 5.4.2.

Another implication the tilting target surface has on the returned signal is its effect on signal strength. As the target surface is tilted at increasing angles with respect to the sensor, the amount of light that is reflected back into the fibre diminishes. This is simply due to the geometrical limitation whereby light is reflected away from the fibre along a different propagation trajectory. The specific amount of light that is reflected back to the fibre at any given tilt angle will depend on the target surface profile – if the surface profile elicits increased scattering when light is incident upon it, then larger tilt angles will likely be possible. The consequence of this, however, is that the return signal strength will be overall lower even when the target surface is perpendicular to the beam propagation due

to the scatter. It is therefore chosen to prioritise sufficient back-reflection to ensure sensor functionality by using a mirror target surface.

5.4 Sensor performance analysis

The metrics for sensor performance are defined here as quantifying the sensor accuracy, sensitivity, and operable range. The operable range can be sub-categorised as: (i) the range of cavity lengths measurable from the target surface and; (ii) the range of tilt angles measurable with respect to the target surface. As the range of measurable cavity lengths have been assessed with a similar fused-silica component design in § 4.5, only the tilt range will be assessed here. All measurement results are acquired using the function-fitting algorithm (FFA) detailed in § 3.3.2.

5.4.1 *Experimental configuration*

The experimental configuration used for fibre tilt sensor performance evaluation is shown in Figure 5.15. An optical sensing interrogator (SM125-700, MicronOptics) is employed as both the light source and the detector. This consists of a swept laser source between 1510-1590 nm, an acquisition rate of 5 Hz, and a resolution of 0.0125 nm. Two channels of the interrogator are connected to the two SMF28 singlemode fibres that comprise the tilt sensor. The reflected interference spectrum is recorded and sent to a computer for processing. A cantilever system is assembled which is prone to angular deviation about the pivot line, where a ceramic blade, which behaves as the pivot, is situated at one end of the cantilever. At the other end is a micrometer which introduces a linear vertical displacement which tilts the cantilever system. The target surface, which in this case is a standard plano silver coated mirror, is placed on the cantilever above the pivot. The two-fibre bundle which collectively forms the tilt sensor is mounted to a fibre rotator, which in turn is mounted to a 3-axis flexure stage for precise positioning of the sensor. The fibre rotator allows for the initial rotational alignment of the sensor with respect to the target surface. The stand-off distance between the fused-silica component and the target surface is approximately 1 mm. The cantilever itself is an aluminium extrusion with a length that allows the pivot to be spaced 800 mm from the micrometer. Therefore, a 0.1 mm displacement introduced by the micrometer corresponds to $\sim 0.007^\circ$ angular deviation of the target surface with respect to the fused-silica component. It is assumed that any change in spacing between the micrometer and the pivot as a result of the vertical linear displacement introduced by the micrometer is negligible.

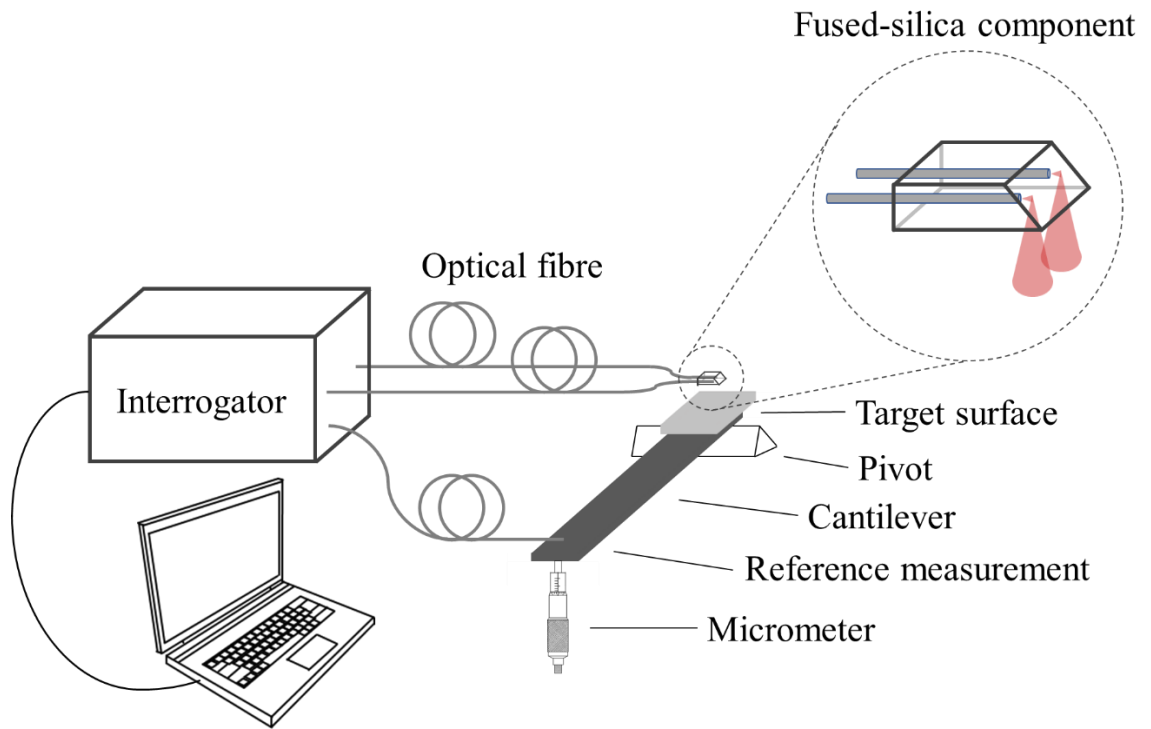


Figure 5.15: Schematic of the experimental configuration used for fibre tilt sensor performance evaluation.

A reference measurement fibre is positioned directly above the micrometer contact point with the cantilever to accurately verify the amount of linear displacement introduced by the micrometer. The reference measurement fibre in question is a FPI 45° angle cleaved fibre gap sensor which utilises the same cavity demodulation and post-processing technique as the tilt sensor (see § 3.2 and § 3.3). This reference measurement fibre can be considered to have a conservative accuracy better than ± 50 nm (see § 3.5.3). Therefore, the input angular displacement accuracy of the cantilever is limited by the accuracy of the spacing between the micrometer and the pivot. Assuming the micrometer has been positioned accurately within 2 mm, a 0.1 mm linear displacement introduced by the micrometer corresponds to an input angular displacement accuracy of $\pm 9 \times 10^{-6}^\circ$.

5.4.2 Results

The sensor accuracy is assessed by comparing a range of tilt angles measured by the fibre sensor and the input tilt introduced by the micrometer upon the cantilever. The comparison is drawn by applying a linear fit to the measurement dataset and evaluating the measurement residuals, where the residuals are the differences of each data point with respect to the fitted line. Perfect agreement would result in a line intercept of 0 and a

slope of 1, however very small misalignments in the configuration may result in values which deviate from the ideal. These are inherently accounted for by evaluating the residuals with respect to the fitted line. The sensor accuracy assessment graph can be seen in Figure 5.16.

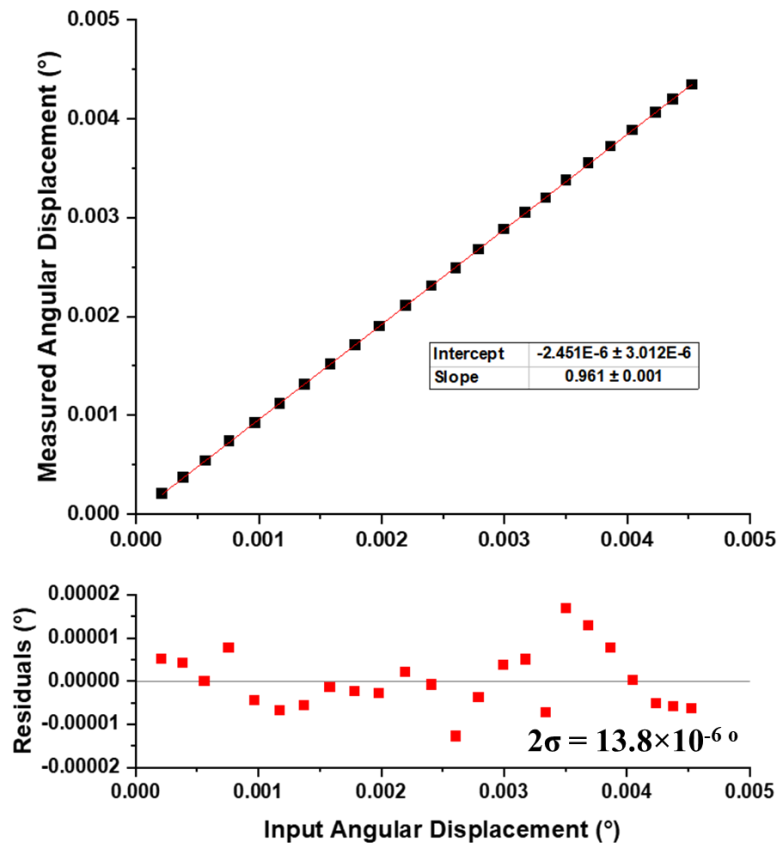


Figure 5.16: Tilt sensor and input angle measurements using the FFA cavity measurements techniques to assess sensor accuracy, consisting of tilt angles $\sim 0.017^\circ - 0.022^\circ$.

By taking two standard deviations (2σ) of the residuals, an accuracy value that falls within 95% confidence is obtained. The tilt sensor accuracy can therefore be considered as $\pm 13.8 \times 10^{-6} \text{ } ^\circ$ (or better*).

The sensor sensitivity is assessed by continually measuring a fixed cantilever tilt angle for a period of time. The fluctuations in the measurement reading during this time are

* The underlying experiment accuracy is determined to be $\pm 9 \times 10^{-6} \text{ } ^\circ$ and so an experimental configuration with better accuracy may yield improved tilt sensor performance results.

representative of the noise floor. The fixed cantilever tilt angle measured over a period of time is shown in Figure 5.17.

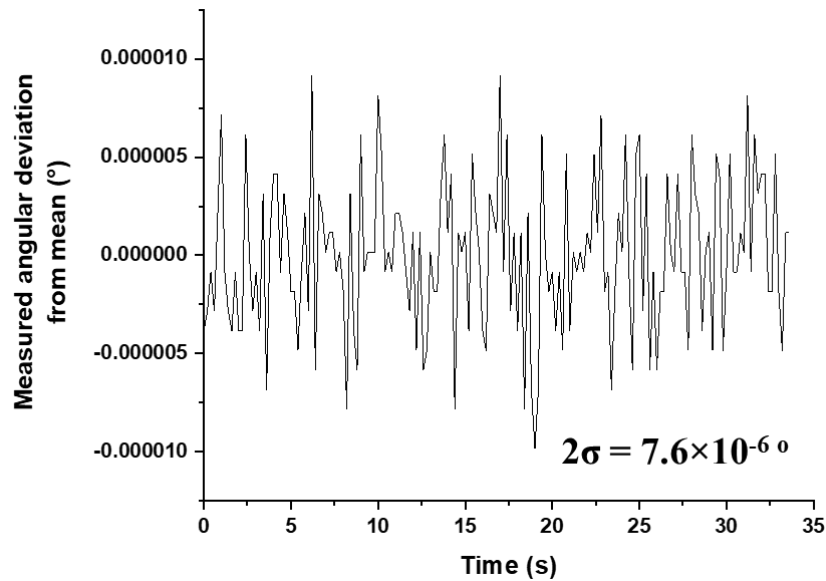


Figure 5.17: Fixed cantilever tilt angle at $\sim 0.017^\circ$ measured by tilt sensor to assess sensor sensitivity.

As with the accuracy assessment, two standard deviations are taken of the measurement fluctuations to obtain a value that falls within 95% confidence. The sensor sensitivity, which is the smallest detectable change in measurand, can therefore be considered as $\pm 7.6 \times 10^{-6}^\circ$.

The sensor tilt range is assessed by simply tilting the cantilever until the return signal is so diminished that the FFA measurement technique is no longer functional (see § 3.5.3 for a detailed discussion regarding this). As such, using a mirror as a target surface, the operable tilt range is measured to be $\pm 0.1^\circ$.

5.5 Conclusions

Regarding structural health monitoring, it may be desirable to obtain more information from the sensors that are deployed to monitor the condition of component parts. This can be achieved by expanding the capabilities of the single-point measurement devices demonstrated in Chapter 4 to a two-point measurement device. By incorporating a fused-silica component design that is mounted to a two-fibre bundle, the tilt of a component part can be determined by means of differential Fabry-Pérot interferometry.

When the target surface is tilted with respect to the beam propagation axis, certain considerations must be recognised. Firstly, the perpendicular axis to the target surface represents a different cavity length to that of the beam propagation axis, which depending on the spacing between the sensor and the target surface, could result in beam trajectories which represent multiple cavities reflecting back to the fibre. It was at first investigated whether this effect would result in broadening of the Fourier transform signal, but analytical evaluation revealed that the broadening is insignificant, and instead indicated that a shift in the Fourier signal peak could occur. This shift in the Fourier signal peak carried implications regarding the accuracy of the sensor, but experimental assessment resulted in a highly accurate sensor. This suggests that the amount that the Fourier signal peak shift that is experienced by both fibres is similarly small to one another, and therefore the differential Fabry-Pérot interferometry approach remains viable.

Secondly, a tilting target surface means less light reflecting back to the fibre at increased tilt angles. This is simply a geometrical limitation of the measurement acquisition method but may be modified by utilising different target surface material profiles. In this case, a silver coated mirror was used as the target surface, which was placed on a cantilever to assess the sensor performance. A summary of the performance metrics assessed are outlined in Table 5.1.

Table 5.1: Summary of tilt sensor performance results acquired using the FFA, rounded to one decimal place.

| Accuracy (°) | Sensitivity (°) | Range (°) |
|---------------------------|--------------------------|-----------|
| $\pm 13.8 \times 10^{-6}$ | $\pm 7.6 \times 10^{-6}$ | ± 0.1 |

Chapter 6

Gas speciation measurements

6.1 Introduction

The detection of certain gas species can provide important information of the various chemical ageing processes occurring within a system. Regarding the context of structural health monitoring that is undertaken here, it is important that this detection mechanism is non-extracting and non-destructive within a hermetically sealed system and is capable of achieving high sensitivity and selective measurements. One particular gas of interest is nitrogen dioxide (NO_2). Two candidate approaches are explored and investigated in this chapter, both which operate on the principle of absorption spectroscopy. These being evanescent wave (EW) fibre optic sensing and incoherent broadband cavity-enhanced absorption spectroscopy (IBBCEAS).

6.2 Principles of absorption spectroscopy

When light propagates through a medium, certain conclusions can be drawn depending on the interaction that occurs. The interaction that is of primary interest here is absorption. Absorption refers to the attenuation of light that arises due to the transfer of energy from the light to the medium within which it propagates. The amount of absorption that is experienced at particular wavelengths can help identify the constituents of the absorbing medium in question. This is generally referred to as absorption spectroscopy. Figure 6.1 illustrates this concept rudimentarily.

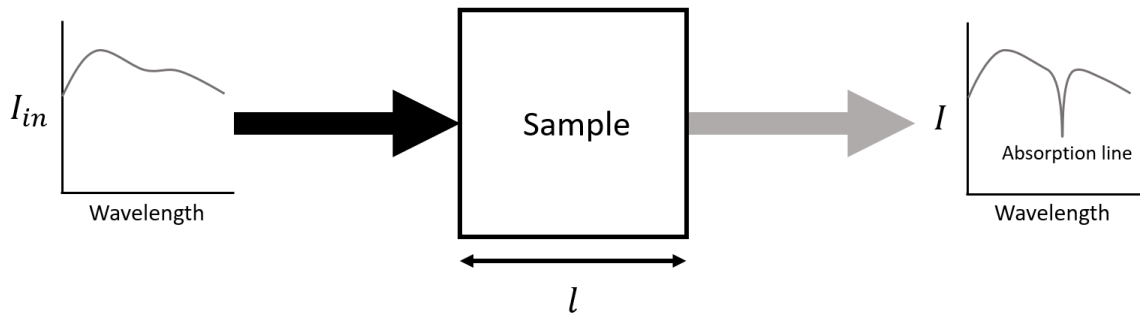


Figure 6.1: Simple illustration of absorption spectroscopy, where light is incident upon an absorbing sample of interaction length l . Where broadband light is incident, absorption line(s) are revealed where, for example, only certain wavelengths are absorbed by the sample.

As light is incident upon an absorbing sample with intensity I_{in} , it will propagate through the sample of path length l , and will result in an attenuated transmitted intensity, I . The amount of attenuation that occurs is referred to as the absorbance, A , and is defined by the incident and transmitted intensities [121], assuming the attenuation due to scattering is negligible [122]:

$$A = \log_{10} \left(\frac{I_{in}}{I} \right) \quad (6.1)$$

At low concentrations, a proportionality can be drawn between the absorbance, the sample concentration, c , and the absorption length, l :

$$A \propto cl \quad (6.2)$$

Equation (6.3) can be derived by including a proportionality constant, ε :

$$A = \varepsilon cl, \quad (6.3)$$

where ε is commonly used when c is quantified as molar concentration. Therefore, ε is also referred to as the molar extinction coefficient. Where c is quantified as volumetric concentration, equation (6.3) becomes

$$A = \sigma cl, \quad (6.4)$$

and σ is the absorption cross-section. Combining equations (6.1) and (6.4) results in a common form of the Lambert-Beer Law [121]:

$$A = \log_{10} \left(\frac{I_{in}}{I} \right) = \sigma cl \quad (6.5)$$

Note that ε typically has units of $M^{-1}cm^{-1}$ and σ typically has units of cm^2 . Another common form of the Lambert-Beer Law can be expressed in terms of the absorption coefficient, α , which inherently within it considers the substance's concentration and is defined in units of cm^{-1} , where [123]:

$$I = I_{in}e^{-\alpha l} \quad (6.6)$$

6.3 Evanescent wave fibre optic sensor

The evanescent wave (EW), or evanescent field, arises in the surrounding medium at the interface between two different media where total internal reflection occurs [124]. It does not propagate, but instead has exponentially decaying energy normal to the plane of incidence which extends into the second medium. In the case for optical fibres, this occurs at the core-cladding interface, where the amount by which the evanescent wave extends into the cladding is known as the penetration depth, d_p , which is defined as the distance at which the EW energy decays to 1/e its original value [125] and is given by:

$$d_p = \frac{\lambda}{2\pi(n_1^2 \sin^2 \theta - n_2^2)^{\frac{1}{2}}}, \quad (6.7)$$

where λ is the wavelength of light propagating in the fibre, n_1 is the core refractive index, n_2 is the cladding refractive index, and θ is the angle of incidence normal to the cladding. Assuming that for a standard SMF28 fibre operating at 1550 nm wavelength there is a core refractive index of 1.45, a cladding refractive index of 1.44, and a θ value of 84.46° (assuming a numerical aperture of 0.14), the penetration depth into the cladding is ~2.56 μm . Given that the cladding has a diameter of 125 μm , the penetration depth is

contained well within the bounds of the cladding geometry. Obviously, this is by design and is necessary for fibre to guide light over very long distances without the surrounding environment influencing the guided wave. It may be possible, however, to modify the fibre geometry such that there exists an EW in the medium which surrounds the fibre, e.g., air within which the analyte gas species is present. In this manner, an evanescent wave fibre optic sensor (EWFOS) could be developed as the absorption which would occur by the interaction between the analyte and the EW could be quantified.

Indeed, there are other methods of facilitating EWs beyond the fibre geometry, such as side-polished fibre block couplers, whereby a fibre is embedded in a groove with a slight bend typically within a silicon wafer and the fibre is mechanically polished to remove a portion of the cladding layer [126]. This approach, however, is limited to effective interaction lengths in the range of several mm's [126], which alone would be insufficient for sensitive gas detection by means of absorption. Additionally, the cladding may also be removed by means of chemical etching with the use of hydrofluoric acid (HF) [127], however the hazards associated with this method are deemed outwith the scope of work described in this thesis. These limitations are further discussed in § 6.3.3.

6.3.1 Fibre tapering

Tapering the fibre down from its original geometry to smaller dimensions has a number of implications. Firstly, the angle of incidence of the guided light with the fibre cladding approaches closer to the critical angle, which increases the penetration depth of the EW. Secondly, the reduced cladding diameter implies a thinner layer of cladding material that the EW is required to penetrate through. Lastly, as the fibre core is tapered by the same proportions as the cladding, increased amounts of light will be guided by the cladding instead of the core (depending on the taper parameters), which may then further facilitate improved EW penetration into the surrounding medium. This concept is illustrated in Figure 6.2.

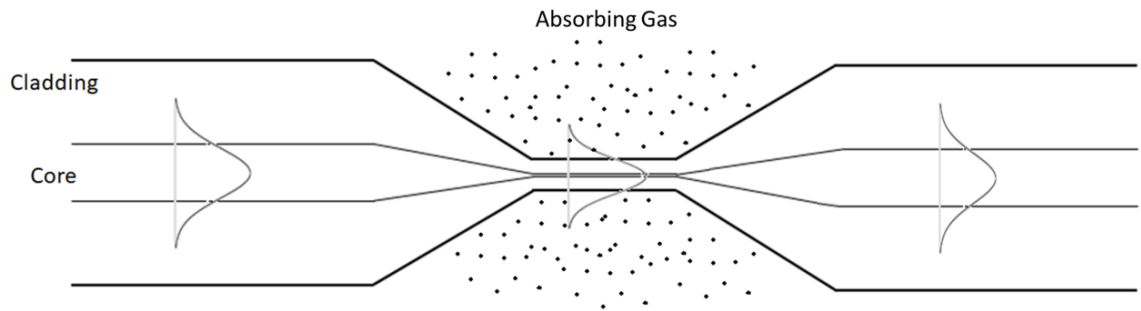


Figure 6.2: Illustration of fibre taper where the cladding and core are tapered to smaller dimensions by equal proportions. The evanescent wave from the guided light penetrates into the surrounding medium and interacts with the analyte along the length of the tapered region, after which light is once again guided by the core when the fibre returns to its original geometry.

Although increasing the EW interaction with the surrounding medium is desired, it is also important to minimise the excess losses due to the taper. In other words, the challenge arises not by solely establishing sufficient interaction between the EW and the analyte, but by establishing this with fibre dimensions that then promote the light to remain guided within the fibre core once the fibre returns to its original dimensions. The fibre taper design can be optimised for this purpose with the use of specialised simulation software. This is discussed in § 6.3.2.

It is first necessary to understand what fibre taper dimensions can practically be achieved prior to attempting design simulations. A Fujikura ArcMaster FSM-100P+ is used to fabricate tapers on standard SMF28 optical fibre. This device, primarily used as a fusion splicer, has extensive capabilities in fibre taper fabrication where a plasma arc is formed between two electrodes positioned on either side of the fibre. High precision motor driven stages then draw out the fibre as it is heated by the arc, creating a tapered fibre region. Once tapered, the built-in camera system is also capable of fibre diameter measurement acquisition. Figures 6.3 and 6.4 show an example fibre taper.

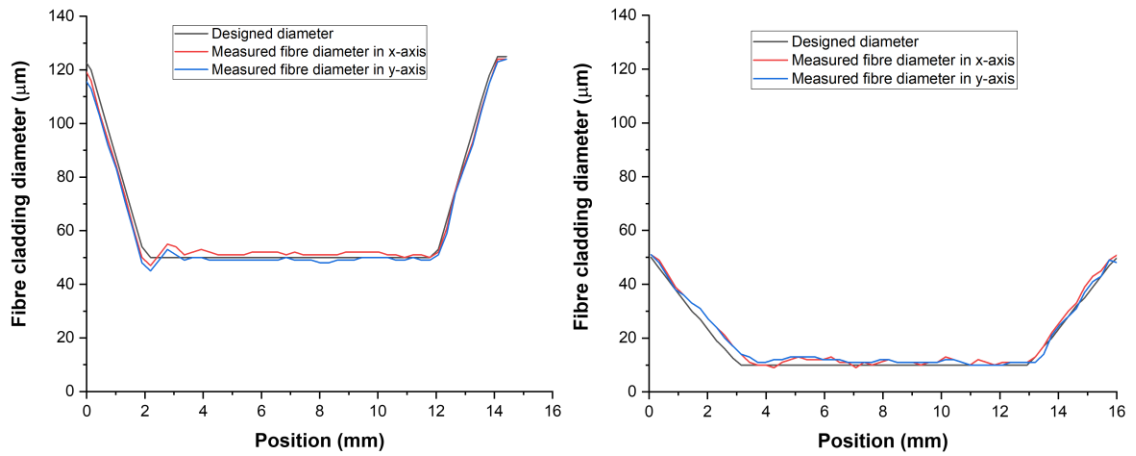


Figure 6.3: Graphs of measured tapered fibre diameter in comparison to the designed taper dimensions. (left) First taper step from 125 µm to ~50 µm. (right) Second taper step from ~50 µm to ~12.5 µm.

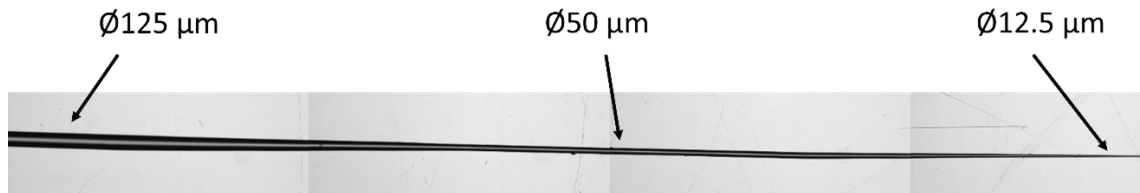


Figure 6.4: Sequenced microscope images of the fibre taper steps consisting of dimensions 125 → ~50 → ~12.5 µm.

A multi-step taper process is implemented to obtain the small taper dimensions seen above. These parameters have been repeated multiple times with similar results. With this splicer, the longest taper length achievable is ~30 mm. An attempt at tapering to diameters below 12.5 µm is made (e.g., 10 µm), but this yields inconsistent results where the taper either breaks or produces taper lengths with poor uniformity. It may be possible to further optimise the input parameters, namely the fibre draw speed and the arc power, to establish a more uniform taper profile. Regardless, the results above help establish practical limitations in the taper diameter which can then be implemented into design simulations.

6.3.2 Evanescent wave simulation

Synopsys BeamPROP is used for design simulation. Based on the experiments in this work, a minimum cladding taper diameter of $\sim 12.5 \mu\text{m}$ fabricated by using a multi-step process is chosen, and so the optimal configuration to maximise EW generation and minimise losses is now investigated. The parameters that are explored are the taper length and the taper diameter. The fibre is modelled by assigning the core a refractive index of 1.45 and assigning the cladding, which is allocated to the surrounding material, a refractive index of 1.44. Due to memory limitations with the computing hardware, modelling air as a third layer was not possible, but proved unnecessary to draw important conclusions, as will be discussed later.

The taper designs are assessed by monitoring the power within the core: Ideally, the power should be low in the tapered region, indicating significant penetration into the cladding, and the power in the core should be high once again once the modelled fibre has returned to its original dimensions. An example of a poorly designed tapered fibre is shown in Figure 6.5.

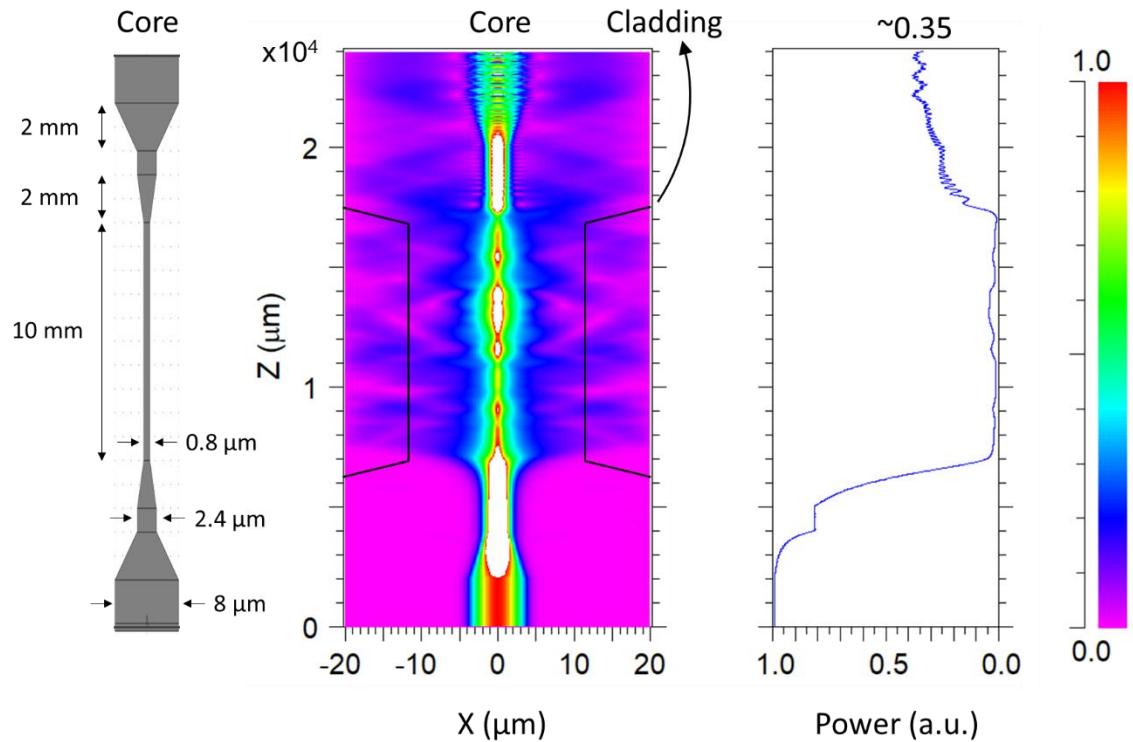


Figure 6.5: Simulation results of a poorly designed fibre taper. (left) Model of tapered fibre core with corresponding taper dimensions; (middle) Visualisation of the power distribution across the modelled fibre length, where black lines are used for reference to represent where the cladding dimensions exist; (right) Monitor of power proportion within the core.

As can be seen, a significant proportion of power exits the fibre core and fails to return. This is largely due to the short taper length of 2 mm but is also in part due to the final taper diameters chosen, i.e., $125 \rightarrow 37.5 \rightarrow 12.5 \mu\text{m}$ (cladding dimensions). Simulation results suggest that reducing the fibre diameter by equal proportions in each taper step is inefficient, where the design is instead improved by implementing an initial taper which greatly reduces the fibre diameter and a second taper which gradually reduces the fibre diameter. Figure 6.6 shows the simulation results of the improved fibre taper design.

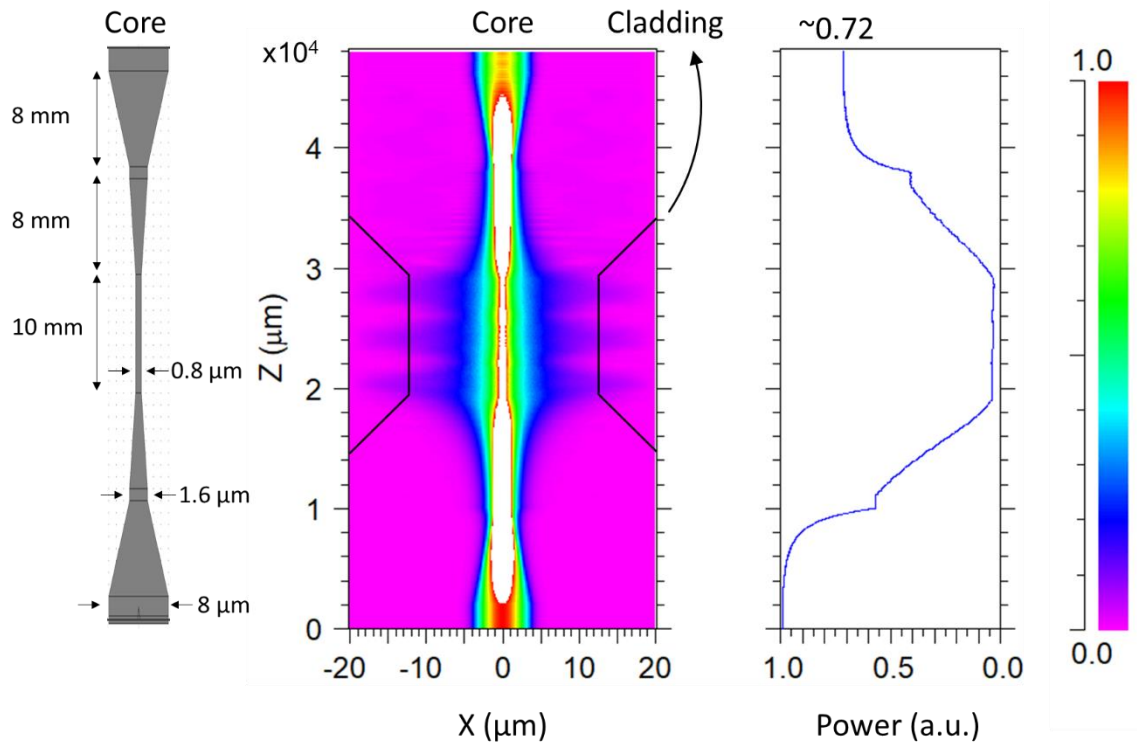


Figure 6.6: Simulation results of optimal fibre taper design given the defined practical limitations. (left) Model of fibre core with corresponding taper dimensions; (middle) Visualisation of the power distribution across the modelled fibre length, where black lines are used for reference to represent where the cladding dimensions exist; (right) Monitor of power proportion within the core.

Although this taper design offers an improvement over that shown in Figure 6.5, the amount of light that reaches the cladding boundary is very small, and therefore the amount of light that would penetrate the cladding into the surrounding air will be insignificant for absorption spectroscopy purposes. It is unclear whether cascading tapered fibres to increase the absorption length would be viable – simulation results indicate that ~72% of the signal is retained after the tapered region, suggesting that the signal loss with each pass of the tapered region may have a significant impact on the detectability of absorption. Possible additional fibre processing approaches to improve the tapered fibre's applicability in absorption spectroscopy are discussed in the next section.

6.3.3 Discussion of limitations

There are various processes that can be applied to optical fibre to improve its absorption spectroscopy performance with regards to the generation of evanescent waves and its

interaction with an absorbing species. Predominantly, such processes consist of modifications to the cladding layer, either by removing it entirely or by replacing it with a chemically sensitive coating to enhance the measurement sensitivity [128].

The removal of the cladding layer can be achieved by mechanical means [129] or by chemical etching [130] (e.g., with a HF solution [127]). Examples exist where, after the cladding has been removed, bending the fibre in the sensing region to form a “U-shape” (the region in which the cladding has been removed) facilitates increased EW generation and interaction with the surrounding analyte [127] [131]. It is not uncommon for U-shaped EW sensors to utilise plastic fibres [128]. Although U-shaped EW sensors which use single-mode fibres have been fabricated, results indicate poorer performance in comparison to multimode fibre [132].

Examples also exist where a mixed oxide coating has been implemented as a modified cladding layer (e.g., Al doped zinc oxide for the detection of methanol gas, palladium supported tungsten oxide for the detection of hydrogen gas, etc.) [129] [133] [134]. Other coating substances such as TSPP* and PAH† have also been used [135].

Applying the concept of U-shaped sensors to the fibre taper simulated earlier is unlikely to yield any benefits to the potential measurement outcome: Although it would likely result in increased EW generation and interaction with the analyte, it will also likely result in increased unguided light and lossy modes (to varying amounts depending on the bend radius applied). The use of plastic fibres (whose core diameter can be close to 1 mm) can alleviate this [136]. Within the context of the application this thesis covers, which includes remote monitoring, the increased signal attenuation experienced by plastic fibres [137] is undesired.

Regarding the various coating substances used, there is a lack in published information regarding the radiation effects that may take place and the implications this may have on sensor functionality with time. Coupled with the extensive chemical processes that are often involved with preparing such sensors (e.g., HF etching), it was deemed that the additional steps required to further progress with the tapered fibre outlined in § 6.3.1 and § 6.3.2 to obtain a sufficiently sensitive gas sensor are outside the scope of work conducted in this thesis.

* Tetrakis-(4-sulfophenyl) porphine

† Poly(allylamine hydrochloride)

6.4 Incoherent broadband cavity-enhanced absorption spectroscopy

In order to establish the capability of detecting trace gases with high sensitivity in the parts per million (ppm) regime and beyond, it is important to maximise the detectable absorbance of the substance while minimising its concentration. Referring to equation (6.5), given that the absorption cross-section is defined by the absorbing substance, sufficient absorbance at low concentrations can be achieved by increasing the absorption length. This can be done in a number of ways, the most rudimentary of which is to simply increase the physical path length, i.e., increase the length of the container within which there is the absorbing substance. There are, however, very obvious practical limitations with this approach, as absorption lengths beyond many metres are often required (on occasion hundreds of metres [138] and even kilometres [139]). Therefore, methods for increasing the *optical* path length are implemented while maintaining comparatively small physical dimensions. One such method investigated here involves the use of high reflectivity mirrors that form an optical cavity where light injected into the cavity reflects back-and-forth many times, interacting with the analyte with each pass. A number of such multi-pass cells have been developed which utilise laser sources, some of the most well-known of which are reported in the literature [85] [86] [140].

In applications where several gas species are to be monitored, or species with broad absorption spectra are to be detected, methods which cover a wide spectral absorption region are necessary. By using an incoherent broadband (white) light source, the amount of absorption that occurs across a range of wavelengths can be determined by spectrally dispersing the emission either before or after passing the sample, in turn identifying the analyte. This method is generally known as incoherent broadband cavity-enhanced absorption spectroscopy (IBBCEAS) [138] [139] [141] [142].

6.4.1 *Mathematical model*

The detection of absorption in IBBCEAS configurations is intensity dependant and is fundamentally based on the superposition principle [27]. The broadband incoherent white light used in IBBCEAS is treated as an infinite series of Gaussian beams, unlike that of a coherent laser beam which is described by a single Gaussian beam. It is therefore impossible to establish excitation of a single mode within an optical cavity, where the white light instead excites many transverse electromagnetic modes (TEM). The

transmitted light from the cavity therefore represents a superposition of the many excited modes.

Consider a stable optical cavity of length d (illustrated in Figure 6.7), formed by two mirrors with reflectivity R_1 and R_2 , continuously excited by an incoherent source with incident light intensity I_{in} (specific cavity design considerations are covered in § 6.4.3).

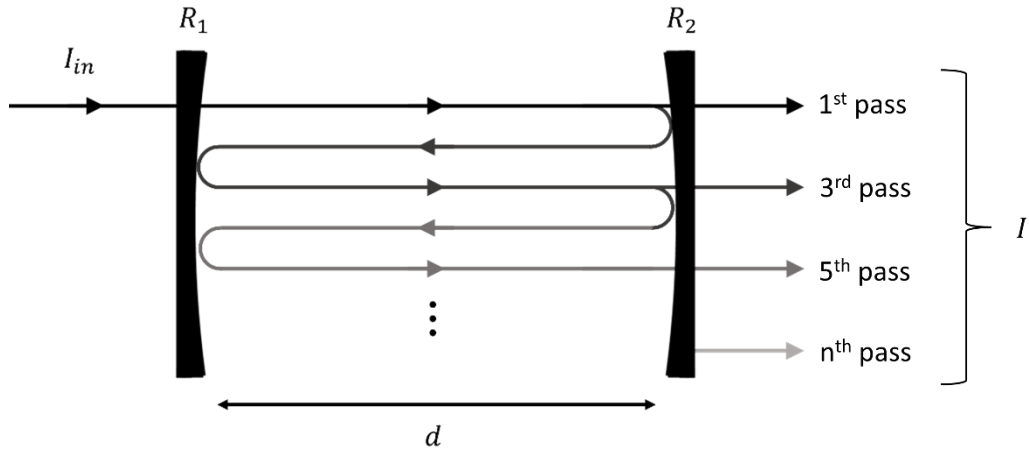


Figure 6.7: Optical cavity of length d formed by mirrors with reflectivity R_1 and R_2 continuously excited by incoherent white light of intensity I_{in} . Light propagation is illustrated by offset beams for clarity.

It is assumed that other than the losses due to imperfect mirrors, $1 - R$, there are additional losses per pass due to the interaction with the absorbing gas species, $1 - L$. An expression for the transmitted light intensity, I , can therefore be derived from the infinite sum which arises from the superposition of the light after an odd number of passes [141]:

$$\begin{aligned}
 I &= I_{in}(1 - R)(1 - L)(1 - R) + && 1^{\text{st}} \text{ pass} \\
 &I_{in}(1 - R)(1 - L)R(1 - L)R(1 - L)(1 - R) + \dots + && 3^{\text{rd}} \text{ pass} \\
 &I_{in}(1 - R)^2R^{2n}(1 - L)^{2n+1} + \dots && n^{\text{th}} \text{ pass} \\
 &= I_{in}(1 - R)^2(1 - L) \sum_{n=0}^{\infty} R^{2n}(1 - L)^{2n}, && (6.8)
 \end{aligned}$$

where $R = \sqrt{R_1R_2}$. Since $R < 1$ and $L < 1$, equation (6.8) converges to:

$$I = I_{in} \frac{(1 - R)^2(1 - L)}{1 - R^2(1 - L)^2} \quad (6.9)$$

For an empty cavity (i.e., where $L = 0$), the reference transmitted intensity, I_0 , is given by:

$$I_0 = I_{in} \frac{1 - R}{1 + R} \quad (6.10)$$

The ratio of intensities without and with the absorbing gas species can therefore be defined as:

$$\frac{I_0}{I} = \frac{1 - R^2(1 - L)^2}{(1 - R^2)(1 - L)}, \quad (6.11)$$

where equation (6.11) can be rearranged in terms of the losses per pass to give:

$$(1 - L) = \frac{+}{(-)} \sqrt{\frac{1}{4} \left(\frac{I_0(1 - R^2)}{I} \right)^2 + \frac{1}{R^2} - \frac{1}{2} \frac{I_0(1 - R)^2}{I R^2}}. \quad (6.12)$$

Continuing with the assumption made earlier that the losses per pass are due to the absorption of the gas species, i.e., Lambert-Beer absorption where $(1 - L) = e^{-\alpha d}$, the absorption coefficient, α , can be written as:

$$\alpha = \frac{1}{d} \left| \ln \left(\frac{1}{2R^2} \left(\sqrt{4R^2 + \left(\frac{I_0}{I} (R^2 - 1) \right)^2} + \frac{I_0}{I} (R^2 - 1) \right) \right) \right|. \quad (6.13)$$

For high reflectivities and small losses per pass ($R \rightarrow 1$ and $L \rightarrow 0$), equation (6.13) can be approximated to [141]:

$$\alpha \approx \frac{1}{d} \left(\frac{I_0}{I} - 1 \right) (1 - R). \quad (6.14)$$

The sensitivity obtained from IBBCEAS can be compared to the single-pass absorption spectroscopy equivalent, where the single-pass configuration is represented when $R = 0$. This allows for the minimum detectable absorption coefficient, α_{min} , to be expressed for both single-pass absorption spectroscopy and IBBCEAS:

$$\alpha_{min, single} = \frac{1}{d} \left(\frac{I_{0, single}}{I_{min, single}} - 1 \right) \quad (6.15a)$$

$$\alpha_{min} = \frac{1}{d} \left(\frac{I_0}{I_{min}} - 1 \right) (1 - R), \quad (6.15b)$$

where $I_{min, single}$ and I_{min} are the minimum detectable intensities for single-pass and IBBCEAS respectively. This demonstrates that the IBBCEAS method provides a sensitivity (or effective path length) enhancement factor of $(1 - R)^{-1}$ compared to the single-pass absorption spectroscopy equivalent. The signal-to-noise ratio (SNR), however, experiences an improvement of $\sqrt{(2(1 - R))^{-1}}$ [143]. For example, using mirrors with 99.9% reflectivity results in a maximum SNR enhancement factor of ~22 compared to a single-pass experiment.

Further comprehensive studies on IBBCEAS can be found in [138] [141] [144], where the implications of certain approximations used above are explored and comparisons between different methods are elaborated.

6.4.2 Modelled absorption of NO₂

One particular gas of interest to AWE for detection is nitrogen dioxide (NO₂). The amount of absorption that may take place can be modelled using the governing equations outlined in the previous section (§ 6.4.1) given that the reference spectrum, I_0 , and the absorption cross-section, σ , are known. The absorption cross-section of various absorbing substances, including that of NO₂, can be found from literature [145] and from the HITRAN database [146]. Figure 6.8 shows the absorption cross-section for NO₂ within a wavelength range of 250-650 nm at room temperature (21 °C).

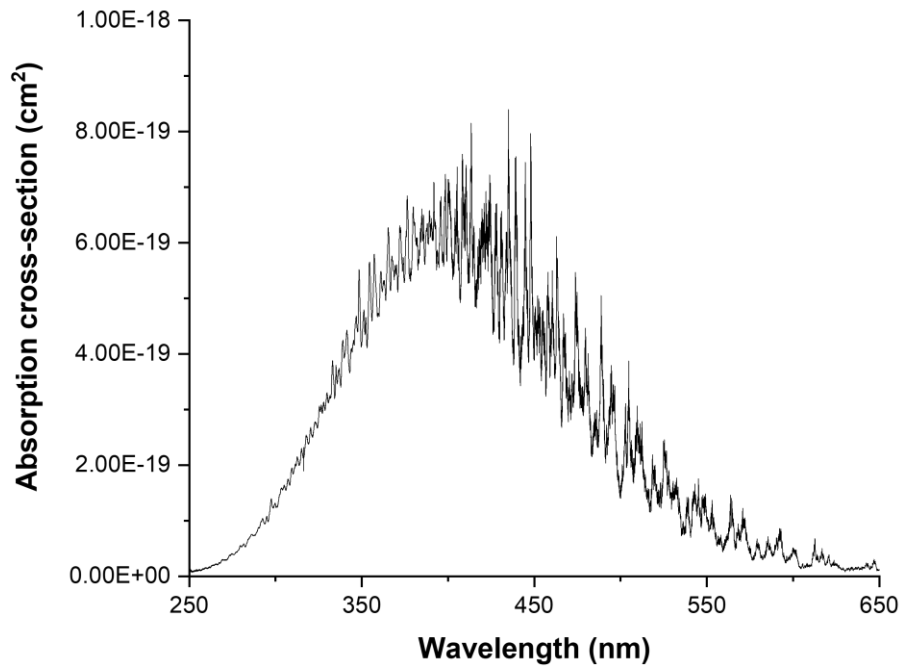


Figure 6.8: Absorption cross-section of NO_2 obtained from the HITRAN Database [146] at atmospheric pressure and a temperature of 21°C between wavelengths 250 – 650 nm.

From here, there are certain aspects of the IBBCEAS design that need to be considered. It has been established in § 6.4.1 that high reflectivity mirrors (>99% reflectivity) are desired for a distinct enhancement factor compared to a single-pass equivalent. From Figure 6.8, it can be seen that the wavelength range that corresponds to the largest absorption cross-section for NO_2 is ~350-450 nm – mirrors that are highly reflective at least within this range are therefore optimal. A preliminary reference signal is acquired from a laser-driven light source (LDLS) at atmospheric pressure in the absence of NO_2 . The details regarding the experimental equipment used are covered in § 6.4.4.

It is desired to evaluate whether NO_2 gas balanced in nitrogen (N_2) with a 5 ppm concentration is suitable for experimentation with 99% reflectivity mirrors. As specified by the suppliers (BOC Ltd), a 10 litre water capacity cylinder at a nominal pressure of 200 bar at 15°C will have a contents volume (i.e., 5 ppm NO_2 bal. N_2) of 1.89 m^3 . It is important to note that there is a distinction between ppm (parts per million) and ppmv (parts per million by volume), where ppm represents a molar ratio such that in this case, $\eta_{\text{NO}_2}/\eta_{\text{total}} = 5 \times 10^{-6}$, where η is the number of moles. Given these parameters, the concentration of NO_2 (in units of molecules per cm^3) can be determined by first calculating η_{NO_2} using the ideal gas law (given in equation (6.16)), calculating the number

of molecules by multiplying η_{NO_2} with Avogadro's constant ($N_A = 6.022 \times 10^{23} \text{ mol}^{-1}$ [147]), the product of which is then divided by the contents volume of the gas cylinder:

$$\eta_{NO_2} = 5 \times 10^{-6} \frac{PV}{\mathcal{R}T}, \quad (6.16)$$

where P and V are the gas cylinder pressure and volume at temperature T , and \mathcal{R} is the universal gas constant.

Although there is a small discrepancy with the temperature at which the absorption cross section is defined (21 °C) and the temperature that is provided in the gas cylinder specification (15 °C), this discrepancy is considered insignificant with regards to the conclusions that can yet be drawn from the modelled absorption spectrum.

With the absorption cross-section defined, the reference signal acquired, and the analyte concentration determined, Table 6.1 outlines the steps undertaken to model the corresponding absorption that would occur in the presence of 5 ppm NO₂ with an absorption length (or gas container length, also known as gas cell length) of 15 cm and mirror reflectivities of 99%.

Table 6.1: Steps for modelling the absorption of 5 ppm NO₂ at atmospheric pressure and a room temperature of 21 °C, with a gas cell length of 15 cm, and mirror reflectivities of 99%.

-
- 1) Determine the absorbance, A , by equation (6.4)
 - 2) Determine the transmittance, where $T = \frac{1}{10^A}$
 - 3) Determine the corresponding loss introduced by the analyte, where $L = 1 - T$
 - 4) Determine the transmitted intensity, I , by equation (6.11)
-

Modelling the absorption across the wavelength range of interest (350-450 nm) results in the absorption spectrum shown in Figure 6.9.

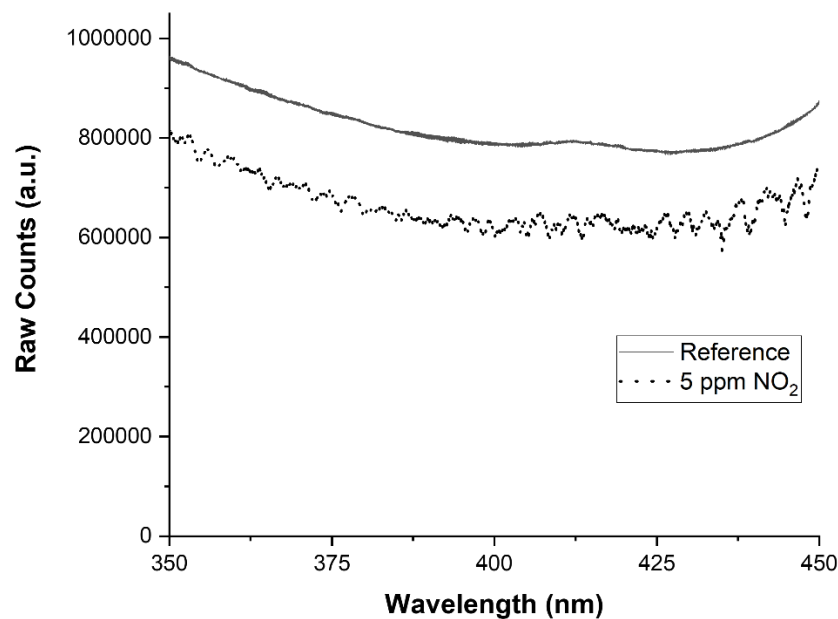


Figure 6.9: Modelled absorption spectrum for 5 ppm NO_2 using IBBCEAS governing equations with mirror reflectivities of 99% and a gas cell length of 15 cm.

As can be seen, this configuration results in distinguishable absorption compared to the reference signal. Note that this assumes that the only source of loss arises from the absorption between the interaction of the incident light and the analyte. Practically speaking, there are likely to be other sources of loss, such as scattering of the sample, scattering due to mirror/window imperfections (dust, scratches, etc.), and absorption of the mirrors/windows [143]. These may vary depending on the specific configuration but are inherently accounted for by the reference measurement.

If, for example, the modelled dataset presented in Figure 6.9 instead represented an experimental dataset and the analyte in question was of an unknown substance and quantity, the absorption coefficient information could be extracted (as shown in Figure 6.10) and compared to literature to identify the analyte.

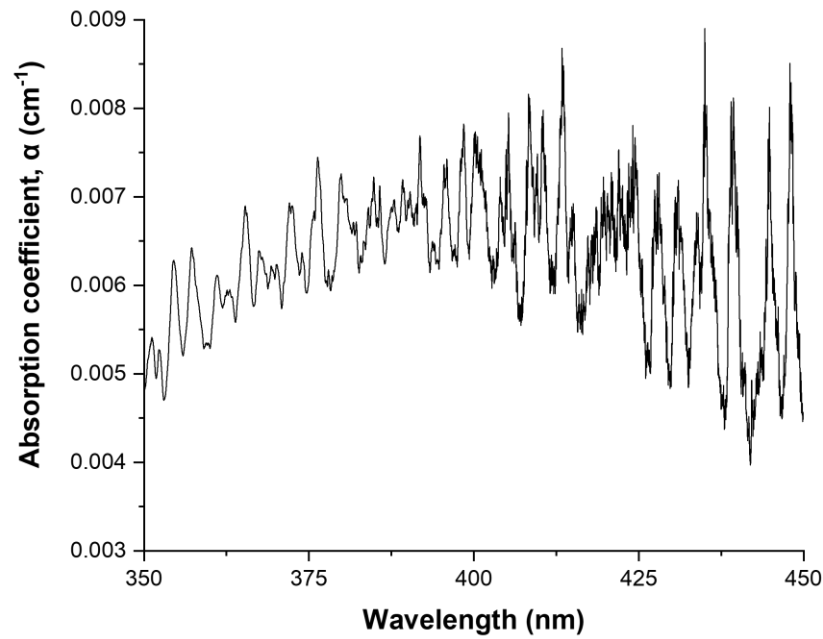


Figure 6.10: Absorption coefficient of modelled absorption shown in Figure 6.9.

6.4.3 Cavity design considerations

One of the primary cavity design aspects to consider is the cavity stability. A cavity is considered unstable when the light confined within the cavity eventually escapes beyond the dimensions of the cavity mirrors and is lost. This is also commonly referred to as “walk-off”. The condition for stability to be established for a two-mirror cavity is defined by the mirror radii of curvature (ROC), r_1 and r_2 , and the mirror separation distance, d . By means of ray transfer matrix analysis, the stability criterion is given by [148]:

$$0 \leq g_1 g_2 \leq 1 \quad (6.16a)$$

$$g_1 = 1 - \frac{d}{r_1}, \quad g_2 = 1 - \frac{d}{r_2}. \quad (6.16b)$$

Plotting g_1 against g_2 results in a stability diagram shown in Figure 6.11.

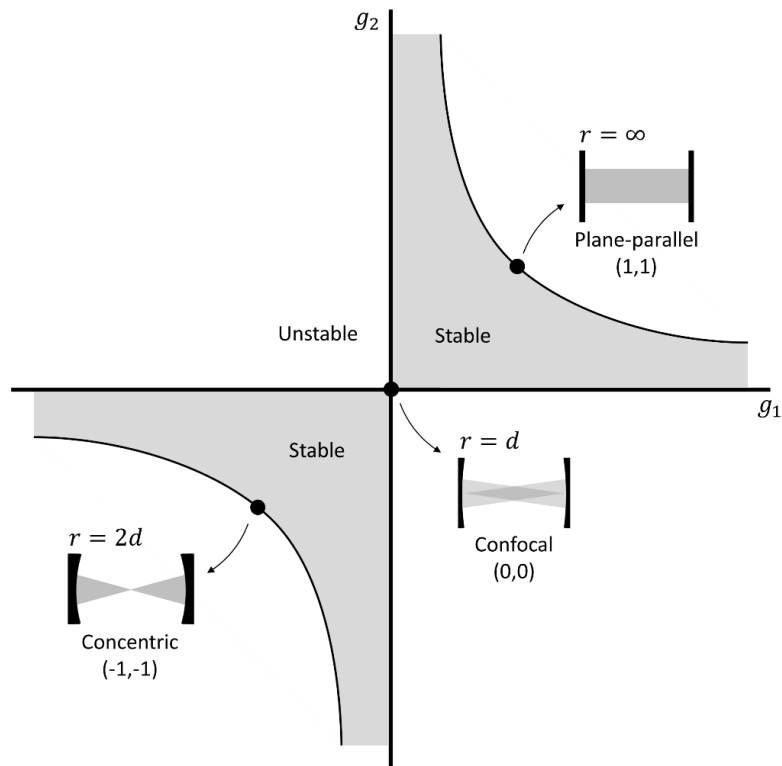


Figure 6.11: Stability diagram for optical cavities. The shaded region represents the cavity parameters which fulfil the stability criterion.

A plane-parallel cavity configuration may be desirable for IBBCEAS for a number of reasons. Lateral alignment of the mirrors to one another is not required as long as the confined light is fully reflected by each mirror surface. Similarly, longitudinal alignment is not required (i.e., the spacing between the mirrors is not limited by the ROC). Not only does this imply that the cavity alignment process may be simpler (as there are fewer degrees of freedom to consider), but specifically in the context of gas sensing, this implies that the absorption length (or gas cell length) is not limited by the dimensions of the mirrors. In a practical sense, however, achieving a stable cavity with a plane-parallel configuration is challenging; the incident beam must be perfectly collimated and the mirrors must be perfectly angularly aligned to one another. The challenge of this becomes especially significant when optical path lengths of >100 m are required.

When spherical mirrors are considered, the focal length is given by $f_m = r/2$. When the cavity-confined light is reflected by each spherical mirror, it is imaged with each pass over and over again. From each of these passes, a small amount of light is transmitted by the second mirror and imaged by a lens. Each instance of light reflection within the cavity may not necessarily be imaged on the same plane, resulting in a defocussed intensity distribution. The only configuration where this is not true is the symmetric confocal

cavity, where $r = d$ [149]. Therefore, the symmetric confocal cavity is adopted for IBBCEAS such that the light transmitted through the second cavity mirror is consistently imaged at the same plane with each round trip. The significance of this is revealed in § 6.4.4 where the mechanism for spectral dispersion is discussed.

In § 6.4.2, a gas cell length of 15 cm is used for modelling the absorption given a defined set of parameters. The optical cavity can be of a different length to that of the gas cell: this is only possible where the gas cell is shorter such that it fits between the cavity mirrors. Generally speaking, there are a number of benefits to such a configuration. Firstly, given that the mirror reflectivities are dependent on the refractive index of the medium within which they are present, if the gas cell is bound by the cavity length, then acquiring measurements without and with the analyte may undesirably change the effective reflectivity of each mirror that forms the cavity. Admittedly, this effect is likely inconsequential for very low concentration gases but can be significant if the analyte is a liquid [143]. Secondly, designing the cavity to be hermetically sealed while allowing access to mirror alignment controls introduces many engineering challenges which can be simply avoided by implementing a gas cell sealed by windows independent from the cavity mirrors. Lastly, alignment of the mirror optics can be achieved with greater precision the further away from each other they are, therefore allowing the procurement of mirrors with the appropriate ROC that accommodates this benefit.

Zemax OpticStudio is used to simulate the IBBEAS optics which consist of cavity mirrors, gas cell windows, and lenses which focus light in and out of the cavity (see Figure 6.12).

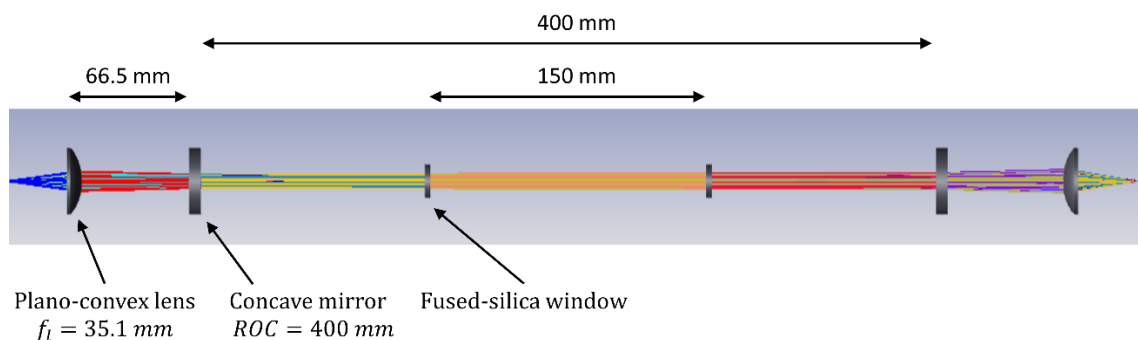


Figure 6.12: Zemax simulation of IBBCEAS optics in a symmetrical configuration consisting of two plano-convex lenses with focal lengths, f_l , of 35.1 mm, two concave mirrors with ROC of 400 mm, and two flat fused-silica windows which form the gas cell.

By means of simulation, the alignment tolerances on the system optics can be estimated. Non-sequential mode is used so that many reflections within the cavity can be realised in the simulation. By introducing misalignment in the form of lateral and tilt misalignment of the first lens and then the first mirror, alignment tolerances can be determined by observing the subsequent beam trajectory. An example of this is shown in Figure 6.13, where a tilt misalignment of 1° is introduced to the first mirror, resulting in a cavity that is unstable. Note that the gas cell windows are removed for simplicity and improved clarity.

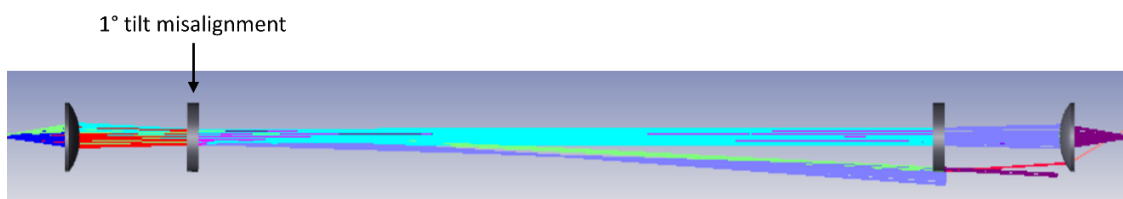


Figure 6.13: Zemax simulation of alignment optics where a 1° tilt misalignment is introduced to the first cavity mirror, resulting in an unstable cavity (gas cell windows removed for clarity).

Repeating this process generates the estimates for alignment tolerance outlined in Table 6.2.

Table 6.2: Estimated alignment tolerances for IBBCEAS optics based on Zemax simulation.

| | Lens | Mirror |
|----------------------|--------------|----------|
| Lateral misalignment | 0.1 – 0.2 mm | 1 – 2 mm |
| Tilt misalignment | 1 – 2° | 0.5 – 1° |

From this, it can be seen that lateral alignment of the lenses require greater precision than that of the mirrors, and tilt alignment of the mirrors require greater precision than that of the lenses.

6.4.4 Experimental configuration

The gas cell design is shown in Figure 6.14, and the collective configuration used for IBBCEAS is shown in Figure 6.15.

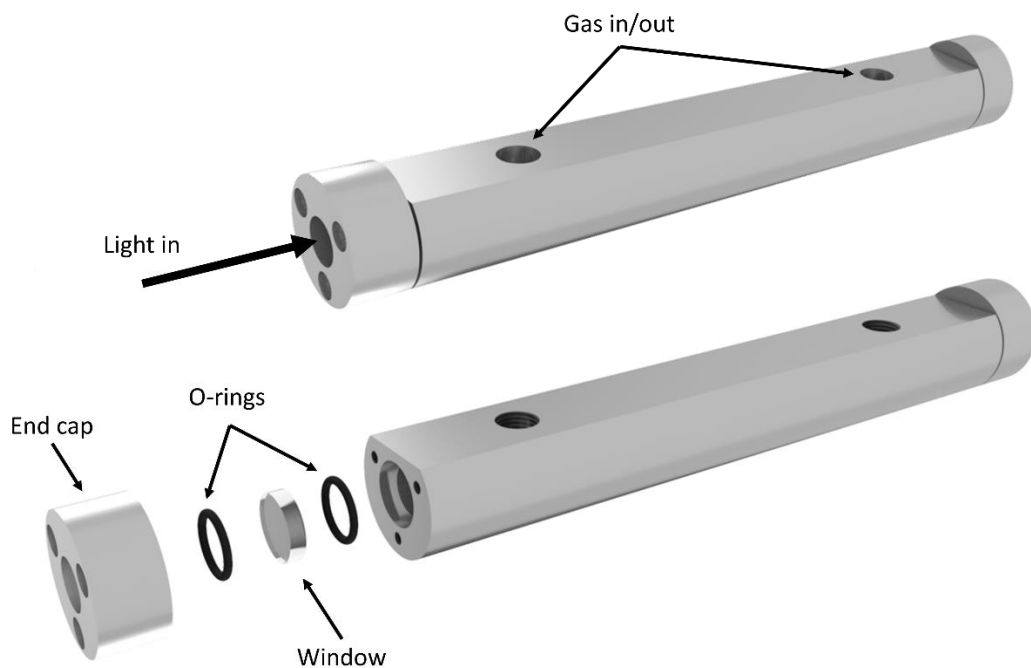


Figure 6.14: (top) Rendered model of gas cell design, (bottom) partially exploded view of gas cell model. The gas cell is comprised of an aluminium extrusion with an internal length of 150 ± 0.2 mm, where end caps are used to secure windows in place between O-rings that create an air-tight seal.

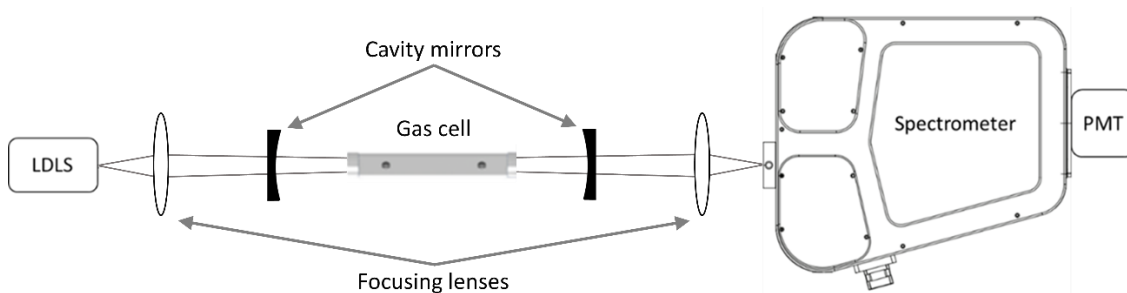


Figure 6.15: Schematic of experimental equipment used for IBBCEAS.

The light source is a laser driven light source (LDLS, EQ-99X Energetiq) which offers very high brightness across the spectrum range ($\sim 170 - 2100$ nm) and operates by delivering an infrared diode laser to a proprietary bulb to form a high intensity plasma. The light from the LDLS is then collected and imaged to the centre of the gas cell by a lens (LA4052, Thorlabs). The light transmitted through the cavity is focussed by another lens with the same specification onto the entrance slit of a spectrometer (IsoPlane SCT 320, Princeton Instruments, 320 mm focal length). Within the spectrometer, the light is incident upon a grating (2400 lines/mm, blazed at H-UV) which spectrally

disperses the light into its constituent wavelengths directed to a photomultiplier tube (PMT) detector (PD-471, Princeton Instruments). A slit width of $\sim 100 \mu\text{m}$ is used for both the entrance and exit slit which results in sufficient signal throughput and corresponds to a theoretical spectral resolution of approximately 0.04 nm at 400 nm wavelength [150]. The analyte used is a 5 ppm ($\pm 1 \text{ ppm}$) NO_2 balanced in N_2 gas mixture which is connected to the gas cell inlet and sealed under constant atmospheric pressure (i.e. no flow). The gas cell outlet is connected to tubing which safely vents outside the laboratory.

Regarding the cavity mirrors, an off-the-shelf solution is pursued. The results obtained in § 6.4.2 demonstrate that a mirror reflectivity specification of at least 99% within a wavelength range of 350-450 nm is desirable but must be less than 100% (a small amount of transmissivity is necessary for light to leak in and out of the cavity). Mirrors that meet this description are procured (#39-958, Edmund Optics) which have a ROC of 400 mm and a reflectivity of $>99.8\%$ between 350-410 nm.

6.4.5 *Experimental investigation and problem identification*

Prior to proceeding with IBBCEAS experiments, the mirror reflectivities are verified. Mirror reflectivity measurements are conducted by monitoring the spectrum across a wavelength range (in this case 300-500 nm) without and with each mirror positioned in the beam path, as illustrated in Figure 6.16. The mirror ROC is considered large enough that the transmitted beam does not divert from its original propagation significantly and is still detected entirely by the PMT, given that the path length from the mirror position and the PMT is $\sim 1.2 \text{ m}$.

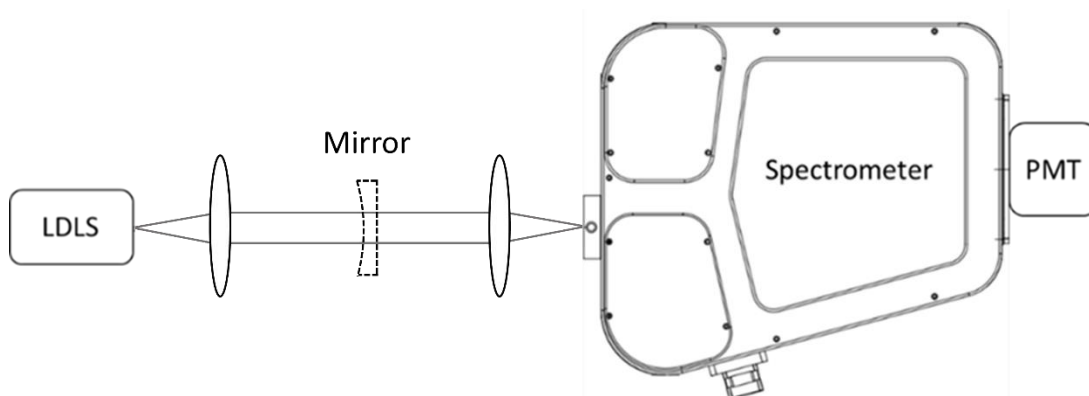


Figure 6.16: Illustration of mirror reflectivity verification measurements, where the light source spectrum across a wavelength range of 300-500 nm is monitored without and with the mirror positioned in the beam path.

A comparison between the reference signal (i.e., the spectrum measurement without the mirror) and the transmitted spectrum through each mirror can be drawn to determine the mirror reflectivities (assuming no other significant losses). Figures 6.17 and 6.18 show the spectrum measurements and the corresponding reflectivity of each mirror respectively. All measurements are acquired using a PMT drive voltage of 230 V, a time integration of 100 ms, and a scan resolution of 0.1 nm.

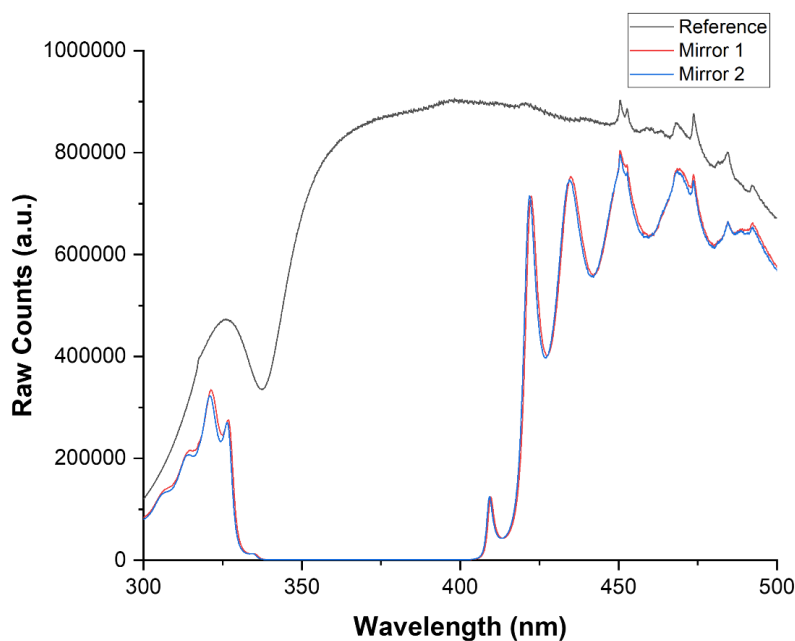


Figure 6.17: Measured spectra between 300-500 nm of the light source, where the “Reference” signal (black line) is that of the light source, and “Mirror 1” (red line) and “Mirror 2” (blue line) are that of the light source with each mirror positioned in the beam path.

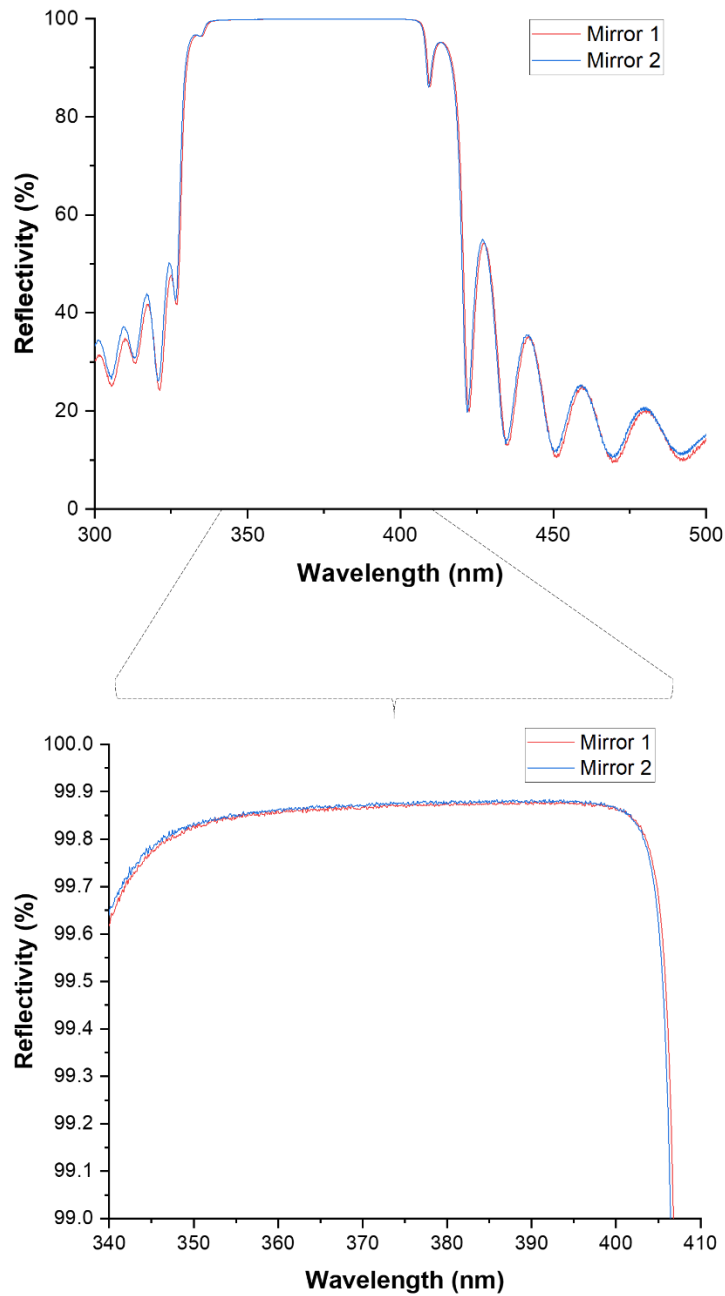


Figure 6.18: Reflectivity assessment of mirrors. (top) Reflectivity of each mirror within a wavelength range of 300-500 nm. (bottom) High reflectivity (vertical axis scaled to display 99-100%) measured within the wavelength range of interest for each mirror.

As seen in Figure 6.18, both mirrors have consistently similar reflectivities. Both mirrors demonstrate reflectivities between 99.8-99.9% across a wavelength range of 346-403 nm. The experimental procedure outlined in § 6.4.4 is undertaken, the results of which are shown in Figure 6.19.

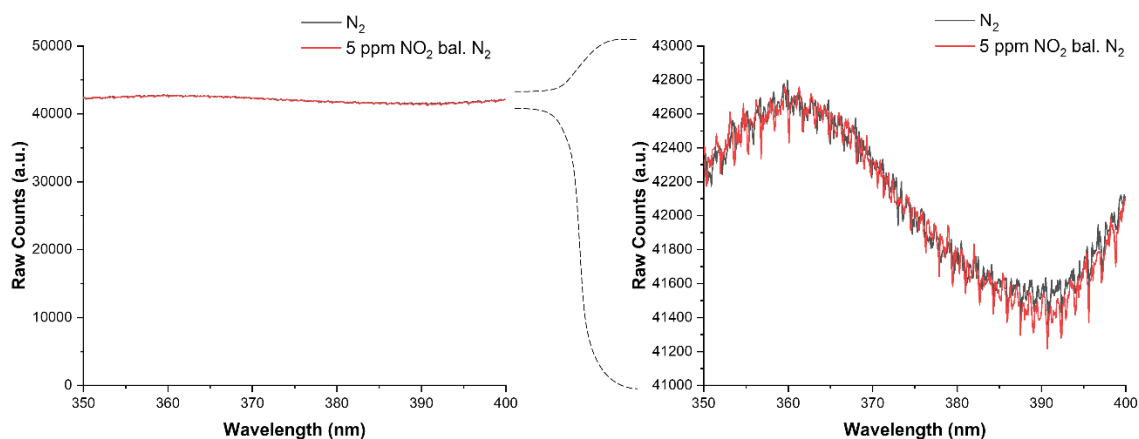


Figure 6.19: Measurement results consisting of reference signal represented by the black line (gas cell filled with N_2 at atmospheric pressure) and analyte signal represented by the red line (gas cell filled with 5 ppm NO_2 balanced in N_2 at atmospheric pressure).

It is apparent that with this configuration, no observable absorption is occurring. One possibility for what may assist with identifying the problem resides with the light which is transmitted through the mirrors outside the high reflectivity wavelength band (i.e., wavelengths up to ~ 340 nm and beyond ~ 410 nm) (see Figure 6.20). When light is incident upon the grating which disperses light within the spectrometer, the grating rotates to direct a specific wavelength towards the PMT detector (Figure 6.20(a)). All other wavelengths dispersed by the grating are directed elsewhere within the spectrometer interior and do not reach the detector by means of the interior optics. Instead, it is possible that light scatters from the interior walls to the detector (Figure 6.20(b)). The amount of light that reaches the detector in this way, compared to the main wavelength of light from the grating, is greatly insignificant. When cavity mirrors are placed in front of the spectrometer inlet (Figure 6.20(c)), the main wavelength is diminished by approximately 99.9%, whereas other wavelengths (where the mirrors are not highly reflective) are only diminished by approximately 20%. This suggests that it is possible that the scattered light from the spectrometer interior is no longer insignificant compared to the main wavelengths of light directed from the grating into the detector.

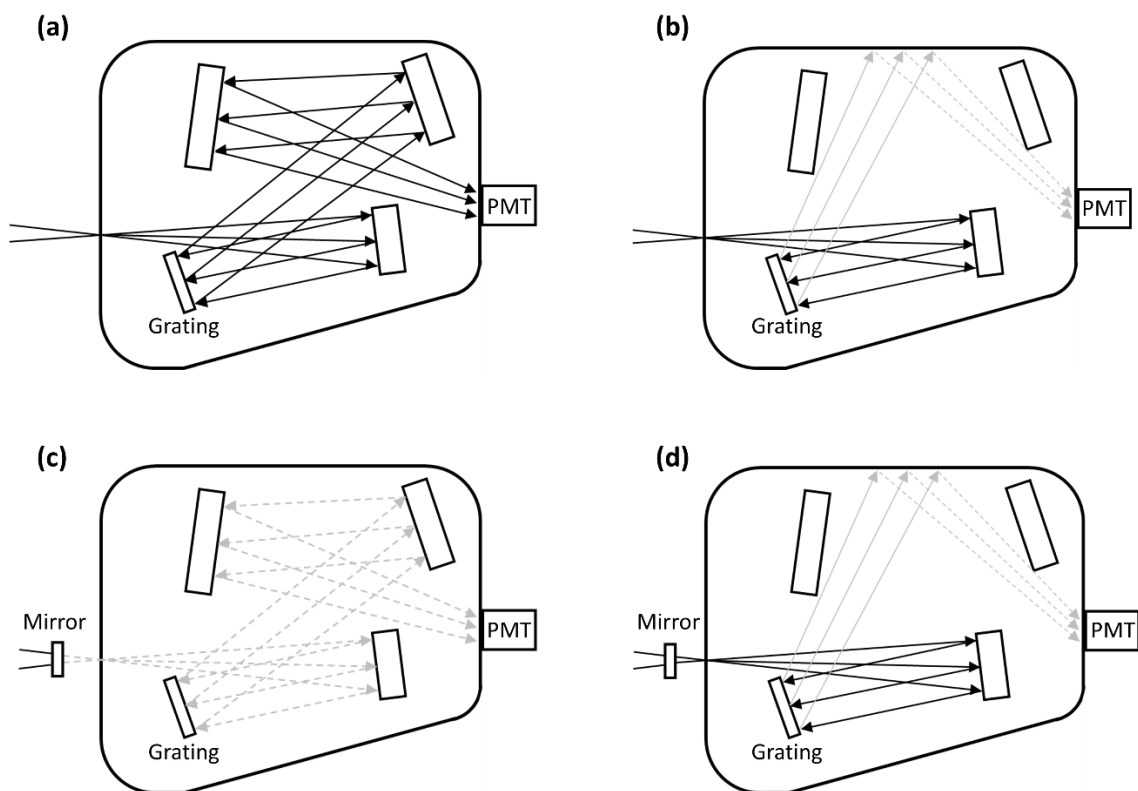


Figure 6.20: Illustration of spectrometer interior, where black solid lines represent the brightest light within the spectrometer, grey solid lines represent light which is comparatively less bright, and grey dotted lines represent the least bright light. (a) Main wavelength of light directed from the grating to the detector. (b) Wavelengths of light dispersed from the grating that scatter towards the detector. (c) Main wavelength of light directed from the grating to the detector with cavity mirrors at the spectrometer inlet. (d) Wavelengths of light dispersed from the grating that scatter towards the detector with cavity mirrors at the spectrometer inlet.

To rectify this, an optical filter (#12-096, Edmund Optics) is placed after the light source to eliminate unwanted light from entering the spectrometer. The adapted experimental configuration is shown in Figure 6.21. The bandpass filter is specified to operate at a centre wavelength of 375 nm with a 50 nm bandpass and with a transmission of >90%.

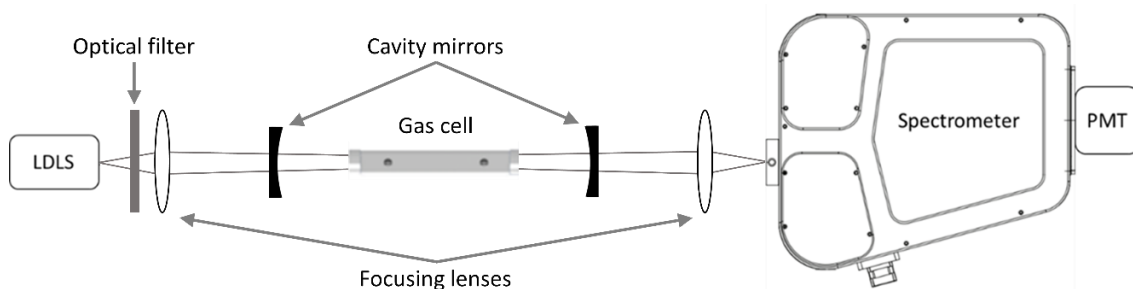


Figure 6.21: Schematic of adapted experimental configuration to include a bandpass optical filter to eliminate unwanted light from entering the spectrometer.

Given the implementation of a new optical element within the configuration, a reassessment of each mirror reflectivity is required (see Figure 6.22).

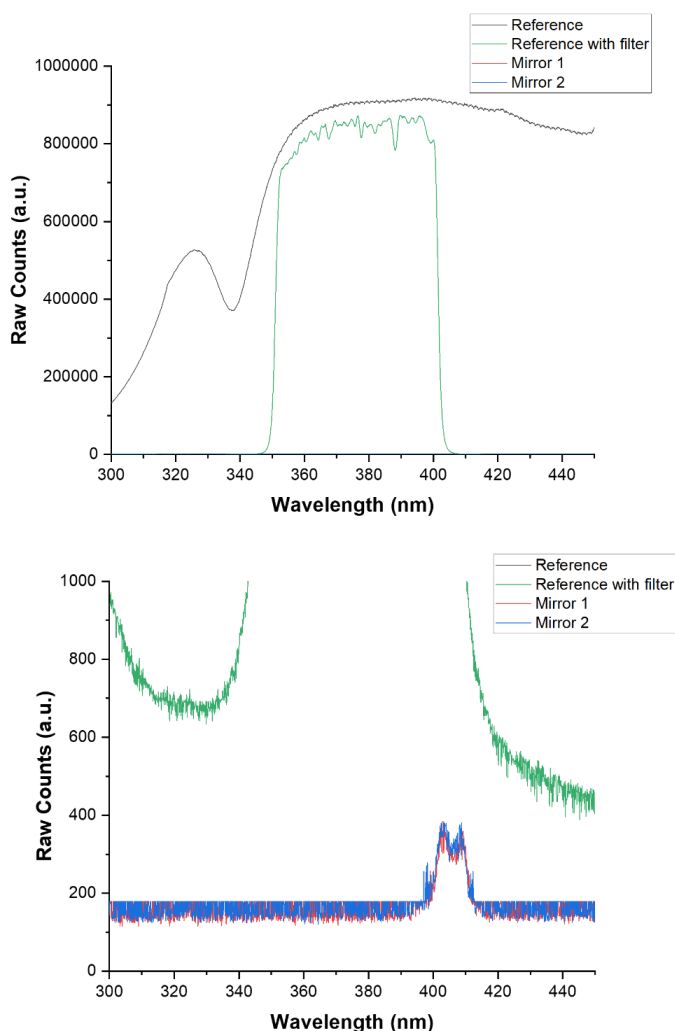


Figure 6.22: Measured spectra between 300-450 nm, where the “Reference” signal (black line) is that of the light source, “Reference with filter” is the filtered spectrum, and “Mirror 1” (red line) and “Mirror 2” (blue line) are that of the light source with each mirror positioned in the beam path.

As can be seen, there is an insufficient amount of light that leaves the optical cavity. Figure 6.22 shows that no detectable light at wavelengths of up to ~400 nm leaves the cavity – this is apparent as no change in the measurement signal is observed when the spectrometer inlet is blocked at these wavelengths. Between wavelengths of ~400-410 nm there appears to be some detectable light – this is likely to be the region where both the optical filter and mirror transmissivity is sufficiently high.

It is unclear as to why there is no detectable light within the wavelength range of interest, although it has been hypothesised. It is possible that given a mirror reflectivity of >99.8% (as per the specification provided by the seller), the remaining ~0.1-0.2% may simply fail to transmit through the fused-silica substrate – this may be due to absorption effects within the substrate and/or scattering due to surface imperfections on the reflective surface or back surface. It may also be possible that the specification provided is incorrect, and in fact the mirrors demonstrate a reflectivity much closer to 100%, rendering the mirrors incompatible with IBBCEAS. In either event, an off-the-shelf solution may not be a viable approach for consistent and reliable implementation in IBBCEAS, as such necessitating the procurement of bespoke mirrors which meet the specification requirements. Due to time limitations, further progress on this work is relinquished with the potential for future continuation.

6.5 Conclusions

The detection of certain gas species, within the framework of structural health monitoring, can assist with identifying chemical ageing processes taking place. One gas in particular that is of interest in this work is nitrogen dioxide (NO₂). Two detection approaches are investigated, both which utilise the same sensing mechanism of absorption spectroscopy: evanescent wave fibre optic sensing (EWFOS) and incoherent broadband cavity enhanced absorption spectroscopy (IBBCEAS).

The evanescent wave (EW), or evanescent field, within a standard singlemode fibre (SMF28) arises at the cladding-core interface and penetrates into the cladding material by ~2.5 μm. When a fibre is tapered down to small dimensions with a large step size (e.g. from a cladding diameter of 125 μm to 12.5 μm), this can facilitate increased evanescent wave generation that penetrates further beyond the core boundary, allowing for improved interaction with the surrounding analyte. In this work, fibres were tapered using a plasma arc-generating electrode system (Fujikura ArcMaster FSM-100P+) that draws the fibre out as it is locally heated. By this method, a fibre taper with a large step size was achieved

by implementing a two-step taper approach where the cladding diameter is first tapered from 125 μm to 50 μm , and then to 12.5 μm . The subsequent EW generation was then simulated using Synopsys BeamPROP, and the taper design was optimised. The optimal taper cladding dimensions (for SMF28 fibre) that allowed for increased EW generation while minimising signal loss was 125 \rightarrow 25 \rightarrow 12.5 μm , which resulted in a simulated signal retention per pass of $\sim 72\%$ ($\equiv 1.43$ dB loss). Results from the simulation suggested insufficient EW cladding penetration for interaction with the surrounding analyte without additional processes applied to the fibre, where such processes consist of the removal or modification of the cladding layer. These processes, however, were deemed beyond the scope of this thesis.

The IBBCEAS configuration consisted of a broadband light source imaged to the centre of a symmetric confocal cavity formed by two high reflectivity mirrors, with a gas cell (which contained NO_2) situated within it. The principle of broadband cavity enhancement is that of superposition, where there are many transverse electric modes that form within the cavity (so many that the resolvability is limited by the detector). Each round trip within the cavity therefore elicits further interaction with the analyte, increasing the absorption length. The absorption that would occur for 5 ppm NO_2 was modelled, and it was determined that mirrors with at least 99% reflectivity would yield desired results. The implications of the optical cavity design were then considered, where a symmetrical confocal cavity was decided upon. Mirrors with $>99.8\%$ reflectivity across the wavelength range of interest (as per manufacturer specification) were procured off-the-shelf, however after rigorous testing, and the implementation of an optical filter, it was discovered that insufficient light was transmitted through the cavity mirrors. Due to time limitations, the rectification of these issues was not possible. It was concluded that for successful IBBCEAS measurements, the procurement of bespoke mirrors is necessary which meet the required specification.

Chapter 7

Discussion and conclusions

7.1 Overview and discussion

In this thesis, various optical sensors have been studied and developed for structural health monitoring purposes. These include the utilisation of Fabry-Pérot interferometry (FPI) and absorption spectroscopy, the implementation of which has mostly exploited the benefits of optical fibre technology.

The health of any given structure is typically defined by its capability to preserve its design intentions and can be monitored in a number of ways. For example, chemical aging processes occur which release certain gases (i.e., outgassing) and this can be indicative of the structure's health. Mechanical deterioration (e.g., creep/cracking) is also a detrimental effect to the structure's health. These are not strictly mutually exclusive, where it is possible for the effects of outgassing to lead to the accumulation (or relaxation) of stress/strain, in turn triggering onset creep/cracking. As such, gas and distance measurement sensors by optical means have been investigated as a comprehensive solution to the structural health monitoring requirements presented here.

Distance/gap measurements have been achieved by means of fibre optic FPI sensors. A signal demodulation approach consisting of applying a fast-Fourier transform (FFT) to the reflected interference spectrum has been developed to yield cavity length information. By this method, sensor performance assessments have demonstrated measurement accuracies and sensitivities of $\pm 1.309 \mu\text{m}$ and $\pm 0.230 \mu\text{m}$ respectively. To further progress upon this, an algorithm in the form of a cavity reconstruction model, referred to as a function-fitting algorithm (FFA) in this work, has been developed which minimises signal noise and improves accuracy. Sensor performance assessments using the FFA have demonstrated measurement accuracies and sensitivities of $\pm 0.021 \mu\text{m}$ and

$\pm 0.004 \mu\text{m}$ respectively. The sensor also demonstrated capabilities of measuring up to a range of approximately 20 mm. The FFA implemented in this work is computationally intensive, where approximately over 25,000,000 data operations occur per second (excluding the processes required for the FFT). The hardware used in this work had the computational capacity to operate two such FFAs simultaneously. In the event where multiplexing to create an array of sensors is desired, the corresponding computational requirements must also be considered.

It is ultimately desired to not simply measure the distance between a target surface and the fibre, but the total absolute distance between two target surfaces parallel to one another. This has been achieved by utilising novel multi-core fibre (MCF), where turning mirrors (i.e., 45° angled facets) have been fabricated on two cores of the MCF which redirect the fibre-guided light perpendicular to the fibre axis in opposite directions. In this way, Fabry-Pérot cavities form on both sides of the MCF: with a known core spacing, the total gap between two surfaces is determinable. Three turning mirror fabrication approaches have been investigated: (i) focused-ion beam (FIB) milling; (ii) laser inscribing the turning mirror features on the MCF cores followed by chemical etching; and (iii) laser inscribing and chemical etching to produce a fused-silica component which is then attached to the fibre. Sensors (i) and (iii) consisted of MCF with a circular cross-section, and sensor (ii) consisted of MCF with a clover-shaped cross-section. This was due to fibre compatibility issues with the chemical etching process and limited access to readily available fibre (i.e., circular MCF was desired due to its conventional shape but no alternative with the same cross-sectional shape was readily available). All three approaches resulted in sensors which performed similarly, where accuracies and sensitivities of around $\pm 0.050 \mu\text{m}$ and $\pm 0.006 \mu\text{m}$ respectively have been demonstrated. Where the sensors differ mostly is with regards to the upper range at which they can continue to accurately measure distance, where the FIB milled sensor (sensor (i)) is capable of measuring up to ~ 16 mm, and the chemically etched sensors are capable of measuring up to distances of ~ 7.5 mm (sensor (ii)) and ~ 14 mm (sensor (iii)). It must be noted that the sample size for making a generalised assessment on the efficacy of each fabrication process is small, and therefore repeat fabrications of each sensor may yield different performance results. However, there are parameters which strongly suggest viable reasons for the diminished measurement ranges experienced by the chemically etched sensors. Firstly, sensor (ii) implements a clover-shaped MCF which elicits increased splice loss in comparison to the circular MCF. Secondly, the chemical etching process appears to result in a rougher surface finish, which promotes increased optical

losses due to scatter. These compounded losses are believed to have caused the diminished measurement ranges presented. The surface profile of the target surface is also important in this regard, where a rough surface finish of the target will scatter light away from the sensor, resulting in further diminished measurable range. In applications where the sensors are to be deployed in environments where their outermost measurement ranges will be required, a prerequisite will be that the target surfaces are first prepared by polishing to a mirror finish or coated appropriately. In the following section, methods to further develop and improve the sensors fabricated by chemical etching are considered.

Following from the single-point measurement devices, a two-point measurement device has been developed based on the laser inscribed and chemically etched fused-silica component design. The expansion to a two-point measurement system has been achieved by designing the fused-silica chip to incorporate two fibres that are laterally offset from one another. By means of differential FPI, where the fibre spacing within the sensor element collective is known, the tilt measurement of a target surface has been established. Where a standard silver mirror has been used as the target surface, tilt sensor performance assessments have resulted in an accuracy and sensitivity of $\pm 13.8 \times 10^{-6} \text{ }^\circ$ and $\pm 7.6 \times 10^{-6} \text{ }^\circ$ respectively, with a measurement range of $\pm 0.1 \text{ }^\circ$. There is likely a dependency on the target surface material profile with regards to the tilt sensor performance. At increased tilt angles, a polished reflective target surface fails to reflect incident light back towards the fibre. A surface which elicits more scattering may allow for the tilt sensor to operate at comparatively larger tilt angles, as long as the reflected signal strength is sufficient for post-processing. Better yet, the optimal configuration to maximise the tilt measurement range may consist of a retroreflecting surface. This has not been experimentally verified but may offer an avenue of investigation if further developmental work is desired. In the work conducted here, the performance assessment using a reflective surface was deemed appropriate, as the application environment is likely to consist of precision engineered and manufactured components.

Optical gas sensors for the purpose of structural health monitoring have also been investigated, where the principles of absorption spectroscopy have been primarily considered. An assessment on the viability of evanescent wave fibre optic sensors (EWFOS) has been conducted. EWFOS operates by facilitating increased evanescent wave (EW) generation by tapering the fibre to small dimensions, where the absorbing interaction that occurs with the surrounding analyte is measured by the fibre-guided spectra. After having determined practical limitations in the taper capabilities, simulation

software has been employed to evaluate optimal taper parameters and assess the amount of potential EW generation. It has been concluded that without additional fibre processing steps, the generated EW is insufficient. Such additional fibre processes consist of modifications to the cladding layer. It is unclear, however, how such cladding layer modifications may behave under the presence of ionising radiation. This concern arises due to the limited open literature in this field. It has been concluded that such an investigation is beyond the scope of the work conducted in this thesis.

Further on gas sensing, incoherent broadband cavity-enhanced absorption spectroscopy (IBBCEAS) has also been investigated. IBBCEAS operates on the principle of superposition: incoherent broadband light is coupled into an optical cavity formed by two highly reflective mirrors where, in effect, there are so many eigenmodes that the measurement resolution is ultimately limited by the resolving capabilities of the detector. The optical cavity is situated within the analyte environment such that the corresponding absorption is detectable as a drop in intensity among the broadband spectra. Given a particular experimental configuration, the absorption of NO₂ has been modelled to assess the required mirror reflectivity (>99%). After the off-the-shelf procurement of the appropriate mirrors, a flaw in the experimental design revealed the necessity of an additional optical element. After this rectification, it was further revealed that off-the-shelf mirror procurement was insufficient to meet the specific and precise specifications necessary for IBBCEAS, where a bespoke order was instead required. Due to time constraints, further investigation has been relinquished.

7.2 Future work

The work that has been conducted in this thesis has identified further avenues of investigation, where technologies presented here may be improved upon, or the developments presented here may be integrated with other technologies. Some noteworthy considerations are listed below.

7.2.1 Lens fabrication on fused-silica component

The capabilities of the laser inscription system used to fabricate the fused-silica components presented in Chapters 4 & 5 extend beyond the fabrication of linear, flat features. Similarly to how cylindrical features have been fabricated as part of the fused-silica component design (i.e., the fibre slot), spherical and parabolic features are also possible. By the implementation of more complex geometries, the divergent beam

incident on the turning mirror can be collimated upon reflection. An example of such a design is shown in Figure 7.1.

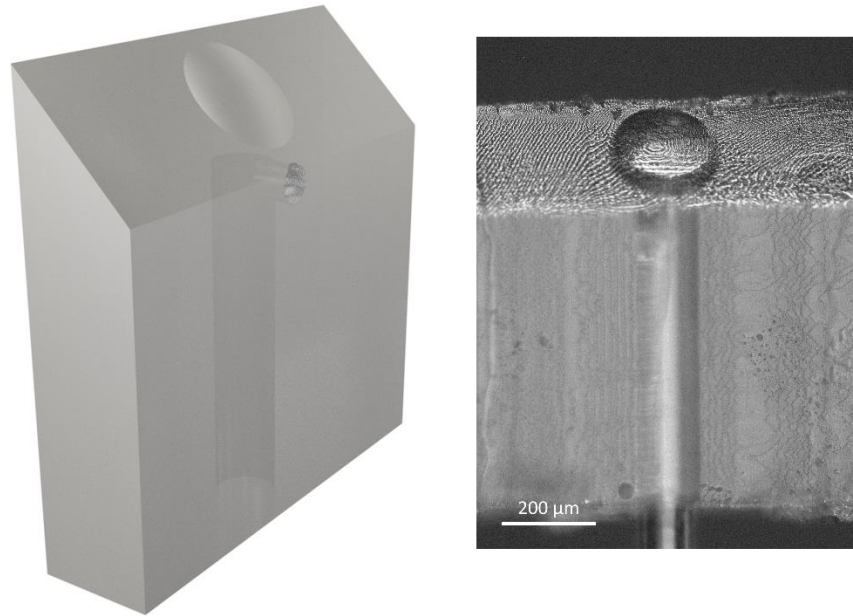


Figure 7.1: (left) Fused-silica component computer model with an exemplary lens at the turning mirror facet; (right) Microscope image of fused-silica component with an exemplary lens fabricated onto the turning mirror facet.

The implementation of a lens in this manner may carry with it certain implications which would require consideration. The angle of incidence that the divergent beam has with the lens interface will likely result in a smaller portion of light satisfying the condition for total internal reflection in comparison to the flat turning mirror design. This may subsequently call upon the necessity to apply a metallic coating to ensure all incident light is collected and reflected by the lensed turning mirror.

A collimated output beam suggests an improvement to the fibre gap sensor performance, particularly with regards to the sensor range. Where signal strength is problematic at longer distances with the existing design, a design which instead incorporates an off-axis parabolic mirror may remedy this. However, there is still the possibility that the surface roughness may be a limiting factor in what can ultimately be achieved with laser inscription and chemical etching.

7.2.2 *Flame polishing*

In order to improve the performance capabilities of the fibre gap sensors which are fabricated by chemical etching, particularly where measurement range is concerned, a mechanism to improve the facet surface finish (i.e., reduce the resultant surface roughness of the chemical etch) may be possible. Conventional methods such as mechanical polishing are not applicable due to the inaccessible geometry of the 45° angled facets on MCF. Laser polishing may be a candidate solution, but a simpler (and cheaper) method resides with flame polishing.

Flame polishing is a process whereby a material, typically a glass or thermoplastic, is exposed to a flame, resulting in the surface to temporarily melt, reform, and flatten due to surface tension as it cools and hardens [151]. To assess the viability of flame polishing on fibre, the cleaved end of a clover MCF is arbitrarily scraped against abrasive paper to introduce surface imperfections, as shown in Figure 7.2 (left). The fibre tip is then swiftly passed across the flame by hand. Figure 7.2 (right) presents the same fibre after approximately 30 swift passes.

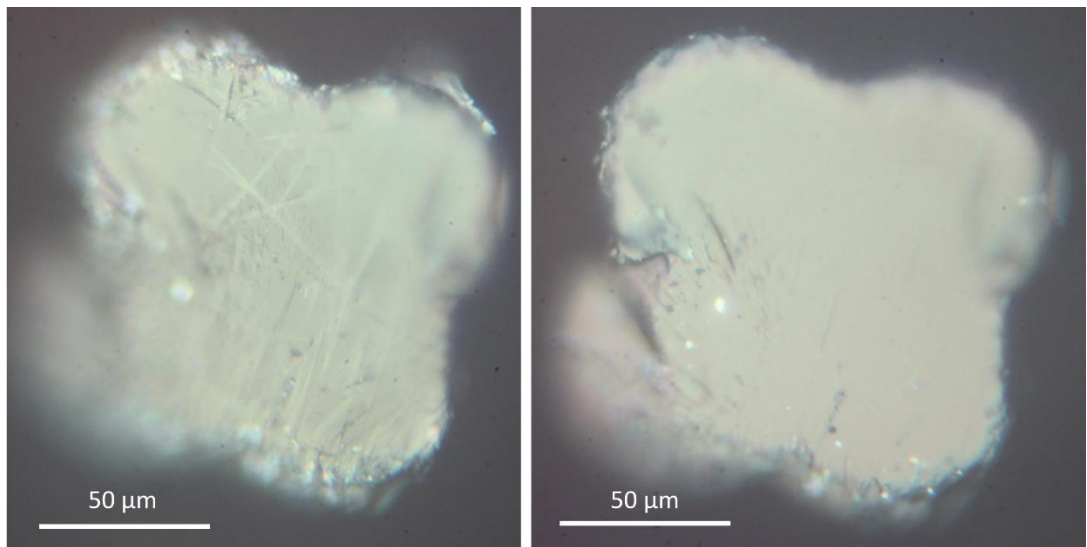


Figure 7.2: Microscope images of cleaved end of clover MCF with surface imperfections introduced by arbitrarily scraping against abrasive paper. (left) Before flame polishing, (right) after flame polishing.

As can be seen, many of the shallow surface imperfections appear to have been removed. To further assess the viability of flame polishing, a clover MCF with turning mirrors fabricated by laser inscription and chemical etching is flame polished. This sensor,

originally disregarded due to microscope images suggesting poor turning mirror fabrication, underwent laser inscription at a pulse energy of 200 nJ (c.f. 160 nJ pulse energy used for fabrication of fibre sensors presented in § 4.4.1). Red (633 nm) light is coupled into the cores of the clover MCF before and after flame polishing, where the light is then perpendicularly redirected by the turning mirrors onto a screen (see Figure 7.3).

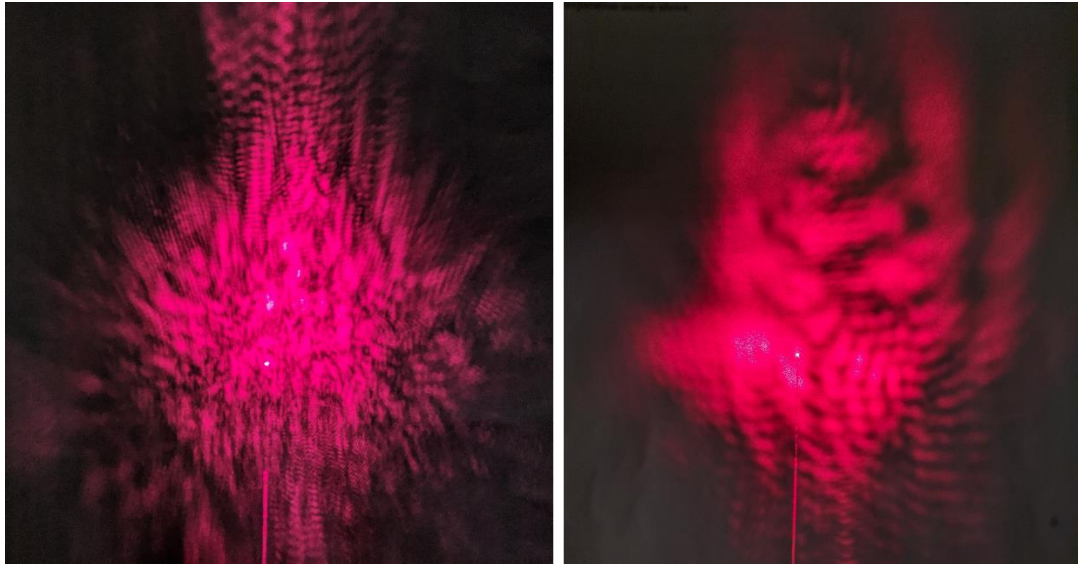


Figure 7.3: Red light directed to a screen by turning mirrors fabricated onto a clover MCF with a laser inscription pulse energy of 200 nJ. (left) Before flame polishing, (right) after flame polishing.

Note that at 633 nm wavelength, the clover MCF fibre guides multiple modes of propagation. Regardless, a qualitative assessment is still possible given the outcome presented in Figure 7.3, where the benefits of flame polishing can be observed. Care needs to be taken, however, as the fibre can easily be deformed by the gasses expelled by the flame polisher if the fibre is in the flame path for too long (no more than a few hundred milliseconds).

Further evaluation regarding the flame polishing parameters is required, along with the development of a robust and consistent configuration, after which a quantitative assessment regarding the amount of improvement introduced by flame polishing can be conducted.

7.2.3 Zeolites

Zeolites are a naturally occurring family of inorganic, crystalline minerals with unique microporous structural properties. Alongside the natural occurrence of zeolites, perhaps more importantly, the synthetic growth of zeolitic structures can facilitate the detectability of certain measurands. The porosity of zeolites, defined by the synthetic growth recipe, can establish selective molecular adsorption based on size exclusion which depends primarily on the crystalline structure [152].

Zeolites, commonly used as sieves, can also be incorporated in the detection of gases [153], where the molecular adsorption manifests some detectable effect such as a change in mass [154] or conductivity [155]. Zeolites can be synthetically grown onto optical fibre [156] and when done so, the adsorption-induced change in optical path length can be measured and correlated to a gas concentration [157]. An example of a zeolite grown on the end of a fibre to detect isopropanol vapour is shown in Figure 7.4.

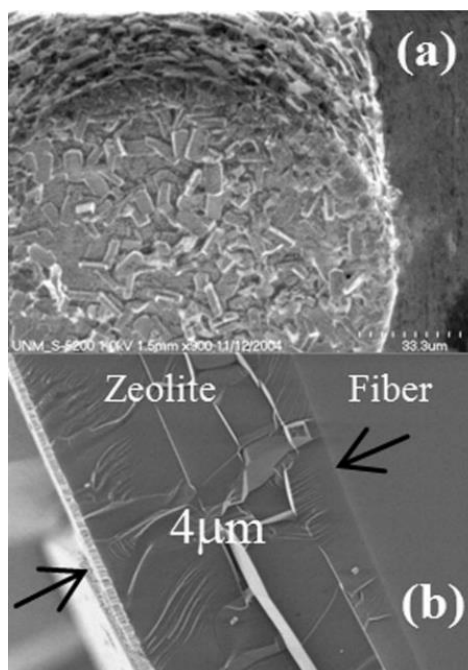


Figure 7.4: (a) Microscope image of zeolite-coated fibre; (b) Cross-section of zeolite-coated fibre to show the zeolite layer thickness. Adapted from [156].

A wide range of gas species and vapours are detectable by zeolites, such as hydrocarbons, CO, CO₂, O₂, and H₂O, to name a few, as outlined in [153]. The synthesis recipe for over 100 zeolitic materials can be found in [158]. Depending on the analyte, detection limits for zeolite-coated Fabry-Pérot fibre gas sensors have been demonstrated in the range of a

few ppm for isopropanol and toluene [159], with similar results for that of formaldehyde [160], whereas detection limits of 1000 ppm have been achieved for the detection of methanol [159]. Coupled with the Fabry-Pérot cavity demodulation techniques developed in this thesis, further progress could potentially be made in this field.

7.3 Concluding remarks

The fibre sensors developed in this thesis offer an effective solution for structural health monitoring in inaccessible systems. Fibre sensors which utilise Fabry-Pérot interferometry have been developed with high accuracy and sensitivity, the fabrication processes of which have been refined. The summary of work conducted to achieve this includes:

- Development of a function-fitting algorithm (FFA) that works in conjunction with a fast-Fourier transform (FFT) of the reflected Fabry-Pérot spectrum to determine cavity length (i.e., the gap between the fibre and the target surface). The developed FFA has been evaluated both computationally and experimentally, with results indicative of an accuracy and sensitivity improvement of approximately one-and-a-half orders of magnitude compared to using a FFT alone.
- Development of turning mirror fabrication processes to allow fibre sensor deployment into confined spaces. These include focused-ion beam (FIB) milling and ultrafast laser assisted etching (ULAE), where the latter has been used to fabricate fused-silica components which are attached to the fibre, as well as applied directly to the cleaved fibre end.
- Expansion from single-core fibres (SCF) to multi-core fibres (MCF). Fabricating outward-facing turning mirrors on two cores of a MCF allows for the total gap between parallel target surfaces to be determined.
- Expansion upon the concept of fabricating fused-silica components to allow for multiple fibres to be attached. In this manner, more information can be collected regarding the target surface as a one-point measurement system has been expanded to that of a two-point measurement system. This has resulted in a fibre sensor capable of measuring the tilt of a target surface with high accuracy and sensitivity.

The developed absolute gap sensors demonstrate measurement accuracy of around $\pm 0.050 \mu\text{m}$, resolution of $\pm 0.006 \mu\text{m}$, has external dimensions of no more than 1 mm, and

is capable of measuring distances as small as 0.1 mm up to 10's of mm. These developments have satisfied the sensor criteria outlined in § 1.4, where distance measurement accuracy and resolution in the nm regime were specified, along with sensor deployability in mm-scale spaces with measurement range capabilities from sub-mm to many mm's.

There are outstanding issues that require addressing for further optical structural health monitoring techniques investigated in this thesis to be feasible:

- Evanescent wave fibre optic sensing has been investigated where a fibre is tapered to small dimensions with the intention to facilitate increased evanescent wave generation beyond the fibre cladding. Optimised taper parameters have been developed, however further investigation is required regarding modifications to the cladding layer and the interaction this may have with ionising radiation.
- Incoherent broadband cavity-enhanced absorption spectroscopy requires very precise mirror specifications and the bespoke procurement of mirrors which meet these requirements are necessary.

References

- [1] P. Bouguer, *Essai d'optique sur la gradation de la lumiere*, Paris, 1729.
- [2] J. H. Lambert, *Photometria sive de mensura et gradibus limunus, colorum et umbrae*, Augustae Vindelicorum, sumptibus viduae Eberhardi Klett, 1760.
- [3] A. Beer, "Bestimmung der Absorption des rothen Lichts in farbigen Flüssigkeiten," *Annalen der Physik und Chemie*, vol. 86, no. 5, pp. 78-88, 1852.
- [4] A. A. Michelson and E. W. Morley, "On the Relative Motion of the Earth and the Luminiferous Ether," *American Journal of Science*, vol. 34, no. 203, pp. 333-345, 1887.
- [5] I. Newton, "New Theory about Light and Colors," *Philosophical Transactions of the Royal Society*, no. 80, pp. 3075-3087, 1672.
- [6] J. v. Fraunhofer, "Bestimmung des Brechungs – und des Farben-Zerstreuungs – Vermögens verschiedener Glasarten, in Bezug auf die Vervollkommnung achromatischer Fernröhre," in *Denkschriften der Königlichen Akademie der Wissenschaften zu München*, 1814, pp. 193-226.
- [7] D. Colladon, "Sur les réflexions d'un rayon de lumière à l'intérieur d'une veine liquide parabolique," *Comptes rendus*, vol. 15, no. 1800, 1842.
- [8] AWE Website, [Online]. Available: <https://www.awe.co.uk/>.
- [9] The Editors of Encyclopaedia Britannica, "Britannica," [Online]. Available: <https://www.britannica.com/science/inch>.
- [10] The Editors of Encyclopaedia Britannica, "Britannica," [Online]. Available: <https://www.britannica.com/science/foot-measurement>.

- [11] D. B. Newell and E. Tiesinga, "The International System of Units (SI)," National Institute of Standards and Technology, 2019.
- [12] "RS PRO 300mm Vernier Caliper," RS Components, [Online]. Available: <https://bit.ly/3t1x3Hj>.
- [13] "RS PRO 600mm Digital Caliper," RS Components, [Online]. Available: <https://bit.ly/2Wq90Wk>.
- [14] "Mitutoyo 293-100-10 External Micrometer," RS Components, [Online]. Available: <https://bit.ly/3Bb6sdB>.
- [15] R. Pieper, A. Cooper and G. Pelegri, "Dual Baseline Triangulation," in *IEEE Proceedings of the Twenty-Seventh Southeastern Symposium on System Theory*, Starkville, MS, USA, 1995.
- [16] G. Berkovic and E. Shafir, "Optical Methods for Distance and Displacement Measurements," *Advances in Optics and Photonics*, vol. 4, pp. 441-471, 2012.
- [17] R. G. Dorsch, G. Häusler and J. M. Herrmann, "Laser Triangulation: Fundamental Uncertainty in Distance Measurement," *Applied Optics*, vol. 33, no. 7, pp. 1306-1314, 1994.
- [18] "Optical Triangulation Devices," MTI Instruments, [Online]. Available: <https://mtiinstruments.com/>.
- [19] H. J. Jordan, M. Wegner and H. Tiziani, "Highly Accurate Non-Contact Characterization of Engineering Surfaces Using Confocal Microscopy," *Measurement Science and Technology*, vol. 9, pp. 1142-1151, 1998.
- [20] H. J. Tiziani and H. M. Uhde, "Three-dimensional image sensing by chromatic confocal microscopy," *Applied Optics*, vol. 33, no. 10, pp. 1838-1843, 1994.
- [21] "Confocal displacement, distance, position and thickness sensors," Micro-Epsilon, [Online]. Available: <https://www.micro-epsilon.co.uk/>.
- [22] "Laser Ranging: A Critical Review of Usual Techniques for Distance Measurement," *Optical Engineering*, vol. 40, no. 1, pp. 10-19, 2001.

- [23] J. S. Massa, G. S. Buller, A. C. Walker, S. Cova, M. Umasuthan and A. M. Wallace, "Time-of-Flight Optical Ranging System Based on Time-Correlated Single-Photon Counting," *Applied Optics*, vol. 37, no. 31, pp. 7298-7304, 1998.
- [24] J. Pehkonen, P. Palojarvi and J. Kostamovaara, "Receiver Channel with Resonance-Based Timing Detection for a Laser Range Finder," *IEEE Transactions on Circuits and Systems I: Regular Papers*, vol. 53, no. 3, pp. 569-577, 2006.
- [25] "UltiSense Laser Range Finder," Safran Vectronix, [Online]. Available: <https://ultisense.safran-vectronix.com/laser-range-finding/>.
- [26] "Time of flight camera," Lucid Vision Labs, [Online]. Available: <https://thinklucid.com/helios-time-of-flight-tof-camera/>.
- [27] M. Born and E. Wolf, in *Principles of Optics*, 6th ed., Pergamon Press Ltd, 1980, pp. 323-327.
- [28] J. C. Wynat, "White Light Interferometry," in *SPIE, Holography: A Tribute to Yuri Denisyuk and Emmet Leith*, 2002.
- [29] Y. N. Denisyuk, "Photographic Reconstruction of the Optical Properties of an Object in Its Own Scattered Radiation Field," *Soviet Physics Doklady*, vol. 7, pp. 543-545, 1962.
- [30] Y. Wu, L. Xia, N. Cai and L. Zhu, "A Highly Precise Demodulation Method for Fiber Fabry-Perot Cavity Through Spectrum Reconstruction," *IEEE Photonics Technology Letters*, vol. 30, no. 5, pp. 435-438, 2018.
- [31] Y.-J. Rao and D. A. Jackson, "Recent Progress in Fibre Optic Low-Coherence Interferometry," *Measurement Science and Technology*, vol. 7, pp. 981-999, 1996.
- [32] B. L. Danielson and C. Y. Boisrobert, "Absolute Optical Ranging Using Low Coherence Interferometry," *Applied Optics*, vol. 30, no. 21, pp. 2975-2979, 1991.
- [33] A. Koch and R. Ulrich, "Fiber-Optic Displacement Sensor with 0.02 μm Resolution by White-Light Interferometry," *Sensors and Actuators A: Physical*, vol. 25, no. 1-3, pp. 201-207, 1990.

- [34] M. L. Dufour, G. Lamouche, S. Vergnole, B. Gauthier, C. Padioleau, M. Hewko, S. Lévesque and V. Bartulovic, "Surface Inspection of Hard to Reach Industrial Parts Using Low-Coherence Interferometry," *Proc. SPIE*, vol. 6343, 2006.
- [35] A. Lee, B. Zhang, C. Ma, A. Wang and Y. Xu, "Fiber-Based White-Light Interferometry for Nanoscale Distance Measurement and Control," *IEEE Photonics Technology Letters*, vol. 24, no. 23, pp. 2136-2138, 2012.
- [36] "High-precision white light interferometers for non-contact distance and thickness measurements," Micro-Epsilon, [Online]. Available: <https://www.micro-epsilon.co.uk/displacement-position-sensors/interferometer/>.
- [37] P. Sandoz, "Wavelet Transform as a Processing Tool in White-Light Interferometry," *Optics Letters*, vol. 22, no. 14, pp. 1065-1067, 1997.
- [38] P. Pavlíček and G. Häusler, "White-Light Interferometer With Dispersion: An Accurate Fiber-Optic Sensor for the Measurement of Distance," *Applied Optics*, vol. 33, no. 15, pp. 2978-2983, 2005.
- [39] F. Depiereux, N. Konig, T. Pfeifer and R. Schmitt, "Fiber-Based White-Light Interferometer With Improved Sensor Tip and Stepped Mirror," *IEEE Transactions on Instrumentation and Measurement*, vol. 56, no. 6, pp. 2279-2283, 2007.
- [40] F. Gueuning, M. Varlan, C. Eugene and P. Dupuis, "Accurate Distance Measurement by an Autonomous Ultrasonic System Combining Time-of-Flight and Phase-Shift Methods," in *IEEE Instrumentation and Measurement Technology Conference*, Brussels, Belgium, 1996.
- [41] "Precise Ultrasonic Distance Sensors," Baumer, [Online]. Available: <https://bit.ly/3Bofi7T>.
- [42] R. Puers, "Capacitive Sensors: When and How to Use Them," *Sensors and Actuators A: Physical*, Vols. 37-38, pp. 93-105, 1993.
- [43] "Capacitive Sensors for Displacement, Distance and Position," Micro-Epsilon, [Online]. Available: <https://bit.ly/2WE1B63>.

- [44] Physik Instrumente, "Sub-Nanometer Resolution Sensors: Nano-Measuring / Nano-Metrology," [Online]. Available: <https://www.pi-usa.us/en/products/capacitive-sensors>. [Accessed 18 10 2022].
- [45] M. C. Escode and M. B. Long, "Rayleigh Scattering Measurements of the Gas Concentration Field in Turbulent Jets," *AIAA Journal*, vol. 21, no. 1, pp. 81-84, 1983.
- [46] A. O. Perez, B. Bierer, P. Eaksen, J. Wöllenstein and S. Palzer, "Gauging Indoor Air Quality with Inexpensive Gas Sensing Technologies," *Procedia Engineering*, vol. 168, pp. 168-171, 2016.
- [47] F. Murena, "Air quality nearby road traffic tunnel portals: BTEX monitoring," *Journal of Environmental Sciences*, vol. 19, no. 5, pp. 578-583, 2007.
- [48] M. Righettoni, A. Amann and S. E. Pratsinis, "Breath analysis by nanostructured metal oxides as chemo-resistive gas sensors," *materialstoday*, vol. 18, no. 3, pp. 163-171, 2015.
- [49] A. H. Naomi Funazaki, S. Ito, Y. Asano, Y. Yano, N. Miura and N. Yamazoe, "Application of semiconductor gas sensor to quality control of meat freshness in food industry," *Sensors and Actuators B: Chemical*, vol. 25, no. 1-3, pp. 797-800, 1995.
- [50] L. Khine, J. M. Tsai, A. Heidari and A. Y.-J. Yoon, "Piezoelectric MEMS Resonant Gas Sensor for Defence Applications," *Defence Science Research Conference and Expo*, pp. 1-3, 2011.
- [51] W. Wang, X. Liu, S. Mei, Y. Jia, M. Liu, X. Xue and D. Yang, "Development of a Pd/Cu Nanowires Coated SAW Hydrogen Gas Sensor with Fast Response and Recovery," *Sensors and Actuators B*, vol. 287, pp. 157-164, 2019.
- [52] Y. -C. Lee, S. -W. Cheng, C. -L. Cheng and W. Fang, "Design and Implementation of Gas Sensor Array Based on Fluorescence Quenching Detection Using CMOS-MEMS Process," in *2017 19th International Conference on Solid-State Sensors, Actuators and Microsystems (TRANSDUCERS)*, Taiwan, 2017.

- [53] P. Shuk and R. Jantz, "Oxygen Gas Sensing Technologies: A Comprehensive Review," in *International Conference on Sensing Technology*, Auckland, New Zealand, 2015.
- [54] A. A. Tomchenko, I. L. Emelianov and V. V. Khatko, "Tungsten Trioxide-Based Thick-Film NO Sensor: Design and Investigation," *Sensors and Actuators B*, vol. 57, pp. 166-170, 1999.
- [55] A. C. Power and A. Morrin, "Electroanalytical Sensor Technology (Chapter 7)," in *Electrochemistry*, InTech, 2013, p. 38.
- [56] "O₂ Sensor InPro6950iG/12/220," Mettler Toledo, [Online]. Available: <https://bit.ly/3j5wWqz>.
- [57] J. R. Stetter, "Amperometric Gas Sensors - A Review," *Chemical Reviews*, vol. 108, no. 2, pp. 352-336, 2008.
- [58] J. Li, Y. Lu, M. Cinke, J. Han and M. Meyyappan, "Carbon Nanotube Sensors for Gas and Organic Vapor Detection," *Nano Letters*, vol. 3, no. 7, pp. 929-993, 2003.
- [59] N. R. Stradiotto, H. Tamanaka and M. V. B. Zanoni, "Electrochemical Sensors: A Powerful Tool in Analytical Chemistry," *Journal of the Brazilian Chemical Society*, vol. 14, no. 2, pp. 159-173, 2003.
- [60] J. Bobacka, A. Ivaska and A. Lewenstam, "Potentiometric Ion Sensors," *Chemical Reviews*, vol. 108, no. 2, pp. 329-351, 2008.
- [61] "PZA-MC25-P Potentiometric Zirconia Oxygen Gas Sensor Module," Angst+Pfister, [Online]. Available: <https://bit.ly/3keODTT>.
- [62] N. Yamazoe and N. Miura, "Potentiometric Gas Sensors of Oxidic Gases," *Journal of Electroceramics*, vol. 2, no. 4, pp. 243-255, 1998.
- [63] J. M. Rheaume and A. P. Pisano, "A review of recent progress in sensing of gas concentration by impedance change," *Ionics*, vol. 17, no. 2, pp. 99-108, 2011.
- [64] C. Baratto, G. Sberveglieri, A. Onischuk, B. Caruso and S. d. Stasio, "Low Temperature Selective NO₂ Sensors by Nanostructured Fibres of ZnO," *Sensors and Actuators B*, vol. 100, pp. 261-265, 2004.

- [65] S. Fanget, S. Hentz, P. Puget, J. Arcamone, M. Matheron, E. Colinet, P. Andreucci, L. Duraffourg, E. Myers and M. L. Roukes, "Gas sensors based on gravimetric detection - A review," *Sensors and Actuators B: Chemical*, vol. 160, no. 1, pp. 804-821, 2011.
- [66] F. M. Battiston, J.-P. Ramseyer, H. P. Lang and H.-J. G. Èntherodt, "A chemical sensor based on a microfabricated cantilever array with simultaneous resonance-frequency and bending readout," *Sensors and Actuators B Chemical*, vol. 77, no. 1-2, pp. 122-131, 2001.
- [67] M. C. Dixon, "Quartz Crystal Microbalance with Dissipation Monitoring: Enabling Real-Time Characterization of Biological Materials and Their Interactions," *Journal of Biomolecular Techniques*, vol. 19, no. 3, pp. 151-158, 2008.
- [68] G. Sauerbrey, "Verwendung von Schwingquarzen zur Wägung dünner Schichten und zur Mikrowägung," *Zeitschrift für Physik*, vol. 155, no. 2, pp. 206-222, 1959.
- [69] A. Mujahid and F. L. Dickert, "Surface Acoustic Wave (SAW) for Chemical Sensing Applications of Recognising Layers," *Sensors*, vol. 17, no. 12, 2017.
- [70] C. Jiao, X. Jiang, H. Chu, H. Jiang and L. Sun, "A Mixed-Valent Cu^I/Cu^{II} Metal-Organic Framework with Selective Chemical Sensing Properties," *CrystEngComm*, vol. 18, no. 44, pp. 8683-8687, 2016.
- [71] R. P. Kovacich, N. A. Martin, M. G. Clift, C. Stocks, I. Gaskin and J. Hobby, "Highly accurate measurement of oxygen using a paramagnetic gas sensor," *Measurement Science and Technology*, vol. 17, pp. 1579-1585, 2006.
- [72] A. C. Manning, R. F. Keeling and J. P. Severinghaus, "Precise atmospheric oxygen measurements with a paramagnetic oxygen analyzer," *Global Biogeochemical Cycles*, vol. 13, no. 4, pp. 1107-1115, 1999.
- [73] D. R. Lide, *CRC Handbook of Chemistry and Physics*, CRC Press, 1992.
- [74] P. Gründler, *Chemical Sensors: An Introduction for Scientists and Engineers*, Dresden: Springer, 2006.

- [75] E. Comini, G. Faglia and G. Sberveglieri, *Solid State Gas Sensing*, Springer, 2008, pp. 241-244.
- [76] G. Korotcenkov, "Practical aspects in design of one-electrode semiconductor gas sensors: status report," *Sensors and Actuators B Chemical*, vol. 121, pp. 664-678, 2007.
- [77] T. Hübert, L. Boon-Brett, G. Black and U. Banach, "Hydrogen sensors – A review," *Sensors and Actuators B: Chemical*, vol. 157, no. 2, pp. 329-352, 2011.
- [78] M. A. Yücel, J. Selb, D. A. Boas, S. S. Cash and R. J. Cooper, "Reducing motion artifacts for long-term clinical NIRS monitoring using collodion-fixed prism-based optical fibers," *NeuroImage*, vol. 85, no. 1, pp. 192-201, 2014.
- [79] C. Kim, I.-B. Sohn, H. Park, Y. J. Lee and H. Lee, "Comparison of laser-assisted damage in soft tissue using bi-directional and forward-firing optical fiber," *Optics & Laser Technology*, vol. 56, pp. 196-201, 2014.
- [80] X. Li, Q. Li, H. Zhou, H. Hao, T. Wang, S. Zhao, Y. Lu and G. Huang, "Rapid, on-site identification of explosives in nanoliter droplets using a UV reflected fiber optic sensor," *Analytica Chimica Acta*, vol. 751, pp. 112-118, 2012.
- [81] J. B. Rosolem, F. R. Bassan, R. S. Penze, A. A. Leonardi, J. P. V. Fracarolli and C. Florida, "Optical sensing in high voltage transmission lines using power over fiber and free space optics," *Optical Fiber Technology*, vol. 26, pp. 180-183, 2015.
- [82] M. L. Polanyi and R. M. Hehir, "In Vivo Oximeter with Fast Dynamic Response," *Review of Scientific Instruments*, vol. 1050, no. 33, 1962.
- [83] A. Lobnik, "Absorption-Based Sensors (Chapter 5)," in *Optical Chemical Sensors*, Erice, Springer, 2004.
- [84] C. E. C. Artime, J. A. Baro, M. A. P. Garcia, R. M. Vega and N. Corral, "On-line Estimation of Fresh Milk Composition by means of VIS-NIR Spectrometry and Partial Least Squares Method (PLS)," in *Instrumentation and Measurement Technology Conference*, 2008.
- [85] D. R. Herriott and H. J. Schulte, "Folded Optical Delay Lines," *Applied Optics*, vol. 4, no. 8, pp. 883-889, 1965.

- [86] J. U. White, "Long Optical Paths of Large Aperture," *Journal of the Optical Society of America*, vol. 32, no. 5, pp. 285-288, 1942.
- [87] A. O'Keefe and D. A. G. Deacon, "Cavity Ring-Down Optical Spectrometer for Absorption Measurements Using Pulsed Laser Sources," *Review of Scientific Instruments*, vol. 59, no. 12, pp. 2544-2551, 1988.
- [88] R. Engeln, G. Berden, R. Peeters and G. Meijer, "Cavity Enhanced Absorption Spectroscopy and Cavity Enhanced Magnetic Rotation Spectroscopy," *Review of Scientific Instruments*, vol. 69, no. 11, pp. 3763-3769, 1998.
- [89] J. Hodgkinson and R. P. Tatam, "Optical Gas sensing: A Review," *Measurement Science and Technology*, vol. 24, no. 1, 2013.
- [90] C.-S. Chu, Y.-L. Lo and T.-W. Sung, "Review on Recent Developments of Fluorescent Oxygen and Carbon Dioxide Optical Fiber Sensors," *Photonic Sensors*, vol. 1, no. 3, pp. 234-250, 2011.
- [91] G. Orellana, "Fluorescence-Based Sensors (Chapter 6)," in *Optical Chemical Sensors*, Madrid, Springer, 2004.
- [92] I. A. A. Terra, R. C. Sanfelice, G. T. Valente and D. S. Correa, "Optical Sensor Based on Fluorescent PMMA/PFO Electrospun Nanofibers for Monitoring Volatile Organic Compounds," *Applied Polymer Science*, vol. 135, no. 14, p. 46128, 2017.
- [93] M. G. Guillén, F. Gámez, T. Lopes-Costa, J. Cabanillas-González and J. M. Pedrosa, "A Fluorescence Gas Sensor Based on Förster Resonance Energy Transfer Between Polyfluorene and Bromocresol Green Assembled in Thin Films," *Sensors and Actuators B*, vol. 236, pp. 136-143, 2016.
- [94] T. He, Y. Wang, X. Tian, Y. Gao, X. Zhao, A. C. Grimsdale, X. Lin and H. Sun, "An Organic Dye With Very Large Stokes-Shift and Broad Tunability of Fluorescence: Potential Two-Photon Probe for Bioimaging and Ultra-Sensitive Solid-State Gas Sensor," *Applied Physics Letters*, vol. 108, no. 1, p. 011901, 2016.
- [95] L. J. Blum and C. A. Marquette, "Chemiluminescence-Based Sensors (Chapter 8)," in *Optical Chemical Sensors*, Cedex, Springer, 2004.

- [96] Z. Zhanf, S. Zhang and X. Zhang, “Recent Developments and Applications of Chemiluminescence Sensors,” *Analytica Chimica Acta*, vol. 541, pp. 37-47, 2005.
- [97] T. Vo-Dinh and F. Yan, “Surface-Enhanced Raman Scattering (Chapter 12),” in *Optical Chemical Sensors*, Tennessee, Springer, 2004.
- [98] H. Tang, C. Zhu, G. Meng and N. Wu, “Review - Surface-Enhanced Raman Scattering Sensors for Food Safety and Environmental Monitoring,” *Journal of The Electrochemical Society*, vol. 165, no. 8, pp. 3098-3118, 2018.
- [99] M. Suter and P. Dietiker, “Calculation of the Finesse of an Ideal Fabry-Perot Resonator,” *Applied Optics*, vol. 53, no. 30, pp. 7004-7010, 2014.
- [100] G. Hernandez, *Fabry-Perot Interferometers*, Cambridge: Cambridge University Press, 1986.
- [101] H. F. Taylor, “Fiber Optic Sensors Based upon the Fabry-Perot Interferometer,” in *Fiber Optic Sensors*, S. Yin, P. B. Ruffin and F. T. S. Yu, Eds., CRC Press, 2008, pp. 35-64.
- [102] E. Hecht, “Polarization by Reflection,” in *Optics*, Pearson Education Limited, pp. 363-366.
- [103] D. B. Judd, “Fresnel Reflection of Diffusely Incident Light,” *Journal of Research of the National Bureau of Standards*, vol. 29, 1942.
- [104] K. T. Ajoy Ghatak, *Introduction to fiber optics*, Cambridge University Press, 1997.
- [105] Thorlabs, “Single Mode Fiber,” [Online]. Available: <https://bit.ly/3C0LGhi>. [Accessed 03 10 2022].
- [106] R. N. Bracewell, *The Fourier Transform and Its Applications*, McGraw-Hill, 1986.
- [107] W. T. Cochran, J. W. Cooley, D. L. Favin, H. D. Helms, R. A. Kaenel, W. W. Lang, G. C. M. Jr., D. E. Nelson, C. M. Rader and P. D. Welch, “What Is The Fast Fourier Transform?,” *IEEE*, vol. 55, no. 10, pp. 1664-1674, 1967.
- [108] J. W. Cooley, P. A. W. Lewis and P. D. Welch, “The Fast Fourier Transform and Its Applications,” *IEEE Transactions on Education*, vol. 12, no. 1, pp. 27-34, 1969.

- [109] Y. Jiang, “Fourier Transform White-Light Interferometry for the Measurement of Fiber-Optic Extrinsic Fabry–Pérot Interferometric Sensors,” *IEEE Photonics Technology Letters*, vol. 20, no. 2, pp. 75-77, 2008.
- [110] T. Bodendorfer, M. S. Müller, F. Hirth and A. W. Koch, “Comparison of Different Peak Detection Algorithms with Regards to Spectrometric Fiber Bragg Grating Interrogation Systems,” *International Symposium on Optomechatronic Technologies*, pp. 122-126, 2009.
- [111] National Instruments, “Peak Detection Using LabVIEW and Measurement Studio,” 04 02 2020. [Online]. Available: <https://bit.ly/3giFrj7>. [Accessed 22 10 2022].
- [112] RP Photonics, “Where to Buy Multi-core Fibers,” [Online]. Available: https://www.rp-photonics.com/bg/buy_multi_core_fibers.html. [Accessed 03 10 2022].
- [113] “FC/APC Fiber Connectors: Single Mode,” Thorlabs, Inc, [Online]. Available: https://www.thorlabs.com/newgrouppage9.cfm?objectgroup_id=6246. [Accessed 09 08 2021].
- [114] M. Hermans, J. Gottman and F. Riedel, “Selective, Laser-Induced Etching of Fused Silica at High Scan-Speeds Using KOH,” *Journal of Laser Micro/Nanoengineering*, 2014.
- [115] J. Qi, Z. Wang, J. Xu, Z. Lin, X. Li, W. Chu and Y. Cheng, “Femtosecond Laser Induced Selective Etching in Fused Silica: Optimisation of the Inscription Conditions with a High-Repetition-Rate Laser,” *Optics Express*, vol. 26, no. 23, pp. 29669-29678, 2018.
- [116] C. A. Ross, D. G. MacLachlan, D. Choudhury and R. R. Thomson, “Optimisation of Ultrafast Laser Assisted Etching in Fused Silica,” *Optics Express*, vol. 26, no. 19, pp. 24343-24356, 2018.
- [117] C. A. Ross, D. MacLachlan, D. Choudhury and R. R. Thomson, “Towards Optical Quality Micro-Optic Fabrication by Direct Laser Writing and Chemical Etching,” in *SPIE LASE*, 2017.

- [118] Y. Suzaki and A. Tachibana, "Measurement of the Gaussian Laser Beam Divergence," *Applied Optics*, vol. 16, no. 6, pp. 1481-1482, 1977.
- [119] A. M. K. Jr. and F. Bucholtz, "Beam Divergence from an SMF-28 Optical Fiber," Naval Research Laboratory, Washington, DC, 2006.
- [120] "Norland Optical Adhesive 61," Norland Products, [Online]. Available: <https://www.norlandprod.com/adhesives/NOA%2061.html>.
- [121] D. F. Swinehart, "The Beer-Lambert Law," *Journal of Chemical Education*, vol. 39, no. 7, pp. 333-335, 1962.
- [122] C. F. Bohren and D. R. Huffman, *Absorption and Scattering of Light by Small Particles*, New York: Wiley, 1983.
- [123] T. G. Mayerhöfer, S. Pahlow and J. Popp, "The Bouguer-Beer-Lambert Law: Shining Light on the Obscure," *ChemPhysChem*, vol. 21, no. 18, pp. 2029-2046, 2020.
- [124] A. Mason, S. C. Mukhopadhyay and K. P. Jayasundera, "Evanescent Wave Absorption Based Fiber-Optic Sensor - Cascading of Bend and Tapered Geometry for Enhanced Sensitivity," in *Sensing Technology: Current Status and Future Trends III*, Springer, 2015, pp. 22-45.
- [125] J. P. Golden, G. P. Anderson, S. Y. Rabbany and F. S. Ligler, "An Evanescent Wave Biosensor - Part II: Fluorescent Signal Acquisition from Tapered Fiber Optic Probes," *IEEE Transactions on Biomedical Engineering*, vol. 41, no. 6, pp. 585-591, 1994.
- [126] S.-M. Tseng and C.-L. Chen, "Side-Polished Fibers," *Applied Optics*, vol. 31, no. 18, pp. 3438-3447, 1992.
- [127] Z. Zhao and Y. Duan, "A low cost fiber-optic humidity sensor based on silica sol-gel film," *Sensors and Actuators B: Chemical*, vol. 160, pp. 1340-1345, 2011.
- [128] A. K. Sharma, J. Gupta and I. Sharma, "Fiber optic evanescent wave absorption-based sensors: A detailed review of advancements in the last decade (2007–18)," *Optik*, vol. 183, pp. 1008-1025, 2019.

- [129] S. Sekimoto, H. Nakagawa, S. Okazaki, K. Fukuda, S. Asakura, T. Shigemiro and S. Takahashi, "A fiber-optic evanescent-wave hydrogen gas sensor using palladium-supported tungsten oxide," *Sensors and Actuators B: Chemical*, vol. 66, no. 1-3, pp. 142-145, 2000.
- [130] S. Sharifpour-Boushehri, S. M. Hosseini-Golgoo and M.-H. Sheikhi, "A low cost and reliable fiber optic ethanol sensor based on nano-sized SnO₂," *Optical Fiber Technology*, vol. 24, pp. 93-99, 2015.
- [131] S. K. Khijwania, K. L. Srinivasan and J. P. Singh, "An evanescent-wave optical fiber relative humidity sensor with enhanced sensitivity," *Sensors and Actuators B: Chemical*, vol. 104, no. 2, pp. 217-222, 2005.
- [132] J. Mathew, Y. Semenova and G. Farrel, "A fiber bend based humidity sensor with a wide linear range and fast measurement speed," *Sensors and Actuators A: Physical*, vol. 174, pp. 47-51, 2012.
- [133] B. Renganathan, D. Sastikumar, G. Gobi, N. R. Yogamalar and A. C. Bose, "Gas sensing properties of a clad modified fiber optic sensor with Ce, Li and Al doped nanocrystalline zinc oxides," *Sensors and Actuators B: Chemical*, vol. 156, pp. 263-270, 2011.
- [134] M. Batumalay, Z. Harith, H. A. Rafaie, F. Ahmad, M. Khasanah, S. W. Harun, R. M. Nor and H. Ahmad, "Tapered plastic optical fiber coated with ZnO nanostructures for the measurement of uric acid concentrations and changes in relative humidity," *Sensors and Actuators A: Physical*, vol. 210, pp. 190-196, 2014.
- [135] R. Jarzebinska, S. Korposh, S. James, W. Batty, R. Tatam and S.-W. Lee, "Optical Gas Sensor Fabrication Based on Porphyrin-Anchored Electrostatic Self-Assembly onto Tapered Optical Fibers," *Analytical Letters*, vol. 45, no. 10, pp. 1297-1309, 2012.
- [136] A. J. Y. Tan and P. Stoddart, "Theoretical Model and Design Considerations of U-Shaped Fiber Optic Sensors: A Review," *IEEE Sensors Journal*, vol. 20, no. 24, pp. 14578-14589, 2020.

- [137] S. Abrate, "Handbook of Fiber Optic Data Communication," Academic Press, 2013, pp. 37-54.
- [138] G. Gagliardi and H.-P. Loock, *Cavity-Enhanced Spectroscopy and Sensing*, vol. 179, Springer, 2014.
- [139] A. Aalto, G. Genty, T. Laurila and J. Toivonen, "Incoherent broadband cavity enhanced absorption spectroscopy using supercontinuum and superluminescent diode sources," *Optics Express*, vol. 23, no. 19, pp. 25225-25234, 2015.
- [140] J. U. White, "Very Long Optical Paths in Air," *Journal of the Optical Society of America*, vol. 66, no. 5, pp. 411-416, 1976.
- [141] S. E. Fiedler, A. Hese and A. A. Ruth, "Incoherent Broad-Band Cavity-Enhanced Absorption Spectroscopy," *Chemical Physics Letters*, vol. 371, no. 3-4, pp. 284-294, 2003.
- [142] J. M. Langridge, T. Laurila, R. S. Watt, R. L. Jones, C. F. Kaminski and J. Hult, "Cavity enhanced absorption spectroscopy of multiple trace gas species using a supercontinuum radiation source," *Optics Express*, vol. 16, no. 14, pp. 10178-10188, 2008.
- [143] S. E. Fiedler, A. Hese and A. A. Ruth, "Incoherent broad-band cavity-enhanced absorption spectroscopy of liquids," *Review of Scientific Instruments*, vol. 76, no. 2, p. 023107, 2004.
- [144] S. E. Fiedler, A. Hese and U. Heitmann, "Influence of the cavity parameters on the output intensity in incoherent broadband cavity-enhanced absorption spectroscopy," *Review of Scientific Instruments*, vol. 78, no. 7, p. 073104, 2007.
- [145] A. C. Vandaele, C. Hermans, P. C. Simon, M. Carleer, R. Colin, S. Fally, M. F. Mérienne, A. Jenouvrier and B. Coquart, "Measurements of the NO₂ absorption cross-section from 42 000 cm⁻¹ to 10 000 cm⁻¹ (238–1000 nm) at 220 K and 294 K," *Journal of Quantitative Spectroscopy and Radiative Transfer*, vol. 59, no. 3-5, pp. 171-184, 1998.
- [146] I. E. Gordon, "The HITRAN Database," [Online]. Available: <https://hitran.org/>. [Accessed 30 07 2021].

- [147] Bureau International des Poids et Mesures, “The International System of Units (SI),” 2019. [Online]. Available: <https://www.bipm.org/en/publications/si-brochure/>.
- [148] A. Yariv, Quantum Electronics, Wiley, 1989.
- [149] W. Demtröder, Laser Spectroscopy: Basic Concepts and Instrumentation, Berlin: Springer, 2003.
- [150] C. Palmer, Diffraction Grating Handbook, New York: Richardson Grating Laboratory, 2000.
- [151] C. A. Harper and E. M. Petrie, Plastics Materials and Processes: A Concise Encyclopedia, New Jersey: John Wiley & Sons, 2003.
- [152] X. Ning, C. L. Zhao, J. Yang and C. C. Chan, “Zeolite Thin Film-Coated Spherical End-Face Fiber Sensors for the Detection of Trace Organic Vapors,” *Optics Communications*, vol. 364, pp. 55-59, 2016.
- [153] X. Xu, J. Wang and Y. Long, “Zeolite-Based Materials for Gas Sensors,” *Sensors*, vol. 6, no. 12, pp. 1751-1764, 2006.
- [154] I. Sasaki, H. Tsuchiya, M. Nishioka, M. Sadakata and T. Okubo, “Gas Sensing with Zeolite-Coated Quartz Crystal Microbalances — Principal Component Analysis Approach,” *Sensors and Actuators B: Chemical*, vol. 86, pp. 26-33, 2002.
- [155] R. Moos, R. Müller, C. Plog, A. Knezevic, H. Leye, E. Irion, T. Braun, K.-J. Marquardt and K. Binder, “Selective Ammonia Exhaust Gas Sensor for Automotive Applications,” *Sensors and Actuators B: Chemical*, vol. 83, no. 1-3, pp. 181-189, 2002.
- [156] H. Xiao, J. Zhang, J. Dong, M. Luo, R. Lee and V. Romero, “Synthesis of MFI Zeolite Films on Optical Fibers for Detection of Chemical Vapors,” *Optics Letters*, vol. 30, no. 11, pp. 1270-1272, 2005.
- [157] B. Wu, C. Zhao and J. Kang, “Formaldehyde Sensor Based on Zeolite Thin Film-Coated Spherical End-Face Fiber,” in *International Conference on Optical Communications and Networks*, 2016.

- [158] S. Mintova, N. Barrier, H. Robson and K. P. Lillerud, Verified Synthesis of Zeolitic Materials, Synthesis Commission of the International Zeolite Association, 2016.
- [159] N. Liu, J. Hui, C. Sun, J. Dong, L. Zhang and H. Xiao, "Nanoporous Zeolite Thin Film-Based Fiber Intrinsic Fabry-Perot Interferometric Sensor for Detection of Dissolved Organics in Water," *Sensors*, vol. 6, pp. 835-847, 2006.
- [160] B. Wu, C. Zhao, J. Kang and D. Wang, "Characteristic Study on the Volatile Organic Compounds Optical Fiber Sensor with Zeolite Thin Film-Coated Spherical End," *Optical Fiber Technology*, vol. 34, pp. 91-97, 2017.